SAPIENZA
UNIVERSITÀ DI ROMA

Hybrid plasmonic nanoparticle assemblies with tunable properties for biophysical applications

Modelli Matematici per l'Ingegneria, Elettromagnetismo e Nanoscienze

Dottorato di Ricerca in Scienza dei Materiali (FIS/03,FIS/07) – XXXII Ciclo

Candidate

Angela Capocefalo

ID number 1414512

Thesis Advisor

Prof. Paolo Postorino

Co-Advisor

Dr. Fabio Domenici

February 2020

Thesis defended on February 19, 2020
in front of a Board of Examiners composed by:

Prof. Massimo Gurioli (chairman)

Prof. Claudio Goletti

Prof. Laura Micheli

Hybrid plasmonic nanoparticle assemblies with tunable properties for biophysical applications

Ph.D. thesis. Sapienza – University of Rome

© 2020 Angela Capocefalo. All rights reserved

This thesis has been typeset by LaTeX and the Sapthesis class.

Author's email: angela.capocefalo@uniroma1.it

Contents

Introduction **v**
Thesis outline viii

1 Plasmonics from nanostructured materials: fundamentals and applications in biosensing **1**
1.1 Localised surface plasmons 2
1.2 Near-field coupling between localised surface plasmons 9
1.2.1 Plasmon hybridisation theory 9
1.2.2 Plasmon coupling in large nanoparticle assemblies 13
1.3 Surface enhanced spectroscopies 15
1.3.1 Surface Enhanced Infrared Absorption (SEIRA) 18
1.3.2 Surface Enhanced Raman Scattering (SERS) 20
1.4 Current trends in plasmonic-based biosensors 22

2 Bioplasmonic assemblies with tunable optical and functional properties **25**
2.1 Theoretical principles of charge patch interactions 27
2.2 Self-assembly and colloidal stability: towards a controlled aggregation 29
2.2.1 Assessing the surface coverage by ζ-potential measurements . 31
2.2.2 Structural characterisation of the assemblies 33
2.3 Tailoring the plasmonic response of the assemblies 37
2.3.1 Assessing the surface coverage by the LSPR redshift 38
2.4 Effect of the pH on the aggregation phenomenology: modulation and reversibility 42
2.5 Monitoring the catalytic activity of the adsorbed proteins 44

3 Nanoparticle-based SERS substrate for cellular pH sensing **49**
3.1 Nanosensor assembling 51
3.2 Nanosensor stability 53
3.2.1 Colloidal stability 54
3.2.2 Photostability 55
3.3 SERS responsiveness to pH variations and calibration of the nanosensor 57
3.4 *In vitro* pH detection of living cells 61

4 Ultrasound delivery of SEIRA-active gold nanoprobes into fibroblast cells and related biological effects **65**
4.1 Analysis of the SEIRA signal enhancement of the nanoprobe 67

4.2 SEIRA-based biorecognition of the nanoprobe 70
4.2.1 US irradiation of the cells 70
4.2.2 Evaluation of the uptake efficiency 71
4.3 Analysis of the biological effects induced by internalisation of the nanoprobe 73
4.3.1 Spectral analysis of the SR-microFTIR spectra of single cells 74
4.3.2 Cytotoxicity and genotoxicity assays 76

5 Antifolate SERS-active nanovectors: quantitative drug nanostructuring and selective cell targeting for effective theranostics 79
5.1 Synthesis of the antifolate nanovectors and therapeutic action 82
5.2 Assessing the drug concentration 84
5.2.1 Colorimetric titration assay 84
5.2.2 SERS-based titration 85
5.3 SERS screening on treated HeLa and HaCaT cells 87
5.4 Comparative cytotoxicity 90
5.5 Coloaded folate/antifolate nanovector 92

6 Plasmon enhanced nano-spectroscopy study of gold nanoparticles interaction with protein fibrils 95
6.1 Principles of Tip Enhanced Raman Spectroscopy 97
6.2 Morphological and nanoscale spectroscopic characterisation of lysozyme fibrils 99
6.3 Analysis of fibril-gold nanoparticles interaction 104

Conclusions 108

A Experimental details 113

List of publications 119

Bibliography 121

Introduction

In recent years nanoplasmonics has attracted increasing scientific interest arising from the possibility of manipulating the optical phenomena at the interface of nanostructured materials [1, 2]. Indeed, advances in nanofabrication techniques enabled for tailoring and enhancing electromagnetic fields at the sub-wavelength scale, opening to a wide range of applications in different scientific contexts, spreading from electronics to biomedicine [3].

Among the different nanoarchitectures available, a relevant position is occupied by systems made of nanoparticles (NPs) of noble metals such as gold and silver. Their optical properties are determined by the excitation of the collective oscillations of the free electron plasma of the metal, namely the localised surface plasmons, that results in the resonant absorption of the electromagnetic radiation and in the confinement of intense electromagnetic fields at the NPs surface. The peculiarity of metallic NPs stems from the wide opportunity of tailoring the resonance frequency of the charge density oscillations, the localised surface plasmon resonance (LSPR), by acting on a series of factors such as the NPs size, shape and material, the nature of the surrounding medium and the spatial organisation of neighboring NPs. This latter aspect probably provides the most versatile degree of freedom in modulating the LSPR. In fact, from dimers to more complex architectures, when NPs are few nanometres distant, the single localised modes interfere giving rise to new interparticle absorption modes at lower frequencies that considerably expand the accessible spectral range [4, 5]. Since for noble metals this spectral window can spread from visible to near- and mid- infrared, these plasmonic materials are particularly employed in the study of biosystems. In addition, even more intense electromagnetic fields result confined in the interstices between adjacent NPs, which are usually defined as “hot spots” [6].

In this view, particular interest has been devoted to the broad possibilities offered by plasmonics in the field of biosensing. Benefiting of the high sensitivity of LSPR to changes in the refractive index at the metal-dielectric interface, plasmonic NPs have been employed for realising optical sensors for the recognition of biomolecular interactions including adhesion of small molecules, ligand–receptor binding, protein adsorption and DNA hybridisation [7, 8, 9].

The nanoscale localisation of intense fields has been extensively harnessed for the spectroscopic investigation of the NPs environment, boosting the sensitivity limits of traditional spectroscopies [10, 11]. Indeed, the focusing of strong electromagnetic fields at the NPs surface results in the enhancement of the optical cross section of analytes located in proximity of the metallic surface, providing a sort of nanoantenna effect. Depending on the spectral region of interest and on the LSPR of the plasmonic

substrate, the most prominent surface enhanced spectroscopies are those based on infrared and Raman vibrational spectroscopies defined as Surface Enhanced InfRared Absorption (SEIRA) and Surface Enhanced Raman Scattering (SERS), respectively. In these fields, the merging of the molecular specificity of vibrational fingerprints and the enhanced sensitivity provided by the plasmonic scaffold paved the way for the development of novel ultrasensitive detection methodologies. Specifically, SEIRA is particularly suitable for studying proteins, lipid bilayers and single cells [12, 13, 14]; while SERS, which experiences the highest signal enhancement, proved is worth as powerful analytical tool early as the late nineties, achieving the single molecule detection [15, 16]. SERS is currently widely employed in biomolecular sensing, being at the basis of devices and sensors capable to actively and selectively interact with complex biological systems, including cells and tissues [17, 18, 19].
Further advances in enhanced spectroscopies have been achieved by the implementation of Tip Enhanced Raman Spectroscopy (TERS), which combines SERS spectroscopy with the high spatial resolution of scanning probe microscopies [20]. The key component of TERS is a plasmonic active tip that simultaneously acts as Raman signal amplifier and topography scanner. The exceptional spatial resolution of this technique led to unique results in mapping protein fibrils with a single amino acid resolution [21] and even in DNA sequencing [22, 23].

Another aspect that makes metallic NPs extremely versatile is the possibility of conjugating their surface with functional groups, that allows for regulating the overall chemical reactivity and dispersibility in various solvents [24]. In this way it has been possible to develop several systems for nanomedicine application, both in diagnosis and in drug delivery. Along with the strongly enhanced scattering cross sections, the conjugation of NPs with molecular labels allowed for the spatial tracing within biological systems, thus providing highly contrasted optical imaging [25, 26]. The possibility for tuning the LSPR in the near infrared spectral range, where the transmission of biological tissues is the highest, by the guided assembly of properly functionalised NPs paved the way for the development of novel therapeutic strategies [27]. In this sense, photothermal cancer therapy exploits the local heating due to the strong absorption of irradiated NPs for inducing cancer cell death [28, 29, 30]. Hybrid plasmonic nanovectors have been employed as invaluable carriers in targeting cancer cells, exhibiting promising loading efficiency of chemotherapeutics as well as selectivity towards different tumours, even in synergistic photothermal and gene combined approaches [31, 19, 32].

My Ph.D. Thesis fits within the above scientific context and it is aimed at addressing the design of plasmonic nanostructures with the desired optical and biological properties. The general idea is to reach a strict control on the spatial organisation and surface properties of gold NP assemblies for mastering the plasmon coupling and the interaction with the external environment. Efforts have been made in quantitatively framing the presented studies in the context of nanoplasmonics theory, and in developing interpretative models for the specific phenomena studied. The results were supported by biological investigation with the purpose of providing a strong scientific background in transferring the obtained findings towards the development of novel biophysical strategies. The broad experimental activity required to this work provided me the opportunity of acquiring a deep knowledge on the

sample synthesis as well as on several experimental techniques such as vibrational and absorption spectroscopies, dynamic light scattering, near field microscopies and small angle scattering.

The research activity was conducted in the Physics Department of Sapienza University of Rome, focusing on three main topics. The first one is the fine tuning of the optical and biofunctional properties of a plasmonic system realised by interfacing gold NPs with a functional protein. The active interplay with the biological component was exploited for modulating the structural organisation of the NPs and thus the optical response of the system. This allowed at the same time for preserving the functional aspect of the protein and for handling its biological activity.

The second research topic involves the application of surface enhanced spectroscopies in biosensing. The surface derivatisation versatility of gold NPs was harnessed by employing molecules with *ad hoc* properties for designing nanodevices showing controllable interaction with the environment or with complex system such as cells, hence enabling their application as local probes for identifying specific features of interest. Specifically, a pH-sensitive Raman reporter was used for developing a SERS-active substrate suitable as pH nanosensor capable for monitoring both the cellular microenvironment and for distinguish the extracellular pH of different type of cells. The ultrasound induced transient poration of the cell membrane was exploited for internalising SEIRA-labelled probes into fibroblast cells and for studying the related bioeffects at the single cell scale. In the perspective of addressing more refined clinical issues, plasmonic nanvectors were synthesised with biofunctional interfaces that allowed for managing the interaction with different cell lines. Folic acid was chosen to this aim, because of its key role in cellular metabolism and reproduction, and due to the overexpression of folic acid receptors on cancer cell membrane that allowed for highly selective targeting.

The last part of this Thesis concerns a research work carried out in the framework of Ph.D. students mobility project *pERSON: Enhanced Raman Spectroscopy fOr Nanomedicine*, funded by Sapienza University. Experiments were performed in collaboration with the *Nanospectroscopy* research group at Friedrich Schiller University of Jena (Germany), under the supervision of Prof. V. Deckert. The main objective of this project was the investigation of the gold NPs interaction with biological molecules. It is in fact known that structural destabilisation of biomacromolecules can be induced by NPs. In particular, this phenomenon was studied in the case of a pathological species, namely the amyloid fibrils, recognising their degradation after interaction with NPs. In the perspective of determining potential mechanisms that could lead to the elimination of toxic species, amyloid fibrils were analysed at the single amino acid level by exploiting the peculiar high spatial resolution of TERS.

Thesis outline

In **Chapter 1**, the theoretical bases of plasmonics from nanostructured materials are presented. The plasmonic response of a single metallic spherical NP is firstly described and discussed with respect to the intrinsic features of the NP and to the dielectric properties of the dispersing medium. The collective optical response of NP assemblies is analysed in the near-field coupling regime, discussing examples of general interest. Afterwards the surface enhanced spectroscopies are presented. Specifically, in the case of SEIRA and SERS, the corresponding optical spectroscopies are introduced in the framework of the radiation-matter interaction and the signal amplification is discussed in terms of the *chemical* and *electromagnetic mechanism* contributions. In the final Section a brief overview of the state of the art in plasmonic-based biosensing is provided.

In **Chapter 2**, the realisation of a bioplasmonic system based on the self-limited assembly in solution of gold NPs decorated by a functional protein, lysozyme, is described. The electrostatic driven assembly process, described by the *charge patch* interaction theory was exploited in order to obtain stable aggregates with selected size. The overall properties of the system were thoroughly analysed, allowing for obtaining a strict control on its structure, optical response and biological function. The theoretical principles of the Velegol and Thwar theory for colloids with non-uniform surface charge are briefly introduced. The experimental results are then presented, focusing at first on the issue of the colloidal stability and subsequently on the modulation of the plasmonic response in the spectral region of interest. Finally, the biological functionality as antibacterial system was tested, highlighting a significant catalytic activity depending on the surface charge of the aggregates.

In **Chapter 3**, the development of a SERS-active pH nanosensor, based on the conjugation of gold NPs with the pH-sensitive molecular probe 4-mercaptobenzoic acid is discussed. All the aspects of the synthesis procedure and of the operating conditions were optimised in order to preserve the sensor stability and to provide the highest responsiveness to pH variations. Exploiting the dependence of the SERS spectrum on the protonation degree of the carboxylic group at the edge of the molecule, the nanosensor was successfully employed for measuring the extracellular pH of two clinically relevant normal and tumorigenic human skin cell lines.

In **Chapter 4**, a study aimed at employing SEIRA-active gold nanoprobes as biorecognition tool is presented. The nanoprobes were realised by conjugating gold NPs with 4-aminothiophenol, an efficient infrared reporter molecule. A careful analysis of the infrared signal amplification induced by the SEIRA effect was provided at varying the NPs size. As a proof of concept application, the nanoprobes internalisation within fibroblast cells was obtained by exploiting ultrasound induced transient poration of the cell membrane, a phenomenon widely studied for drug delivery purposes. The bioeffects induced by the combined nanoprobe-ultrasound treatment were analysed at the single cell level by coupling synchrotron radiation and SEIRA microspectroscopy. The information inferred by the spectra analysis were compared to biological viability assays.

In **Chapter 5**, an application of plasmonic nanovectors in single cell cancer theranostics is presented. A step further was implemented in the NPs conjugation, by exploiting 4-aminothiophenol as both a spectroscopic label and as a molecular bridge

for adding a biofunctional layer around NPs. Antifolate SERS-active nanovectors were synthesised by conjugating 4-aminothiophenol functionalised gold NPs with the folic acid competitors aminopterin and methotrexate. A detailed analysis of the nanovector SERS spectra was performed for precisely quantifying the amount of drug loaded on each NP. An efficient SERS screening protocol was developed by taking advantage of the different expression of folate binding proteins on the membrane of normal and cancer cells. A comparative cytotoxicity study is presented, highlighting the greater efficacy of the drug-loaded NPs in comparison with the molecular form of the drug. Finally, the optimisation of the nanovector selectivity is proposed and tested by designing a hybrid folate/antifolate coloaded nanovector.

In **Chapter 6**, the TERS based analyses, coupled with atomic force microscopy and SERS, performed in the context of the project *pERSON* at Friedrich Schiller University of Jena are described. After presenting the main working principles and experimental details of a TERS setup, a thorough morphological and spectroscopic characterisation of the amyloidogensis process is described. Afterwards, the interaction with gold NPs is carefully analysed and discussed, hypotesising possible mechanisms involved in the observed fibril rupture.

In the **Conclusions**, the final remarks summarise the obtained results and point out the open issues and the future perspectives of this work.

In **Appendix A** the details on the apparatus and measurement protocols of the several experimental techniques employed in this work are described. The materials and protocols employed for samples preparation and for the treatment of the biological samples are also reported.

Chapter 1

Plasmonics from nanostructured materials: fundamentals and applications in biosensing

Plasmonics studies the optical phenomena occurring at metallic interfaces or in metallic nanostructures. It is based on interaction processes between electromagnetic radiation and conduction electrons, leading to enhanced optical near field confined in the sub-wavelength scale [1]. These phenomena are due to elementary excitations called surface plasmons, *i.e.* coherent collective oscillations of electrons with respect to the lattice. There are two main types of surface plasmons: propagating surface waves called surface plasmon polaritons and non-propagating, standing excitations called localised surface plasmons (LSPs).
Metallic nanostructures, and in particular noble metal nanoparticles (NPs), are characterised by the non-propagating LSPs, that remain confined at their surface and experience a strong coupling with the electromagnetic radiation. LSPs arise naturally from the scattering problem of a small, sub-wavelength conductive NP in an oscillating electromagnetic field. The curved surface of the particle excerts an effective restoring force on the driven electrons, so that a resonance can arise, leading to field amplification both inside and in the near-field zone outside the particle. This resonance is called the Localised Surface Plasmon Resonance (LSPR), and depends on the shape of the NP, which determines how the charge accumulates at different positions on the surface, and on the electron density, which determines the amount of charge that accumulates.

The physics of LSPs is herein explored following S. A. Maier [1]. The interaction of a single metal NP with an electromagnetic wave is firstly considered, in order to get the resonance condition. Subsequently the effects of plasmon coupling in NPs assemblies are discussed in terms of near-field interactions. Surface enhanced spectroscopies are presented, in the framework of the light-matter interaction theory. The two main mechanisms of signal enhancement, *chemical* and *electromagnetic*, are analysed, enlightening the role of plasmon coupling. Finally, current trends in plasmon-based biosensing are briefly reviewed.

1.1 Localised surface plasmons

Starting with with bulk metals that allow for introducing the concept of plasmon excitations, by means of the simple Drude model for the free electron gas, we will move to metal NPs, where plasmons are confined in all three dimensions, leading to strong resonances at specific frequencies. The interaction of a single sub-wavelength NP with the electromagnetic radiation is analysed within the simple quasi-static approximation, in which the NP acts as an electric dipole, resonantly absorbing and scattering electromagnetic fields, while the generation of multipolar modes is neglected. This approximation provides a good description for spherical particles with dimensions smaller than about 20 nm [33], illuminated with visible or near-infrared radiation. When particles are of larger dimensions a rigorous electrodynamic approach is required. A complete theory of the scattering and absorption of electromagnetic radiation by a sphere was developed by Mie in 1908, to describe the colors of colloidal gold NPs [34].

The dielectric function of a free electron gas

The simplest model for the dielectric response of a metal is the Drude free-electron model. In the Drude model, the conduction electrons are modeled as a plasma of free, non-interacting electrons, which relax through collisions with the lattice or other scatterers. The details of the lattice potential and of the electron-electron interactions are not considered in the model, and the effects of the band structure are incorporated into the effective optical mass m_e of each electron.
When an external electromagnetic field $\mathbf{E} = \mathbf{E}_0\, e^{-i\omega t}$ with frequency ω is applied, the electrons oscillate and their motion is damped with a characteristic collision frequency $\nu = \frac{1}{\tau}$, where τ is the relaxation time of the free electron gas. Under these assumptions, the motion $x(t)$ of a single electron of the plasma can be described by the equation:

$$m_e \frac{d^2\mathbf{x}}{dt^2} + \frac{m_e}{\tau}\frac{d\mathbf{x}}{dt} = -e\mathbf{E} \tag{1.1}$$

where e is the elementary electron charge.

A particular solution of this equation, describing the oscillation of the electron with the same frequency ω of the electric field, is given by:

$$\mathbf{x}(t) = \frac{e}{m_e(\omega^2 + i\,\omega/\tau)}\mathbf{E}(t) \tag{1.2}$$

where the complex amplitude incorporates any phase-shift between driving field and response.
Hence, the induced macroscopic polarisation $\mathbf{P}$ and the dielectric displacement $\mathbf{D}$ can be calculated:

$$\mathbf{P} = -ne\mathbf{x} = -\frac{ne^2}{m_e(\omega^2 + i\,\omega/\tau)}\mathbf{E} \tag{1.3}$$

$$\mathbf{D} = \varepsilon_0\,\mathbf{E} + \mathbf{P} = \varepsilon_0\left(1 + \frac{\omega_p^2}{\omega^2 + i\,\omega/\tau}\right)\mathbf{E} \tag{1.4}$$

where ε_0 is the electric permittivity of vacuum, n is the density of the conduction electrons and the plasma frequency of the free electron gas has been defined as

$$\omega_p = \sqrt{\frac{ne^2}{\varepsilon_0 \, m_e}} \tag{1.5}$$

The constitutive relation, $\mathbf{D} = \varepsilon_0 \, \varepsilon(\omega) \, \mathbf{E}$, yields the expression of the dielectric function of the free electron gas:

$$\varepsilon(\omega) = 1 + \frac{\omega_p^2}{\omega^2 + i \, \omega/\tau} \tag{1.6}$$

whose real and imaginary components, $\mathrm{Re}[\varepsilon(\omega)]$ and $\mathrm{Im}[\varepsilon(\omega)]$, are

$$\mathrm{Re}[\varepsilon(\omega)] = 1 - \frac{\omega_p^2 \, \tau^2}{1 + \omega^2 \, \tau^2} \tag{1.7}$$

$$\mathrm{Im}[\varepsilon(\omega)] = \frac{\omega_p^2 \, \tau}{\omega(1 + \omega^2 \, \tau^2)} \tag{1.8}$$

For $\omega < \sqrt{\omega_p^2 + 1/\tau^2}$, the real part of the dielectric function is negative, therefore in this frequency range the electromagnetic radiation cannot penetrate the material, leading to the formation of surface excitation as the surface plasmons. In the case of noble metal, such as gold and silver, this happens for frequencies in the UV and visible spectral range. The imaginary part describes the energy dissipation associated with the motion of the electrons in the metal. The tabulated dielectric functions for gold, silver and copper are reported in Figure 1.1.
The dielectric function of the free electron gas (1.6) provided by the Drude model adequately describes the optical response of metals for photon energies below the threshold of transitions between electronic bands.

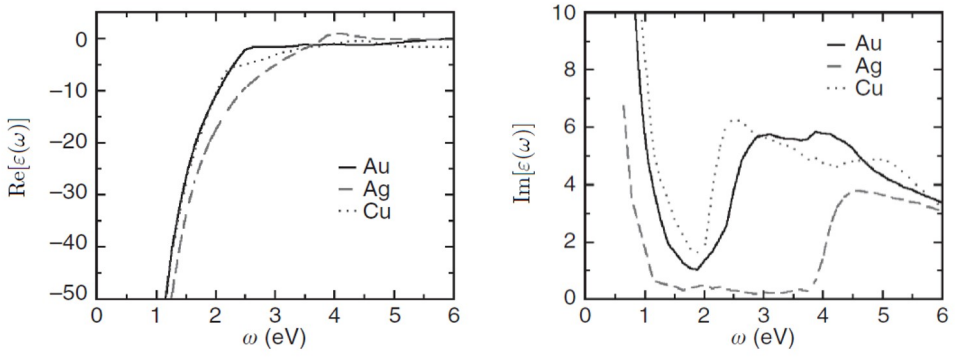

Figure 1.1. Comparison of tabulated empirical dielectric functions for gold (Au), silver (Ag) and copper (Cu). Real (left panel) and imaginary (right panel) part of the dielectric function. Image adapted from ref. [2].

Quasi-static approximation for a sub-wavelength metal sphere

The quasi-static approximation describes the interaction of a NP with the electromagnetic radiation, assuming that the particle size $2a$ is much smaller than the wavelength λ of incident radiation ($a \ll \lambda$). In this case, the phase of the harmonically oscillating electromagnetic field can be considered constant over the particle volume and retardation effects can be neglected. The spatial field distribution

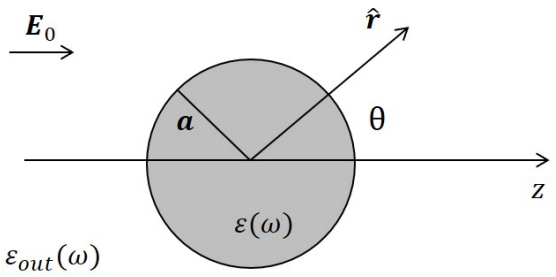

Figure 1.2. Sketch of a homogeneous sphere of radius a and dielectric function $\varepsilon(\omega)$ placed into an electrostatic field. Adapted from ref. [1].

is therefore calculated assuming an electrostatic field and then including in the solution the harmonic time dependence.
The NP is represented by a homogeneous, isotropic sphere of radius a located at the origin in a uniform, static electric field $\mathbf{E}_0 = E_0\hat{\mathbf{z}}$ (Figure 1.2). At sufficient distance from the sphere, the field lines are parallel to the z direction. The surrounding medium is considered isotropic and non-absorbing with dielectric constant ε_{out}, while the dielectric response of the sphere is described by the dielectric function $\varepsilon(\omega)$ of a free electron gas (equation 1.6).

In the electrostatic approach, the electric field can be expressed in terms of the scalar potential Φ, defined by: $\mathbf{E}_0 = -\boldsymbol{\nabla}\Phi$. The solution of the Maxwell's equations in the absence of external sources can be therefore calculated by solving the Laplace equation $\nabla^2\Phi = 0$. The boundary conditions of the problem are given by the equality, at the NP interface, of the tangential components of the electric field and of the normal components of the displacement field. Moreover, the requirement that $\Phi_{out} \to -E_0 z = -E_0\, r\cos\theta$ as $r \to \infty$, where $\boldsymbol{r}$ is the position vector and θ the angle it forms with the z-axis, has to be taken into account.
Under these assumptions, the solution for the scalar potentials Φ_{in} inside and Φ_{out} outside the sphere are given by [35]:

$$\Phi_{in} = -\frac{3\,\varepsilon_{out}}{\varepsilon(\omega) + 2\,\varepsilon_{out}} E_0\, r\cos\theta \tag{1.9}$$

$$\Phi_{out} = -E_0\, r\cos\theta + \frac{\varepsilon(\omega) - \varepsilon_{out}}{\varepsilon(\omega) + 2\,\varepsilon_{out}} E_0\, a^3 \frac{\cos\theta}{r^2} \tag{1.10}$$

Interesting, equation (1.10) describes the superposition of the applied electric field and that of a dipole located at the particle center. Introducing the dipole moment

p:

$$\mathbf{p} = 4\pi\,\varepsilon_0\,\varepsilon_{out}\,a^3\,\frac{\varepsilon(\omega)-\varepsilon_{out}}{\varepsilon(\omega)+2\,\varepsilon_{out}}\mathbf{E}_0 \tag{1.11}$$

it is possible to write the scalar potential in the surrounding medium as:

$$\Phi_{out} = -E_0 r\cos\theta + \frac{\mathbf{p}\cdot\mathbf{r}}{4\pi\,\varepsilon_0\,\varepsilon_{out}\,r^3} \tag{1.12}$$

The (complex) polarisability α of a small sphere of sub-wavelength diameter in the electrostatic approximation, defined by $\mathbf{p} = \varepsilon_0\,\varepsilon_{out}\,\alpha\mathbf{E}_0$, is finally obtained:

$$\alpha = 4\pi\,a^3\,\frac{\varepsilon(\omega)-\varepsilon_{out}}{\varepsilon(\omega)+2\,\varepsilon_{out}} \tag{1.13}$$

The polarisability experiences a resonant enhancement under the Fröhlich condition:

$$\mathrm{Re}[\varepsilon(\omega)] = -2\,\varepsilon_{out} \tag{1.14}$$

The frequency for which the condition is satisfied is called the dipole surface plasmon resonance of the metal particle. The resonance condition holds only if the real part of the dielectric function is negative, therefore it is satisfied only for specific materials and for frequencies below ω_p. For silver and gold, the resonance condition 1.14 is satisfied in the near ultraviolet and visible spectral ranges. The incomplete vanishing of the denominator of equation (1.13), due to $\mathrm{Im}[\varepsilon(\omega)] \neq 0$, limits the magnitude of α at resonance.

By combining the Drude model and the Fröhlich condition it is possible to express the frequency of the plasmon resonance as a function of ε_{out}:

$$\omega_{res}(\varepsilon_{out}) = \sqrt{\frac{\omega_p^2}{1+2\,\varepsilon_{out}} - \frac{1}{\tau^2}} \tag{1.15}$$

Noteworthy, equation (1.15) explicitly points out the strong dependence of the resonance frequency on the dielectric environment surrounding the NP. Specifically, the resonance redshifts with increasing ε_{out}, as shown in Figure 1.3. This relation between the LSPR and the dielectric properties of the environment surrounding the plasmonic materials is widely exploited in developing NP-based sensor and in monitoring the chemical environment at the interface of NPs.

The distribution of the electric fields $\mathbf{E}_{in}$ inside and $\mathbf{E}_{out}$ outside the sphere can be evaluated from the potentials (1.9) and (1.10), respectively:

$$\mathbf{E}_{in} = \frac{3\,\varepsilon_{out}}{\varepsilon(\omega)+2\,\varepsilon_{out}}\mathbf{E}_0 \tag{1.16}$$

$$\mathbf{E}_{out} = \mathbf{E}_0 + \frac{3\,\hat{\mathbf{n}}\,(\hat{\mathbf{n}}\cdot\mathbf{p}\,) - \mathbf{p}}{4\pi\,\varepsilon_0\,\varepsilon_{out}}\,\frac{1}{r^3} \tag{1.17}$$

where $\hat{\mathbf{n}}$ is the radial unit vector. As expected, as a consequence of the resonance in α, a resonant enhancement of both the internal and dipolar fields also occurs. Many prominent applications of metal NPs in optical devices and sensors rely on this field-enhancement at the plasmon resonance.

The representation of a small sphere, with radius $a \ll \lambda$, as an ideal dipole is valid in the quasi-static regime, *i.e.* allowing for time-varying fields but neglecting spatial retardation effects over the particle volume. The harmonic time dependence can be therefore added to the solutions of equations (1.16) and (1.17), accounting for the electromagnetic fields radiated by a small particle excited at its plasmon resonance. Under plane-wave illumination with $\mathbf{E}(r,t) = \mathbf{E}_0\, e^{-i\omega t}$, the field induce an oscillating dipole moment $\mathbf{p}(t) = \varepsilon_0\, \varepsilon_{out}\, \alpha\, \mathbf{E}_0\, e^{-i\omega t}$, with α given by the electrostatic result (1.13). The radiation of this dipole leads to the scattering of the plane wave by the sphere, which can be represented as radiation by a point dipole.
Another consequence of the resonantly enhanced polarisation α is a concomitant enhancement in the light scattering and absorption efficiency of a metal NP. The corresponding cross sections, σ_{sca} and σ_{abs}, for scattering and absorption can be calculated *via* the Poynting vector [36]:

$$\sigma_{sca} = \frac{k^4}{6\pi}|\alpha|^2 = \frac{8\pi}{3}k^4a^6\left|\frac{\varepsilon(\omega)-\varepsilon_{out}}{\varepsilon(\omega)+2\,\varepsilon_{out}}\right|^2 \tag{1.18}$$

$$\sigma_{abs} = k\,\mathrm{Im}[\alpha] = 4\pi\, ka^3\,\mathrm{Im}\left[\frac{\varepsilon(\omega)-\varepsilon_{out}}{\varepsilon(\omega)+2\,\varepsilon_{out}}\right] \tag{1.19}$$

where $k = \frac{2\pi}{\lambda}$. Notably, the absorption cross section scales as a^3, while the scattering cross section scales as a^6. Hence, for small particles with $a \ll \lambda$ the efficiency of absorption dominates on the scattering efficiency. Moreover, for metal NPs, both absorption and scattering (and thus extinction) are resonantly enhanced at the dipole particle plasmon resonance, *i.e.* when the Frölich condition is met. The explicit expression for the extinction cross section σ_{ext} of a sphere of volume V is:

$$\sigma_{ext} = \sigma_{sca} + \sigma_{abs} = 9\,\frac{\omega}{c}\,\varepsilon_{out}^{3/2}\,V\frac{\mathrm{Im}[\varepsilon(\omega)]}{\left(\mathrm{Re}[\varepsilon(\omega)]+2\,\varepsilon_{out}\right)^2+\left(\mathrm{Im}[\varepsilon(\omega)]\right)^2} \tag{1.20}$$

where c is the speed of light in vacuum.

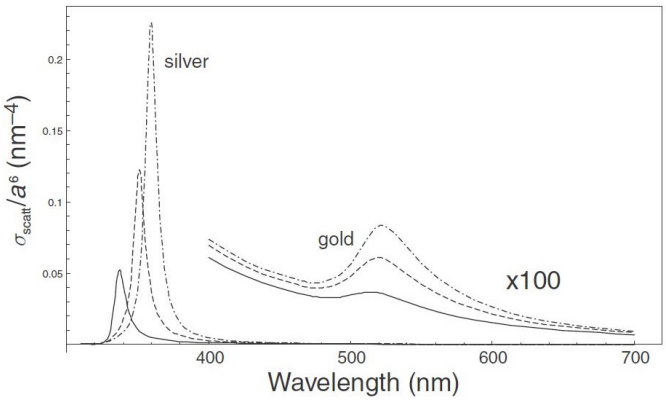

Figure 1.3. Scattering cross section, for gold and silver NPs surrounded by different dielectric media with increasing refractive index. The spectra are normalised to a^6, to eliminate the dependence on the NP radius. Solid line: vacuum, dashed line: water, dashed-dotted line: glass. Reproduced from ref. [2].

Mie theory

The Mie theory solves Maxwell's equations for the scattering of electromagnetic radiation by spherical NPs [34]. Its rigorous electrodynamic approach accounts for phase-changes of the driving field over the particle volume, explaining the optical properties of NPs larger than 20 nm.

The approach is to expand the internal and scattered fields into a set of normal modes described by vector sperical harmonics $\mathbf{M}_l$ and $\mathbf{N}_l$. The scattered electromagnetic field is therefore given by a linear superposition of spherical waves, each generated by an electric and a magnetic multipole [36]:

$$\mathbf{E}_{sca} = \sum_{l=1}^{\infty} i^l E_0 \frac{2\,l+1}{l(l+1)} \left(i a_l \mathbf{N}_l^{(e)} - b_l \mathbf{M}_l^{(o)} \right) \tag{1.21}$$

$$\mathbf{H}_{sca} = \frac{k}{\omega} \sum_{l=1}^{\infty} i^l E_0 \frac{2\,l+1}{l(l+1)} \left(i b_l \mathbf{N}_l^{(o)} - a_l \mathbf{M}_l^{(e)} \right) \tag{1.22}$$

where the superscripts o and e specify the odd and even parity, respectively, of the vector spherical harmonics. Here the magnetic permeability of the particle and the surrounding medium were assumed to be the same. The amplitudes a_l and b_l are given by:

$$a_l = \frac{n\Psi_l(nx)\Psi_l'(x) - \Psi_l(x)\Psi_l'(nx)}{n\Psi_l(nx)\xi_l'(x) - \xi_l(x)\Psi_l'(nx)} \tag{1.23}$$

$$b_l = \frac{\Psi_l(nx)\Psi_l'(x) - n\Psi_l(x)\Psi_l'(nx)}{\Psi_l(nx)\xi_l'(x) - n\xi_l(x)\Psi_l'(nx)} \tag{1.24}$$

where Ψ_l and ξ_l are the Riccati-Bessel functions, $x = ka$ is the size parameter, and $n = \frac{n_{in}}{n_{out}}$, with n_{in} and n_{out} the relative refractive indices of the particle and the medium, respectively. As expected, a_l and b_l vanish as n approaches unity: when the particle disappears, so does the scattered field. The scattering and extinction cross sections can be finally expressed as the sum of the contributions of single multipoles:

$$\sigma_{sca} = \frac{2\pi}{k^2} \sum_{l=1}^{\infty} (2l+1)(|a_l|^2 + |b_l|^2) \tag{1.25}$$

$$\sigma_{ext} = \frac{2\pi}{k^2} \sum_{l=1}^{\infty} (2l+1)\mathrm{Re}[a_l + b_l] \tag{1.26}$$

A resonance for a particular l occurs if the frequency or the radius are such that one of the denominators of equations (1.23) and (1.24) is very small. The resonant conditions for the a_l and the b_l modes are, respectively:

$$\frac{\xi_l'(x)}{\xi_l(x)} = \frac{1}{n} \frac{\Psi_l'(nx)}{\Psi_l(nx)} \tag{1.27}$$

$$\frac{\xi_l'(x)}{\xi_l(x)} = n \frac{\Psi_l'(nx)}{\Psi_l(nx)} \tag{1.28}$$

By a power series expansion of the first mode of the Mie theory [37] it is possible to obtain an expression for the polarisability of a sphere of volume V:

$$\alpha_{sphere} = \frac{1 - (\frac{1}{10})(\varepsilon(\omega) - \varepsilon_{out})x^2 + O(x^3)}{(\frac{1}{3} + \frac{\varepsilon_{out}}{\varepsilon(\omega) - \varepsilon_{out}}) - \frac{1}{30}(\varepsilon(\omega) + 10\varepsilon_{out})x^2 + O(x^3)} V \tag{1.29}$$

The first order of this expansion yields the expression of the polarisability in the quasi-static approximation of equation 1.13. The additional, quadratic terms of equation 1.29 depend on the size parameter x, thus accounting for the retardation effect of the exciting field over the volume of the sphere, leading to a shift in the plasmon resonance. For Drude and the noble metals, the overall shift is towards lower energies: the spectral position of the dipole resonance redshifts with increasing particle size, as shown in Figure 1.4. Intuitively, this can be understood by recognising that the distance between the charges at opposite interfaces of the particle increases with its size, thus leading to a smaller restoring force and therefore a lowering of the resonance frequency. For the same reason, also the shape of the NP affect the LSPR frequency.

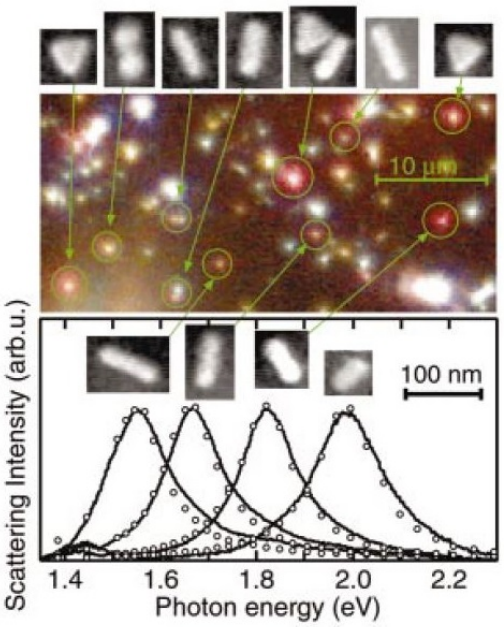

Figure 1.4. Optical dark-field image of scattered light from gold NPs with different size and shape, together with SEM images of the corresponding particles (top). Scattering spectra from gold nanorods with incident light polarised parallel to the long axis. Reproduced from ref. [37].

1.2 Near-field coupling between localised surface plasmons

As seen in the previous Section, the LSPR of a single metallic NP can be shifted in frequency depending on particle shape, size and on modification of the dielectric medium. In particle ensembles, additional frequency shifts of the plasmon resonance occur due to electromagnetic interactions between the localised modes. Coupling effects between plasmon resonances can occur in the far-field and near-field regime, depending on the distance d between NPs, compared with the wavelength λ of the incident radiation. Far-field coupling occurs when $d \sim \lambda$ and the plasmon modes interact through fields scattered off the particles [1, 38]. Here, we focus on near-field coupling of NPs, which occurs when $d \ll \lambda$ and results from the Coulomb interaction between the surface charges on the different particles.

The coupling intensity increases with the decrease of the distance between NPs, leading to the formation of large charge dipoles across the gap between the particles. This results in a intense local field that can be much greater than the sum of the local fields that would be produced by the isolated particles. This so-called "hot spot" of intense local field provides strong coupling to analytes trapped in the gap, so that NP pairs are excellent nanoantennas for coupling light into and out of localised emitters [39]. Materials in the gap will also affect the strength of the coupling, producing shifts in plasmon resonance frequencies that can be used for sensitive chemical detection [40].

The coupling between localised plasmon modes can be described by means a intuitive, semianalytical picture in the quasistatic limit by treating the metals using a Drude model without damping [41, 42, 43]. The model, known as the "plasmon hybridisation" model, provides a formal analogy between plasmon coupling and the hybridisation of atomic orbitals in molecules. The plasmon modes of a particle ensamble are expressed in terms of interactions between the plasmon resonances of its elementary components. In the same way that individual atomic orbitals in a diatomic molecule hybridise to form bonding and antibonding states, individual plasmon resonances in NP assembles couple to form higher energy and lower energy collective modes.

1.2.1 Plasmon hybridisation theory

In the plasmon hybridisation model the conduction electrons are depicted as a charged, incompressible fluid placed in a rigid, uniform positive background with the same charge density ρ_0, which represents the ion cores [42]. The entire system is assumed to be neutrally charged. The plasmon modes are self-sustained deformations of the electron fluid, described by the field velocity $\mathbf{v}(\mathbf{r})$ and in turn by the current $\mathbf{j}(\mathbf{r}) = n_0\, e\, \mathbf{v}(\mathbf{r})$, where $n_0 = \rho_0/e$ is the electron number density. Incompressible deformations are taken into account by $\mathbf{j} = n_0\, e \boldsymbol{\nabla}\phi$, where the scalar potential ϕ satisfies the Laplace equation $\nabla^2\phi = 0$. Since the liquid is incompressible, in the linear response limit the only effect of such (infinitely small) deformations is the appearance of a surface charge density $\sigma(\Omega)$, where Ω is the solid angle. The continuity equation at the NP surface, assuming the electron fluid confined within

the volume of the particle, relates $\mathbf{j}$ and σ:

$$\frac{\partial \sigma}{\partial t} = \hat{\mathbf{n}} \cdot \mathbf{j} = n_0 \, e \, \hat{\mathbf{n}} \cdot \boldsymbol{\nabla} \phi \tag{1.30}$$

where $\hat{\mathbf{n}}$ denotes the surface normal unit vector.

Expanding the solution of the Laplace equation as a function of a complete sets of scalar potentials $\phi_\mu(\mathbf{r})$, where μ is an index for the individual basis functions in any given NP geometry, yields:

$$\phi(\mathbf{r}, t) = \sum_{\mu} \frac{dA_\mu(t)}{dt} \, \phi_\mu(\mathbf{r}) \tag{1.31}$$

where the time dependent coefficients $A_\mu(t)$ represent the fluid deformation amplitudes of each primitive plasmon $|\mu\rangle$. Under these assumptions, the dynamics of the small deformations of the fluid is described by the following Lagrangian:

$$L = \frac{1}{2} \int_S n_0 \, m_e \phi \boldsymbol{\nabla} \phi \, d\mathbf{S} - \frac{1}{2} \iint_S \frac{\sigma(\mathbf{r}) \sigma(\mathbf{r}\,')}{|\mathbf{r} - \mathbf{r}\,'|} d\mathbf{S} d\mathbf{S}' \tag{1.32}$$

where the two integrals represents the kinetic and the potential energy of the system and are calculated over all the boundaries of the particle surface.

In the case of a solid metallic sphere of radius a, the scalar potential can be expanded by the spherical harmonics $Y_{lm}(\Omega)$, where l and m are the angular momentum and the azimuthal number, respectively:

$$\phi(\mathbf{r}, t) = \sum_{l,m} \frac{dA_{lm}(t)}{dt} \sqrt{\frac{1}{l a^{2l+1}}} \, r^l \, Y_{lm}(\Omega) \tag{1.33}$$

and the Lagrangian of the system can be written as:

$$L = \frac{1}{2} n_0 \, m_e \sum_{l,m} \left[\left(\frac{dA_{lm}}{dt} \right)^2 - \omega_l^2 A_{lm}^2 \right] \tag{1.34}$$

where $\omega_l = \omega_p \sqrt{l/(2l+1)}$.

The Lagrangian of equation 1.34 represents the normal-mode dynamical equation of a harmonic oscillator with frequency ω_l. Notably, ω_l is exactly equal to the plasmonic frequencies predicted by the resonance conditions of the Mie theory, reported in equations (1.27) and (1.28). In a complex geometry, the primitive plasmon modes interact *via* the Coulomb potential and are therefore no longer the eigenmodes of the system. The normal modes of the coupled system are obtained assuming harmonic motion for all modes and searching self-sustained solutions of the new Lagrangian. The resulting hybridised modes will therefore be superpositions of the individual primitive plasmon modes. From the equations of motion, the optical absorption of the complex coupled nanostructure can be finally calculated.

This method provides a simple and conceptually straightforward understanding of how plasmon resonances in a complex or multicomponent structure arise from the plasmon modes of their individual components. Since its initial demonstration, this approach has been utilised for the analysis of an increasing variety of plasmonic systems [5, 44]. In the following the coupling among plasmon modes of some notable structures is briefly discussed.

Plasmonic dimers

Proceeding from the theory previously discussed, here we consider hybridisation between the plasmons in a pair of spherical NPs with center-to-center distance D. Inside each sphere, ϕ is written in terms of the normal modes of that sphere, with the angular-momentum axis taken to be the line that joins the centers of the particles. When the overall size of the system is significantly much smaller than the plasmon wavelength, retardation effects can be neglected and the dynamics of the plasmons is determined by the instantaneous Coulomb interaction between the surface charges [43]. The Lagrangian of the system is given by the sum of the Lagrangian L_1 and L_2 of the single non-interacting particles, plus an interaction term:

$$L = L_1 + L_2 - V_{12}(D) \tag{1.35}$$

where

$$V_{12}(D) = \frac{(n_0 e)^2}{a^3} \sum_{\substack{l_1,m_1 \\ l_2,m_2}} \sqrt{l_1 l_2} A_{l_1,m_1}(t) A_{l_2,m_2}(t) \iint \frac{Y_{l_1,m_1}(\Omega_1) Y_{l_2,m_2}(\Omega_2)}{|\mathbf{r}_1 - \mathbf{r}_2|} d\mathbf{S}_1 d\mathbf{S}_2 \tag{1.36}$$

Given the geometry of the problem, the interaction is diagonal in the azimuthal quantum number m. Consequently, the plasmon modes corresponding to different values of m decouple and the Euler-Lagrange equations result in an eigenvalue problem of the form:

$$\det\left[\Lambda_{ij}^{(m)} - \omega\right] = 0 \tag{1.37}$$

where the matrix Λ is defined by:

$$\Lambda_{ij}^{(m)} = \omega_i^2 \delta_{ij} + \frac{\omega_p^2}{8\pi} V_{ij}^{(m)} \tag{1.38}$$

Here the subscripts i and j denote the non-interacting plasmon modes. In this notation, i refers to a plasmon mode of energy ω_i and the matrix elements $V_{ij} = V_{ji}$ describe the coupling between the modes i and j ($V_{ij} = 0$ if the indices refer to modes of the same particle), resulting in separation dependent shifts of the dimer plasmon levels.

Hence, the dimer plasmons can be viewed as bonding and antibonding combinations of the individual NP plasmons, closely resembling a homogeneous diatomic molecule, and its molecular orbital diagram. Based on this parallelism, coupled metallic NP pairs are referred to as plasmonic "dimers".

The energy diagram of the plasmonic dimer, together with an example of the optical response in the case of gold NPs is shown in Figure 1.5. The dipolar plasmon mode of each individual nanoparticle splits into two distinct collective modes, known as the low-energy "bonding" mode and the higher-energy "antibonding" mode. The bonding mode has mutually aligned longitudinal dipoles, resulting in a large induced dipole and a strong coupling to an incident plane wave polarised along the axis connecting the particles. It is therefore referred also to as a "bright" plasmon mode. The antibonding mode has anti-aligned dipoles, resulting in no net dipole moment and the inability of this mode to couple to the far field, so it is called as a "dark"

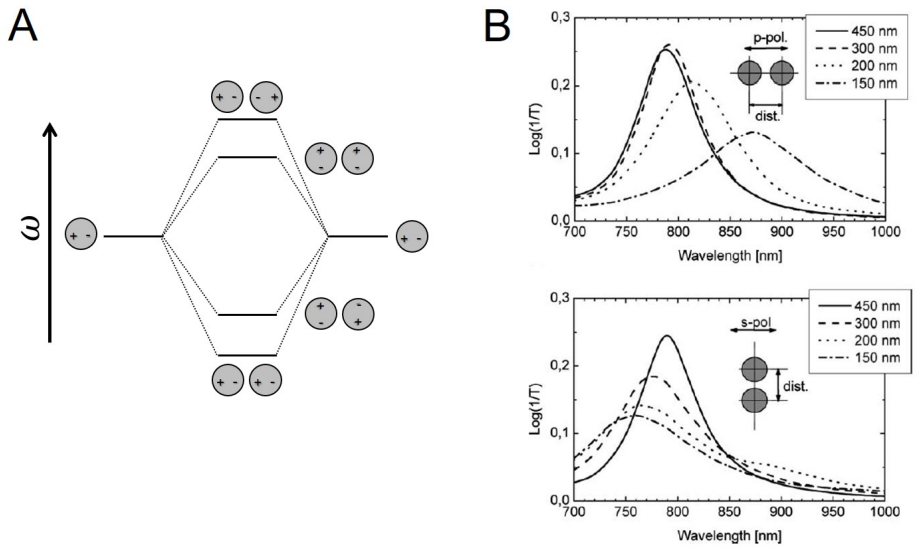

Figure 1.5. (A) Scheme of the plasmon hybridisation in a NP dimer. The individual nanosphere plasmons on the two particles interact and form bonding and anti-bonding dimer plasmons, depending on the polarisation. When the dipoles are arranged end to end, the two dipoles are in phase, and the coupled dipole resonance is shifted to lower frequencies. When the the dipoles are arranged side by side, the dipoles are out of phase, leading to couple modes at higher frequencies. Image inspired by [45]. (B) Extinction spectra of an array of gold NP with different interparticle distances at varying the polarisation of the exciting field, parallel (top) and orthogonal (bottom) to the interparticle axis. Reproduced from [46].

plasmon mode. For both longitudinal and transverse coupled dipoles, the bright and dark modes are shifted from the single-particle frequencies by the same amount.

As the interparticle separation is reduced, the magnitude of the coupling increases, scaling as $1/D$. In the limit where the NP are nearly touching, mixing between the $l = 1$ states and all higher order modes of the neighboring nanoparticle will occur [47]. The resulting hybridisation produces an increased redshift of the bonding mode with decreasing dimer separation. This behavior is characteristic of a dimer excited by light polarised along its interparticle axis. For light polarised orthogonal to this axis, interparticle coupling is minimal, and a small blue shift of the individual NP plasmon is observed (see Figure 1.5B).

The plasmon hybridisation theory herein described can be generalised to multi-nanoparticle systems, allowing to express the fundamental plasmon modes as linear combinations of plasmons of individual NPs, in a manner analogous to molecular orbital theory. The sums over particles should be extended to include all particles present in the structure and the interaction integral I should be evaluated:

$$I^{i,i}_{l,m,l',m'}(a) = \frac{1}{a^2} \int \frac{Y_{l,m}(\Omega_i) Y_{l',m'}(\Omega_j)}{r_j^{l'+1}} dS_i \tag{1.39}$$

where the integration is centred on particle i and made over a spherical surface of radius a.

In case of non-extended structures with definite geometries such as trimers, quadrumers and NP oligomers, this method provides a good analytical description of the optical properties [48, 44]. In the more general case of plasmonic systems composed by a large number of particles with complex geometries, computational methods such as Discrete Dipole Approximation or Finite Difference Time Domain methods are employed to solve the Maxwell's equations and to obtain the electromagnetic fields distribution of the plasmonic structures [49].

1.2.2 Plasmon coupling in large nanoparticle assemblies

The modification of the plasmon resonance become substantial when the number of particle composing the plasmonic structure is increased. The coupling among the plasmon modes of several NPs in the three dimensions leads to a broadening and redshift of the plasmon resonance which can be extended until the infrared spectral region, depending on the number of NPs [5]. Large NP aggregates are attractive for plasmonic applications since allow for obtaining very intense local fields due to the high density of hot spots [50].

Besides to be determined by the intrinsic properties of the single plasmonic constituents (*e.g.*, particle shape and size), the optical response of these systems is crucially dependent on the interparticle distance and on the morphology of the cluster. The strict control on these parameters for obtaining plasmonic assemblies with the desired optical properties represents a challenge of the current fabrication procedures.

In colloidal fractal aggregates, each particle is surrounded by a strongly anisotropic

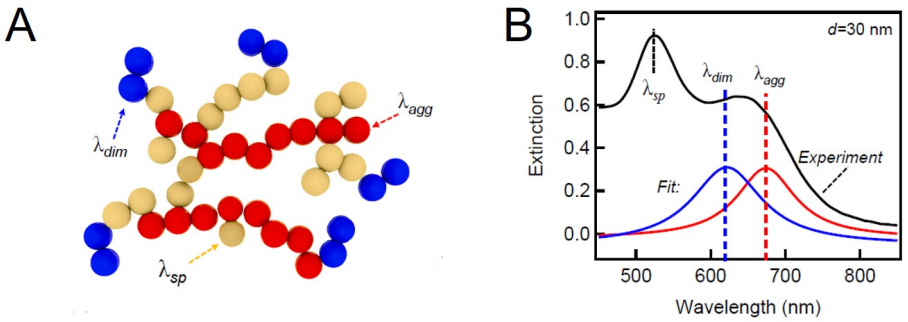

Figure 1.6. (A) Sketch of a fractal NP aggregate in which sub-nanostructures such as chains (red), dimers (blue) and single particle structures can be recognised. The LSPR of each one is identified by λ_{agg}, λ_{dim} and λ_{sp}, respectively. (B) Representative extinction spectrum of a fractal aggregates, composed by gold NPs with a diameter of 30 nm. The plasmon contributions corresponding to the single particle, dimers and chain sub-structure are highlighted. Adapted from ref. [51].

environment composed of other particles. Therefore, how the dipole-dipole interactions of the single plasmon modes overlap to define the global optical response of the cluster strictly depends on the particle spatial organisation [52]. Moreover, the clustering process generates a distribution of sub-nanostructures with different coordination numbers. For each of these sub-structures it is possible to identify an optical response and a plasmon resonance [51]. Therefore, the overall optical

response of the system is determined by the overlap of the strong interaction between closely located particles and the presence of a large number of particles forming the complex structures [53] (Figure 1.6).

The optical response of two- and three-dimensional clusters of NPs can be interpreted in terms of the excitation of simple units composed of different length resonant chains [53]. As reported by Herrmann *et al.* [54], self-assembled gold NP clusters support strongly localized plasmon modes whose resonant energy sensitively depends on their position within the aggregate. As shown in the spectral map of Figure 1.7, the regions corresponding to a more intense field indicate the presence of a radiative localised plasmon mode which resonantly couples to incident light of the given wavelength. Consequently, the local electric field is strongly enhanced at this position. Therefore, shorter wavelength modes, corresponding to sub-structures with low coordination numbers, are found in the periphery of the cluster. Instead, longer wavelength modes, corresponding to more complex sub-structures predominantly stretch along extended NP chains, typically found in the core of the aggregate.

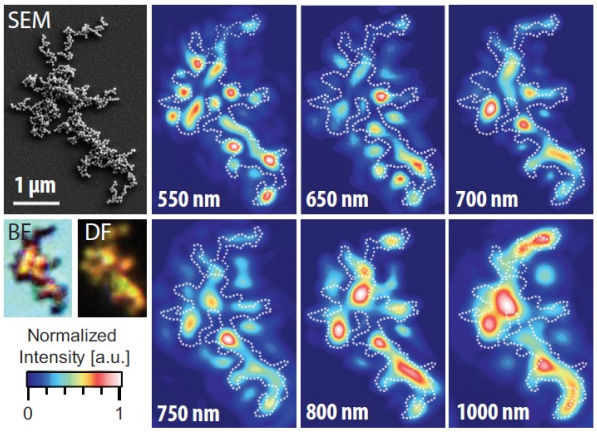

Figure 1.7. Scattering response of a self-assembled gold NP cluster. Scanning electron microscope image of the cluster together with optical bright (BF) and dark field (DF) images. The spatial distribution of the scattering response of the cluster at different wavelengths (right). The gray dotted lines represent the outline of the cluster as extracted from the SEM image, the exciting wavelengths are indicated at the bottom of each image. For higher energies(550-650 nm), single particle and dimer modes dominate the response and are mainly located in the periphery of the cluster. At longer wavelengths ($\sim$ 800 nm), the cluster modes start to successively concentrate along the longer chains in the denser parts of the aggregate, since only these extended resonant structures can support such low energy modes. Starting from 1000 nm, the spatial response spreads along almost the entire core of the aggregate. Reproduced from ref. [54].

1.3 Surface enhanced spectroscopies

The confinement of the electromagnetic field at the interface of plasmonic materials has been tailored for pushing the sensitivity limits of traditional vibrational spectroscopies. Indeed, the localisation of these intense fields results in the enhancement of the optical cross section of molecules located in proximity of the metallic surface that has been exploited in the so called surface enhanced spectroscopies. Among them, the most prominent are based on Infrared (IR) absorption and Raman scattering, known as Surface Enhanced InfraRed Absorption (SEIRA) and Surface Enhanced Raman Scattering (SERS), respectively. The signal amplification is strongly dependent on the feature of LSPR of the nanostructure employed as plasmonic substrate, such as center frequency and width. Single metallic NPs or small NP aggregates, that show LSPRs predominantly in the visible spectral region, are suitable to be emloyed as SERS substrates. On the other hand, sub-micrometric NP aggregates, NP periodic arrays and core-shell systems, with LSPR ranging from the near-infrared to higher wavelengths, are the typical substrates employed in SEIRA. Another aspect that affects the signal amplification in both surface enhanced spectroscopies is related to the electronic properties of the analyte, that can result modified upon the interaction with the metallic nanostructure.

In this Section the basic principles of the radiation-matter interaction are discussed, in order to derive the expression for the IR absorption and Raman scattering cross section. Afterwards, SEIRA and SERS spectroscopies will be presented together with the mechanisms involved in the signal enhancement.

Radiation-matter interaction

When a system is illuminated by electromagnetic radiation, considering the approximation of linear optics, the incident photons can be absorbed, scattered, or transmitted without interacting with the sample. In absorption processes, only

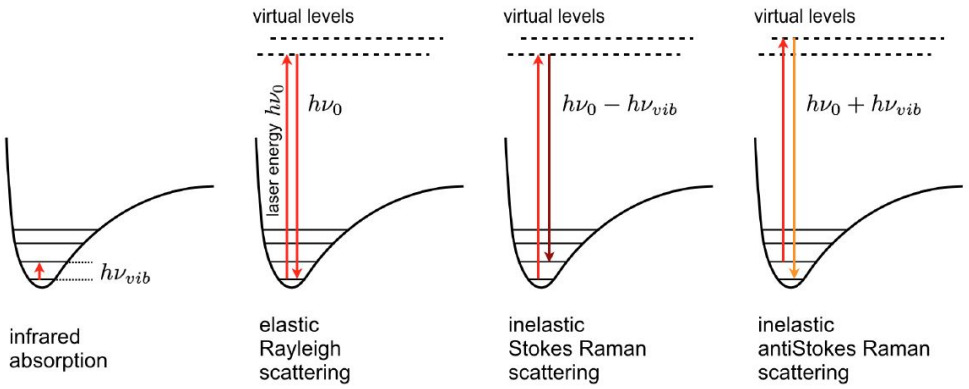

Figure 1.8. Schematic representation of vibrational absorption and elastic and inelastic scattering processes. Reproduced from [55].

one photon is involved and it is absorbed if its energy is resonant with a proper

excitation in the system. Typical vibrational energies match the energies of photons in the infrared spectral range. Therefore, IR photons will be absorbed and induce a vibrational transition in the system (Figure 1.8A). In scattering processes, instead, two photons are involved. The first one is absorbed and excites the system to an intermediate state, the second one is re-emitted in the disexcitation. The system can relax both to the initial level or to a different level. In the fist case, the emitted photon has the same energy of the absorbed one and the process is called Rayleigh elastic scattering (Figure 1.8B). In the second case, the energy difference between the incident and scattered photons provides the energy spacing of the vibrational levels of the system and the process is called inelastic Raman scattering. Depending whether the emitted photon has energy lower or higher than the absorbed photon one refers to Stokes or anti-Stokes process (Figure 1.8C-D), respectively.

In order to derive the expression for the cross section in the case of IR absorption and Raman scattering, let us consider the interaction between the electromagnetic radiation and N particles located in the positions $\{\mathbf{r}_j\}$ with charge q_j, mass m_j and momentum $\mathbf{p}_j$ interacting with a potential $V(\{\mathbf{r}_j\})$. The total Hamiltonian of the system is:

$$H = \sum_j \frac{\mathbf{p}_j^2}{2m_j} + V(\{\mathbf{r}_j\}) + H_{rad} + H_{int} \tag{1.40}$$

where H_{rad} is the radiation Hamiltonian and the interaction Hamiltonian H_{int} is given by:

$$H_{int} = -\frac{1}{c}\sum_j \frac{q_j}{m_j}\mathbf{p}_j \cdot \mathbf{A}(\mathbf{r}_j, t) + \frac{1}{2c^2}\sum_j \frac{q_j^2}{m_j}\mathbf{A}^2(\mathbf{r}_j, t) \tag{1.41}$$

which is obtained from the system Hamiltonian by applying the minimal substitution $\mathbf{p} \to \mathbf{p} - \frac{q}{c}\mathbf{A}(\mathbf{r}, t)$ where $\mathbf{A}(\mathbf{r}, t)$ is the vector potential

$$\mathbf{A}(\mathbf{r}, t) = \sum_{\mathbf{k},l} \sqrt{\frac{2\pi c^2}{V\omega_{\mathbf{k}}}} \left[\hat{\boldsymbol{\epsilon}}_l a_{\mathbf{k},l}\, e^{-i(\mathbf{k}\cdot\mathbf{r}-\omega_{\mathbf{k}}t)} + \hat{\boldsymbol{\epsilon}}_l^* a_{\mathbf{k},l}^\dagger\, e^{i(\mathbf{k}\cdot\mathbf{r}-\omega_{\mathbf{k}}t)}\right] \tag{1.42}$$

where $a_{\mathbf{k},l}$ and $a_{\mathbf{k},l}^\dagger$ are the creation and destruction operators of photons with wavevector $\mathbf{k}$ and polarisation $\hat{\boldsymbol{\epsilon}}_l$.
The transition probability W_{if} between an initial state $|i\rangle$ and a final state $|f\rangle$ with energies E_i and E_f respectively, is given by the Fermi's golden rule:

$$W_{if} = \frac{2\pi}{\hbar} |\langle f|\ S\ |i\rangle|^2 \delta(E_f - E_i) \tag{1.43}$$

where the scattering matrix S is expressed by:

$$S = \sum_n \left(-\frac{i}{\hbar}\right)^n \frac{1}{n!} \int dt_1 \dots dt_n \hat{T}[H_{int}(t_1) \dots H_{int}(t_n)] \tag{1.44}$$

From equation 1.43 it is possible to derive the expression of the differential cross section $d\sigma$ for a given process, knowing the flux per unit time and surface of the incident photons Φ_{inc}:

$$d\sigma \propto \frac{W_{if}}{\Phi_{inc}} \tag{1.45}$$

We are interested in processes involving one or two photons, which correspond to linear and quadratic terms in the vector potential. Hence we consider the terms of the S matrix up to the second order of the perturbative series expansion and neglect the terms with order higher than $\mathbf{A}^2(\mathbf{r},t)$. A generic element of the transition matrix for the scattering processes is therefore given by:

$$\begin{aligned}\langle f|\, S\,|i\rangle = \sum_j -\frac{q_j}{m_j\, c}\ \langle f|\, \mathbf{p}_j\cdot\mathbf{A}(\mathbf{r}_j,t)\,|i\rangle + \sum_j \frac{q_j^2}{2m_j\, c^2}\ \langle f|\, \mathbf{A}^2(\mathbf{r}_j,t)\,|i\rangle + \\ \sum_{n\neq i}\sum_{j,j'} \frac{q_j\, q_{j'}}{m_j\, m_{j'}\, c^2}\frac{\langle f|\, \mathbf{p}_j\cdot\mathbf{A}(\mathbf{r}_j,t)\,|n\rangle\,\langle n|\, \mathbf{p}_{j'}\cdot\mathbf{A}(\mathbf{r}_{j'},t)\,|i\rangle}{E_i - E_n}\end{aligned} \tag{1.46}$$

where one can refer to the three terms in equation 1.46 as $S^{(1)}(\mathbf{A}(\mathbf{r},t))$, $S^{(1)}(\mathbf{A}^2(\mathbf{r},t))$ and $S^{(2)}(\mathbf{A}^2(\mathbf{r},t))$, respectively.

The first term describes the radiation-matter interaction processes in which one photon is absorbed or emitted. By employing the dipole approximation for the electromagnetic field ($e^{-i\mathbf{k}\cdot\mathbf{r}}\sim 1$) and considering only the terms relative to the absorption($E_f > E_i$), it is possible to derive the following expression for the matrix element:

$$S^{(1)}(\mathbf{A}(\mathbf{r},t)) = \sum_{\mathbf{k},l}\frac{i(\omega_f-\omega_i)}{c}\sqrt{\frac{2\pi c^2}{V\omega_{\mathbf{k}}}}\,\langle f|\sum_j -q_j\mathbf{r}_j\cdot\hat{\boldsymbol{\epsilon}}_l\,|i\rangle \tag{1.47}$$

By employing the definition of dipole moment $\boldsymbol{\mu}=\sum_j \mathbf{r}_j\cdot q_j$, the transition probability W_{abs} for the absorption of a photon is given by:

$$W_{abs} = \frac{\omega}{V}\left(\frac{2\pi}{\hbar}\right)^2\sum_l |\,\langle f|-\boldsymbol{\mu}\cdot\hat{\boldsymbol{\epsilon}}_l\,|i\rangle\,|^2\delta(\omega_{if}-\omega) \tag{1.48}$$

where $\omega_{fi}=\omega_f-\omega_i$. The expression for W_{abs} allows for recognising some typical features of the IR absorption. Specifically, since the dipole moment is an odd operator, only transitions between states with different parity are allowed. Moreover, from equation 1.48 it is possible to determine the cross section for the infrared absorption. During molecular vibrations, the dipole moment $\boldsymbol{\mu}$ undergoes infinitesimal changes, hence it can be expanded as a Taylor series in the normal coordinates Q_k near the equilibrium position Q_0:

$$\boldsymbol{\mu}\approx\boldsymbol{\mu}_0+\sum_k\left(\frac{\partial\boldsymbol{\mu}}{\partial Q_k}Q_k\right)_{Q_0}+O(Q_k^2) \tag{1.49}$$

Since the first term of the expansion gives a null contribution, the IR absorption cross section σ_{IR} is determined by the first derivative of the dipole moment:

$$\sigma_{IR}\propto\left(\frac{\partial\boldsymbol{\mu}}{\partial Q}\right)^2 \tag{1.50}$$

Returning to equation 1.46, the second term $S^{(1)}(\mathbf{A}^2(\mathbf{r},t))$ describes transitions in which the molecular state does not change, *e.g.* $|f\rangle=|i\rangle$.

The cross section for the inelastic Raman scattering involving two photons can be derived from the third term $S^{(2)}(\mathbf{A}^2(\mathbf{r},t))$. By defining the molecular polarisability tensor as

$$\boldsymbol{\alpha}_{\beta,\gamma} = \sum_{\beta,\gamma}\sum_{n}\left\{\frac{\langle f|\,\mu^{\beta}\,|n\rangle\,\langle n|\,\mu^{\gamma}\,|i\rangle}{E_i - E_n - \hbar\omega_f} + \frac{\langle f|\,\mu^{\gamma}\,|n\rangle\,\langle n|\,\mu^{\beta}\,|i\rangle}{E_i - E_n - \hbar\omega_i}\right\} \tag{1.51}$$

where β and γ cartesian components of the dipole moment $\boldsymbol{\mu}$ and $|n\rangle$ intermediate states, the transition probability W_{Raman} for the inelastic Raman scattering can be written as

$$W_{Raman} = \sum_{l,l'}\sum_{\mathbf{k},\mathbf{k}'}\frac{(2\pi)^3\,\hbar}{V^2}\omega_{\mathbf{k}}\omega_{\mathbf{k}'}^3|\boldsymbol{\epsilon}_l\cdot\boldsymbol{\alpha}_{\beta\gamma}\cdot\boldsymbol{\epsilon}_{l'}|^2\delta(\omega_{fi}-\omega) \tag{1.52}$$

Analogously to the IR, also in this case it is possible to expand the polarisability as a Taylor series in the normal coordinates, allowing for expressing the Raman cross section in terms of the changes of the polarisability with the vibrational coordinates

$$\sigma_{Raman} \propto \left(\frac{\partial\boldsymbol{\alpha}}{\partial Q}\right)^2 \tag{1.53}$$

Raman scattering is second order process, therefore from an experimental point of view, it will be hindered by the possible first order resonant processes, such as rotovibrational transitions (energies comparable with IR photons) or electronic transitions (typical energies comparable to UV photons). Taking these aspects into account, the more useful spectral regions to perform Raman spectroscopy are the visible and near-infrared range. Notably, resonant Raman can occur when the denominator in equation 1.51 is close to zero. This phenomenon takes place if the transition in the Raman process does not target a virtual state but an electronic excited state of the system.

1.3.1 Surface Enhanced Infrared Absorption (SEIRA)

The increase in the infrared signal of molecular monolayers adsorbed onto a metallic film was observed for the firs time in 1980 by Hartstein *et al.* [56]. The SEIRA effect consists in the increase of the molecules absorption rate per unit volume that is proportional to the energy density of the field at the appropriate frequency [57]. The spectral enhancement can be explained by taking into account two different phenomena affecting the IR cross section, which are referred to as *electromagnetic* and *chemical mechanism* [58].

The *electromagnetic mechanism* arise from the coupling between radiation and surface plasmons which have resonance frequencies in the IR spectral range. Typical plasmonic systems that sustain these modes are metallic islands, usually obtained by the evaporation of metals [59], and mesoscopic NP assemblies [14]. Other SEIRA substrates include lithography-assisted NP arrays [60, 61] and hybrid core-shell particles [62]. The SEIRA effect also occurs in non-metallic materials such as dielectrics and semi-conductors, arising from the interaction of the electromagnetic field with surface phonons [12]. Following the Drude formalism and employing a dielectric function for non-metallic materials, the resonance condition given by

equation 1.14 is fulfilled in the IR region [63, 64]. Compared to the plasmon resonance, the phonon resonance shows a sharper curve, due to lower damping [63].

The *chemical mechanism* is associated with the variation in the dipole moment of analytes that occurs upon interaction with the substrate, resulting in the increase of the absorption cross section. Specifically, each infrared band associated to a fundamental vibrational mode is intrinsically determined by the partial derivative $(\partial\boldsymbol{\mu}/\partial Q)$, as reported in equation 1.50, hence the modification of the dipole moment is reflected in the intensity and shape variations as well as in shifts of the centre frequency. This effect is more pronounced for chemisorbed molecules as compared to physisorbed ones [58], since the possible formation of chemical bonds substantially alters the molecular orbitals of the adsorbed molecules and could even lead to the formation of new electronic states. A further factor for signal intensity amplification is associated to the surface selection rules, which entail the preferential enhancement of modes associated to variations of the dipole moment along the normal direction with respect to the plasmonic surface [57]. As an example, Osawa *et al.* reported the SEIRA spectrum of p-nitrobenzoate adsorbed onto a silver substrate, highlighting that the antisymmetric stretching mode of NO_2, corresponding to variations of $\boldsymbol{\mu}$ parallel to the silver surface, results poorly amplified [65].

A theoretical frame of the SEIRA effect, that explains the band shape modifications and quantitatively predicts the spectral enhancement, accounting both for *electromagnetic* and *chemical* mechanisms, has been proposed by Bjerke *et al.* [66]using effective medium theories, including Maxwell-Garnett and Bruggeman descriptions [67].

SEIRA enhancement factor

In order to quantify the efficiency in enhancing the spectroscopic signal of a given molecule by a surface enhanced spectroscopy, the enhancement factor EF can be defined as [68]:

$$EF = \frac{I_{enh}/N_{enh}}{I_{trad}/N_{trad}} \tag{1.54}$$

where I_{enh} and I_{trad} are the surface enahnced and traditional signal intensities, while N_{enh} and N_{trad} are the average number of molecules contributing to the signal in the two cases, namely those adsorbed on the plasmonic active substrate and those located in the illumination volume in the traditional spectroscopy, respectively. In general, the signal intensity $I(\omega)$ is proportional to the number N of active molecules in the excitation spot, to the molecules cross section σ for a given process and to the intensity $I_0(\omega)$ of the incoming excitation beam:

$$I(\omega) \propto N\,\sigma\,I_0(\omega) \tag{1.55}$$

The electromagnetic mechanism leads to the enhancement of the incoming field at the interface of the plasmonic substrate. This local field enhancement can be expressed by a gain factor $g(\omega) = |E_{loc}(\omega)|/|E_0(\omega)|$, where $|E_0(\omega)|$ and $|E_{loc}(\omega)|$ are the amplitudes of the incoming electric field and of that localised at the plasmonic active site, respectively. In the case of SEIRA spectroscopy, the intensity of the localised enhanced field has to be taken into account as excitation source in equation

1.55, therefore the signal intensity can be expressed as:

$$I_{SEIRA} \propto N_{SEIRA}\, \sigma_{IR}^{ads}\; g^2(\omega)\, I_0(\omega) \tag{1.56}$$

where the gain factor is squared since we are dealing with the field intensity and σ_{IR}^{ads} is the cross section of the IR-active molecules adsorbed on the substrate.

The expression for the SEIRA enhancement is obtained by combining equations 1.54 and 1.56:

$$EF_{SEIRA} = \frac{\sigma_{IR}^{ads}}{\sigma_{IR}}\, g^2(\omega) \tag{1.57}$$

where the ratio between the cross section of the molecules adsorbed on the plasmonic substrate and that of the free molecules, σ_{IR}^{ads} and σ_{IR} respectively, contains the contribution to the enhancement of the *chemical mechanism*.

From equation 1.57 it emerges that the SEIRA signal benefits of a field enhancement proportional to the second power of the amplification experienced by the incoming field. The numerical values for the enhancement factor in SEIRA spectroscopy are reported in the $10 - 10^3$ orders of magnitude range for substrates based on metallic NPs [61, 14] and can raise up to 10^5 in the case of plasmonic nanoantenna arrays [69].

1.3.2 Surface Enhanced Raman Scattering (SERS)

SERS effect consists in the strong increment of the Raman intensity experienced by molecules located close to a nano-curved metallic surface. It was the very first case of surface enhanced spectroscopy discovered, indeed the first reports of enhanced Raman scattering by pyridine molecules adsorbed onto a silver electrode appeared on 1974 [70]. Analogously to SEIRA, it is possible to distinguish an *electromagnetic* and a *chemical mechanism* at the base of the phenomenon. The *electromagnetic* one depends on the features of the metallic substrate and results from the coupling between electromagnetic radiation in the frequency range spanning from the UV to the near-infrared and the LSPs. The *chemical mechanisms* originates from the changes in the Raman cross section of molecules induced by the modification in the environment and by eventual chemical binding. Specifically, the formation of a metal-ligand complex and charge-transfer phenomena that can occur between the molecule and the metal affect the molecular polarisability and in turn increase the Raman cross section of the molecule [71]. These effects could also result in slight variation of the typical vibrational energies of the molecule, thus the SERS spectra are often characterised by frequency shifts. In addition, the interaction with the metallic surface could affect the Raman selection rules, leading to the appearance of peaks corresponding to vibrational modes that are hindered in the traditional Raman spectra.

Another mechanism that can have a role in the signal enhancement is the resonant Raman, that occurs when the excitation energy is close to the molecular electronic transition energy. For this reason, the signal of resonant Raman scattering often appears together with fluorescence, but its quenching near the metal surface allows for revealing the Raman signal [72].

SERS enhancement factor

Since two photons are involved in Raman scattering processes, in SERS spectroscopy both the incoming and scattered fields benefit from signal enhancement. Following the definition of equation 1.54 reported in the previous Section, the total SERS intensity is given by:

$$I_{SERS} \propto N_{SERS}\, \sigma^{ads}_{Raman}\, g^2(\omega_0)\, g^2(\omega_1)\, I_0(\omega_0) \tag{1.58}$$

where σ^{ads}_{Raman} is the cross section of the Raman-active molecules adsorbed onto the plasmonic substrate and $g(\omega_0)$ and $g(\omega_1)$ are the field gain factors before and after the interaction with the sample. The SERS enhancement factor is therefore:

$$EF_{SERS} = \frac{\sigma^{ads}_{Raman}}{\sigma_{Raman}}\, g^2(\omega_0)\, g^2(\omega_1) \tag{1.59}$$

and also in this case the ratio between the cross section of the molecules adsorbed on the plasmonic substrate and that of the free molecules, σ^{ads}_{Raman} and σ_{Raman}, accounts for the *chemical mechanism*. In the case of $\omega_0 \sim \omega_1$, which holds when the Raman frequency shift is much smaller than the excitation frequency and the LSPR of the SERS substrate is broad enough, so that $g(\omega_0) \sim g(\omega_1)$, the power law $EF_{SERS} \propto g^4(\omega_0)$ holds. The proportionality of the *electromagnetic* enhancement factor to the fourth power of the field enhancement factor allows for obtaining higher signal enhancements with respect to SEIRA. SERS enhancement indeed can reach $10^{14} - 10^{15}$ order of magnitude, making even possible the single molecule detection [16, 15].

1.4 Current trends in plasmonic-based biosensors

Plasmonic nanostructures offer great opportunities in controlling and confining light well below the the diffraction limit as well as in providing high flexibility in interfacing their surface with molecules and macromolecules of biological relevance, enabling to develop novel and highly performing platforms for biosensing purposes. The crucial challenge in the realisation of biosensors is the efficient signal detection of specific molecules at low concentration in a solution or in a mixture [73]. Indeed, concentration thresholds required for tracing the presence of a molecule with common techniques are typically limited to the micromolar range, far beyond the biologically relevant amounts. Moreover, for actual diagnostic application, biosensing methods require detection and discrimination capability for specimens in complex biological media, with reproducible results, cost and time effectiveness, and ease of use under most conditions. These requirements can be fulfilled by employing properly derivatised plasmonic substrates that enable for detecting analytes at ultra-low concentration beside monitoring biochemical and biophysical processes, and inferring information on the interaction of analytes with the metal surface at varying environmental parameters. Moreover, plasmonic substrates can be easily integrated in microfluidic devices and multiplexing lab-on-a-chip systems, providing a high-throughput and label-free analysis of molecular interactions in real time. Colloidal noble metal NPs of various size and shape are the most commonly employed plasmonic substrate due to their easy synthesis and functionalisation and to the possibility of controlling their organization on solid substrates with high precision [74]. Concerning the material, that strongly affects the signal amplification, silver and gold are prominent. Specifically, silver shows the most intense plasmonic response often paid with lower stability, while gold provides rewarding chemical stability in different environmental conditions and good biocompatibility that make it more suitable for biomedical applications.

Plasmonic-based biosensors follow two main approaches: the first one is based on the variations induced in the LSPR of the plasmonic substrate by the interaction with the analyte, while the second strategy is aimed at amplifying the intensity of the spectroscopic signal associated to the analyte of interest [75]. Representative examples are reported in Figures 1.9 and 1.10.

In the first case, the shift of the LSPR induced by changes in the local refractive index is exploited for monitoring the adsorption of molecules at the metal-dielectric interface [76]. This procedure can be further refined by functionalising the plasmonic substrate with active molecules such as antibodies or aptamers able to selectively bind specific analytes [75]. The analysis of the LSPR signal shift, which is proportional to the substrate surface coverage [9], allows for determining the thermodynamical parameters driving the interaction kinetics. In this context, LSPR-based sensing allowed for studying antibody-antigen interaction [77], ligand-receptor kinetics [78], enzyme-substrate reaction [79] and for the detection of micro-RNA sequences [80, 81]. Moreover, the substantial modification of the LSPR that occurs when NPs aggregate as a result of the three-dimensional plasmon coupling is at the basis of colorimetric assays for the recognition of biomolecular processes such as DNA hybridisation [82] and detection of target molecules such as exosomal proteins [83] and heparin [84].

The second approach adopted in the development of plasmonic-based sensors

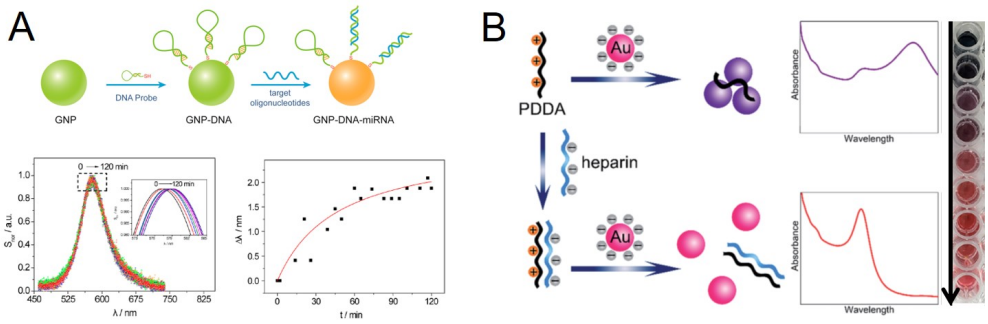

Figure 1.9. Plasmonic-based biosensors designed to monitor the LSPR variations of the plasmonic substrate upon interaction with a target analyte. (A) Detection of oligonucleotide sequences by means of DNA-modified gold nanoparticles. The hybridisation event between the target sequence and the single-strand DNA conjugated to the nanoparticles is identified by the shift of the LSPR due to the change of refractive index at the nanoparticle surface. Extinction spectra are reported on the bottom left, the corresponding LSPR as a function of time are reported on bottom right. Image adapted from ref [80]. (B) Colorimetric sensor for the detection of heparin based on its anti-aggregation effect on poly(diallyldimethylammonium chloride)(PDDA)-gold nanoparticles conjugates. The negatively charged gold nanoparticles aggregate in presence of the positively charged PDDA due to electric neutralisation. In contrast, the negatively charged heparin strongly bind PDDA, preventing nanoparticle aggregation. The different aggregation stages of the nanoparticles result in different colors of the dispersing solution, depending on the heparin concentration. Image adapted from ref. [84].

resides in leveraging the strong signal amplification provided by surface enhanced spectroscopies. Offering a wide choice of plasmonic scaffolds with LSPR spreading from visible to mid-infrared spectral regions, SERS and SEIRA are nowadays widely employed in sensing methodologies, allowing for probing molecular structures and conformation of biomolecules at extraordinarily low concentration with common spectroscopic setups.

SEIRA is particularly suitable for studying protein conformation [85] and lipid dynamics [13] due to the strong absorption of biological samples in the amide region (1450-1800 cm^{-1}), which allows for inferring the secondary structure of proteins, and in the CH_2-CH_3 stretching region (2800-3000 cm^{-1}) that is sensitive to structural variations in cell membranes and lipids phase transitions [14]. Nevertheless, in liquid samples the strong absorption of water often prevent the acquisition of IR spectra of good quality. This drawback is compensated by Raman spectroscopy where the water contribution is well separated from the fingerprint region of biological samples, allowing measurements in near-physiological conditions. In this respect, SERS-active substrate are broadly employed for investigating living cells and tissues [86, 18], especially for early cancer diagnostics. In these applications, plasmonic substrates are tipically obtained by functionalising NPs with a SERS label and a functional biointerface, able to interact with specific cellular receptors. The SERS label is a molecule showing a characteristic Raman signature that enables for recognising and localising the nanostructure within the sample. An effective alternative is to label the substrate with a molecule that exhibits structural changes, and in turn modifications of the SERS spectrum, in response to a specific variation in

the surrounding environment (*e.g.* in pH or temperature), transforming the SERS-labeled structure into a local nanoprobe of chemical processes occurring in cells [87, 17]. The SERS-active nanostructure might also hold therapeutic features by substituting the biointerface with properly selected anti-cancer drugs [31].

The interaction of these systems with cells is usually triggered by the biointerface [19], but alternative internalisation methods such as ultrasound induced transient poration of the cell membrane can be suitably employed [14, 88]. Once the nanoprobes are internalised or located in the proximity of a cell, their controlled aggregation can be induced for obtaining a higher signal intensity due to the formation of hot spots [89, 90].

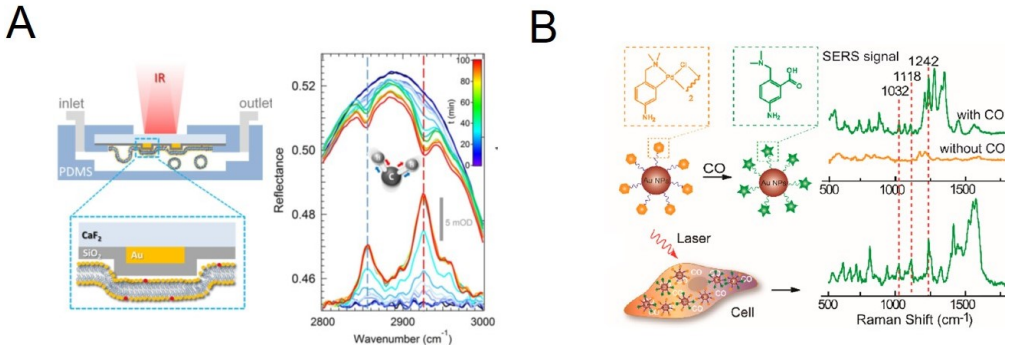

Figure 1.10. Plasmonic biosensors based on surface enhanced spectroscopies. (A) SEIRA biosensor consisting in array of gold nanoantennas assembled onto a CaF_2 substrate. The high SEIRA signal in the lipid fingerprint region (CH_2-CH_3 stretching at 2800-3000 cm^{-1}) allowed for monitoring in real-time the formation kinetic of planar biomimetic lipid membranes. Image adapted from ref. [13]. (B) Detection of intracellular carbon monoxide (CO) by a SERS sensor based on the carbonylation reaction of palladacycle (PD). The sensor was realised by conjugating gold nanoparticles with PC, acting as reporter molecule with good SERS activity and reactivity with CO. The presence of CO results in the carbonilation of the PC leading to considerably modified SERS spectra of the PC-gold nanoparticles conjugates, allowing for the detection of CO in single cells under physiological conditions. Image adapted from ref [87].

Chapter 2

Bioplasmonic assemblies with tunable optical and functional properties

A key issue in designing versatile nanoplasmonic systems is to reach a deep mastery on the assembly of metallic NPs for strictly controlling their spatial arrangement, which also affects, through plasmon coupling, the overall optical properties. To this aim, two main approaches have been pursued: on one side, the deterministic arrangement of NPs on solid support provides substrates suitable for highly sensitive and reproducible biosensing [74, 91]; on the other side, the assembly of NPs in solution driven by molecular interactions opens up to the development of plasmonic-based applications in nanomedicine [92, 29].

In the latter framework, the strategy mainly adopted relies on interfacing NPs with biological macromolecules, which convey their intrinsic biocompatibility and programmable intermolecular interactions in providing the opportunity of assembling hybrid nanomaterials with the desired structure and functionality [93]. Among biomacromolecules, proteins provide easy manipulation and versatility along with well-defined structure, and, compared to DNA, they allow for addressing issues related to challenging syntheses and costliness [94]. In addition, their responsiveness to external stimuli such as temperature, pH, incident light, electric or magnetic fields supplies further degrees of freedom in controlling the assembly and the properties of the whole system [95, 96]. In order to take full advantage of such potentialities, it is essential to gain a fine control not only on the guided assembly, but also on the effects prompted by the environmental conditions. In this respect, several studies report on the protein-induced aggregation of NPs [97, 98, 99, 100], but a comprehensive explanation of all the mechanisms involved is still lacking. In particular, how the adsorption of molecules affects the colloids surface properties and triggers the aggregates formation is far from being fully elucidated.

Here it is reported a thorough study of the protein driven self-assembly of citrate-stabilised colloidal gold NPs (AuNPs), aimed at obtaining hybrid clusters with tunable structural, optical and biological properties. As first focus, the challenge of obtaining stable AuNPs aggregates in solution with selected size was pursued moving from the Velegol and Thwar theory [101, 102] for *charge patch* interactions,

which describes the self-limited aggregation of colloidal particles with non-uniform surface charge distributions. Among proteins, lysozyme (Lyz), an enzyme with size of 3 nm and robust globular folding, was chosen due to its high isoelectric point (pH 11.3) [103] which provides an overall positive charge at physiological pH. Moreover, Lyz performs an antibacterial activity through the lysis of bacterial cell wall [104]. Lyz-decorated AuNPs (Lyz-AuNPs) represent an ideal model system for the charge patch interactions theory, because of the surface charge inhomogeneity induced by the adsorption of proteins onto the anionic AuNPs. In addition, the incompressibility and structural stability of the assembly components allow the direct, quantitative comparison of experiments with the Velegol and Thwar model, overcoming effects related to conformational degrees of freedom. Two different sizes for AuNPs (100 nm and 60 nm), one order of magnitude higher as compared to the protein, were employed to finely tune the charge inhomogeneity on the colloids surface.

Before the presentation of the obtained results, the theory of charge patch interaction is briefly recalled in Section 2.1. Afterwards, a detailed characterisation of the aggregation in solution as a function of the different parameters involved in the process was presented. Dynamic light scattering (DLS), atomic force microscopy (AFM), Small Angle X-ray Scattering (SAXS) and UV-Visible absorption spectroscopy measurements were combined for establishing a correlation between the plasmonic response of the Lyz-AuNPs complexes and their structural and electrostatic features, in terms of cluster morphology and ζ-potential. The possibility of tailoring the size of the formed clusters was therefore exploited in order to select the optical properties of the plasmonic assemblies. Moreover, the lysis activity of the samples was assayed to figure out how the presence of AuNPs and the aggregation process affect the functionality of the whole system.
A sketch of the experiment is reported in Figure 2.1.

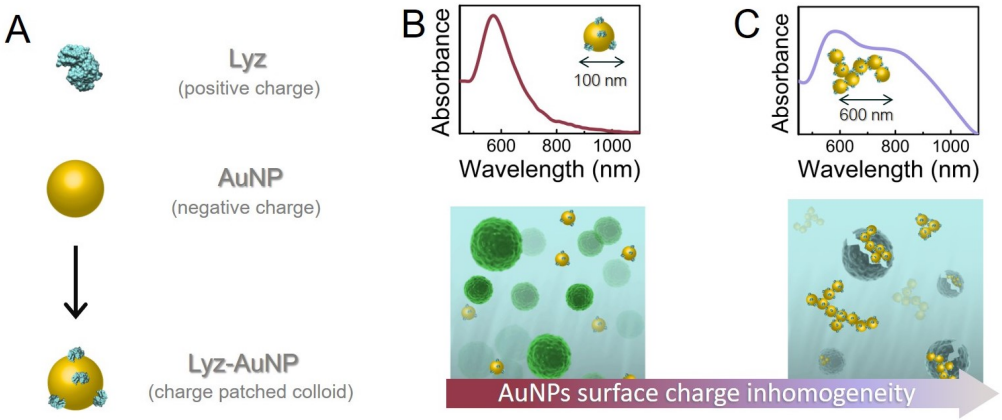

Figure 2.1. Sketch illustrating the strategy adopted for obtaining Lyz-decorated AuNPs assemblies. (A) Formation of charge patched colloids by adsorption of positively charged protein onto negatively charged AuNPs. Scheme of the modulation of the properties of Lyz-AuNPs complexes at increasing their surface ζ-potential. Representative absorption spectra and hypothesised mode of action in performing antibacterial activity of single (B) and aggregated (C) AuNPs are shown.

2.1 Theoretical principles of charge patch interactions

A non-uniformly distributed electric charge at the surface of colloidal particles in aqueous solution results in an interparticle potential that, even if the net charges on the two particles have the same sign, may show a significant attractive component [102]. Intuitively, such attraction originates from the interplay of short range, local interaction between oppositely charged "patches" on the approaching particles and the screening of the overall Colombic repulsion due to the ionic strength of the solution.
In this framework, several experimental studies on the self-assembly of charged colloidal particles, when mixed with oppositely charged polymers or macromolecules in an aqueous solvent pointed out a complex phenomenology, characterised by the formation of long-lived finite-size mesoscopic aggregates [105, 106], as shown in the representative size trend reported in Figure 2.2A. The rapid, correlated adsorption of the molecules on the surface of the colloidal particles generates such "patchy colloids", yielding the formation of aggregates although the individual particles are (considering the net charge) like-charged [102]. Notably, these aggregates are stable and their size (for given values of pH, temperature, ionic strength and concentration) is controlled by the polymer-particle charge ratio. In fact, changes in the polymer concentration both affect the net charge of the polymer-decorated colloids and the non-uniformity of charge distribution. Due to the progressive reduction of the net charge of the primary polymer-decorated colloids, at increasing the polymer content in the solution, increasingly larger clusters are observed. Close to the isoelectric point, where the charge of the adsorbed polymers neutralises the original charge of the colloids surface, the aggregates reach their maximum size.
The correlated adsorption of polymers is also responsible for the overcharging phenomenon, which occurs when more polymers adsorb onto the colloids than would be needed to completely neutralise their surface charge, so that eventually the sign of the net charge of the decorated surface is reversed. The interplay between the attractive charge patch interaction and the repulsion due to the overcharging results in a "reentrant condensation" of the decorated colloids as the charge ratio increases. Therefore, any further increase of the polymer-particle charge ratio causes the formation of aggregates with progressively reduced size. Eventually, aggregation does not occur at all if the repulsion between the overcharged decorated colloids becomes strong and/or the polymer coverage uniform.

A simple model, capable to describe this complex phenomenology and to explain the mechanism which drives the aggregation and formation of clusters with a well-defined size, was proposed by Velegol and Thwar [101]. The model, based on the Derjaguin approximation [107] and on an extension of the Hogg-Healy-Fuerstenau model [108], describes the interaction of non-uniformly charged colloidal particles through an interparticle potential of electrostatic nature. According to Velegol and Thwar, the pair interaction potential $\langle V \rangle$, between two spherical particles with radii R_1 and R_2 and non-uniform distribution of charge on their surface, can be expressed in terms of the average values ζ_1 and ζ_2 of the electrostatic surface potentials and the corresponding standard deviations σ_1 and σ_2. In units of the thermal energy

k_BT:

$$\langle V\rangle = \frac{\epsilon\pi R_1 R_2}{R_1+R_2}\Bigg[\left(\zeta_1^2+\zeta_2^2+\sigma_1^2+\sigma_2^2\right)\ln\left(1-e^{-2\kappa h}\right) + 2\,\zeta_1\,\zeta_2\ln\left(\coth\frac{\kappa h}{2}\right)\Bigg] \tag{2.1}$$

where h is the distance between the surfaces of the two approaching particles, ϵ the permittivity of the medium and κ^{-1} the Debye screening length. In this expression the Derjaguin approximation is included, that allows for writing the generic force $F(h)$ between the surfaces of two spheres at a distance h in terms of the potential $G(h)$ that would be observed between the surfaces of two infinite planes at the same distance [109]:

$$F(h) \propto \frac{R_1 R_2}{R_1+R_2}G(h) \tag{2.2}$$

The interparticle potential of equation 2.1 combines a net charge-dependent monopole term (for $\zeta_1, \zeta_2 \neq 0$), which is repulsive for like-charged particles, and a multipole term, arising from the charge heterogeneity ($\sigma_1, \sigma_2 \neq 0$), which is always attractive. The two terms have a different range of interaction, thus, for non-uniformly and like-charged particles, they combine to give a global maximum, which represents the potential barrier that two approaching particles must overcome to stick together. The height V_{max} of this potential barrier for two identical particles with radius a ($R_1 = R_2 = a$), average surface charge ζ and standard deviation of the surface charge σ is given by:

$$V_{max} = \pi\epsilon a\left\{\left(\zeta^2+\sigma^2\right)\ln\left[1-\left(\frac{\zeta^2}{\zeta^2+\sigma^2}\right)^2\right]+\zeta^2\ln\left(\frac{2\zeta^2+\sigma^2}{\sigma^2}\right)\right\} \tag{2.3}$$

As already highlighted by equation 2.2, the barrier height increases with the radius of curvature a of the colloids surfaces and, for a given value of the standard deviation σ, increases with the average surface potential ζ (or, roughly, the 'net charge').

An additional attractive term V_{vdW} can be considered in equation 2.1 to account for the ubiquitous van der Waals interactions, whose contribution can not be neglected when the screening length κ^{-1} becomes comparable with the interaction range of the van der Waals forces, for high concentrations or ionic strengths of the solution [110]. In figure 2.2B the total interaction potential $V = \langle V\rangle + V_{vdW}$ is represented as a function of h. Van der Waals interactions induce the lowering of V_{max} and the appearance of a secondary minimum, which increases with the ionic strength of the solution and the size of the aggregates. The aggregation kinetics and the thermodynamic stability of the dispersion result therefore modified [102]. Potentially, van der Waals interactions can destabilize the colloidal dispersion and clusters keep growing until, ultimately, they separate in phase.

In the experimental case herein discussed, the spherical particles are the lysozyme-decorated AuNPs, whose average surface potential has been evaluated by the ζ-potential values measured by electrophoretic mobility measurements as described in the Appendix. The non-uniformity of the surface charge distribution is generated by to the adsorption of lysozyme, which sparsely decorates the colloids surface (Figure 2.1A).

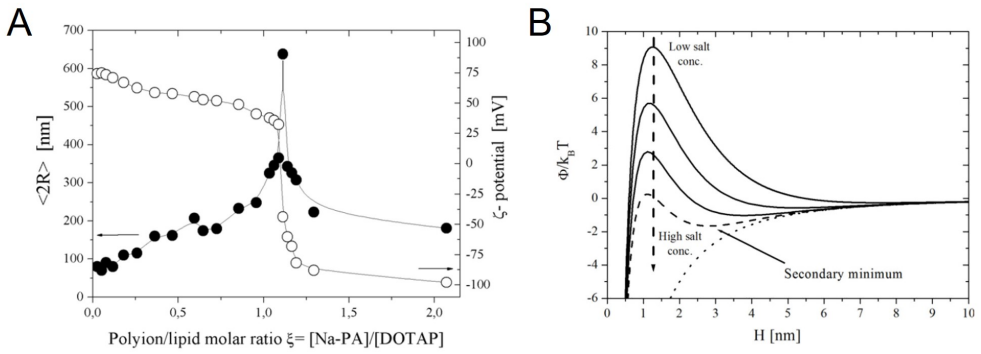

Figure 2.2. (A) Hydrodynamic diameter (black filled points) and ζ-potential (empty points) of colloidal liposomes complexes as a function of the molar charge ratio between sodium polyacrylate (Na-PA) and the synthetic lipid DOTAP. (B) Evolution of the total pair interaction potential $V = \langle V \rangle + V_{vdW}$, at increasing ionic strength of the solution. At low ionic strength van der Waals interactions can be neglected and the aggregation process is only tuned by the energy barrier that the approaching particles must overcome to stick together. Above a well-defined ionic strength, a secondary minimum appears. At higher ionic strength the repulsive barrier disappears and there is only one deep minimum. The screening parameter κ varies from 0.5 nm^{-1} (full line) to 3 nm^{-1} (dotted line). Adapted from ref. [102].

2.2 Self-assembly and colloidal stability: towards a controlled aggregation

Commercially available citrate stabilised AuNPs with nominal size of 100 nm and 60 nm were provided at the concentrations of 9.3 pM and 43 pM, respectively. Samples were prepared at room temperature by dissolving chicken hen egg white lysozyme powder in a sodium citrate buffer diluted 10 times to obtain solutions with different protein concentrations at controlled pH. Lyz-AuNPs colloids were therefore prepared at different protein-AuNP molar ratios ξ by adding to each protein solution the same volume of AuNPs stock solution and incubating for 2 minutes at room temperature. In the experiments herein presented, the protein concentration in the samples ranges between 4.65 pM and 5.38 μM. The characterisation of the system components perfomed by Dynamic Light Scattering (DLS), in terms of ζ-potential and size, and by UV-Visible absorption spectroscopy is reported in Table 2.1.

Table 2.1. DLS characterisation (ζ-potential and size) of AuNPs and lysozyme, and UV-Visible characterisation of AuNPs at pH 6.5. For the characterisation, lysozyme stock solutions was prepared at the concentration of 70 μM.

system component	ζ-potential (mV)	size (nm)	LSPR (nm)
AuNPs 100 nm	-54.0 ± 2.0	102.0 ± 2.0	572
AuNPs 60 nm	-42.0 ± 3.0	63.0 ± 2.0	536
Lysozyme	+4.0 ± 0.3	2.9 ± 0.2	-

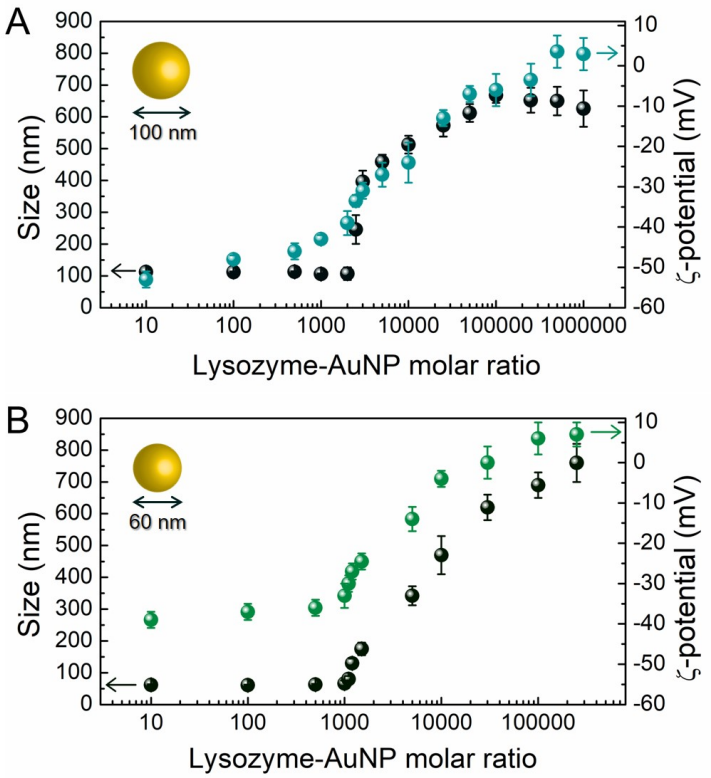

Figure 2.3. DLS measurements (size and ζ-potential trends) of Lyz-AuNPs as a function of the lysozyme-AuNPs molar ratio, using AuNPs of 100 nm (A) and 60 nm (B).

The colloidal aggregation of AuNPs upon adsorption of lysozyme was studied at pH 6.5 at varying the molar ratio ξ between the two species. AuNPs with two different sizes were employed to investigate how the different ratio between the protein and the colloids size affects the process. The size and ζ-potential trends of Lyz-AuNPs as a function of ξ are reported in Figure 2.3. Notably, the experiments point out a self-limited aggregation of colloids into assemblies whose size is determined by the lysozyme-AuNP molar ratio. Three different stages of the aggregation phenomenology can be recognised. At low molar ratios ($\xi \leq 2000$ for 100 nm AuNPs, panel A, and $\xi \leq 1000$ for 60 nm AuNP, panel B) size values remain stable around those of single AuNPs, while slight variations occur in the ζ-potential of colloids. For higher molar ratios, a steeper variation of the ζ-potential is observed, concomitant to the formation of aggregates starting from ζ = -33.5 ± 1.5 mV for 100 nm AuNPs and from ζ = -30.0 ± 2.0 mV for 60 nm AuNPs. The threshold molar ratios, corresponding to the onset of the aggregation process, are $\xi_{100} \approx 2500 \pm 500$ and $\xi_{60} \approx 1100 \pm 100$, respectively. Notably, the obtained clusters appear stable in solution, with a finite size increasing with ξ up to maximum values of 640 ± 30 nm for 100 nm AuNPs and 760 ± 60 nm for 60 nm AuNPs. When the ζ-potential values approach zero the size distributions become broader and a tendency to the formation of large unstable aggregates is observed, *i.e.* the measured size is not constant for repeated measures and the aggregates precipitate. For the highest molar ratios (starting from $\xi \approx 500000$ for 100 nm AuNPs and from $\xi \approx 100000$ for 60

nm AuNPs) a slight overcharging is also observed, with positive ζ-potential values always lower than 10 mV.

The overall phenomenology is consistent with a charge patch driven aggregation [106, 111, 112], described by the Velegol and Thwar model [101, 102]. For small protein amounts, the slight increase in the ζ-potential of the colloids, attributable to lysozyme adsorption onto the AuNPs surface, is not sufficient for triggering the aggregation, as pointed out by size measurements. The process is induced when enough proteins adsorb on AuNPs both to shield the long-range electrostatic repulsion and to originate surface charge inhomogeneity which induces significant short-range attraction between colloids. For both the sizes investigated, the onset of the aggregation occurs in correspondence of similar ζ-potential values, hence the repulsive Coulombian contribution to the interaction energy between colloids is of the same order of magnitude. The attractive contribution is also similar in the two cases. In fact the ratio $\xi_{100}/\xi_{60} = 2.3 \pm 0.5$ is consistent with the ratio between the surface areas of the two colloids (equal to 2.8). Assuming that the number of adsorbed molecules only depends on the protein concentration in solution (*i.e.* the adsorption of a molecule is not affected by the presence of other molecules onto the gold surface), this implies that the inhomogeneity degree on the colloids surfaces (*i.e.* the portion of the surface covered with proteins) are roughly the same at the aggregation onset.
In proximity of the isoelectric point, the aggregates reach their maximum size. Notably, the maximum size of the aggregates is slightly larger for the 60 nm AuNPs. Again, this finding is consistent with the Velegol and Twar model. As it is easy to show [101, 102], within the Derjaguin approximation employed (equation 2.2), the potential barrier that must be overcome in order that two particles (or two aggregates) stick together is proportional to the factor $\frac{R_1 R_2}{R_1+R_2}$, where R_1 and R_2 are the radii of curvature of the two approaching objects, so that the limiting size is reached faster when the primary particles are larger.
At high molar ratios, the absorption of more lysozyme molecules onto the AuNPs is hindered. This could be due either to steric hindrance (the number N_{max} of proteins corresponding to the full coverage of the AuNPs surface by a monolayer can be evaluated as ~ 4900 for 100 nm AuNPs and ~ 1800 for 60 nm AuNPs [113, 114]) and/or to the electrostatic repulsion between an approaching lysozyme molecule and the already adsorbed proteins on the Lyz-AuNPs [102].

2.2.1 Assessing the surface coverage by ζ-potential measurements

A quantitative analysis of the aggregation phenomenology can be carried out by employing the Velegol and Thwar model for the charge patch interactions discussed in Section 2.1.

If the net charge carried by each protein is higher than that of the portion of the AuNP surface on which the molecule adsorbs, the resulting patches bear a net charge which is opposite in sign to that of the bare particle surface. To verify this hypothesis and to evaluate σ, the number N_{lyz} of absorbed proteins per AuNP can be calculated as the ratio between the variation Δq of the effective surface charge of a single colloid upon absorption of lysozyme and the effective charge q_{lyz} transported

by each protein [97]:

$$N_{lyz} = \frac{\Delta q}{q_{lyz}} = \frac{q - q_0}{q_{lyz}} \tag{2.4}$$

where q is the effective charge of a lysozyme-decorated AuNP and q_0 that of a bare AuNP. It is therefore possible to express N_{lyz} in terms of the measured values of the ζ-potential, by combining the relations of Smoluchowsky and Hückel:

$$\zeta = \frac{\mu_e \, \eta}{\epsilon} \tag{2.5}$$

$$q = 6\pi\eta \, r \mu_e \tag{2.6}$$

where η and ϵ are the viscosity and permittivity of the dispersing medium, μ_e the electrophoretic mobility of the spherical particle and r its hydrodynamic radius. With these assumptions equation 2.4 writes:

$$N_{lyz} = \frac{a \, (\zeta - \zeta_0)}{r_{lyz} \, \zeta_{lyz}} \tag{2.7}$$

where ζ_0 and ζ_{lyz} are the ζ-potentials of the bare AuNPs and of the lysozyme, respectively, and r_{lyz} is the hydrodynamic radius of the protein.
The AuNPs surface coverage Φ, *i.e.* the portion of the AuNPs surface covered by the adsorbed proteins, is then obtained by the ratio between N_{lyz} and the maximum number N_{max} of proteins that can be absorbed onto each AuNP, given by [113, 114]:

$$N_{max} = 0.65 \, \frac{(a + 2\, r_{lyz})^3 - a^3}{r_{lyz}^3} \tag{2.8}$$

It is now possible to derive an expression for σ by defining as ζ_{cov} the value of the surface potential in correspondence of the regions covered by the protein (or in other words the average surface potential of fully covered AuNPs), and assuming that the surface charge density in the other regions is not affected by the protein adsorption. Under such assumptions the variation $\Delta\zeta$ of the surface potential is proportional to the surface coverage:

$$\Delta\zeta = \zeta - \zeta_0 = (\zeta_{cov} - \zeta_0)\Phi \tag{2.9}$$

and the following expression holds for the standard deviation:

$$\sigma = \sqrt{(\zeta_0 - \zeta)^2 \, (1 - \Phi) + (\zeta_{cov} - \zeta)^2 \, \Phi} \tag{2.10}$$

Combining equations 2.9 and 2.10 and defining $\Delta\zeta_{max} = \zeta_{cov} - \zeta_0$, which represents the maximum variation of the surface potential corresponding to the full coverage of AuNPs, yields the two equivalent expressions:

$$\sigma = \Delta\zeta_{max} \sqrt{\Phi \, (1 - \Phi)} = (\zeta - \zeta_0) \sqrt{\frac{1 - \Phi}{\Phi}} \tag{2.11}$$

The first expression represents an arc of circumference in the plane (Φ, $\sigma/\Delta\zeta_{max}$), starting in the origin of the axes and increasing up to the maximum value $\sigma/\Delta\zeta_{max} = 0.5$ for half coverage conditions ($\Phi = 0.5$). This behaviour, directly deriving from the

general assumption that the coverage Φ is proportional to the measured ζ-potential variation of equation 2.9, is consistent with that obtained by Sennato *et al.* [106] in modelling the electrostatic adsorption of polyelectrolytes to liposomes. The second expression of equation 2.11 allows for calculating σ using the measured ζ-potential values. The average number N_{lyz} of proteins adsorbed on each AuNP, of the surface coverage Φ, of the standard deviation σ of the surface ζ-potential, and of the height V_{max} of the potential barrier, calculated for the different lysozyme-AuNP molar ratios employed in the experiments, are reported in Table 2.2 and 2.3 for the two NP sizes analysed.

Table 2.2. Values of the parameters of the Velegol and Thwar interaction potential, calculated at varying the lysozyme-AuNPs molar ratio ξ for the 100 nm Lyz-AuNPs. The values corresponding to the aggregation threshold of the Lyz-AuNPs are highlighted in blue.

ξ	ζ (mV)	N_{lyz}	Φ (%)	σ (mV)	V_{max} (k_BT)
10	-53.0 ± 1.5	9	0.2	24	72.5
100	-48.0 ± 1.5	52	1.1	58	25.5
500	-46.0 ± 1.5	69	1.4	67	18.3
1000	-43.0 ± 1.5	95	1.9	78	11.5
2000	-39.0 ± 3.0	129	2.6	91	6.3
2500	-33.5 ± 1.5	177	3.6	106	2.7

Table 2.3. Values of the parameters of the Velegol and Thwar interaction potential, calculated at varying the lysozyme-AuNPs molar ratio ξ for the 60 nm Lyz-AuNPs. The values corresponding to the aggregation threshold of the Lyz-AuNPs are highlighted in green.

ξ	ζ (mV)	N_{lyz}	Φ (%)	σ (mV)	V_{max} (k_BT)
10	-40.5 ± 2.0	8	0.4	23	22.3
100	-37.0 ± 2.0	26	1.4	42	9.9
500	-36.0 ± 2.0	31	1.7	46	8.1
1000	-33.0 ± 2.0	47	2.5	56	4.6

Notably, for both AuNPs sizes when the onset of the aggregation process occurs, the calculated values of V_{max} approach the thermal energy ($\sim$ 25 meV at 25°C).

2.2.2 Structural characterisation of the assemblies

To gain more insight on the morphology of the Lyz-AuNPs complexes, AFM measurements were performed on clusters deposited onto silicon substrated previously modified with (3-Aminopropyl)triethoxysilane (APTES) as described in the Appendix. The deposition procedure was optimised with respect to incubation time in order to considerably reduce undesired aggregation. Notably, the electrostatic interaction between the array of positively charged amine groups exposed by APTES

molecules and the negatively charged Lyz-AuNP complexes results in an accelerated and stable adsorption that allows for reducing the time of deposition and for eliminating the solvent without affecting the organisation of the complexes on the substrate. Representative AFM images are reported in Figure 2.4. Consistently with DLS results, the size of the aggregates measured by AFM increases with the lysozyme-AuNP molar ratio ξ. Clusters with low coordination number (Figures 2.4A and 2.4C), observed just above the aggregation threshold, appear compact, while at higher molar ratios (Figure 2.4B and 2.4D) they became less regular and branched. In this fractal-like organisation, resulting upon the two-dimensional rearrangement on the substrate, the aggregates are mainly composed by only one stack of AuNPs (superimposed AuNPs are rarely observed), suggesting a branched and sparse three-dimensional conformation characterised by a low fractal dimension.

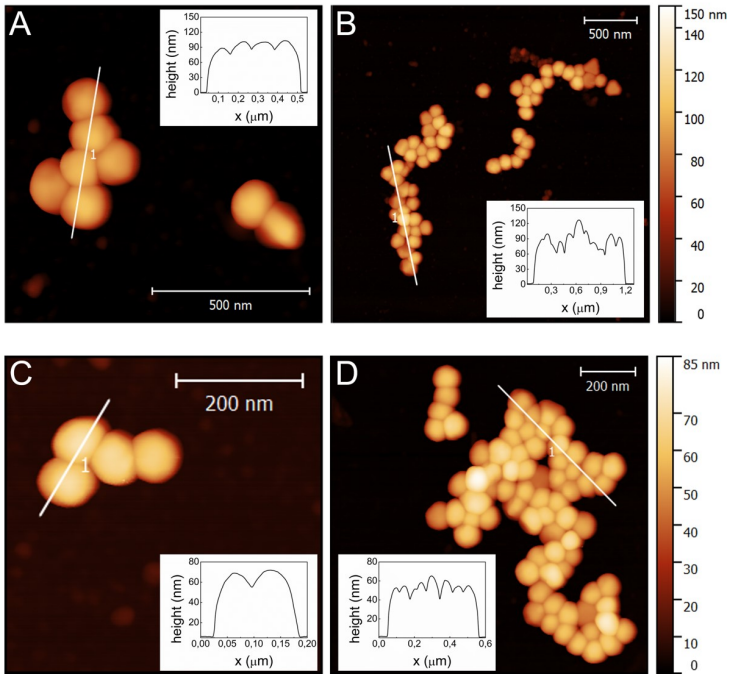

Figure 2.4. Representative AFM images acquired on clusters corresponding to $\xi = 3000$ (A) and $\xi = 10000$ (B) for 100 nm AuNPs and to $\xi = 1200$ (C) and $\xi = 5000$ (D) for 60 nm AuNP; the corresponding height profiles are reported in the insets of the AFM images.

To further investigate this aspect, the structure of the clusters in solution was analysed by means of SAXS. Experiments were carried out at the SWING beamline of Soleil Synchrotron (see Appendix for experimental details). The measured scattered intensity $I(q)$ is given in terms of the particle form factor $P(q)$ and the system structure factor $S(q)$ (equation A.2). $P(q)$ describes the ensemble averaged shape of the scattering objects whereas the structure factor $S(q)$ accounts for the interference introduced by interparticle correlations. The scattering curves for 100 nm and 60 nm AuNPs at varying ξ are shown in Figure 2.5. The aggregation of the Lyz-AuNPs complexes can be easily identified from the scattering curves by looking at the low q region ($q < 0.006\,\text{Å}^{-1}$). Here, the curves of non-aggregated AuNPs show a

plateau towards decreasing q, while the onset of the aggregation is identified by the variation of the scattering curve trend that results in a steeper slope. The onset of the Lyz-AuNP aggregation so identified is accordance with the aggregation onsets extrapolated by DLS measurements ($\xi_{100} \approx 2500 \pm 500$ and $\xi_{60} \approx 1100 \pm 100$, respectively).

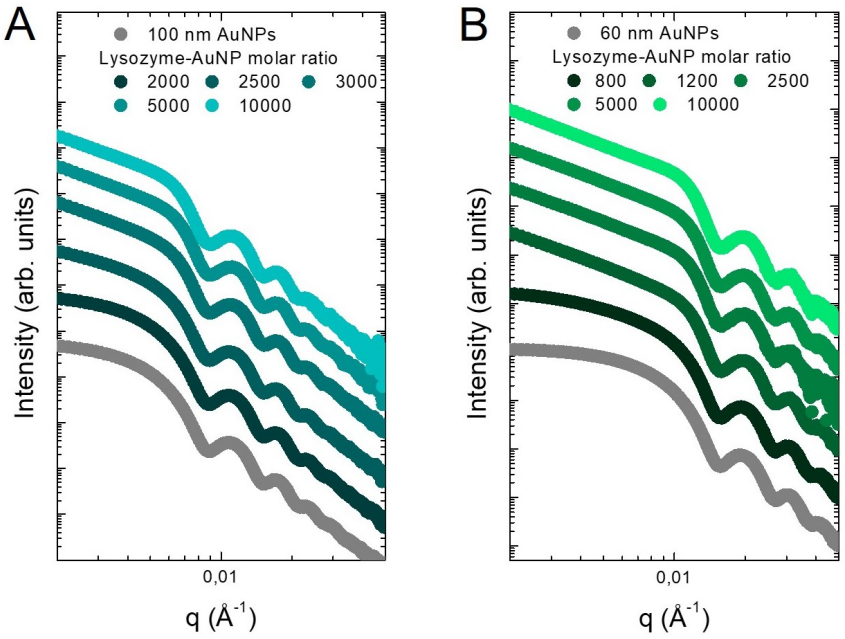

Figure 2.5. SAXS curves acquired at different lysozyme-AuNP molar ratio for 100 nm (left) and 60 nm (right) AuNPs. The scattering curve measured for the corresponding AuNPs stock solutions are also shown in grey for comparison. Curves have been vertically shifted for clarity.

Concerning the spatial oragnisation of the complexes, a key parameter which defines the structure of a disordered aggregate is the mass fractal dimension D_f. It is essentially a measure of the scaling of the mass M with the size of the aggregate, defined as the exponent of the expression $M \propto R^{D_f}$, where R is a linear measure of the size [115]. This parameter can be determined by the negative slope of the linear region in the log-log plot of $I(q)$ vs. q [116]. The extrapolated values of the fractal dimension are reported as a function of ξ in Figure 2.6 for 100 nm and 60 nm, respectively. For both NP sizes the estimated D_f is lower than 2, pointing out a diffusion-limited colloidal aggregation [117]. Such phenomenology is typical of systems where the aggregation rate is limited by the average time interval between the collisions of two particles or two clusters, which increases upon aggregation due to the lowering of the diffusion coefficient of larger objects and of their concentration in solution. This leads to the formation of non-compact and branched clusters. Notheworty, the decreasing trends of D_f for both NPs sizes appear consistent with AFM images that show more branched clusters at higher coordination numbers.

More insights on the short-range interparticle correlations were obtained by removing the contribution of the form factor and analysing the resulting structure

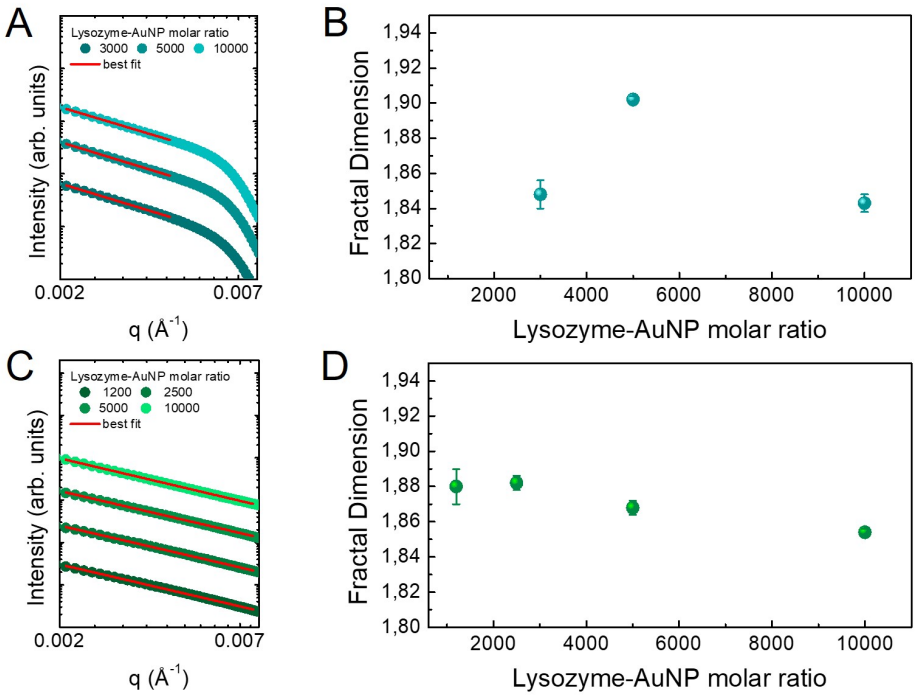

Figure 2.6. Analysis of the mass fractal dimension of Lyz-AuNP complexes peformed on SAXS curves above the aggregation onset, for 100 nm (top) and 60 nm (bottom) AuNPs. Zoom of the SAXS curves in the low q region (A, C); best fits (solid lines) are superimposed to the experimental points (filled circles). Mass fractal dimension D_f as a function of the molar ratio (B, D).

factor $S(q)$ [118]. Pratically, this is obtained by dividing the scattering intensity of the Lyz-AuNPs samples for that of the non interacting AuNPs, for which $S(q) \sim 1$ (grey curves in figure 2.5). The so obtained structure factors were fitted by a sticky hard spheres model, defined by a Percus-Yevick approximation with an attractive square well potential [119, 118]. Such model allows for extrapolating the interparticle distance between two adjacent NPs knowing the gyration radius of the colloids, obtained by fitting the SAXS curves measured on the AuNPs stock silution with a spherical form factor. The obtained values of interparticle distance are reported as a function of ξ in Figure 2.7, for the two AuNPs sizes investigated. For both the NP sizes, the interparticle distances, of few nanometres, increase with ξ, pointing out that the separations of few nanometres increase for larger and more branched aggregates. Instead, concerning the extrapolated values, the 60 nm AuNPs clusters result more packed than the 100 nm AuNPs ones. This findings is consistent with the charge patch theory, since for higher radius of curvature of the colloids a stronger repulsive component is expected to contribute in the interaction potential.

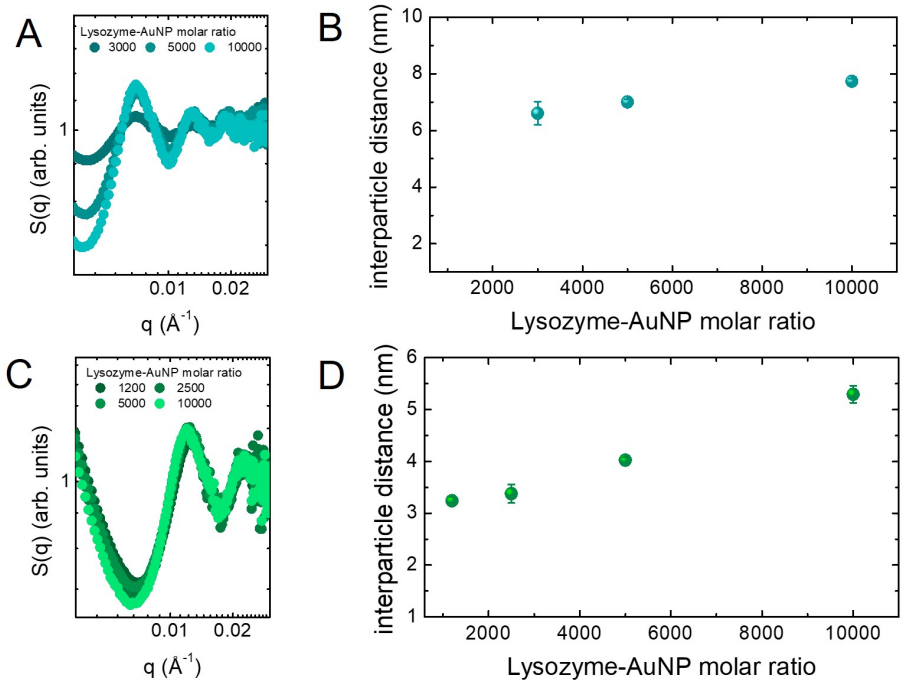

Figure 2.7. Analysis of the interparticle distance of Lyz-AuNP complexes, peformed on SAXS curves above the aggregation onset, for 100 nm (top) and 60 nm (bottom) AuNPs. Structure factor $S(q)$ obtained from the ratio between the scattering intensity of the Lyz-AuNPs samples and that of the non interacting AuNPs (A, C). Interparticle distance as a function of the molar ratio (B, D).

2.3 Tailoring the plasmonic response of the assemblies

In the previous Section the effectiveness of the protein-mediated self-assembly of AuNPs as an efficient route for the fabrication of clusters with controllable finite size was demonstrated. Here, the optical response of the obtained assemblies is investigated in detail, with the purpose of tailoring their plasmonic response (*i.e.* the LSPR) in a broad optical range between the visible and the near-infrared. To this end, the absorption spectra of Lyz-AuNPs complexes were measured for selected values of the molar ratio ξ, according to the aggregation trends of Figure 2.3. Representative spectra are reported in Figure 2.8 for 100 nm (panel A) and 60 nm (panel B) AuNPs. For both the AuNP sizes the spectra show a similar evolution, depending on the lysozyme-AuNPs molar ratio. At low ξ values, the absorption peak corresponding to the LSPR of AuNPs shows a progressive quenching in the intensity and a redshift compared to that of the stock solution. Starting from $\xi \approx 2500$ for 100 nm AuNPs and from $\xi \approx 1100$ for 60 nm AuNPs, a shoulder at higher wavelengths appears in the plasmonic profiles, together with a further broadening and shift of the LSPR of the primary colloids. The spectral changes proceed at increasing the molar ratio with the rise of a wider absorption band extending well into the near-infrared region, more extensively for 100 nm AuNPs, up to an asymptotic condition (starting from $\xi \approx 50000$ for 100 nm AuNPs and from $\xi \approx 10000$ for 60 nm AuNPs).

A strict correspondence can be recognised between the evolution of the Lyz-

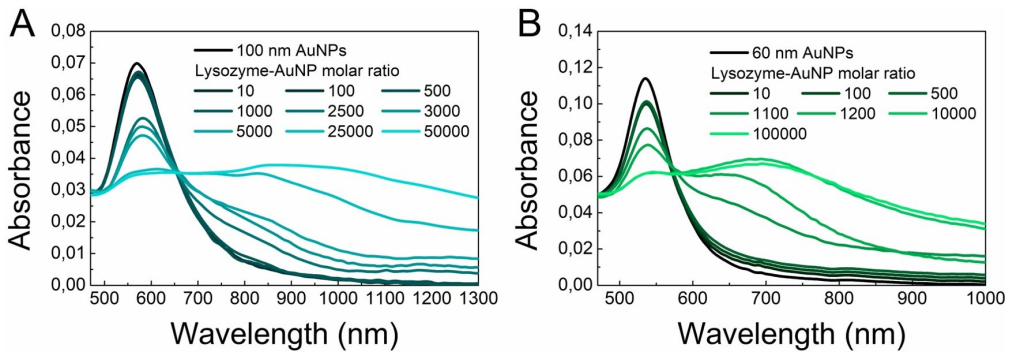

Figure 2.8. Representative absorption spectra acquired at different lysozyme-AuNP molar ratio for 100 nm (left) and 60 nm (right) AuNPs. The spectra measured for the corresponding AuNPs stock solutions are also shown for comparison.

AuNPs absorption spectra as a function of the molar ratio ξ and the stages of the colloidal aggregation discussed in Section 2.2. The initial redshift and quenching of the LSPR absorption peak are consistent with changes in the dielectric environment at the AuNPs interface induced by the adsorption of lysozyme [9], in accordance with the slight increase of the measured ζ-potential. The shoulder in the plasmonic profiles, which appears in correspondence of the onset of the aggregation process, originates from the rise of coupled interparticle plasmonic modes due to the constructive interference between the electronic oscillation modes of neighboring AuNPs [4, 5]. The redshift and broadening of the absorption band observed upon increasing the lysozyme concentration reflect the size and ζ-potential increasing trends of Figure 2.3. Analogously, further evolution of the optical response is not observed after the isoelectric point of the complexes. Focusing on the spectra corresponding to the aggregation onset, the observed changes are ascribable to the formation of dimers and small aggregates [120, 54]. The further redshift and broadening of the absorption band at increasing the lysozyme amount point out a higher number of coupled plasmons due to the formation of larger aggregates, which absorb light in a wider range of wavelengths. Such optical behaviour is consistent with the plasmonic response of three-dimensional fractal aggregates of AuNPs, characterised by the superposition of several interparticle modes corresponding to different interaction strength between plasmons [54, 53] (see Section 1.2.2). With reference to the analysis of the interparticle distances (Figure 2.7), the observed inhomogeneous distributions for both the AuNPs sizes justify the non-sharp separation between longitudinal and transverse plasmonic modes in the spectra. Actually, it would be interesting to analyse in detail this correspondence between structure and optical response of clusters by near-field electromagnetic simulations of the coupled plasmonic modes [54, 53], for which the microscopic and spectroscopic characterisation herein reported would represent an important experimental basis.

2.3.1 Assessing the surface coverage by the LSPR redshift

By analysing the initial redshift of the plasmonic profiles, highlighted in Figure 2.9, it is possible to extrapolate quantitative information on the surface coverage of

AuNPs due to lysozyme adsorption.

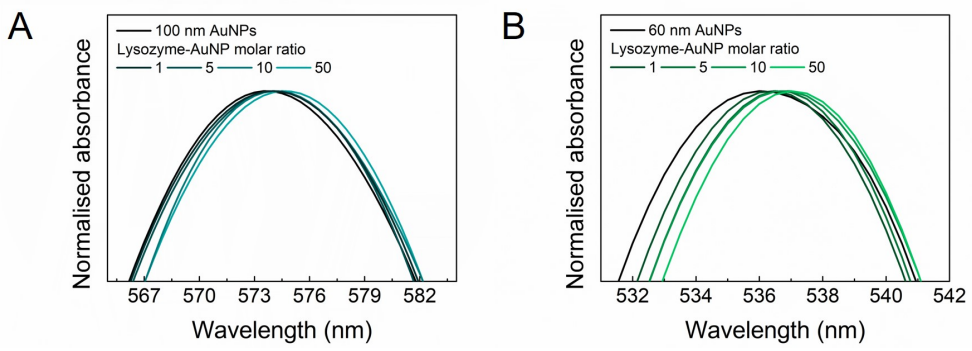

Figure 2.9. Zoom on normalised LSPR peaks obtained on samples prepared at low relative molar ratios using 100 nm (A) and 60 nm (B) AuNPs.

By expressing the LSPR resonance frequency ω_{res} of a spherical metallic NP (equation 1.15) as a function of the refractive index n_{out} ($\varepsilon_{out} = n_{out}^2$) of the medium surrounding the metal interface, a first order expansion allows to derive the expression for the shift $\Delta\lambda$ of the resonance wavelength λ_{res} occurring due to changes in n_{out}:

$$\Delta\lambda = \lambda_{res}(n_{out}) - \lambda_0 = m(n_{out} - n_0) \tag{2.12}$$

where n_0 is the initial value of the refractive index, $\lambda_0 = \lambda_{res}(n_0)$, and m is a sensitivity factor, given by

$$m = 2n_0 \left[\frac{\omega_p}{2\pi c\,(1 + 2n_0^2)}\right]^2 \lambda_0^3 \tag{2.13}$$

In the presence of an adsorbate layer, *i.e.* when the refractive index is non-uniform in the space surrounding the NP, it is possible to derive an expression for the effective value of n_{out} to account for in equation 2.12. Following Xu *et al.* [121], the effective refractive index n_{eff} at the interface of a single NP can be calculated by the weighted average of the refractive index $n(r, \theta, \varphi)$ in each position in the solvent. Specifically, the weighting function is the intensity of the localised electric field $\mathbf{E}(r, \theta, \varphi)$, given in the quasi-static, dipolar approximation by [1] (see also Section 1.1):

$$\mathbf{E}(r, \theta, \varphi) = \frac{3(\hat{\mathbf{r}} \cdot \mathbf{p})\,\hat{\mathbf{r}} - \mathbf{p}}{4\pi\varepsilon_0\varepsilon_{out}} \frac{1}{r^3} \tag{2.14}$$

where $\mathbf{p}$ is the dipole moment, $\mathbf{r}$ the position of the point of interest, $\hat{\mathbf{r}}$ the corresponding unit vector, and $\varepsilon = \varepsilon_0\varepsilon_{out}$ is the permittivity of the surrounding medium. The general expression obtained for n_{eff} is:

$$n_{eff} = \frac{\int_0^{2\pi} d\varphi \int_{-1}^{1} dcos\theta \int_a^{+\infty} dr\, r^2\, n(r, \theta, \varphi)|\mathbf{E}(r, \theta, \varphi)|^2}{\int_0^{2\pi} d\varphi \int_{-1}^{1} dcos\theta \int_a^{+\infty} dr\, r^2 |\mathbf{E}(r, \theta, \varphi)|^2} \tag{2.15}$$

where a is the NP radius. The value of n_{out} is then obtained by the average of n_{eff} calculated over all the NPs in the system:

$$n_{out} = \langle n_{eff} \rangle \tag{2.16}$$

The actual calculation of n_{eff} can be obtained by defining a model for $n(r, \theta, \varphi)$. By defining as n_{ads} the refractive index in correspondence of an adsorbed molecule, and by assuming that *i*) the adsorbed molecules have all same size d, and *ii*) each NP is covered by one shell of molecules at most (*i.e.*, $n(r, \theta, \varphi) = n_0$ for $r > a + d$), two simple cases can be distinguished: full coverage and non-uniform distribution of molecules on the NP surface.
In the first case, $n(r, \theta, \varphi)$ is equal to n_{ads} for $a < r < a + d$ and n_{eff} is the same for all the NPs in the system, hence:

$$n_{out} = n_{eff} = n_0 + (n_{ads} - n_0) \left[1 - \left(\frac{a}{a+d} \right)^3 \right] \tag{2.17}$$

In case of a non-uniform distribution of molecules, assuming that there is no correlation between the positions of molecules adsorbed to different NPs, the probability of finding a molecule in a point (θ, φ) of the spherical surface is given by the surface coverage Φ. Therefore, for $a < r < a + d$ the function $n(r, \theta, \varphi)$ assumes the value n_{ads} with probability Φ and the value n_0 with probability $1 - \Phi$. By solving equations 2.15 and 2.16 the following expression is obtained:

$$n_{out} = \langle n_{eff} \rangle = n_0 + \Phi(n_{ads} - n_0) \left[1 - \left(\frac{a}{a+d} \right)^3 \right] \tag{2.18}$$

This is equivalent to assume a shift in the refractive index linear with the adsorbate concentration at the interface [122]. Note that for $\Phi = 1$ the case of uniform layer is recovered.

The final expression for the LSPR redshift comes combining equations 2.12 and 2.18:

$$\Delta\lambda = m(n_{ads} - n_0) \left[1 - \left(\frac{a}{a+d} \right)^3 \right] \Phi \tag{2.19}$$

With the aim of quantitatively analysing the absorption of lysozyme onto the AuNPs surface on the basis of the model herein discussed, the LSPR shift on the absorption spectra acquired at low molar ratios (see Figure 2.9) was measured and the sensitivity factors m of AuNPs were evaluated according to equation 2.13. The values $\hbar\omega_p = 8.50$ eV for gold [123], $n_0 = 1.33$ being the external medium water and the values of λ_0 measured on the AuNPs stock solutions and reported in Table 2.1 were employed in the calculation. The so obtained sensitivity factors, 1135 nm/RIU for 100 nm AuNPs and 934 nm/RIU for 60 nm AuNPs, are consistent with those reported in literature for similar systems [124, 125, 126].

The surface coverage corresponding to each sample can be therefore calculated by equation 2.19. Noteworthy, the obtained values are in striking accordance with those calculated by the ζ-potential measurements reported in Table 2.2 and 2.3, validating the two procedure proposed for assessing the surface coverage of the AuNPs.

It is now possible to plot the surface coverage as a function of the lysozyme concentration in solution c_{lyz} for deriving the isothermal curves reported in Figure 2.10. By fitting data to a Langmuir isotherm:

$$\Delta\lambda = \Delta\lambda_{max} \frac{c_{lyz}}{K_d + c_{lyz}} \tag{2.20}$$

where K_d and $\Delta\lambda_{max}$ are the fitting parameters, $\Delta\lambda_{max}$ being the maximum shift corresponding to the full coverage of the AuNPs surface, it is possible to extrapolate the apparent dissociation constants, $K_d = 28 \pm 7$ pM for 100 nm AuNPs and $K_d = 160 \pm 40$ pM for 60 nm AuNPs.

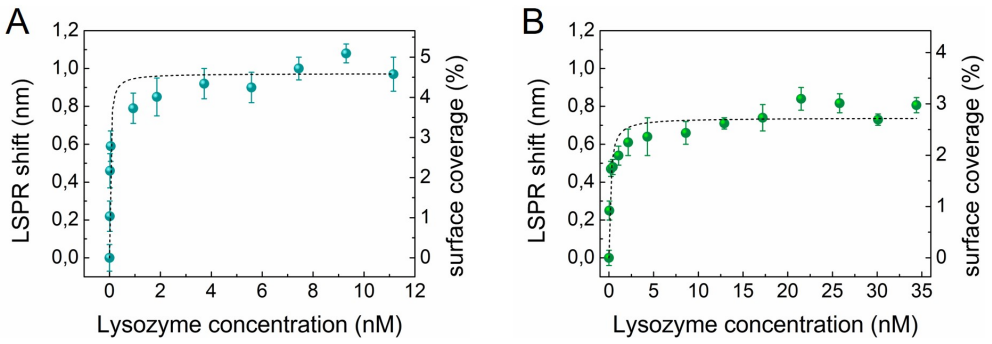

Figure 2.10. Adsorption isotherms obtained from the measured shift of the LSPR as a function of the lysozyme concentration, for 100 nm (A) and 60 nm (B) AuNPs. The surface coverage values, calculated according to equation 2.19, are reported on the right scale. Best fits (dashed black lines) are superimposed to the experimental points.

At this point, a side consideration can be done: on the basis of these results, non-aggregated AuNPs emerge as an appealing sensor able to detect small amounts of protein molecules in solution, down to pM concentrations (4.5 pM for 100 nm AuNPs and 21.5 pM for 60 nm AuNPs). The values obtained for the apparent dissociation constants are consistent with those reported in literature for the adsorption of proteins to NPs [127, 128]. The lower ($\sim$ 6-fold) K_d obtained for 100 nm AuNPs can be ascribed to the ζ-potential, which is larger in modulus as compared to 60 nm AuNPs (Table 2.1). The larger radius of curvature may also contribute to strengthen the binding of adsorbing proteins, entailing that a wider portion of the nanoparticle surface is involved in the interaction.

Coming back to the optical response of the aggregates, a clear correspondence between the optical behaviour of the system and the size and the morphology of the Lyz-AuNPs clusters emerges, unveiling the potentiality of the presented route for synthesising self-assembled materials with the desired optical properties. Noteworthy, especially in the case of the larger AuNPs, the aggregation bands are very prominent in the near-infrared spectral region, making the system intriguing for biophysical and biomedical *in vivo* applications [92, 29, 94], due to the reduced absorption of biological tissues in this wavelength range. On this line, the further investigations are focused on the 100 nm AuNPs.

2.4 Effect of the pH on the aggregation phenomenology: modulation and reversibility

To further assess the charge patch interactions as the driving mechanism for the aggregation phenomenology, the process was studied in a solution with pH 4 using 100 nm AuNPs.

Table 2.4. DLS characterisation (ζ-potential and size) of AuNPs and lysozyme at pH 4.

system component	ζ-potential (mV)	size (nm)
AuNPs 100 nm	-48.0 ± 2.0	102.0 ± 2.0
Lysozyme	+14.0 ± 1.0	2.9 ± 0.2

In such conditions variations in the aggregation behaviour are expected, as a consequence of the pH-dependent charge of both the proteins and of the AuNPs. Below the isoelectric point, in fact, the overall protein charge shows a clear dependence on the pH [129], becoming markedly positive in acidic environment. Specifically, the measured ζ-potential of the protein shifts from 4 mV at pH 6.5 to 14 mV at pH 4. In addition, the protonation of some carboxylic groups of the citrate molecules capping the AuNPs, occurring at pH 4, induces a slight shift of the ζ-potential of the bare 100 nm AuNPs. The measured ζ-potentials are -48 mV at pH 4 and -54 mV at pH 6.5 (see Tables 2.1 and 2.4).

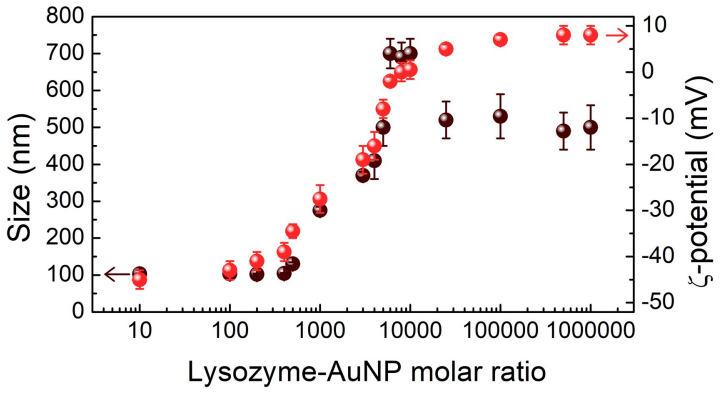

Figure 2.11. DLS measurements (size and ζ-potential trends) of Lyz-AuNPs as a function of the lysozyme-AuNPs molar ratio, using AuNPs of 100 nm at pH 4.

The ζ-potential and size trends as a function of the lysozyme-AuNP molar ratio measured at pH 4 are reported in Figure 2.11. If compared to the measurements at pH 6.5 (Figure 2.3), the overall experimental trends appear similar for both pH conditions, with the difference that at lower pH the aggregation onset is shifted to lower lysozyme concentrations ($\xi \approx 500$), and therefore at the same molar ratio larger clusters are observed. The isoelectric point of the complexes is reached for $\xi = 10000$, one order of magnitude lower with respect to that at pH 6.5. Correspondingly, the maximum size of the Lyz-AuNPs is of $\sim$ 700 nm. For higher lysozyme concentrations

($\xi \geq 25000$), a marked overcharging is observed, and the formed aggregates have a reduced size. This phenomenon is coherent with a re-entrant condensation [102] (see also Section 2.1).
The dependence of the aggregation process on the pH of the solution, and thus on the net charge of the system components, clearly asses the role of the electrostatic interactions in the cluster formation and stability, thus suggesting that acting on their strength it is possible to manipulate the process.

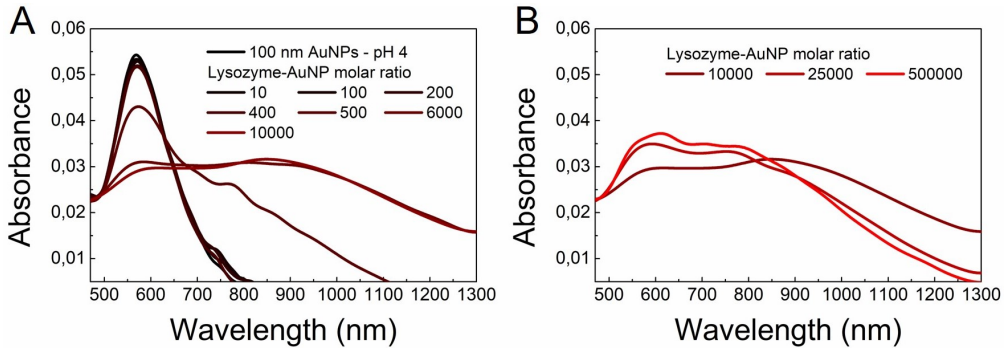

Figure 2.12. Representative absorption spectra acquired at different Lyz-AuNP molar ratios for 100 nm AuNPs at pH 4 before (left) and after (right) overcharging.

The systematic study of the optical response of Lyz-AuNPs was conducted also on samples prepared at pH 4. Selected absorption spectra are reported in Figure 2.12. Analogously to experiments at pH 6.5, the optical response of the samples strictly follows the aggregation trend. Interestingly, it is even possible to recognise the re-entrant condensation from the absorption spectra, which correspondingly show a shrinkage and blue-shift of the interparticle plasmonic band together with the increase of the absorption peak corresponding to the plasmonic modes of the primary colloids.

By exploiting the dependence of the aggregation process on the pH of the solution, the possibility of modulating the system optical properties of pre-assembled clusters was explored. A representative example is shown in Figure 2.13, where the absorption spectra (panel A) of the sample prepared at ξ=2000 are shown together with the corresponding size (panel B) and ζ-potential (panel C) distributions.

The images enlighten modification in both the optical response and the aggregation process, occurring when the pH of the solution is changed from 4 to 6.5 and back to 4. Specifically, when the pH increases the net charge transported by each protein molecule lowers (see ζ-potential measurements reported in Table 2.1 and 2.4) and the resulting surface charge distribution of the lysozyme-decorated AuNPs (ζ-potential shifted from -20 mV to -40 mV) is no longer suitable to maintain the AuNPs aggregated in the initial configuration. Their disaggregation is therefore observed with mean size of the aggregates decreased from 500 nm to 150 nm and the absorption spectrum showing the narrowing and a blueshifting of the plasmonic interparticle band together with the intensity increase of the single particle LSPR. When the pH is lowered back, an opposite behaviour is observed, resulting in a re-aggregation of the Lyz-AuNP complexes, as proved by the increase in the size and by the broadening of the interparticle plasmonic band (light red curves). This latter

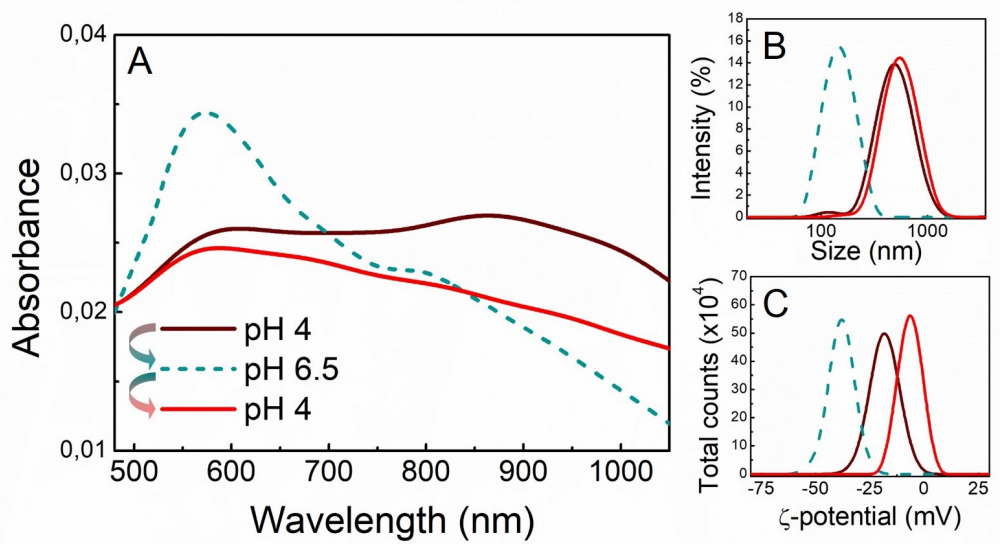

Figure 2.13. Modulation of the Lyz-AuNPs assembling and optical properties by acting on the pH of the solution: absorption spectra (A), size (B) and ζ-potential (C) distributions of 100 nm Lyz-AuNPs prepared at $\xi = 2000$.

result points out the reversibility of the phenomenon. The slight differences observed between the ζ-potential values measured at pH 4 before and after the modulation can be ascribed to the increased ionic strength in the solution, resulting from the addition of NaOH and HCl, and the consequent decrease of the effective range of the screened electrostatic forces that increases the importance of the attractive contribution of van der Waals interactions [102, 106].

2.5 Monitoring the catalytic activity of the adsorbed proteins

Lysozyme is an antimicrobial enzyme that catalyses the cleavage of peptidoglycan, the major constituent of gram-positive bacterial cell wall [104]. The cutting of even a small number of these polysaccharide chains leads to the cell wall rupture and in turn to the bacteria cell burst as a result of the osmotic stress [130]. The active site of the protein consists of two amino acids, Glu35 and Asp52, which are negatively charged in conditions of full activity (pH 6.5 and 25°C). This feature is highlighted in the electrostatic potential map of the lysozyme reported in Figure 2.14A. The charge distribution at physiological pH suggests an orientation of the proteins adsorbed onto the anionic AuNPs with the active site exposed outwards due to electrostatic repulsion, in accordance with the study of Zhang *et al.* [131] which claims that the binding site of lysozyme to 90 nm AuNPs involves the residues Phe3, Cys6 and Cys127. These residues, together with those constituting the active site, are highlighted in Figure 2.14B. In addition, the hypotesised binding site of the protein contains a consistent number of positive residues [132], promoting the electrostatic interaction of the protein with the citrate ions on the AuNPs surface [133].

Lyz-AuNP complexes represent a suitable specimen of nanozymes, a term recently

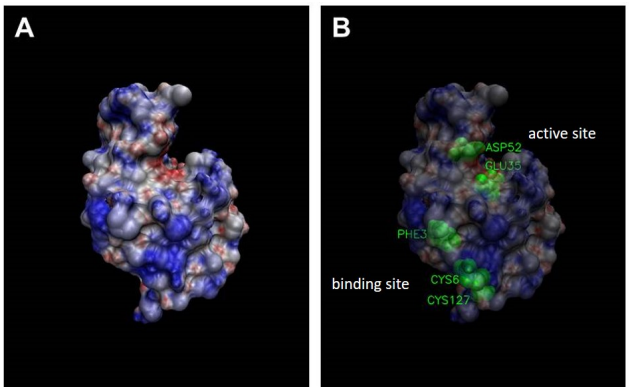

Figure 2.14. Electrostatic potential map of lysozyme, with negatively charged residues in red and positive ones in blue. In panel A is reported the map obtained at pH 6.5; in panel B the active site (Glu35 and Asp52) and the possible binding site with AuNPs (Phe3, Cys6 and Cys127) are highlighted.

coined to indicate artificial nanomaterials with enzyme-like properties, which are proving to be very effective as self-therapeutic systems in treating multi drug resistant bacteria [134]. Going in this direction, the lysis capability of the Lyz-AuNP complexes was tested by means of a turbidimetric activity assay performed on *Micrococcus lysodeikticus* bacteria. Briefly, aliquots of the sample were added to a bacterial suspension and the subsequent decrease in the absorbance at 450 nm, due to bacteria death, was monitored in time to derive the activity ϱ according to the equation [135, 136]:.

$$\varrho = \frac{\frac{dA_{450}}{dt}|_{sample} - \frac{dA_{450}}{dt}|_{blank}}{\frac{dA_{450}}{dt}|_{unit}} \tag{2.21}$$

where $\frac{dA_{450}}{dt}|_{unit} = 3 \times 10^{-5}$ abs. unit/min, is the slope induced in the absorbance at 450 nm by one unit of active lysozyme, rescaled to the actual volume employed in the experiments (30 μL). Representative examples of the obtained absorbance trends for differents molar ratios are reported in Figure 2.15. Notably, a marked lysis capability of the Lyz-AuNPs samples in comparison to the bacteria control (empty circles) and to the bare AuNPs (dark yellow filled points) clearly appears in the absorbance trends.

To demonstrate and evaluate the contribution to the measured activity of the proteins effectively confined onto the Lyz-AuNPs complexes, the samples were centrifuged and the turbidimetric assay was performed on the supernatant, *i.e.* on non-adsorbed proteins. Independent turbidimetric assays were performed also on the free protein at the same concentration employed to prepare the sample. In all the analysed samples, activity measured on the supernatant resulted lower than both that of the full system and that of the free lysozyme (see Figure 2.15). This finding highlights a contribution to the activity of the adsorbed protein molecules, given by the difference between the activity of the sample and that of the supernatant. To examine more in depth this aspect, several Lyz-AuNPs samples prepared at different molar ratios were tested and the catalytic efficiency of the protein confined within complexes was evaluated with respect to that of the same amount of free protein. The ratio between the two quantities, yields the normalised activity of the confined

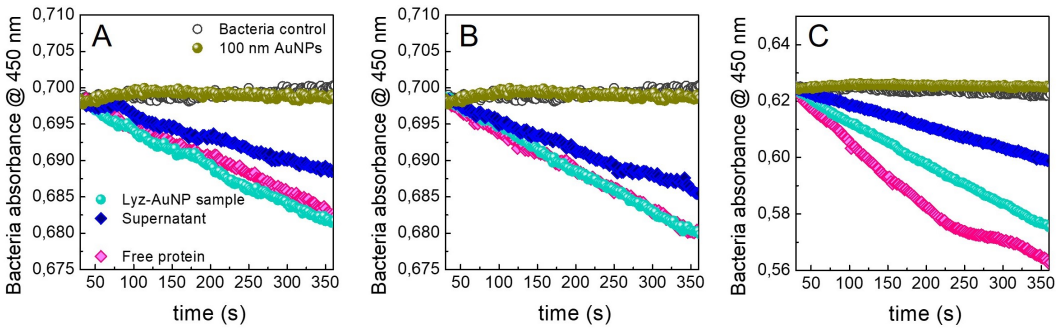

Figure 2.15. Lysozyme activity assay performed on the Lyz-AuNPs complexes made up of 100 nm AuNPs, with $\xi = 3000$ (A), $\xi = 10000$ (B) and $\xi = 50000$ (C). In all the graphs the absorbance at 450 nm of the bacterial suspension is reported as a function of time for the control bacteria suspension (empty circles), bare 100 nm AuNPs (dark yellow points), Lyz-AuNPs sample (light blue points), supernatant (blue points) and free protein (pink points).

lysozyme, calculated according to the equation:

$$\varrho_{norm} = \frac{\varrho_{Lyz-AuNPs} - \varrho_{supernatant}}{\varrho_{free\,Lyz} - \varrho_{supernatant}} \tag{2.22}$$

The obtained values for ϱ_{norm} are reported in Figure 2.16 as a function of the ζ-potential of the complexes.

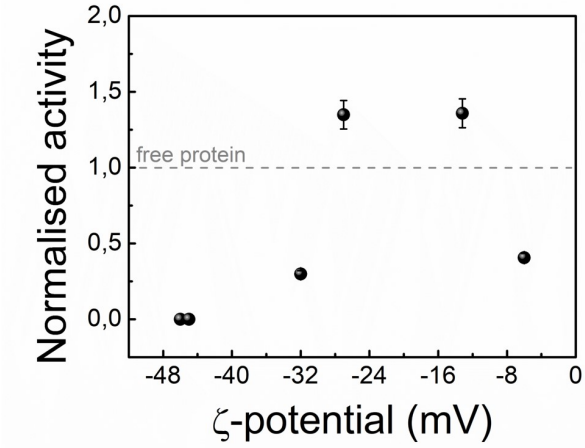

Figure 2.16. Normalised activity of the protein confined on the Lyz-AuNPs complexes, calculated according to equation 2.22, as a function of the ζ-potential of the complexes.

Noteworthy, it is possible to extrapolate a correspondence between the surface charge of the aggregates and their lysis capability, identifying three different scenarios: *i*) at high absolute values of the ζ-potential the system does not show a significant activity; *ii*) at intermediate values, starting from the aggregation threshold, the efficiency in the lysis capability increases, until, *iii*) approaching null ζ-potential, the activity drops significantly. This trend can be interpreted with reference to previous studies which report on the influence of the interfacial electrostatic potential of

different bacteria on the interaction with NPs [137, 138]. In particular, the gram-positive bacteria employed in this study have a negative ζ-potential of –15.6 mV, consistent with the value reported in literature [139]. At low molar ratios, the highly negative ζ-potential of the single AuNPs prevents the interaction with bacteria. At increasing the molar ratio, the electrostatic repulsion between the Lyz-AuNPs and the bacterial wall progressively decreases, and the system shows an increasing lysis capability. Noteworthy, for ζ-potential values in the range between -27 mV and -13 mV, Lyz-AuNPs complexes appear more efficient as compared to the free protein. The decrease in the ζ-potential implies that the attractive specific interactions between the enzyme and its substrate progressively overcome the repulsive electrostatic ones, thus promoting the binding of the aggregates on the bacteria membrane. The huge concentration of proteins confined onto the AuNPs results in the locally enhanced cleavage, with the hydrolysis of several polysaccharide chains in the same portion of the cell wall. This favours and accelerates the burst of the bacteria cells, leading to a higher catalytic activity. When the size of the Lyz-AuNPs clusters rises up to several hundred of nanometres, their diffusivity decreases remarkably, thus clusters hit the bacteria wall with an extremely lowered rate when compared to the free protein. In addition, a relevant amount of proteins results hindered within cluster and does not have access to the bacteria wall, making the system less efficient in comparison to smaller clusters. This effect could explain the drop observed in the activity of samples with approaching null ζ-potential.

The analysis herein reported, pointing out that proteins adsorbed to AuNPs retain their functional activity depending on the aggregation state, highlights a further intriguing, tunable property. In the perspective of actually employ the anti-bacterial bioplasmonic system *in vivo*, citotoxicity assay should be carried out. Nevertheless, studies performed on similar systems show promising results since do not show negative effects on cellular viability [140].

Chapter 3

Nanoparticle-based SERS substrate for cellular pH sensing

Among surface enhanced spectroscopies, a relevant position is occupied by SERS which, benefiting of the highest signal enhancement, allows for overcoming the intrinsic limit of low intensity of Raman signal and hence has emerged as one of the most widely used technique in biosensing [141]. Recent advances in SERS-based detection methods involve the development of novel chips for immunoassays with enhanced sensitivity and specificity for the study of protein affinity [142] and for the identification of pathogens based on the nucleic acid recognition [143]. Beyond the application as ultrasensitive spectroscopy, SERS turned out to be an invaluable technique capable to actively and selectively interact with complex biological systems, including cells and tissues [19, 86, 18].

In particular, by employing weak acids as reporter molecule and gold or silver NPs as enhancing scaffold, it has been possible to develop pH sensors capable to convey the SERS potential in providing localised and molecular specific information [144, 145, 146, 147]. The development of tools for the evaluation of pH at the nanoscale enables to obtain information on small sample volumes, *e.g.* those in microfluidic devices or even in single cells [148, 149]. In the latter framework, alterations of the local pH of cellular compartments could have dramatic effects on cells and organelles, encouraging the occurrence of diseases. Furthermore, the extracellular pH of cancer cells is expected to be more acidic with respect to that of healthy ones [150]. Despite the broad scientific landscape involving the employment of SERS-based pH sensors, many key issues concerning their assembling, calibration and stability, that could significantly affect the precision and accuracy of the pH measurements, need to be clarified.

Here it is reported the detailed characterisation of a SERS-active pH nanosensor based on the conjugation of gold NPs (AuNPs) with the pH-sensitive molecular probe 4-mercaptobenzoic acid (4MBA), a benzene derivative with a thiol group (-SH), which covalently binds to the AuNPs surface, and a carboxylic acid (-COOH) in the opposite position. This molecule is particularly suitable to realise a SERS sensor since the protonation degree of the carboxyl moiety acts as pH indicator [151, 152] that, combined with the strong SERS cross section typical of benzene-derived molecules, results in a spectrum sensible even to weak pH variations [144, 147]. Moreover, the

orientation with respect to the thiol group provides minimised steric hindrance and maximum exposure outwards of the carboxylic moiety in comparison with other carboxyl-modified benzoic acid derivatives. This allows for a more packed coverage of AuNPs by 4MBA and therefore for a more efficient response to pH variations. With specific reference to the biological application of measuring the cellular pH, the choice of employing of AuNPs as plasmonic scaffold ensures higher chemical stability and biocompatibility with respect to different SERS-active metals such as silver [153].

The final purpose of the present study is to develop a systematic and general protocol for the characterisation and employment of a nansosensor in different environments. To this aim, all the underlying aspects of the synthesis procedure and of the operating conditions have been analysed and rationalised to provide the highest sensitivity to pH variations and to preserve the sensor stability. In particular, the colloidal stability and the photostability of the system were considered, identifying a variability range of the measurement parameters to reduce the radiation-induced molecule degradation. All the spectral modifications, directly and indirectly associated to pH variations, have been analysed and discussed to achieve a close control on all the aspects involved in the measurement. In the perspective of obtaining a fine tuning of the nanosensor features, particular emphasis has been placed in analysing the acidic properties of the molecular probe conjugated to the AuNPs. Three calibration curves have been provided in terms of relative intensity of selected pH-dependent SERS bands as a function of the pH and the dynamic range of sensitivity of the nanosensor was identified. The suitability of the 4MBA-AuNPs pH nanosensor for biological applications was demonstrated by measuring the extracellular pH of two cellular models.
The main results here reported are published in ref. [17].

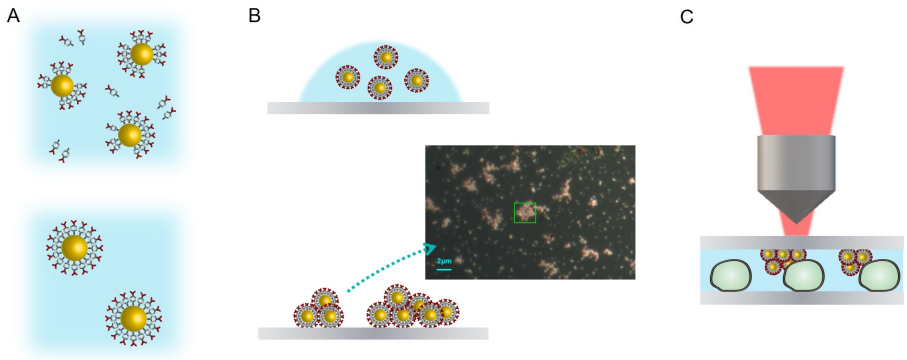

Figure 3.1. Scheme of the experimental protocol employed to synthesise the 4MBA-AuNPs nanosensor and to perform the SERS measurements. The functionalisation reaction between 60 nm AuNPs and 4MBA molecules was conducted in water for 3 h and the unbound molecules were removed by 24h dialysis against MilliQ water (A). A droplet of the 4MBA-AuNPs solution was deposited on a glass coverslip and dried at room temperature. A representative optical microscopy image (scale bar 2 μm) of the self-assembled clusters with micrometric size, is reported. (B). SERS measurements on cells were performed by superimposing the glass substrate with the self-assembled 4MBA-AuNPs to a glass slide with the cell culture (C).

3.1 Nanosensor assembling

The pH nanosensor employed in this study consists of a plasmonic core made of 60 nm AuNPs functionalised by a layer of 4MBA. The molecular functionalisation, as sketched in Figure 3.1A, was performed by exploiting the spontaneous S-Au bond formation between the thiol group of the 4MBA and the AuNPs surface in aqueous solution. An ethanol solution of 4MBA at the concentration of 0.1 mg/mL was added to the AuNPs stock solution to have the final concentration of 0.025 mg/mL of 4MBA. A large excess of 4MBA molecules with respect to the gold colloids was employed to obtain a full coverage of the AuNP [50], which based on steric hindrance considerations can be estimated to $\sim 2{\times}10^4$ molecules per AuNP. In this way it was possible to ensure the stability of the colloidal dispersion and to maximise the SERS cross section of the nanosensor. In addition, a high coverage of the AuNPs prevents the molecule degradation that might be induced by the interaction of the carboxyl moiety with the gold surface [151], as discussed in detail in Section 3.2. The solution was incubated for 3 hours at room temperature and the assembled 4MBA-AuNPs were purified to remove unbound molecules by 24 hours dialysis against Milli-Q water. Finally, the colloids were induced to self-organise in clusters onto a glass coverslip surface by evaporating the water at room temperature. The overall functionalisation procedure was monitored by UV-Visible absorption and Raman spectroscopies. The absorption spectrum of the 4MBA-AuNPs in comparison with that of the bare AuNPs is reported in Figure 3.2.

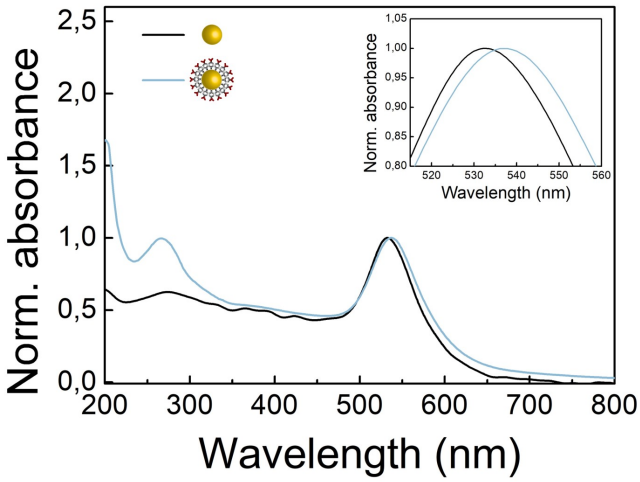

Figure 3.2. UV-Visible absorption spectra of AuNPs before (black curve) and after (light blue curve) the functionalisation with 4MBA. In the inset it is reported a zoom of the peak corresponding to the LSPR of the AuNPs, normalised to the maximum absorbance value. The measured redshift of ∼4 nm from 533 to 537 testifies a successful functionalisation.

Being related to the presence of 4MBA, both the absorption bands in the UV region [154] and the redshift of $\sim$ 4 nm of the LSPR of the AuNPs (LSPR at 533 nm for bare AuNPs), driven by the change in the dielectric environment at the AuNPs

surface [155], are indicative of the effective conjugation.

The Raman spectra of 4MBA-AuNPs and bulk 4MBA, both deposited on a glass slide are shown in Figure 3.3. The complete assignment of the main Raman and SERS bands is reported in Table 3.1.

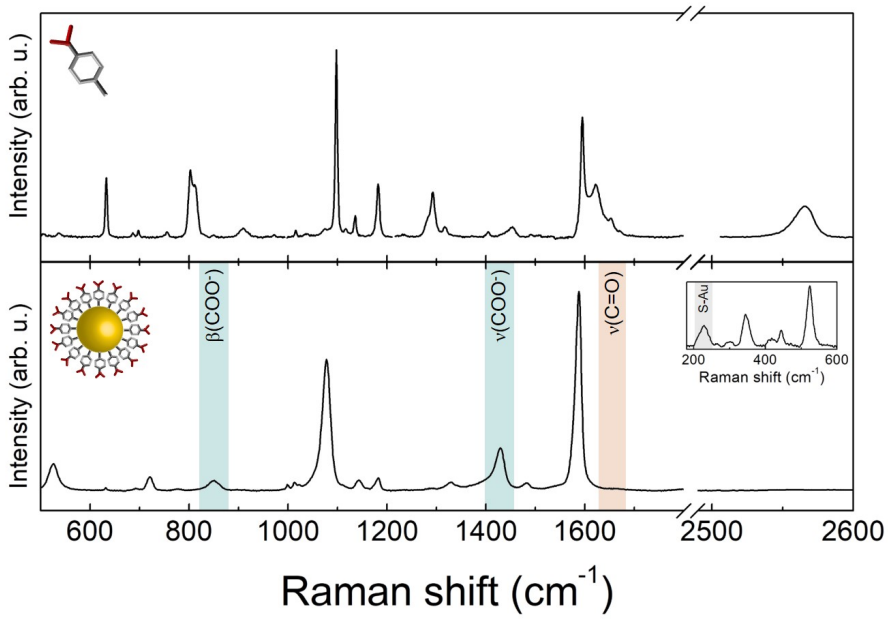

Figure 3.3. Raman spectrum of bulk 4MBA (top) and SERS spectrum of 4MBA conjugated to AuNPs and dried onto a glass slide (bottom). The peaks of the pH-dependent bands in the SERS spectrum are highlighted: $\beta(COO^-)$ and $\nu(COO^-)$ in blue and $\nu(C{=}O)$ in red. The disappearance of the $\nu(SH)$ band at 2565 cm^{-1} in the SERS spectrum witnesses a successful functionalisation of the AuNPs by S-Au covalent binding. In the inset the spectral region of the S-Au band is reported

The SERS spectrum of 4MBA-AuNPs is characterised by two intense bands at 1076 and 1586 cm^{-1}, corresponding to the vibrations of the aromatic ring of the molecule [151], both redshifted with respect to their Raman counterpart. It is known that a relaxation of Raman selection rules occurs when molecules are in proximity to a metal surface, under near-field illumination: this can cause the appearance, in the SERS spectra, of bands that are hindered in the conventional Raman spectra [156, 157, 158]. For analogous reasons, frequency shifts can take place as a result of molecule-metal charge transfer phenomena [159]. The successful functionalisation by S-Au covalent binding is witnessed by the appearance of the band at 228 cm^{-1} (see the inset of Figure 3.3), corresponding to the gold-sulfur vibration [160] and by the concomitant disappearance of the band at 2565 cm^{-1}, corresponding to the thiol S-H stretching vibration [50]. Furthermore, the absence of the latter peak certifies that all the molecules concurring to the SERS signal are covalently bound to the AuNPs.

The bands sensitive to pH variations are those related to the carboxylic moiety

Table 3.1. Peak assignment of the main Raman and SERS bands of the spectra reported in Figure 3.3 according to refs. [151, 160, 152, 147]. Greek letters indicate the vibrational modes: ν, stretching; β, bending; ω, wagging; γ, out-of-plane vibration. Benzene modes are reported according to the Wilson notation [161]. The rows highlighted in light blue identify the bands whose intensity increase with pH, while the one whose intensity decreases with the pH is highlighted in light red. The bands corresponding to the S-Au and ν(SH) vibrations, used to control the functionalisation of AuNPs with 4MBA, are highlighted in gray.

Peak assignment	Raman shift (cm^{-1})	SERS frequency (cm^{-1})
S-Au	-	228
$\nu(CS)$	-	525
ν_{6b}	632	631
$\beta(CO_2) + \nu(CS)$	686	-
$\nu_{4b} + \gamma(CCC)$	-	720
ν_{10a}	801	-
$\nu_{17b} + \omega(CO_2)$	812	-
$\beta(COO^-)$	-	849
$\beta(SH)$	915	-
ring deformation	-	1011
ν_{12} - ring breathing	1098	1076
$\nu_{19b} + \nu(CS)$	1116	-
ν_{9a}	1135	-
$\nu(CCOO^-) + \nu(CS)$	-	1143
$\beta(CH)$	-	1183
ν_3	1292	-
$\nu(COO^-)$	-	1428
ν_{84} - ring breathing	1594	1586
$\nu(COO^-)$	1620	1710
$\nu(SH)$	2565	-

at the edge of the 4MBA molecule, *i.e.*, the bending and stretching vibrations $\beta(COO^-)$ and $\nu(COO^-)$ at 849 and 1428 cm^{-1}, and the weak band at 1710 cm^{-1} corresponding to the ν(C=O) stretching vibration [152, 147]. The first two bands arise when the carboxylic groups are in the deprotonated form, in basic environment; while the ν(C=O) band appears more intense in acidic condition, when the moiety is protonated. In the SERS spectrum of Figure 3.3, the bands corresponding to COO^- vibrations are prominent, suggesting that most of the carboxylic residues of the 4MBA-AuNPs deposited after the functionalisation are in the deprotonated form.

3.2 Nanosensor stability

In this paragraph all the aspects concerning the colloidal stability of the nanosensor, pivotal to refine the performances in liquid environment are presented. After-

wards, the chemical alterations that might occur in the molecular probe due to the laser illumination are discussed.

3.2.1 Colloidal stability

Moving into the issues concerning the actual applicability of the nanosensor, the stability of the 4MBA-AuNPs colloidal dispersion was analysed by dynamic light scattering (DLS) measurements, in terms of size distribution and ζ-potential, and by UV-Visible absorption spectroscopy at varying the pH of the solution (see Appendix for experimental details). The combined measurements allowed for correlating the aggregation of the system, which occurs upon pH variations due to the related changes in the 4MBA-AuNPs surface charge, with its optical response. The ζ-potential of particles in solution, which is proportional to their average surface charge, is a well-established indicator of the stability of a colloidal dispersion, quantifying the electrostatic repulsion between like-charged particles [162].

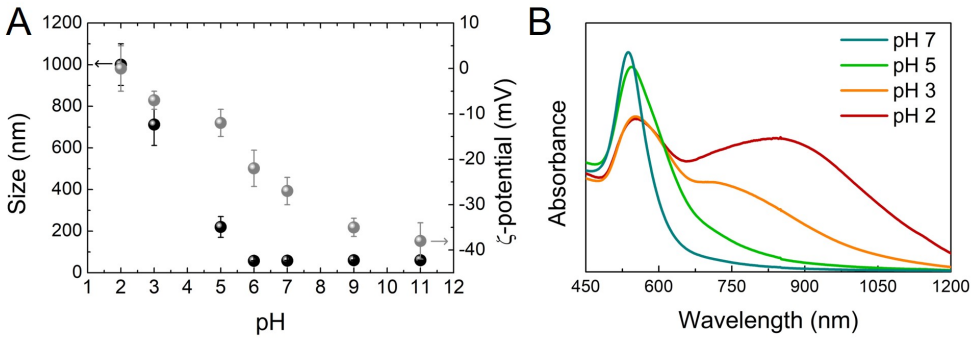

Figure 3.4. (A) Size (black) and ζ-potential (grey) of 4MBA-AuNPs obtained by DLS measurements as a function of the pH of the solution. The error bars represent the standard deviations of the measured size and ζ-potential distributions. (B) Selected UV-Visible absorption spectra of the 4MBA-AuNPs corresponding to the DLS measurements.

Size and ζ-potential results are shown in Figure 3.4 A. In both cases, a remarkable pH-dependence is clearly observed. At basic pH and down to pH 6, the absolute value of the ζ-potential is high enough (-38 mV $<$ ζ $<$ -22 mV) to prevent the 4MBA-AuNPs aggregation, with size distributions centered on that of single AuNPs. Starting from pH 5, the ζ-potential decreases in modulus and the colloids form aggregates whose dimensions increase with lowering the pH. At pH values lower than 3, 4MBA-AuNPs aggregates reach a micrometric size and could precipitate, as the ζ-potential approaches zero. Notably, in the region between pH 5 and pH 6, the ζ-potential shows the highest slope, corresponding to the maximum sensitivity of the surface charge of the nanosensor with respect to pH variations. Since the 4MBA-AuNPs surface charge basically depends on the protonation degree of the exposed carboxyl moieties, this finding strongly suggests that the working point of the SERS-active nanosensor lies in the same pH range. For the same reason, at pH $>$ 9 the ζ-potential remains essentially unchanged, pointing out that all the carboxylic groups are in the deprotonated form.
In this condition, the average number N of 4MBA molecules bound to each AuNP

is equal to the number of elementary charges on the surface of each 4MBA-AuNPs colloids. This allows for validating the geometrical estimate of the 4MBA coverage (N $\sim 2\times 10^4$ molecules per AuNP) using the electrophoretic mobility value measured at pH 11. By employing the Hückel relation (equation 2.6), it is possible to derive a value for the effective charge Q_{eff} of the colloids and compare it to that obtained independently from N using the model of Aubouy for spherical particles [163, 164]. The good accordance between the two values (Q_{eff} = -90 ± 10 e and Q_{eff} = -94 e, where e is the elementary charge) confirms the reliability of the estimate of the coverage herein provided.

Selected absorption spectra corresponding to the DLS measurements are reported in Figure 3.4B. The resonance frequency of the LSPR is strongly influenced by the aggregation of the NPs, leading to the substantial shift and broadening of the plasmons absorption peak due to the coupling among the single particle plasmonic modes of adjacent nanoparticles [5]. The optical response of the samples changes coherently with the measured aggregation trends. Noteworthy, starting from pH 5, inter-particle plasmonic modes appear at higher wavelength with respect to the LSPR of non-aggregated colloids and the associated absorption band progressively broadens toward the infrared spectral region with the lowering of the pH. These modifications in the shape, amplitude and frequency of the plasmon resonance could critically affect the outcome of the SERS measurement, resulting in possible variations of the spectral enhancement at a given excitation wavelength [49]. Hence, the plasmon resonance modifications that occur upon NPs aggregation could compromise the plasmonic efficiency of the enhancing SERS scaffold. Moreover, the precipitation of the sensor upon aggregation at low pH could restrict the range of pH values that allows reliable measurements. Such issues have to be taken into account for properly controlling and interpreting the measurements in liquid environment. The approach adopted in this work to obtain a SERS enhancement independent on the pH of the solution relies in the self-assembly of the 4MBA-AuNPs in micrometric clusters onto glass slides, as shown in Figure 3.1B. Such aggregates show a stable plasmonic absorption band in the red spectral region [50, 74]. The related SERS enhancement is therefore not affected by a different coupling between plasmonic modes upon aggregation, but only by dimensional scale effects of the cluster size which can be overcome by a normalisation procedure respect to the intensity of selected pH-independent bands, as discussed below.

3.2.2 Photostability

A furthers step is to tackle the issue of the nanosensor photostability, and the related reproducibility of the SERS response. Indeed repeated, extended illumination could cause a degradation of the molecule. Specifically, 4MBA molecules are known to be subject to decarboxylation, *i.e.*, the loss of the carboxylic moiety, as a result of the interaction with plasmonic-active surfaces [165, 147]. The occurrence of this phenomenon is recognised in the spectra by the appearance of two new peaks at 996 and 1019 cm^{-1}, which are attributable to the benzene monosubstituted thiophenol [151]. The two bands are mainly related to the ring out-of-plane and in-plane deformations, respectively [166].
Since the loss of the carboxylic moiety directly affects the nanosensor sensitivity to

pH variations, we carried out a study with the aim of identifying the experimental conditions to minimise the decarboxylation process. SERS spectra of the 4MBA-AuNPs deposited on glass slides at varying the illumination time and the laser intensity are shown in Figure 3.5, over the spectral region where are located the spectral markers of decarboxylated 4MBA.

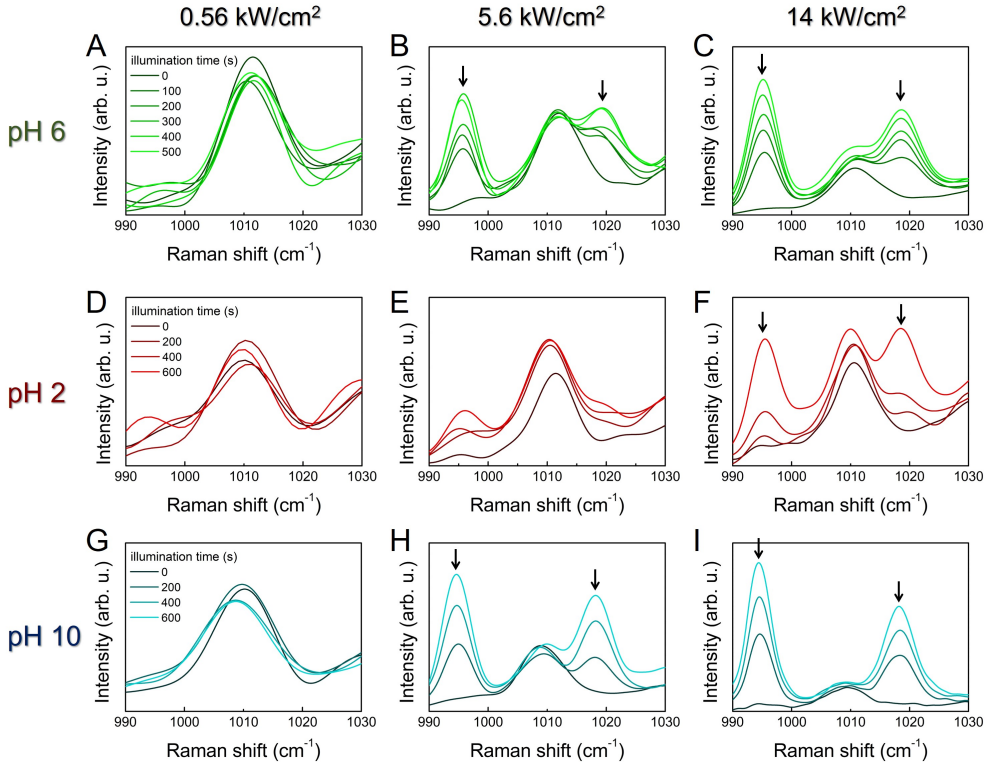

Figure 3.5. SERS spectra of 4MBA-AuNPs deposited on a glass slide and exposed to solution at nearly neutral (pH 6, top) acidic (pH 2, middle) and basic (pH 10, bottom) pH. The onset of the spectral markers of the irradiation-induced decarboxylation at 996 cm^{-1} and 1019 cm^{-1} are highlighted by the arrows. The spectra are acquired at varying the illumination time with laser intensity of 0.56 kW/cm^2 (A, D, G), 5.6 kW/cm^2 (B, E, H) and 14 kW/cm^2 (C, F, I).

When comparing the reported spectra at pH 6, a clear dependence of the decarboxylation process on the laser intensity can be recognised. Noticeable, at 0.56 kW/cm^2 the loss of the carboxylic group does not occur, even upon repeated measurements (Figure 3.5A). At 5.6 kW/cm^2, the thiophenol peaks appear already after 100 s illumination (Figure 3.5B). The observed phenomenon is ascribed to plasmon-derived "hot" electrons extracted from the nanoparticle upon plasmon excitation. These are transferred to the molecule, where they promote the decarboxylation reaction which is also accelerated by the local heating [165]. To deepen the investigation on the decarboxylation phenomenon, SERS spectra were acquired also by exposing 4MBA-AuNPs to acidic and basic solutions, as reported in Figure 3.5D-I. A dependence on the pH of the solution appears evident. In particular, for acidic pH the decarboxylation threshold is shifted to higher laser intensities. This effect is mainly ascribed to the orientation of the 4MBA molecules with respect to the AuNPs surface.

At basic pH, indeed, 4MBA preferentially adopts a flat configuration when adsorbed on the surface [167], promoting the interaction of the deprotonated carboxylic moiety with the gold surface and in turn the plasmon-induced decarboxylation. At acidic pH, on the other hand, the molecules stand upright with respect to the surface, and the carboxylic group is further away from the metal surface.

3.3 SERS responsiveness to pH variations and calibration of the nanosensor

The analyses reported in the previous Section were aimed to the optimisation of the experimental conditions for both the synthesis and the employment of the 4MBA-AuNPs sensor. Here, the SERS response to pH variations of the assembled nanosensor is investigated, with the purpose to determine its dynamic range of sensitivity. Proceeding from this, a thorough study concerning the acidic properties of the molecule has been conducted to explore the possibility to obtain a modulation of the working point of the nanosensor.

A preliminary test of the sample responsiveness has been provided by sequentially immersing the nanosensor to solutions with extreme pH values. The results, corresponding to cyclic measurements performed at pH 3 and pH 10 are reported in Figure 3.6. The features of the spectra show a good responsiveness of the sensor

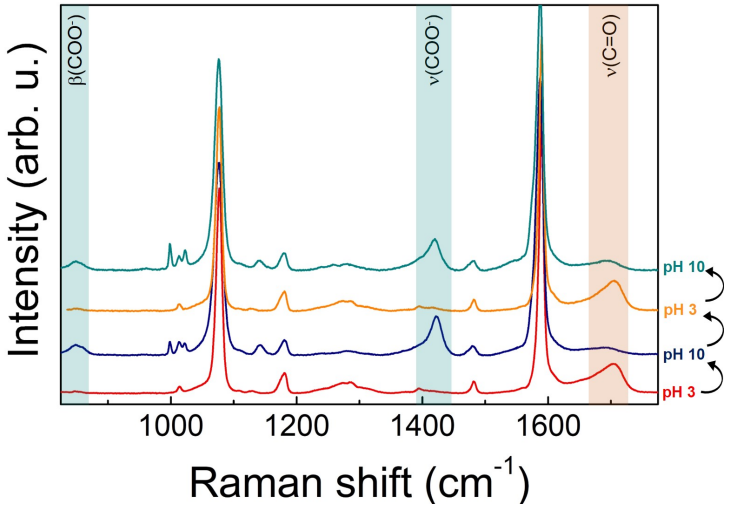

Figure 3.6. SERS spectra of 4MBA-AuNPs acquired on samples alternately exposed to solutions at pH 3 and pH 10. The pH-dependent peaks have been highlighted: $\beta(COO^-)$ and $\nu(COO^-)$, in blue; $\nu(C=O)$ in red. It should be noticed that the occurrence of the decarboxylation (appearance of the peaks around 1000 cm^{-1}), promoted at basic pH, is restricted to the region corresponding to the laser spot.

and a high reproducibility for consecutive measurements. In any case, to avoid the presence of salt residues affecting the SERS spectrum [168], after each measurement and before the exposure to the next solution, the substrate was rinsed with pure water.

As starting point for the nanosensor calibration, spectra of 4MBA-AuNPs deposited on a glass slide and exposed to solutions at different pH were acquired. Selected SERS spectra are reported in Figure 3.7.

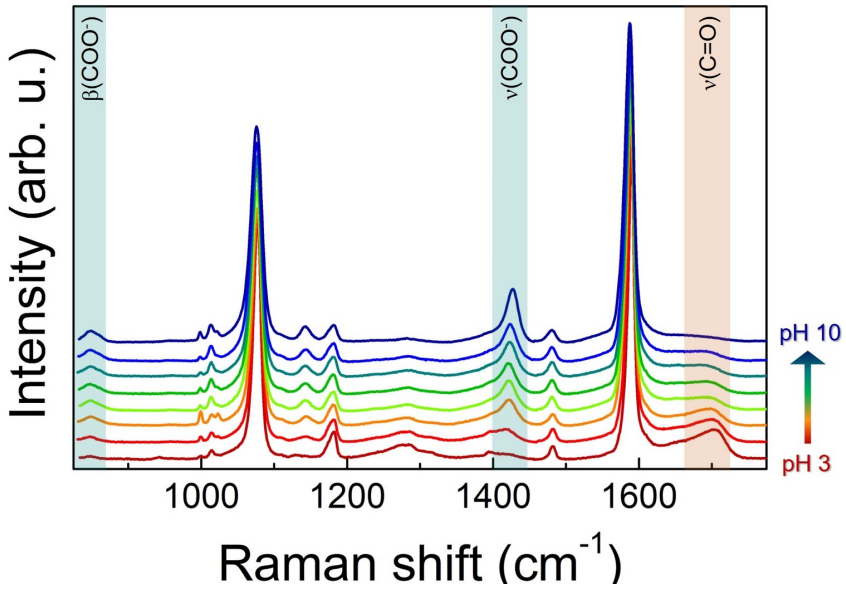

Figure 3.7. Representative SERS spectra of 4MBA-AuNPs exposed to solutions at different pH. The peaks corresponding to the vibration of the carboxylic group are highlighted, in the deprotonated ($\beta(COO^-)$ and $\nu(COO^-)$, in blue) and protonated case ($\nu(C{=}O)$ in red), respectively.

To better visualise the spectral differences, and to compensate possible effects of the number of molecules concurring to the SERS signal as well as of the SERS enhancement due to the non-homogeneous morphology of the clusters, which affects the signal intensity, all the spectra shown are normalised to the integrated intensity of the pH-independent peak at 1586 cm^{-1}, ascribed to the aromatic ring breathing mode. Only a slight redshift of the peak upon pH increase can be observed, due to the coupling with the stretching mode of the carboxyl, more intense in case of deprotonated 4MBA [169]. Notice that the intensity of the peak at 1076 cm^{-1}, also ascribed to the benzene ring, and thus pH-independent, appears with the same intensity after the normalisation. Clear modifications appear in the spectra upon pH variations from the acidic to the basic pH (from red to blue in the Figure). The most pronounced are those occurring in the peaks corresponding to the $\beta(COO^-)$ and $\nu(COO^-)$ bending and stretching modes and to the $\nu(C{=}O)$ stretching. As mentioned above, the first two are related to the progressive deprotonation of the 4MBA molecules at high pH that results in a progressive increase in the intensity of the bands related to the COO^- group vibrations. On the contrary, with lowering pH, the number of the protonated carboxylic groups COOH increases, resulting in the appearance of the band at 1710 cm^{-1} which becomes more intense at the lower pH values.

In order to actually employ the 4MBA-AuNPs as nanosensor for pH measurements, we analysed the SERS spectra to construct suitable calibration curves. To

this end, we calculated the integrated intensities I of the above-mentioned pH-dependent peaks in the normalised spectra highlighted in Figure 3.7. The three calibration curves obtained, reported in Figure 3.8, show a sigmoidal-like trend, in line with those reported in literature for similar systems [170, 145, 148]. For each

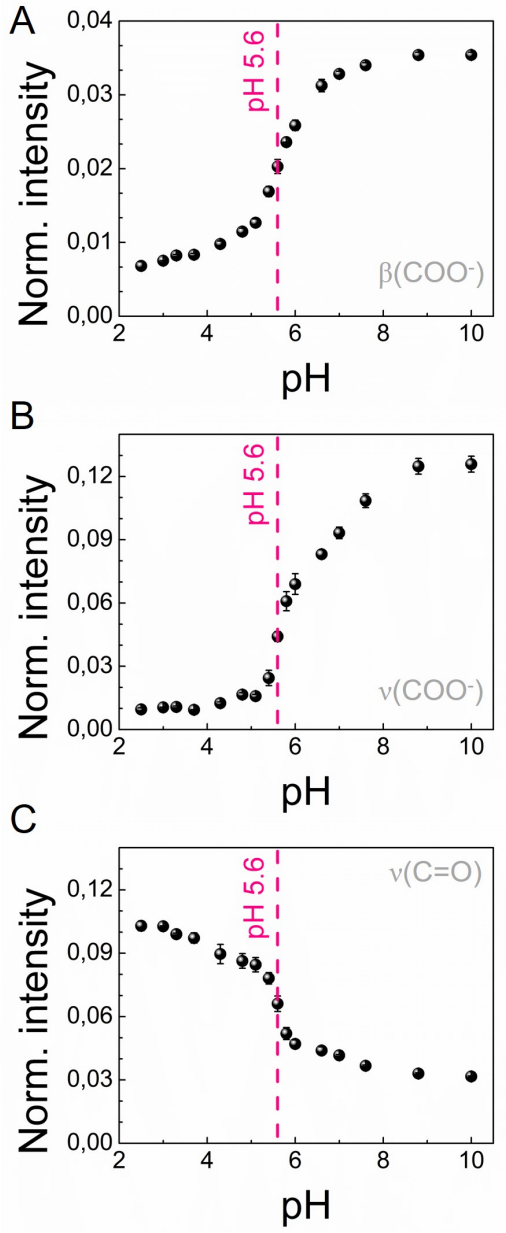

Figure 3.8. Calibration curves for the 4MBA-AuNPs nanosensor obtained for three different pH-dependent SERS bands: $\beta(COO^-)$ bending mode at 849 cm^{-1} (A), $\nu(COO^-)$ stretching mode at 1428 cm^{-1} (B) and $\nu(C=O)$ stretching mode at 1710 cm^{-1}. In all the graph the region of maximum sensitivity respect to pH variations has been indicated. Error bars represent the standard deviations, calculated on at least five independent measurements.

curve we determined the working point of the nanosensor, namely the pH value corresponding to the highest sensitivity $\frac{dI}{dpH}$, at pH 5.6, in good agreement with the range identified by ζ-potential measurements. Amongst all the three curves analysed, the one which gives the highest sensitivity to pH variations is that derived from the COO^- stretching mode (Figure 3.8B).
With reference to other similar pH nanosensors reported in literature [148, 171, 147, 149], showing a region of sensitivity in the pH range 7–8, the sharp working range identified for our nanoscale pH sensor turns out to be more suitable for monitoring pH-dependent biological processes on single cells. In fact, variations of cellular pH are generally identified at pH values between 5 and 7 [172]. Going to analyse the chemical aspects in detail, the working range extrapolated from the SERS calibration curves corresponds to the dissociation constant, namely the pK_a, of the indicator employed as probe [173]. Moreover, the confinement of molecules at nanostructured interfaces could affect their acidic properties, depending on the surface curvature [174, 175, 176]. To deepen this aspect, we performed a standard acid-base titration curve on the bulk 4MBA molecule, reported in Figure 3.9, obtaining a pK_a of 4.2 pH units for the carboxylic acid.

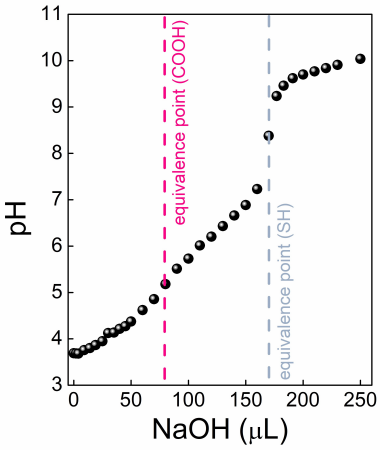

Figure 3.9. Acid-base titration curve for free 4MBA molecule performed employing NaOH as titration agent. In general, the vertical inflection point of a titration curve is the equivalence point and identifies the pH value at which all the acid is converted in its conjugate base. The pK_a value of the acid is obtained from the half-equivalence point, located where the volume of the titration agent is halved respect to that of the equivalence point. In fact, at this point the concentration of the acid is the same of that of the conjugate base, thus following the Henderson-Hasselbalch equation the pH of the solution is equal to the pK_a of the acid [176]. The acid-base titration curve of 4MBA yields two equivalence points, at pH 8.4 and at pH 5.2, corresponding to the thiol and to the carboxyl moiety, respectively. The derived pK_a values are thus 5.4 and 4.2, consistent with those reported in literature for the 4MBA [176]. Moreover, the reported value of the pK_a of the benzoic acid is also 4.2 [177], thus ensuring that the presence of the sulfhydryl moiety does not affect the acid properties of the carboxyl.

The SERS-based calibration curve and the ζ-potential measurements, instead, highlight a weakening of the acidic properties of the 4MBA when bound to the plasmonic nanostructure. Since the deactivation of the thiol moiety upon conjugation

with the AuNPs does not affect the acidic properties of the system, the observed pK_a shift is attributable only to the confinement of 4MBA molecules on the nanostructured surface. Interestingly, this latter aspect points out the possibility of modulating the pK_a value of the nanosensor by acting on the properties of the nanostructured surface on which the molecular probe is confined.

The overall modifications that occur in the SERS spectra depending on the pH, not only supply the information that can be used to determine the nanosensor performances, but provide unique molecular and stereochemical information which are related as well to the pH variation. With reference to Figure 3.7, it is possible to notice the appearance of a further peak moving to basic pH, centered at 1143 cm^{-1}, mainly assigned to the $\nu(CCOO^-)$ stretching mode [169]. Moreover, a modification of the shape of the $\nu(COO^-)$ peak at $\sim$ 1400 cm^{-1} is observed with increasing pH. This is due to the increasing weight of a second component of the band, centered at $\sim$ 1380 cm^{-1}, related to the vibrations at lower energy of the COO^- groups that are interacting with the metallic surface. The parallel orientation of the 4MBA molecules with respect to the AuNPs surface, resulting in the COO^- group being closer to the gold interface, is in fact favored at higher pH [151] due to the negative charge of the carboxylate. The great deal of information that can be inferred over the whole fingerprint region reduces considerably the presence of artifacts that might occur with potentiometric methods or paper-based sensors [178].

3.4 *In vitro* pH detection of living cells

The calibration curves obtained for 4MBA-AuNPs point out that the dynamic working range of the nanosensor lies in the pH range 5–7, suggesting a high reliability for pH measurements at the single cell level. Therefore, as a proof-of-concept to demonstrate the actual applicability of our SERS-active pH nanosensor we measured the extracellular pH (pH_e) of two clinically relevant human skin cell lines: normal HaCaT and cancer SK-Mel5. The pH_e, being involved in cell progression, differentiation and proliferation [168], is an important parameter that allows for discriminating unhealthy cells from healthy ones [179]. Indeed, cancer cells lead to an acidification of the extracellular milieu due to their enhanced glucose metabolism [179, 180]. The two cell lines were cultured on a glass coverslip and, for the SERS measurements, the cells were put in contact with the nanosensor by superimposing a second glass coverslip with the 4MBA-AuNPs previously assembled, as sketched in Figure 3.1C. In Figure 3.10 two optical microscopy images of the HaCaT and SK-Mel5 cells where the 4MBA-AuNPs clusters are clearly visible are shown. Corresponding SERS spectra collected on the cells are also reported on the right side.

The SERS spectra of the 4MBA-AuNPs in contact with the cells do not show spectral distortions and are in excellent agreement with the 4MBA-AuNPs spectra reported in the previous Sections. Noteworthy, the peaks corresponding to the ring vibrations of Phenylalanine, at 1000 and 1610 cm^{-1}, can be clearly identified due to the huge Raman and SERS cross section of this amino acid [141]. The two peaks can be hence considered as cellular spectral markers (see Figure 3.11 and the Table herein reported for the complete peak assignment), certifying that the pH nanosensor is effectively in contact with the cells.

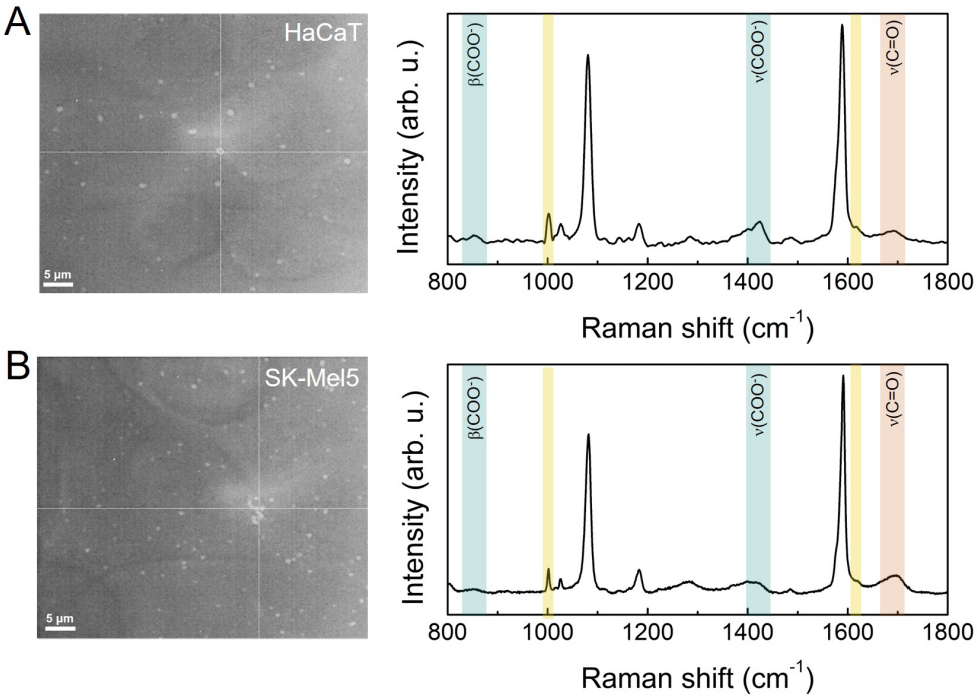

Figure 3.10. Optical microscope images and SERS spectra of HaCaT (A) and SK-Mel5 (B) cells exposed to the nanosensor. The bright spots are the 4MBA-AuNPs clusters assembled onto the glass coverslip superimposed to the cells. The grids in the images identify the spatial point corresponding to the SERS spectra. The pH-dependent SERS peaks are highlighted in blue ($\beta(COO^-)$ and $\nu(COO^-)$) and in red ($\nu(C{=}O)$), while the spectral markers of the cell (Phenylalanine at 1000 cm^{-1} and at 1610 cm^{-1}) are highlighted in yellow.

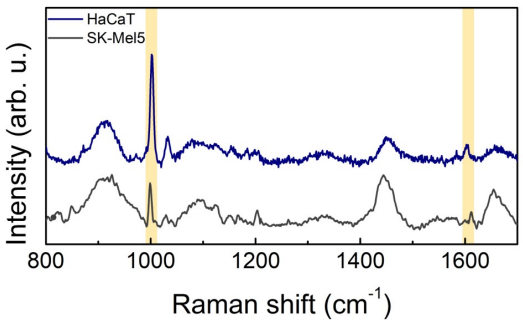

Peak assignment	Raman shift (cm^{-1})
tyrosine	853
phenylalanine	1000
phenylalanine	1027
PO_2^- symmetric stretching	1093
adenine + amide III	1252
adenine + CH_2 deformation	1313
lipid CH_2 deformation	1445
phenylalanine	1610
amide I	1660

Figure 3.11. On the left, Raman spectra of HaCaT (blue) and SK-Mel5 (grey) cell lines. The peaks corresponding to the Phenylalanine have been highlighted in yellow. On the right, peak assignment of the Raman spectra of cells according to [181, 182]. The rows highlighted in yellow identify the spectral markers of the cells recognised in the SERS spectra of Figure 3.10.

For each sample, the integrated intensities of the pH-dependent SERS bands in the normalised spectra, according to the previous Section, have been determined to extrapolate the pH_e from the calibration curves. The obtained results for each of the

three bands are reported in Table 3.2, together with the standard deviations. The distributions of the obtained pH values point out that our 4MBA-AuNPs nanosensor yields a good estimate of the pH_e [172] and, even better, it is suitable to discriminate between normal and cancer cells. In fact, for each of the pH-dependent SERS bands,

Table 3.2. Estimated pH_e values for the normal HaCaT and cancer SK-Mel5 cell lines, extrapolated from the SERS spectra of Figure 3.10.

	$\beta(COO^-)$	$\nu(COO^-)$	$\nu(C=O)$
HaCaT	7.0 ± 0.4	7.4 ± 0.7	6.5 ± 0.9
SK-Mel5	5.6 ± 0.2	6.3 ± 0.2	5.6 ± 0.2

the measured pHe of the cancer SK-Mel5 cells results to be more acidic respect to that of the normal HaCaT cells. Analysing in detail the obtained pHe values, the $\nu(COO^-)$ peak systematically yields a slightly higher pH value if compared with the $\beta(COO^-)$ and the $\nu(C=O)$ peaks. This can be ascribed to the superimposition with the band corresponding to the CH_2 deformation of the cell membrane lipids. Since the SERS probe is located in proximity of the cell membrane, the spectral contribution of this band results convoluted to that of the $\nu(COO^-)$ band, leading to a slight overestimation of the integrated intensity. Concerning the spectral region in which are located the other two pH-dependent SERS bands, at 853 cm^{-1} it is only present a narrow and not intense peak, ascribed to the Tyrosine ring breathing and, at higher frequencies, the amide I band at 1660 cm^{-1} is usually suppressed in SERS spectra [183]. These considerations implies that the $\beta(COO^-)$ and the $\nu(C=O)$ peaks are not affected by the spectral contribution of the cells and allow for obtaining a measurement of the pH_e from the average of the values reported in Table 3.2, which is equal to 6.8 ± 0.5 for the HaCaT and to 5.6 ± 0.1 for the SK-Mel5 cells. More in general, the derivation of three different calibration curves for the pH evaluation based on the SERS measurement allows for choosing the most appropriate, addressing issues associated with the superimposition of spectral band of the sample and of the probe.

Concerning the spatial resolution of the pH measurements, this is mainly determined by the size of the 4MBA-AuNPs clusters that varies between hundreds of nanometres and few micrometres. Actually, the effective spatial resolution of the nanosensor is much higher since the SERS signal originates from the nanometric volumes close to the plasmonic substrate. In the specific case of the evaluation of the extracellular pH, the realised nanosensor allowed for performing localised measurements with good spectral reproducibility in spatial regions with sub-cellular dimension, as can be seen in Figure 3.10.

Based on these evidences, 4MBA-AuNPs pH nanosensor turned out to be effectively suitable to perform localised pH measurements on single cells and, even more appealing, it has the potential to distinguish between normal and cancer cells. The overall obtained results pave the way for realising efficient SERS-active microplate substrates suitable for biomedical applications, offering the possibility to perform localised pH measurements at subcellular level.

Chapter 4

Ultrasound delivery of SEIRA-active gold nanoprobes into fibroblast cells and related biological effects

The ability of ultrasound (US) to transfer mechanical energy into cells and tissues allowing for the transient enhancement of the cell membrane permeability [184, 185] has attracted an ever-growing interest in targeting functional nanomaterials to specific biological sites. The phenomenon, known as reparable sonoporation (SP), is indeed a very effective modality for drug delivery and gene therapy because energy that is non invasively transmitted through the skin can be focused deeply into the human body in a specific location and employed to release drugs in a safe and efficient way [186, 187]. For this reason, the effects of SP are now intensively studied in nanomedicine offering a pivotal chance to design improved anticancer strategies for the targeting of nanocarriers through the cytoplasmic membrane [188].

In the latter framework, recent advances in nanoscience and nanotechnology have paved the way for engineering several diagnostic and therapeutic delivery vectors showing key roles in selectively seeking out, tracing and promoting cell by cell ablation of tumour tissues [189, 190, 191]. Nevertheless, progress in the field has been limited by an insufficient understanding of potential side effects for biological systems deriving from the employment of US and nanomaterials. The US produced by medical equipment, indeed, may cause osmotic stress, promote inflammatory processes and even weaken the occlusive mechanical barriers of endothelium and skin tissues. More generally, cells exposed to the US field can exhibit concomitant effects depending on the exposure parameters such as frequency, intensity and exposure time [192, 88, 193]. The potential irreversibility of these damages could hamper the cellular self-repair mechanisms, leading to the risk of genotoxic and cytotoxic damage and thus constituting a serious risk to human health [194, 195].

In this Chapter, the study on the US mediated internalisation of suitably designed nanoprobes into the the well-established fibroblast model cell line NIH-3T3 is presented. This cell line, which is prominent in the connective tissue, has been

successfully employed in studying US induced bioeffects [192, 88, 196]. The experimental conditions to obtain reversible enhancements in membrane permeability of NIH-3T3 and human keratinocytes cell lines at very low intensity megasonic fields (in the subcavitational regime) have been recently pointed out [88, 197]. In these conditions, the transient alterations of the plasma membrane allowed for efficiently internalising molecules with hydrodynamic diameters of the order of magnitude of 10 nm, observing no severe cell damage. Taking advantage of this finding, the internalisation of nanomaterials *in vitro* by SP, here is attempted and investigated. Among all the different nanomaterials that can be used as both carriers and probes, gold NPs (AuNPs) have received much biomedical attention based on their peculiar properties and suitable biomolecular conjugation [32, 198]. In addition, the plasmonic-mediated capability of AuNPs to enhance the infrared absorption cross section of specific organic and biological molecules located in proximity of their surface [199, 200, 159, 58], namely the SEIRA effect, is shedding new light on the development of novel ultrasensitive detection and specific signalling methodologies [201, 202, 203]. In this framework, AuNPs can be easily functionalised with the hetero-bifunctional linker 4-aminothiophenol (4ATP), to produce an efficient IR marker 4ATP-AuNP conjugate, characterised by several intense SEIRA vibrational modes ranging from 1700 to 900 cm^{-1} [199, 159].

Synchrotron Radiation Fourier Transform Infrared microspectroscopy (SR-microFTIR) is one of the most employed and valuable analytical tool for studying biochemical changes induced by external agents at the single cell level [204]. In fact, the high brilliance and the highly focused beam of SR-microFTIR allow for obtaining detailed chemical information on small samples. In addition, the signal-to-noise ratio on cellular samples can be $\sim$ 10 to 30 times higher if compared with traditional IR source [205]. The synergistic use of SR-microFTIR spectroscopy and SEIRA allowed for recognising the spectroscopic and biochemical influence of SEIRA-activated AuNPs, which entered the cell by SP. The possible biological and toxicological implications resulting from the nanoprobe internalisation have been investigated by coupling the spectroscopic analyses with viability and chromosomal damage end point assays.

The main steps of sample preparation for spectroscopic analysis are sketched in Figure 4.1. At first, a FTIR analysis of the nanovector, focused on the influence of the AuNPs size on the amplification of the IR signal induced by SEIRA effect is presented. Moving from this, the evidence that such spectroscopic nanoprobe is suitable to be internalised in fibroblast cells through medical US and recognised by SR-microFTIR spectroscopy at the single cell level is discussed. Moreover, the biological information inferred from the analysis of the SEIRA-amplified spectra of single cells is presented and compared to the evaluation of the corresponding cytotoxic and genotoxic impact.
The main results here reported are published in ref. [14].

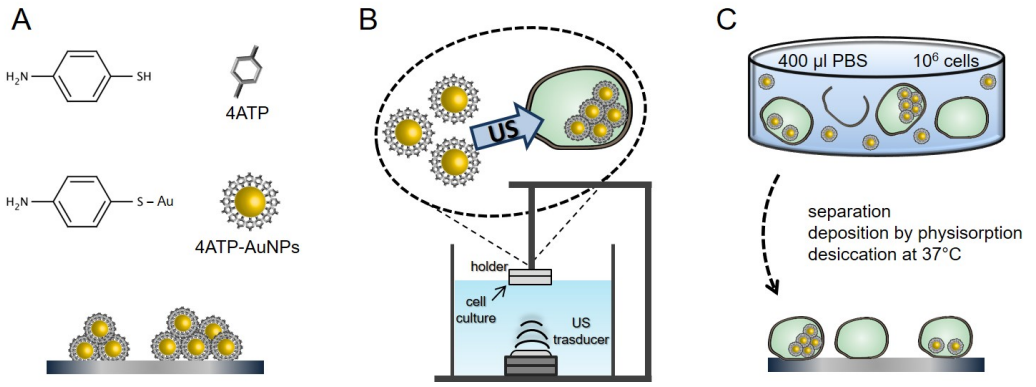

Figure 4.1. Scheme of the protocols employed for the SR-microFTIR analyses. (A) The nanoprobe assembling was obtained by functionalising the AuNPs with the IR marker 4ATP; spectra were acquired after depositing the nanoprobes onto silicon wafers. (B) The internalisation of the nanoprobes within NIH-3T3 cells was triggered by low intensity 1 MHz US; the exposure setup employed consists of a water filled tank, a transducer positioned at its bottom and a micro-volume cell holder vertically aligned with the transducer; the sonication was performed on a PBS dispersion of $\sim 10^6$ cells. (C) The samples for SR-microFTIR measurements were prepared by separating the cells from the supernatant and depositing them on silicon substrates by physisorption.

4.1 Analysis of the SEIRA signal enhancement of the nanoprobe

The analysis shown in this Section is aimed at identifying the size of 4ATP-AuNPs probe that better accomplish both efficient US mediated internalisation within cells and maximisation of the SEIRA signal. Both these requirements are pivotal for the development of an efficient biorecognition tool. To this purpose, different nanovectors have been assembled by conjugating the infrared reporter 4ATP with AuNPs, with size ranging between 2 and 20 nm. The upper size of 20 nm was fixed to fulfill the first requirement, according to a previous study [88]. To address the second requirement, the response of the differently sized nanovectors, using both traditional and Synchrotron Radiation (SR) light source was analysed. The spectra of the

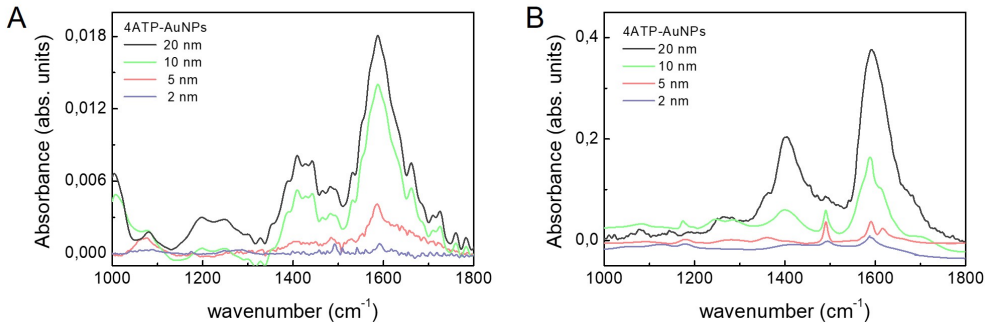

Figure 4.2. SEIRA spectra of the 4ATP-AuNPs nanoprobes prepared using AuNPs of different size measured by traditional IR source (A) and by SR-microFTIR (B).

Table 4.1. Peak assignment of the main IR and SEIRA bands of the spectra reported in Figure 4.2 and 4.4 according to ref. [159]. Greek letters indicate the vibrational modes: ν, stretching; δ and γ, bending. The row highlighted in gray identifies the band ν(CC), which shifts upon conjugation with AuNPs and allows for recognising the linker conjugated to AuNPs.

Peak assignment	wavenumber (cm^{-1})	SEIRA frequency (cm^{-1})
$\gamma(CCC)$	1010	1008
$\nu(CS)$	1090	1079
$\delta(CH)$	1176	1176
$\nu(CH)$	1284	1280
$\nu(CC) + \delta(CH)$	1423	1493
$\nu(CC)$	1595	1586
$\delta(NH)$	1620	1629

nanoprobes at varying the AuNPs size are reported in Figure 4.2. The corresponding spectral assignment is reported in Table 4.1. An increase of the IR cross section of the 4ATP, due to the SEIRA effect, occurs depending on the AuNPs size. In particular, the peak at 1595 cm^{-1}, corresponding to the asymmetric stretching ν(CC) of the double bond between carbons of the 4ATP phenyl ring of the bulk sample, experiences both a shift to 1586 cm^{-1} and an intensity enhancement in the nanoprobe samples [14]. Such changes in the spectrum of 4ATP provide evidence that it is effectively conjugated to the AuNPs surface [159]. Notice that a direct comparison of Figure 4.2A (conventional source) with Figure 4.2B (SR) on the same set of 4ATP-AuNPs shows an evident spectral quality improvement of the SR-microFTIR spectra with respect to the conventional FTIR source. Namely, the vibrational bands associated to 4ATP-AuNPs are neatly identifiable above the noise level even for 2 nm AuNPs. Some spectral weight redistributions are observed in the spectra of Figure 4.2 due to the different morphology of the 4ATP-AuNPs clusters at varying the AuNP size. In fact, the different size as well as the different surface density of 4ATP-AuNPs, which depend on the AuNP size, result in a different spatial organisation of 4ATP-AuNPs onto the substrate in terms of overall clusters size, number of AuNP composing each cluster and mean interparticle distance. All these factors affect the LSPR of the aggregated system, determined by the LSPR of the single plasmonic constituents, by the interparticle distance and by the morphology of the cluster (see Section 1.2.2), leading to variable field enhancement, preferentially amplifying different spectral regions. In general, the substrate morphology critically affects the intensity and shape of SEIRA spectra, leading at worst also to spectral distortions, as observed in the case of metal island film at varying the island dimension [206]. Moreover, the 4ATP orientation could be affected by the different packing of the AuNPs within the clusters, thus contributing to the observed spectral weight redistribution.
For each AuNPs size, taking as reference the peak corresponding to the ν(CC) of the aromatic ring, the SEIRA enhancement factor has been estimated as the ratio between the absorbance measured on the 4ATP-AuNPs samples and that of the bulk 4ATP, each normalised to the number of irradiated molecules in the absorption

volume [58, 68], according with the definitions reported in Section 1.3. Such analysis reveals a null gain for the 2 nm AuNPs, a rather low SEIRA enhancement (~ 4.5) for 5 nm AuNPs, while the enhancement is considerably higher for 10 nm (~ 137) and 20 nm (~ 200) AuNPs.

Exhibiting the highest enhancement, the following investigations are focused on the 4ATP-AuNPs made up of 20 nm AuNPs. A detailed characterisation of the assembling procedure of this nanoprobe was performed by means of UV-Visible spectroscopy, dynamic light scattering (DLS), and scanning electron microscopy (SEM). The experimental details are reported in the Appendix. The results in terms of size, ζ-potential and LSPR are reported in Table 4.2. The SEM images of the 20 nm AuNPs before and after the functionalisation are reported in Figure 4.3.

Table 4.2. DLS and UV-Visible characterisation of 20 nm AuNPs, before and after the functionalization with 4ATP.

	size(nm)	ζ-potential (mV)	LSPR (nm)
AuNPs 20 nm	22 ± 4	-34 ± 1	520.0 ± 0.5
4ATP-AuNPs	27 ± 4	-25 ± 2	522.5 ± 0.5

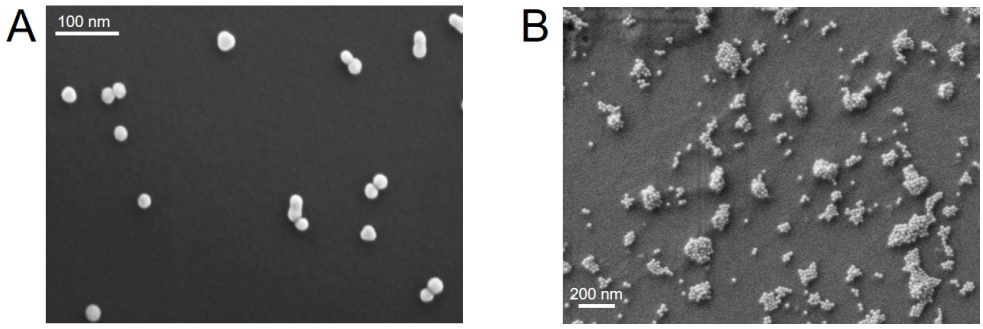

Figure 4.3. SEM images of 20 nm AuNPs (A) and 4ATP-AuNPs (B) colloids evaporated on a silicon substrate.

From the comparison with non-functionalised AuNPs, the analysis points out a redshift of the absorption peak, together with variations in the size and in the ζ-potential of the nanoprobe. These evidences support the spectroscopic analysis, confirming that 4ATP is linked to the AuNPs surface. The negative ζ-potential value witnesses a colloidal stabilisation of the nanovector and ensures the electrostatic repulsion with the cell membrane, which is also negatively charged, reducing the risk of alterations of the cell membrane integrity due to non-specific binding [207, 208]. With reference to Figure 4.3B, the 4ATP-AuNPs deposited on a silicon substrate appeared assembled in submicrometric aggregates of closely packed AuNPs. Such nanostructured assemblies can sustain plasmonic oscillations in the IR spectral range that is employed in this experiment, thus yielding huge signal enhancement [61, 209]. The SR-microFTIR spectrum acquired on the same substrate is reported in Figure 4.4 in comparison with that of bulk 4ATP. The obtained signal amplification of two

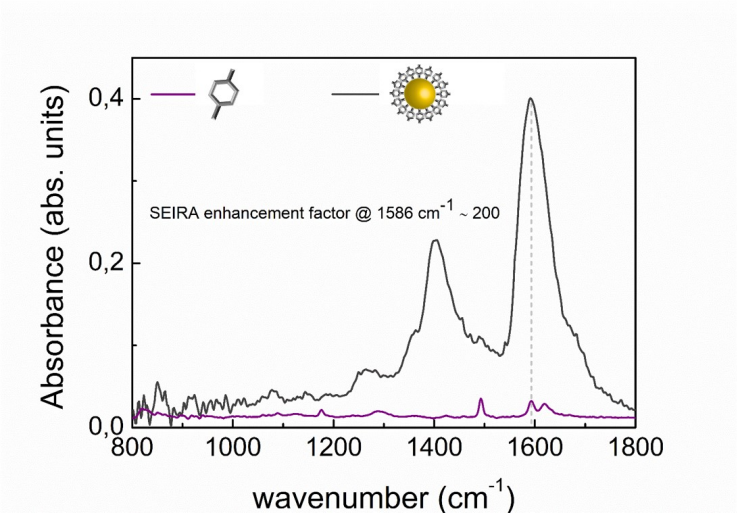

Figure 4.4. SR-microFTIR spectra of bulk 4ATP (purple line) and of 20 nm 4ATP-AuNPs (grey line) acquired at the Diamond Light Source. The estimated enhancement factor due to the SEIRA effect is of ~ 200.

orders of magnitude is remarkable, in fact SEIRA enhancement factors reported in literature for AuNPs based substrates can reach values of the orders of 10^2-10^3 at best [57, 61, 210, 211]. Hence, 20 nm 4ATP-AuNPs appear as an efficient SEIRA probe for studying the effects of US mediated drug delivery in vitro. Moreover, differently from fluorescent probes employed in other cell signalling strategies, SEIRA probes are not subjected to photobleaching, which critically affects the reproducibility of the measurements.

Based on these evidences, a SR-microFTIR spectroscopic study, aimed at recognising the US mediated internalisation of the 20 nm 4ATP-AuNPs within NIH-3T3 cells has been carried out, as reported in Section 4.2.

4.2 SEIRA-based biorecognition of the nanoprobe

4.2.1 US irradiation of the cells

A medical device consisting of a submersible piezoceramic circular unfocused transducer (6 cm diameter) tuned at 1 MHz was used for the cell US exposure (see Figure 4.1B). The employed setup [192] consists in a ultrasonic transducer placed at the bottom of a tank 30 × 30 × 30 cm filled with degassed water at a fixed temperature of 25° C. A special cell for micro-volumes (400 μL filling volume), hermetically lidded, was positioned in contact with the water surface coaxially aligned with the transducer. The calibration of the US field was performed by measuring the acoustic intensity at varying the source-sample distance (SSD), *i.e.* the distance between the transducer and the lower surface of the plate, by means of a needle hydrophone of 1 mm diameter with sensitivity at 1 MHz of 1670.4 mV/MPa ($\pm$ 14%). A SSD of 5 cm was selected, providing a stable and reproducible US field. The intensity of the acoustic field was analysed in terms of *spatial peak temporal average intensity* (I_{spta}), which represents the spatial maximum of the temporal

averaged intensity measured for the whole period of treatment.
NIH-3T3 cells grown in Petri plates were detached by Trypsin-EDTA solution and centrifuged (1200∼1500 rpm). The pellet was resuspended in 200 μL of PBS and added to 200 μL of 4ATP-AuNPs dispersion or Milli-Q water. The sample was then transferred in the cell for micro-volumes and treated by US in a continuous sinusoidal regime with I_{spta} = 16 mW/cm^2 (significantly below the threshold of the cavitation regime of 100 mW/cm^2) with exposure times of 15 and 30 minutes. Such exposure conditions allow for the internalisation of particles with size of tens of nanometers, according to literature [88]. After the SP treatment a restoring time of 10 minutes was scheduled for the resealing of the pores in the cell membrane.

4.2.2 Evaluation of the uptake efficiency

The nanoprobe internalisation was evaluated by means of SR-microFTIR spectroscopy at the single cell level focusing on the modifications reflecting the presence of the SEIRA nanoprobe coupled with cells. Two types of reproducible spectra reflecting the nanopobe internalisation can be recognised on the samples, besides the ones unperturbed with respect to the control, non-treated cells. For each case, a representative example acquired on cells treated for 15 minutes is reported in Figure 4.5A, in comparison with the control. The first type (black curve in the Figure) shows a marked intensity enhancement (up to 10 fold) and evident changes in the spectral shape, mainly in the protein amides region (amide I at 1655 cm^{-1} and amide II at 1545 cm^{-1}, according to the band assignment of ref. [196]), together with the appearance of two peaks, at 1400 cm^{-1} and 1586 cm^{-1}. In the second type (dark cyan curve in the Figure), the intensity enhancement is less evident and it is not possible to recognise the two additional peaks. Nevertheless, even in this case, some modifications of the spectral shape are observed, mainly in the amides region.

In Figure 4.5B the representative spectrum of the first type, showing the markedly amplified intensity and the two additional peaks, is compared to that of the nanocarrier alone. Since the SEIRA intensity enhancement is induced by AuNPs clusters large enough to achieve a plasmonic resonance in the IR spectral region, the amplification of the spectrum reported in Figure 4.5 demonstrates that a sufficient number of nanoprobes have been internalised by cells. The two additional peaks can be clearly ascribed to the presence of 4ATP-AuNPs [159], as highlighted by the superimposition of their spectral profile. This provides a further evidence of the nanoprobe internalisation and states that the molecular probe is still anchored to the gold surface, thus pointing out the stability of the carrier. It should also be noted that the increased intensity in both CH and NH stretching spectral regions, at 2800-3000 cm^{-1} and 3200-3500 cm^{-1} respectively (Figure 4.5A), is a strong indication of the coupling of 4ATP-AuNPs probe and cells, which occurred to sonicated samples only.

The internalisation efficiency was evaluated by the percent ratio of the number of amplified spectra where it is possible to recognise the peaks associated to the 4ATP marker, out of a total of 20 screened cells. A 10% uptake was obtained on samples treated for 15 minutes and a 30% on those treated for 30 minutes. These values are rather low if compared with those previously reported on cells treated in the same conditions using Dextran with hydrodynamic diameter of $\sim$ 12 nm (50% uptake

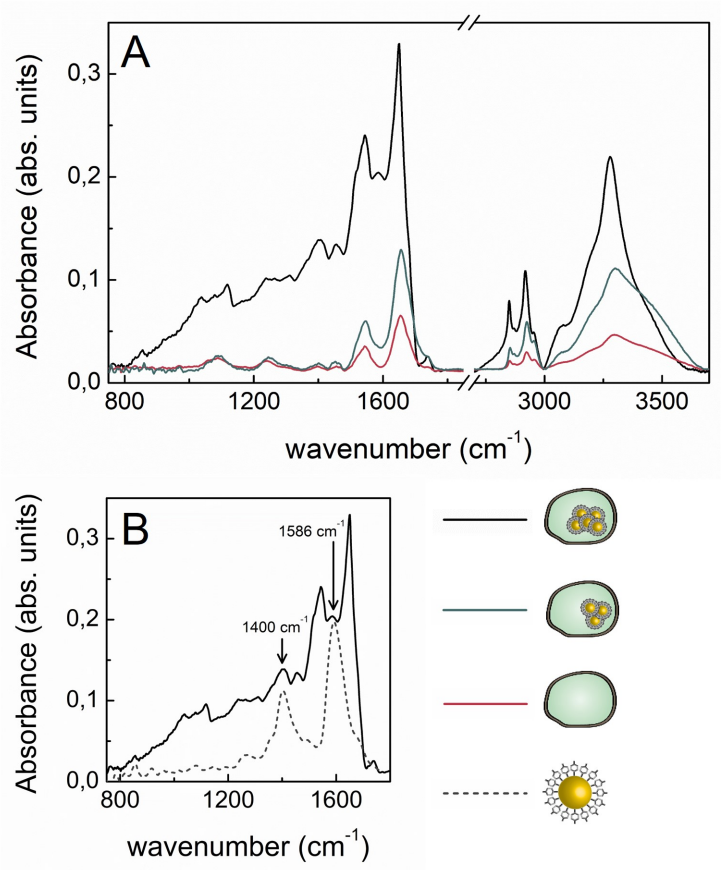

Figure 4.5. (A) SR-microFTIR spectra of non-treated cells (pink curve) compared with those of cells treated with 20 nm 4ATP-AuNPs for 15 minutes, which have internalised a different number of nanoprobes by SP, hence showing different modifications of the spectral profile. (B) SR-microFTIR representative spectrum of a NIH-3T3 cell irradiated with US (16 mW/cm^2, 15 minutes) in presence of the 20 nm 4ATP-AuNPs nanoprobe (black line), compared to the SEIRA spectrum of the nanoprobe alone (dashed grey line); its characteristic peaks at 1400 cm^{-1} and 1586 cm^{-1} can be identified in the spectrum of the treated cell, pointing out the internalisation of the nanoprobe.

upon 15 minutes treatment) [88]. A more coherent estimation can be obtained if also the second type of cell spectra, in which the signal amplification is lower, is taken into account. This yields uptake efficiencies of 40% and 60% for exposure times of 15 and 30 minutes, respectively.

Another important aspect concerning the internalisation efficiency is the cell sonication procedure. Indeed, cells were treated in suspension, and then laid onto the silicon substrate for SR-microFTIR analysis. With respect to other SP treatments that are usually made on on cells growing in adhesion conditions, the protocol herein employed, has some advantages: *i*) it allows for working with high cell concentration in small volumes in order to limit the dilution of the nanoprobe, *ii*) it avoids some possible artefacts due to the interaction of cells with silicon surface, *iii*) it maximises the exposed surface of cell plasma membrane, and *iv*) it avoids membrane perturbation by post SP biochemical treatments (*e.g.*, cells detachment procedures).

The obtained results appear particularly relevant in terms of both uptake efficiency and sensitivity at the single cell level considering that the SEIRA signal enhancement depends on the number of 4ATP-AuNPs internalised per cell and that the initial concentration of the AuNPs dispersion is extremely low ($\sim$ nM). However, by adopting a strategy to concentrate 4ATP-AuNPs at the cell-medium interface undergoing US, these results may be, in principle, further improved. As mentioned, the SEIRA methodology using SR-microFTIR can offer the advantages of ease of preparation and accuracy compared with fluorescence and electronic microscopies where the sample preparations are quite laborious, prone to artifacts, invasive and the biochemical information is difficult to be achieved [212]. In addition, the detection sensitivity of AuNPs by microfluorescence techniques is dramatically reduced because of the phenomenon of fluorescence quenching of dye molecules near the gold surface. For completeness, the FTIR evidences induced by US and AuNPs combined treatment were compared also with those provided by US or AuNPs separately. Although neither additional peaks nor spectral amplifications due to SEIRA phenomenon were detected with respect to the control samples treated only with the nanoprobe, a detailed analysis to understand contributions of individual stimuli to the biochemical structure was performed and reported in Section 4.3. The lack of SEIRA nanoprobe perturbation in the FTIR profile of non-sonoporated cells clearly indicates that for an efficient internalisation of 4ATP-AuNPs probe the membrane SP is required. On this line, as reported in detail in the Chapter 5, the 4ATP-AuNPs can be further functionalised with molecules that provide specific affinities with receptors expressed by cells in a particular stage of their life cycle, or which are in particular pathological conditions [19, 31], to be selectively recognised on the cell plasma membrane. This would mean that the nanoprobe can be suitably improved to be employed for triggering combined chemical and US cell targeting and spectral imaging. In this direction, a combined analysis of the changes in the FTIR spectrum of native NIH-3T3 cells together with cytotoxic assays of the treatments is also reported in Section 4.3.

4.3 Analysis of the biological effects induced by internalisation of the nanoprobe

In section 4.2, the efficient internalisation of ATP-AuNPs nanoprobes within NIH-3T3 cells by exploiting transient membrane SP has been demonstrated together with the possibility for recognising the nanoprobe at the single cell level, with extremely high sensitivity, thanks to the SEIRA spectral amplification. Here, the biological side effects related to the nanoprobe internalisation are studied. To this aim, the modifications occurring in the SR-microFTIR spectra of cells treated with US in presence of 4ATP-AuNPs for 15 and 30 minutes were evaluated. The spectral analysis was supported with cytotoxicity and genotoxicity assays for distinguishing between the different types of cell death that can occur, namely apoptosis or necrosis. Apoptosis is a programmed cell death that can be activated as defence mechanism by the cell. Necrosis, instead, occurs when an external trauma results in serious damages of the cell that undergoes to a premature death characterised by the rupture of the plasma membrane.

4.3.1 Spectral analysis of the SR-microFTIR spectra of single cells

The spectral analysis was focused on a significant portion of treated cells in whose spectra the additional peaks attributed to the nanoprobe do not appear and the intensity enhancement is not pronounced (dark cyan spectrum of Figure 4.5). A rather low number of internalised 4ATP-AuNPs is in fact expected in the corresponding cells, thus spectral distortions associated to the SEIRA effect [213, 214] are minimised, as well as possible biological responses due to the crowding of the nanoprobes in the cytosol. Thus any observed effect can be reasonably attributed to cell-nanoprobe biochemical interactions. Specifically, as reported in Figure 4.6, the analysis were focused on the fingerprint region (between 800 and 1800 cm^{-1}), where all the most significant bands associated with the molecular vibrations of proteins and nucleic acids are located, and the CH_2-CH_3 (between 2800 and 3000 cm^{-1}) where the characteristic vibrations of lipid are present [215].

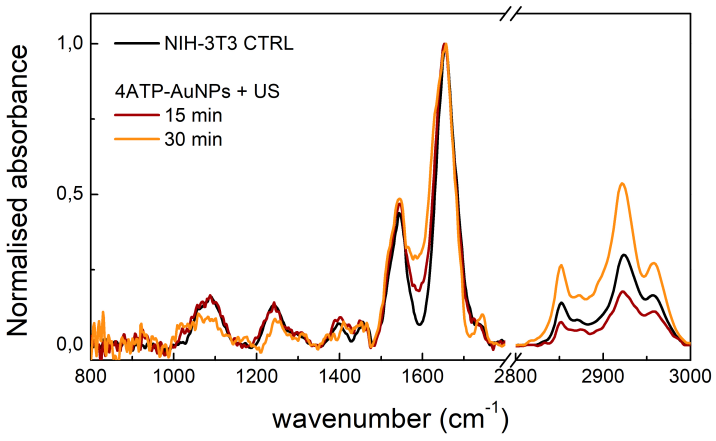

Figure 4.6. SR-microFTIR spectra of cell samples underwent US-nanoprobe combined treatments for 15 (red curve) and 30 (orange curve) minutes, in comparison with the non-treated control sample (black curve).

The spectra of treated samples show evident shift and broadening of the amide I band, particularly marked in cells treated for longer time. In the sample treated for 30 minutes with 20 nm 4ATP-AuNPs, a concomitant slight decrease occurs in the intensity of the bands at 1086 and 1238 cm^{-1}, corresponding to the DNA phosphate stretching modes. Such decrease is indicative of chromatin condensation [216]. According to the literature, all the observed spectral modifications can be attributed to the onset of apoptotic processes in the treated cells [216, 217]. In addition, weak variations are observed in the intensity of the CH_2 and CH_3 stretching modes at 2851 and 2958 cm^{-1}, respectively, which might be related to structural alterations in the cell membrane, also associated with apoptotic events [192, 218].

With the purpose to deepen the analysis of the biological effects induced by the combined treatment with US and 4ATP-AUNPs, the analysis was focused on the amides region, between 1450 and 1800 cm^{-1}, where the most evident spectral changes are located. The spectra of NIH-3T3 cells treated for 15 and 30 minutes were therefore compared with those of the corresponding samples exposed to US or 4ATP-

AuNPs separately, in order to disentangle the different contributions. Each spectrum was analysed by a Gaussian curves deconvolution, as shown in the representative graph of Figure 4.7. Four major components were assigned to the amide I band and reported in Table 4.3.

Table 4.3. Peak assignment of the spectral components resulting from the amide I band Gaussian deconvolution, according to ref. [215, 219].

Peak centre (cm^{-1})	Assignment
1624	β-sheets
1639	random coils
1658	α-helices
1678	β-sheets and β-turns

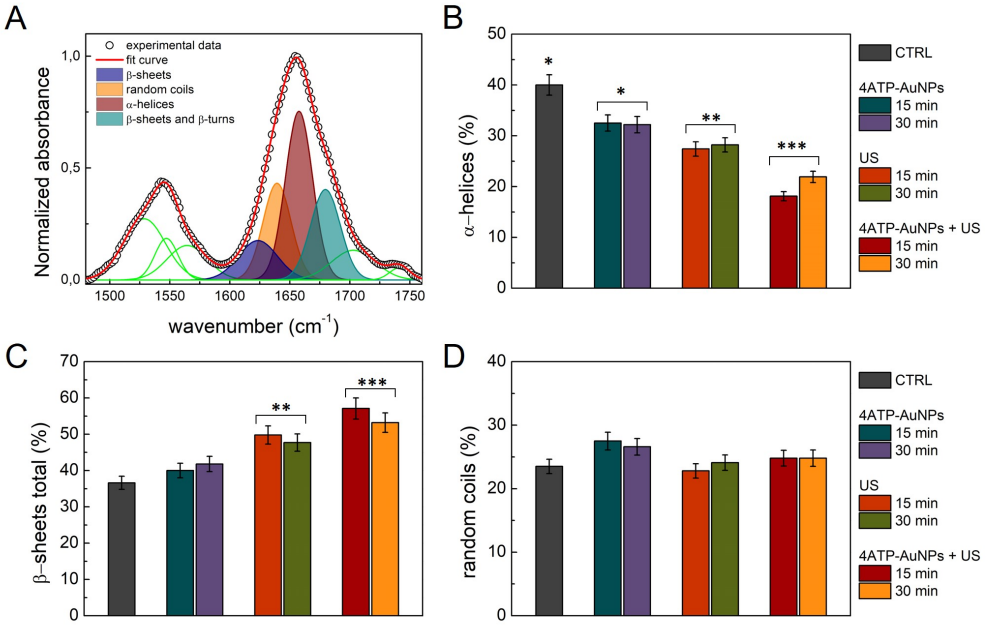

Figure 4.7. (A) Representative spectral deconvolution by the Gaussian fitting procedure; the spectral components associated to the protein secondary structure are highlighted by filled coloured areas (the other spectral components are represented in green). Histograms representing the weight of α-helices (B, top), β-sheets (C, bottom left) and random coils (D, bottom right) spectral components in the amide I band for each sample analysed; each weight was determined as the percent area with respect to the total area of the band. The β-sheets percentage accounts for both the β-structure contributions (1624 cm^{-1} and 1678 cm^{-1}). Columns and bars represent the average and standard deviation values obtained on at least three independent experiments. *p < 0.05, **p < 0.01 and ***p < 0.001.

The percent area of each component, with respect to the total area of the band, was determined for all the samples and reported in the histograms of Figure 4.7B-D, in comparison with those of the control non-treated cells. Samples treated with the

nanoprobe only (non-sonicated) do not show substantial spectral variations respect to the control sample. Only a slight decrease in the α-helices components is observed, along with an increase in the β-sheets percentage depending on the treatment time. Concerning the exposure to US (without the nanoprobe), the spectral changes are more pronounced. In particular, the weight of the β-sheets components rises up to 50% from the 37% of the control. Such US induced modifications of the protein secondary structure are coherent with those previously reported [196]. The samples treated with both US and 4ATP-AuNPs show a dramatic drop of the α-helices components, associated to an increase of the β-sheets contributions. The weight of random coils does not show significant changes for all the examined samples (Figure 4.7D). Therefore the observed structural changes may be symptomatic of early stages of the apoptotic cellular response. In this regard, the correlation of the shift of amide I with apoptosis has been already observed in photo-dynamically treated human glioma cells [220]. The shift of 26 cm^{-1} was attributed to conformational transition of the secondary structure of proteins from α-helix to β-sheet structure. On this basis, it is reasonable to suppose that some apoptosis events may occur starting from 15 minutes of US-nanoprobe combined treatments. If confirmed, this hypothesis might have some relevance in therapy scenarios where US can be highly focused in specific points of the body to trigger a controlled cell death.

4.3.2 Cytotoxicity and genotoxicity assays

To shed light on the biological effects revealed by the SR-microFTIR analysis, a flow cytometry Annexin V and Propidium Iodide (PI) combined assay was carried out. In this way, it was possible to monitor the eventual onset of apoptosis and necrosis processes. FITC-labelled Annexin V binds the phosphatidylserine translocated to the outer cell membrane layer during apoptosis, while PI is internalised within cells only upon membrane damage, occurring during late apoptosis and necrosis processes. The combined assay thus allows for distinguishing between the different cell death pathways. The results, obtained on samples underwent the different treatments, are reported in Figure 4.8, where the cell viability as the percentage of viable cells with respect to the total population analysed is also shown.

The analysis points out a slight loss of viability when cells undergo US-nanoprobe combined treatment for 15 minutes. Marked effects occur for the 30 minutes treatments. This is consistent with the results of Section 4.2 on the 4ATP-AuNPs uptake. The cells undergoing US or 4ATP-AuNPs individual treatments show a weak cytotoxic impact independently from incubation time, with a slightly lower impact on mortality of US. In accordance with the SR-microFTIR analysis, it can be thus deduced that the US-nanoprobe combined effect activates some cell death pathway. On the other hand, it has been reported that the US irradiation of NP can enhance cavitation effects. It is therefore possible that this phenomenon also contributes to the observed increase of the cytotoxic response in samples that underwent combined US-nanoprobe treatments with respect to those treated by US or 4ATP-AuNPs separately [188].

In agreement with literature [88], these results also indicate that after 30 minutes treatment, US pressure waves begins to cause irreversible damage to the cell membranes. Figure 4.8 also suggests that the US or 4ATP-AuNPs individual treatments

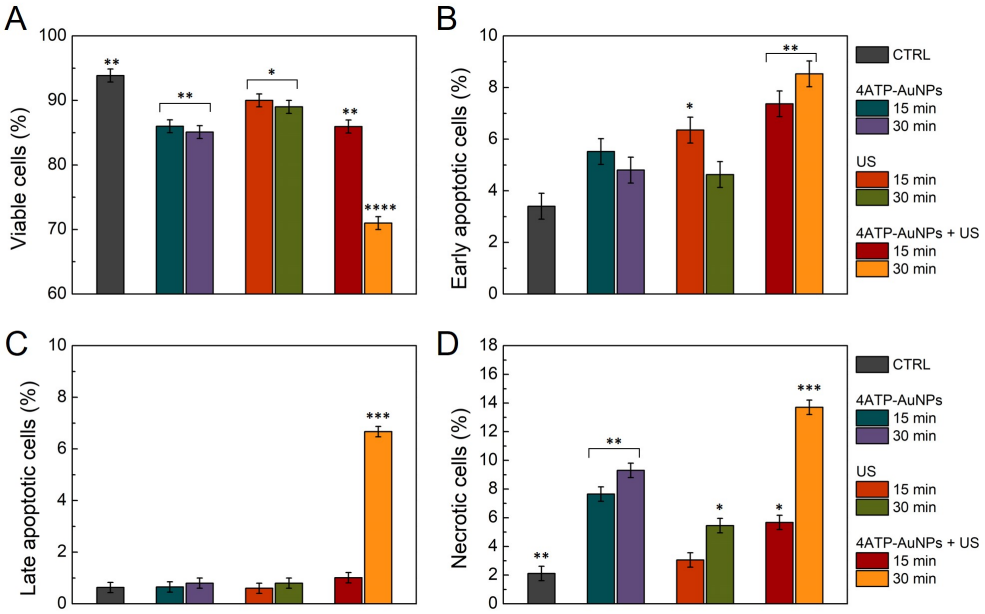

Figure 4.8. Flow cytometry analysis of the NIH-3T3 cells performed by the AnnexinV/PI combined assay. The cell viability was determined as the percent number of viable cells with respect to the total population of samples analysed. Columns and bars represent the average and standard deviation values obtained on at least three independent experiments. *p<0.05, **p<0.01, ***p<0.001 and ****p<0.0001.

provide an analogous effect in triggering the first events that then lead to apoptosis. Likewise, combined US-nanoprobe treatments (15 and 30 minutes) give an almost identical percentage of early apoptotic cells and show a small increase of apoptosis compared to the individual treatments at the same times. The flow cytometry results confirmed the hypothesis based on the SR-microFTIR analysis. It is worth noting that overall treatments slightly affect the cell viability mostly due to necrosis. More interesting, the combined US and nanoprobe treatments also induce a quite significant percentage of apoptotic events. Specifically, early apoptotic cells which appeared in response to the 15 minutes combined treatment became late apoptotic after 30 minutes, allowing us to conclude that the time of combined 4ATP-AuNPs and US exposure is crucial to trigger irreversible apoptotic events on NIH-3T3 cells.

A Cytokinesis-block MicroNucleus (CBMN) assay was performed to evaluate potential genomic instability at chromosomal level and the frequencies of micronucleated cells on the samples that underwent the different treatments. The results of the analysis are reported in Figure 4.9 in terms of number of micronucleated cells.

The results demonstrate, in a seemingly surprising way, that the samples treated with US only show a slight increase in the number of micronucleated cells, which becomes significant when cells are exposed to US for 30 minutes (in Figure 4.9 compare violet and green histogram columns, respectively, with the control one in dark grey). Contrarily, the US-nanoprobe combined treatments correspond to comparatively lower micronuclei frequency which does not differ significantly from those measured in the control samples. According to the cytotoxicity analyses, after

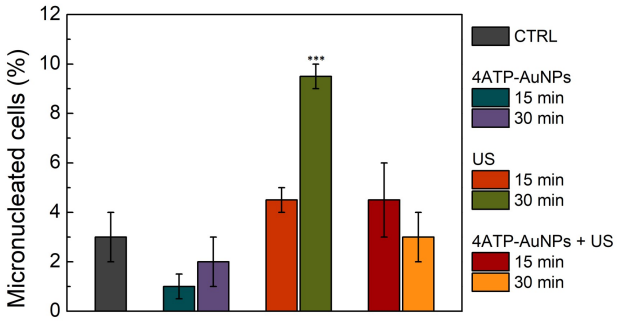

Figure 4.9. Average number of micronucleated cells (error bars represent the standard deviation), determined upon the different treatments by the CBMN assay. The values were obtained analysing a population of 500 cells for each sample. ***$p<0.001$

the US and 4ATP-AuNPs treatments, late apoptotic cells appeared, and, in this respect, both events of cell death via apoptosis and decrease of binucleated cells may be related. Moreover, the intensity decrease in the DNA phosphate stretching infrared modes observed on the same sample (Figure 4.6), indicative of chromatin condensation, is correlated to apoptotic cell death [216]. The potential genotoxic impact of medical ultrasound has been only slightly investigated so far [193, 195]. The positive results obtained for 30 minutes treatment under sub-cavitation conditions support the hypothesis that in addition to the effect of transient sonoporation of the plasma membrane [197], some probable effect on the genomic integrity might be expected. Any chromosomal damage related to the phenomenon of micronucleation induced by US could result from a direct mechanical stress on the nucleus or indirectly transmitted to it [221]. In this regard, some speculations can be made considering our specific irradiation conditions. Indeed, although the nucleus is the most rigid cellular organelle (*i.e.* 2-10 times more rigid than the surrounding cytoskeleton), the instantaneous pressure values involved herein (10-60 kPa), while being too low to directly induce reactive oxidative species, were higher than the "threshold stress" (0.1-10 kPa) needed to induce nuclear deformation [222]. According to the literature, mechanical inputs on the nuclear membrane barriers [222] and at the level of the mitotic spindle structure of the cell [223, 224] is one of the mechanisms through which the present effect becomes manifest (*i.e.* post-mitotic micronuclei from lagging chromatids or chromatin bridges between anaphase chromosomes).

Chapter 5

Antifolate SERS-active nanovectors: quantitative drug nanostructuring and selective cell targeting for effective theranostics

One of the open challenges in modern medicine is the detection and treatment of cancer at the earliest stage of its progression [225]. By boosting the threshold for cancer detection, a successful therapeutic route would promptly act against few, isolated cancer cells. This would allow significantly limiting the side effects of aggressive tumour therapies [226]. It is known that chemical, physical and biological environmental conditions induce genetic and epigenetic alterations resulting in a wide heterogeneity in tumour development [227]. Therefore, novel treatment protocols need to be designed for addressing the specificity of the tumour type with a rationally programmed targeting of cancer tissues [228, 229]. This can be realised by exploiting the preferential interaction of cancer cells with specific theranostic nanosystems, suitably designed to couple a strong diagnostic capability to the therapeutic action [230].

A theranostic nanovector (NV) is a nanosized system capable of travelling in bodily fluids to reach and selectively interact with a specific (cancer) cell type [231]. It is typically constituted by a traceable element, a targeting biolayer or biomolecule and a drug that selectively kills the cancer cells [231, 232, 233]. Fluorescent molecules are often employed as traceable elements in the imaging and diagnostics of cancer tissues or cells [234]. Nevertheless, photobleaching can limit the measurement reproducibility of fluorescent tags, and their optical sensitivity is often not optimised for ultrasensitive, early tumour screening. In the last decades, efforts have been dedicated to the development of alternative, newly designed systems for diagnostic and imaging applications [235]. Noble metal NPs represent an interesting possibility, due to their plasmonic properties that allow for confining extremely intense electromagnetic fields at the nanostructure surface. This opens promising possibilities, as the super-resolution imaging and the ultrasensitive spectroscopic

investigation of single or few molecules by SERS [235, 236, 18]. SERS-activated NPs can be employed for tumour targeting (both *in vivo* [237, 238] and *in vitro*, at single cell level) and for the molecular imaging of receptors which are overexpressed in tumours [239, 235, 19, 240].

Cellular targeting with theranostic NVs is often performed *via* the specific biorecognition of the nanosystem by cellular receptors: the NV acts by locally binding or penetrating inside the targeted cell. The biorecognition often involves protein–antibody interactions, widely employed in immunoassays and standard staining protocols [241, 242]. Unfortunately, proteins can suffer for structural and functional instability upon environmental variations of temperature and pH. Furthermore, the NV functionality could be inhibited by the formation of a protein corona [243], that can occur, in complex media, in absence of additional protecting molecular layers [244, 245]. As an alternative to proteins, selected smaller, more stable molecules can be adopted. Among these, folic acid (FA), a group B vitamin necessary for amino acid and nucleic acid synthesis inside cells, has been successfully employed in selective cancer cell targeting, based on the higher density of folate binding proteins on cancer cell membranes [246, 247]. A previous study conducted in our research group reported on a SERS-active folate-NV, based on the conjugation of 4-aminothiophenol functionalised gold NPs (4ATP-AuNPs) with FA. The folate-NV was employed for a comparative study on the targeting of different cell lines: the quantitative analysis of SERS signal enabled for discriminating between cancer and non-cancer cells, proving that the folate-NV binding efficiency reflects the folate receptor expression on a specific cell [19]. This nanosystem has a relevant potential in the development of single-cell cancer screening, for both bioptic samples and the detection of circulating tumour cells in blood samples, as proposed by Pallaoro *et al.* [248]. The therapeutic features of plasmonic NVs can be activated by exploiting the strong energy absorption of metal nanostructures illuminated at the LSPR. This increases the local temperature and kills the targeted cell by photothermal therapy [249, 250]. This approach is mainly effective in treating superficial tumours, due to the limited transparency of biological tissues. A more versatile strategy is the drug loading on or inside a tumour-selective nanosystem, allowing for a local release of the active anticancer agents, reducing the systemic toxicity [251, 252].

Starting from the diagnostic capabilities of the folate NV, here the FA is substituted with antifolate drugs, specifically aminopterin (AMT) and methotrexate (MTX) [253, 254, 255]. Antifolates exhibit strong structural similarities to folate, and this allows for the use of the same chemical approach in loading them onto the SERS-active NVs. Furthermore, this design allows to possibly conserve the SERS-based diagnostic capabilities already established for the FA-NV, while adding the therapeutic action, since antifolates are internalised inside the cell through the same pathways used for FA supply [256, 257]. Bearing these aspects in mind, in the study herein presented theranostic NVs were synthesised and carefully characterised. The cytotoxicity results obtained on HeLa cells demonstrate the therapeutic potentialities of the system. Furthermore, a SERS-based approach for assessing in real time the amount of drug loaded on the NV was developed. Based on the SERS titration results, the antifolate AMT-NV was selected for a comparative study on different cell types. To do so, two human cell lines, both previously used in folate-based targeting

experiments [19, 258, 259] were employed: immortalised HaCaT keratinocytes were selected as non-tumourigenic cell model [260, 261, 262], while tumourigenic cervical HeLa cells acted as cancer model [263, 264, 265]. Firstly, the NV binding efficiency at single cell level was assessed by SERS screening. Then, the cytotoxic effect of the drug in the molecular and nanostructured form was evaluated. An improvement of the NV selectivity was attempted by synthesising a coloaded nanosystem, conjugated with both folate and antifolate molecules.
The main results here reported are published in ref. [31].

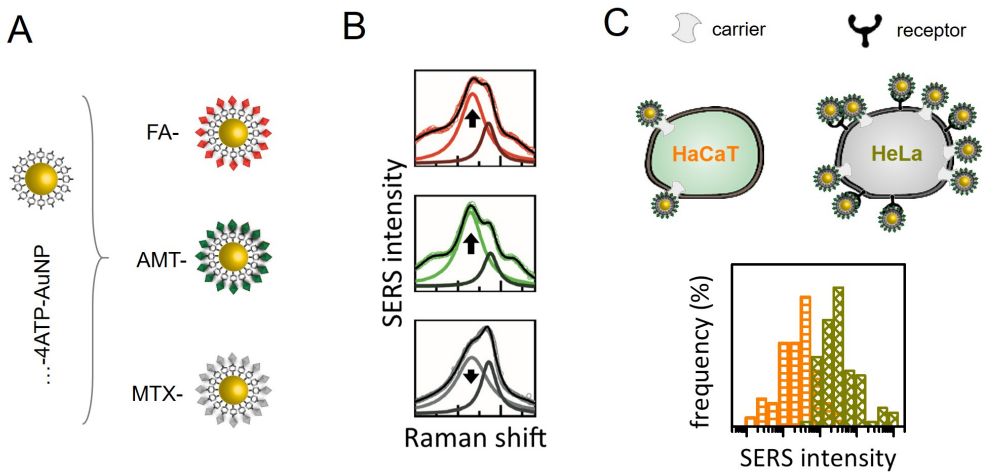

Figure 5.1. Sketch of the experiment. (A) Synthesis of different folate/antifolate NVs: 60 nm 4ATP-AuNPs have been further conjugated with folic acid (FA, red), aminopterin (AMT, green), methotrexate (MTX, grey). (B) The loading efficiency was extimated by the spectral weight redistribution of some specific SERS bands of the NVs. (C) AMT loaded NV was chosen due to its higher conjugation efficiency to perform a SERS screening experiment on non-tumourigenic HaCaT and tumourigenic HeLa cell lines. The different expression of FA receptors on the cell membranes allowed for distinguishing between the two cell lines depending on the SERS signal intensity.

5.1 Synthesis of the antifolate nanovectors and therapeutic action

Folate binding proteins on normal and cancer cells

Folate supply in cells is mediated by different FA binding proteins, as sketched in Figure 5.2. There are two classes of facilitative transporters, *i.e.* solute carrier proteins that are the reduced folate carrier (RFC) and the proton-coupled folate transporter (PCFT), and different types of folate receptors that internalise FA *via* endocytosis [246]. Among the different isoforms of folate receptors, folate receptor α (FR-α), is known to be overexpressed in numerous cancer cell lines, among which HeLa cells [258, 259, 263, 264]. In HaCaT cells, on the other hand, FA supply is mainly covered by the same types of solute carriers that are found in human keratinocytes [260]. For this reason, HeLa cells can be a significative model for folate receptor positive cancer cells; HaCaT line, on the other hand, represents a valid proof of concept for investigating the possible cytotoxic effects of antifolate NVs on normal human keratinocytes. Antifolate drugs indeed, even at low dosage, can induce skin toxicity effects, skin breakdown and keratinocyte dystrophy [266, 267, 268].

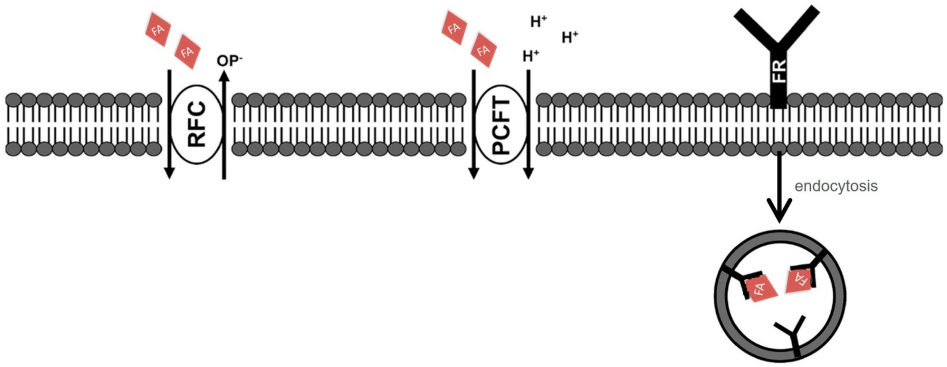

Figure 5.2. Sketch illustrating the most common folate binding proteins and their internalisation mechanisms. RFC and PCFT are facilitative transporters that mediate the folate transport by the counter-transport of organic ions (OP^-) or by the concomitant transport of protons (H^+), respectively. FRs mediate transport by a non-classical endocytosis involving formation of endosomes that migrate to the cytoplasm. Image adapted from ref. [246].

Synthesis of the antifolate NVs

The NVs were prepared with the same structural template, made of a plasmonic core (60 nm sized AuNPs), functionalised with the well-known spectroscopic label 4ATP [50] (see also Chapter 4) and further conjugated with folate/antifolate molecules. The preparation parameters were optimised to grant good performances in SERS-based imaging and NV tracking, as demonstrated for the folate-NV [19], while selecting a NP size that allows the successful internalisation in the cell [269]. The biofunctionalisation reaction is reported in Figure 5.3. Folate and antifolate molecules bears in their structure two carboxylic groups that constitute the reactive electrophilic centers involved in the nanovector biofunctionalisation. The

chemical conjugation is achieved with the activation of these groups by means of 2 cross-linker specific molecules, which react with the molecule in sequence. The first one, EDC (1-ethyl-3-[-dimethylaminopropyl] carbodiimidehydrochloride), is a "coupling" reagent, while the second one, NHS (Nhydroxy-succinimide), is a second activator. The first step of the reaction is a nucleophilic addition with the formation

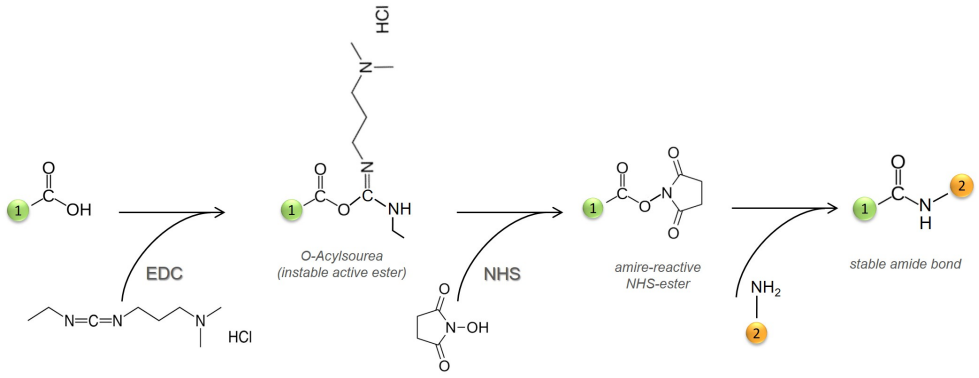

Figure 5.3. Chemistry of the EDC–NHS reaction employed for the functionalisation of 4ATP-AuNPs with folate and antifolate molecules. EDC reacts with a carboxylic-acid group on the molecule and forms an amine reactive O-Acylisourea intermediate. The addition of NHS stabilises the intermediate by converting it to a NHS-ester. Finally, the activated carboxylic groups can react with the amine group of the 4ATP leading to the formation of a stable amide bond.

of a "high-energy" ester intermediate, the O-Acylisourea, which is is unstable in aqueous solutions. In the following step, NHS creates amine-reactive intermediates. EDC couples NHS to carboxyls, forming an NHS-ester that is considerably more stable than the O-Acylisourea intermediate and allows for efficient conjugation to primary amines at physiologic pH. Therefore, the carbonyl of the folate/antifolate molecule is now electrophilic enough to be attacked by a nucleophilic agent, such as the amino group of 4ATP. Finally, a second nucleophilic substitution takes place with the release of NHS and the formation of a stable amide bond.

Cytotoxic effects on Hela cells

The antifolates AMT and MTX are structurally very similar to FA; they are indeed internalised in the cell by the very same folate receptors/carriers [270]. The negative surface charge provided by the carboxylic groups of the drug molecules ensure the NV stability in water, saline buffer and cell culture medium. To demonstrate the comparatively higher cytotoxicity of antifolate-NVs, their effect on HeLa cells, which are often selected as targeted cell model due to their marked overexpression of FR-α, have been monitored. Along with the NV structure, in Figure 5.4 the results of an MTT assay (see Appendix for details) that allows monitoring the cell growth of HeLa treated cells are presented. Cells were incubated for 24 hours with the folate/antifolate-NVs at 5 pM concentration in an incubator under physiological conditions (37° and 5% CO_2). While the folate-NV does not seem to affect critically the cell viability, this is strongly suppressed in the culture treated with antifolate-NVs.

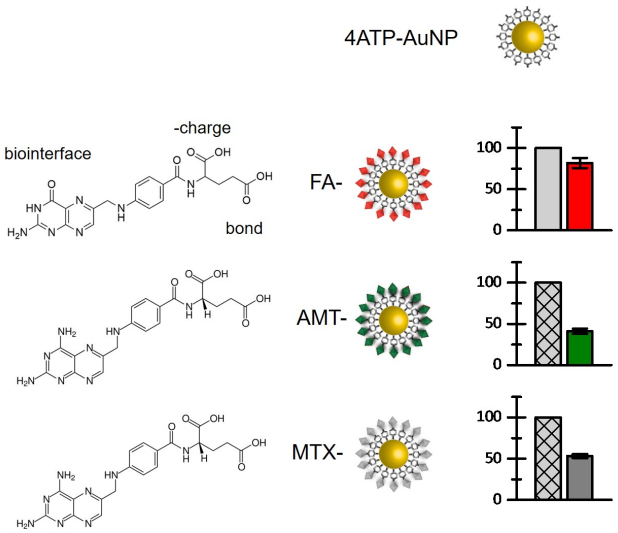

Figure 5.4. The molecular structures of folate and antifolates is displayed along with the sketch of the 3 different nanovectors. In the case of FA, the role of the different parts of the biomolecule in the NV have been highlighted: one of the carboxyl groups is involved in binding to the 4ATP-NP, the other one confers a negative charge to the NV ensuring its colloidal stability, the pteroyl domain is responsible for the cell biorecognition and results conveniently exposed on the NV surface. On the right, the viability of HeLa cells treated with FA- (red), AMT- (green), and MTX-NVs (dark gray bar) to the viability of a control cell population (gray, gridded bars) is compared. The treatment was performed by incubating the cells with the different nanovectors (5 pM, 24 hours).

5.2 Assessing the drug concentration

5.2.1 Colorimetric titration assay

As the NV structure is optimised for the interaction with cellular receptors, its cytotoxic action should be related to the receptor binding efficiency and to the amount of drug loaded on a single NP. If these parameters do not change throughout the application, as in this case, the uptake efficiency mainly depends on the receptor type and density on the cell membrane, hence on the cell line, according to previous studies [19]. For estimating the drug loading amount, the shift of the LSPR which occurs upon chemical conjugation and is correlated to the change in the dielectric medium around the plasmonic NP [271], can be monitored. UV-Visible absorption measurements performed on colloidal water dispersion of bare (citrate capped), 4ATP-AuNPs, and NVs are shown in Figure 5.5. The LSPR absorption peak is redshifted upon conjugation of the NPs with 4ATP, and further redshifted by different amounts for folate/antifolate conjugation. The different overall peak shift suggests that changing the drug molecule yields a different conjugation efficiency. Nevertheless, this result can hardly be used for a quantitative estimate of the drug loaded on the NP surface [272]. A more reliable estimate of the drug loading efficiency is provided by colorimetric titration assays, also based on optical absorption spectroscopy. In this kind of assay, a specific dye is added to the NV dispersion in order to selectively bind to the free amines of 4ATP molecule. The measurement of its optical absorption allows for indirectly inferring the number of drug molecules anchored on the NP

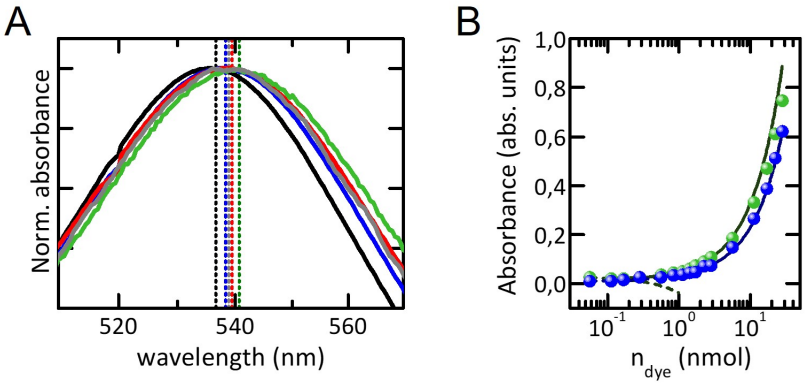

Figure 5.5. (A) Optical absorption measurements in the region of the LSPR peak of AuNP for bare NPs (black), 4ATP-conjugated NPs (blue), FA-NVs (red), AMT-NVs (green), MTX-NVs (gray). Spectra are normalised to the maximum of absorption. A redshift up to 5 nm of the LSPR peak is appreciable in the NV spectra. (B) Colorimetric titration results by Orange II dye. Absorption of the unconjugated dye residual in the supernatant vs. the total added amount of dye to a dispersion of 4ATP-NPs (blue) and to the complete AMT-NV (green). Dots are experimental data, solid lines are the fitting trends.

surface. Results are reported in panel 5.5B for the case of AMT. Titration assays show that the ratio of drug-binding to unconjugated 4ATP molecules is such that there are 1.9 AMT molecules every 10 4ATP molecules (2760 ± 300 drug for 14600 ± 1500 ligand), similar (1.6 : 10) in the case of FA, slightly lower (0.75 : 10) in the case of MTX. It is important to stress that the chemical titration measurements performed to obtain these data require a large number of experimental steps, and are thus time consuming and demanding in terms of sample quantity. For this reason, they could not be performed at every sample synthesis. In the following Section, the efficacy of SERS spectroscopy in estimating the amount of drug conjugated to the AuNPs is demonstrated.

5.2.2 SERS-based titration

As shown in Figure 5.6, the SERS spectroscopic fingerprints of the three NVs are very similar owing to the structural similarities between the binding molecules (see Figure 5.4A). Nevertheless, a very reproducible and reliable modification to the SERS spectra occurs upon folate or antifolate functionalisation. This is a marked spectral weight redistribution between the symmetric and antisymmetric components of the ring CC stretching vibrational band, around 1580 cm^{-1}. The occurrence of similar changes in the shape of the SERS spectra of simple reporter molecules is well accepted in the literature. It has been discussed early in 2012 by Kho and coworkers [273] and their work set the basis for the design of various proposals of SERS-immunoassays. These typically quantify the binding of analytes to SERS reporter molecules on a NP surface by monitoring the modifications revealed in the SERS response [274, 275, 276, 277]. These spectral changes have been ascribed to modifications induced on the SERS reporter by analyte binding, either arising from

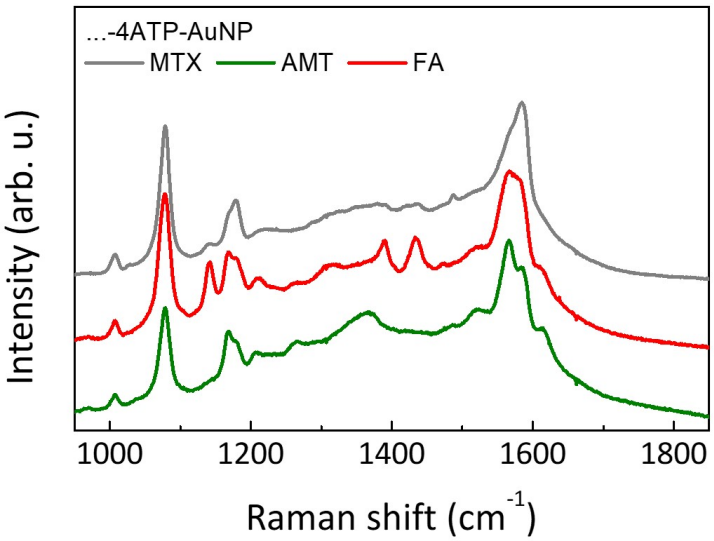

Figure 5.6. SERS spectra in the fingerprint region acquired on FA- (red), AMT- (green), MTX-NVs (gray line). Spectra are presented after a linear baseline subtraction and are vertically shifted for clarity.

the reorientation of the reporter molecule with respect to the metal surface, causing a change in the Raman selection rules, or from a deformation of the molecular structure and the consequent rearrangement of the molecular electronic cloud.

In Figure 5.7A, the SERS spectra of 4ATP-AuNPs and folate/antifolate NVs are reported: an enhancement of the intensity of the antisymmetric component is systematically observed upon drug conjugation, the effect being more or less pronounced, depending on the specific molecule. The observed spectral modification allows for monitoring the conjugation of the 4ATP ligand with the drug molecule even without relying on a SERS band ascribed to a specific chemical bond arising upon drug-4ATP binding.

It is possible to quantify the spectral weight redistribution by the definition of the parameter $\rho = I_{\nu(CC)\,antisym}/I_{\nu(CC)\,sym}$, where $I_{\nu(CC)\,antisym}$ is the intensity of the antisymmetric CC stretching component, centered at 1567 $\pm$ 1 cm^{-1}, and $I_{\nu(CC)\,sym}$ is the intensity of the symmetric CC stretching component, centered at 1586 $\pm$ 1 cm^{-1}. The error in the frequency is estimated by the experimental reproducibility. In Figure 5.7B the correlation between the conjugation efficiency as estimated by chemical titration methods is reported, defined as $r_{titr} = 10 \times (n_{drug}/n_{4ATP})$ where n is the number of molecules, and the conjugation efficiency as estimated by SERS spectroscopy, $r_{SERS} = \rho_{drug}/\rho_{4ATP}$. The excellent correlation between the two measurements demonstrates the feasibility of a titration measurement based on the spectroscopic signal, owing to the high sensitivity of SERS spectroscopy. It is worth noticing that the measurement is very fast and can be performed to characterise the theranostic NV every time it is synthesised.

The results presented in Figures 5.5 and 5.7 refer to an optimised synthesis of the nanovector. The different yield of the drug conjugation reaction observed for the different molecules can be reasonably ascribed to the specific characteristics of

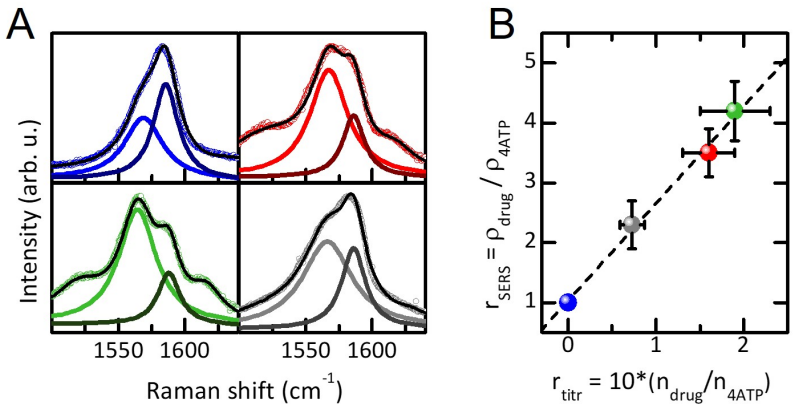

Figure 5.7. (A) SERS spectra in the region of the ring CC stretching vibration for 4ATP conjugated NPs (blue) as reference system, and FA- (red) AMT- (green) and MTX- (gray) NV. Scattered points are experimental data, solid black lines are the cumulative fitting plots, and solid colored lines highlight the main spectral components of the fitting, ascribed to antisymmetric (low frequency, light color) and symmetric (high frequency, dark color) CC stretching modes. (B) Correlation between the titration ratios obtained by colorimetric measurements (r_{titr}) and by SERS measurements (r_{SERS}) (see text for details). Error bars are estimated based on the experimental reproducibility.

the molecular species itself. For example, the lower yield for MTX probably owes to a lower solubility of MTX in the water dispersion used for the preparation.
As the conjugation yield is higher for AMT, the AMT-NV was selected for performing a SERS screening study and a deeper cytotoxicity investigation, comparing the effect of molecular and nanostructured AMT on the two cell lines.

5.3 SERS screening on treated HeLa and HaCaT cells

In Figure 5.8A, the spectra of HaCaT and HeLa cells grown on a silicon substrate and treated with the AMT-NV at 5 pM concentration for 24 hours are presented. All the bands ascribed to the NV are well evident in the 1000–1600 cm^{-1} region. A band associated to the silicon substrate is also present within the same spectral window (Figure 5.8A) and is there used for the spectral normalisation. A weak spectral feature is also evident on the high frequency side of more intense SERS spectrum, around 1650 cm^{-1}. This band is absent in the NV spectrum (see Figure 5.6) and can therefore be ascribed to the amide band of the cellular components [19]. The strong intensity of the SERS signal masks the other spectral features of the cell, overlapping with the SERS bands of the NV. The comparatively high intensity of the SERS features in the HeLa cell spectrum is a general result, as revealed by the systematic screening of the SERS intensity performed on wide 100-cell populations, as discussed below. In Figure 5.8B, the results of the screening of the normalised SERS intensity measured on a population of 100 single HaCaT and HeLa cells treated with the AMT-NV (5 pM, 24 hours) are reported. The normalised SERS intensity was calculated per single cell by performing a low resolution spectroscopic map of

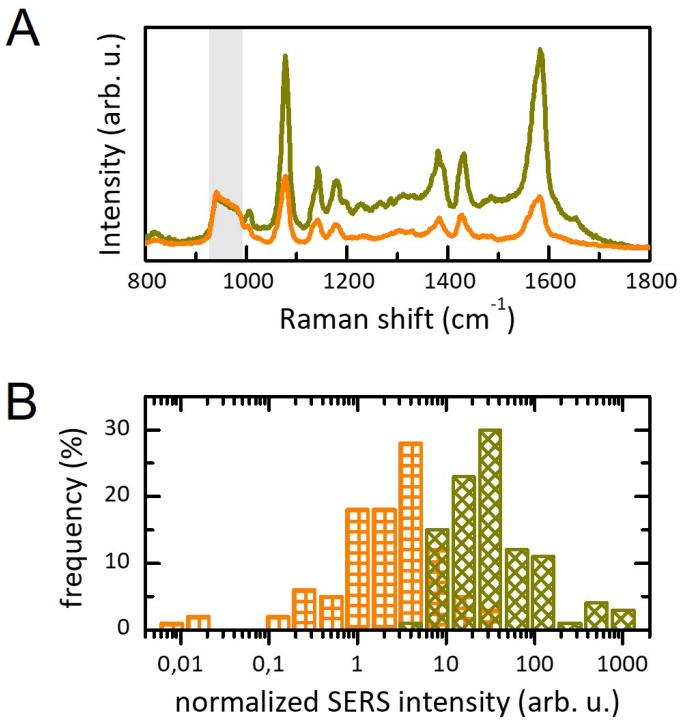

Figure 5.8. (A) Representative SERS spectra collected on single HaCaT (orange solid line) and HeLa cells (dark yellow solid line) treated with the AMT-NV at 5 pM concentration. The bands associated to the AMT-NV are evident in the 1000–1600 cm^{-1} region. The peak associated to the second-order Raman band of silicon, arising from the substrate, is highlighted by the gray-shaded area. On HaCaT cells, an overall lower SERS signal was detected. Spectra were normalised to the substrate contribution and are presented after linear background subtraction. (B) Histogram of the SERS intensity, normalised to the substrate contribution, measured on a population of 100 HaCaT (orange, right squared pattern) and HeLa (dark yellow, tilted squared pattern) single cells.

the cell in the spectral region shown in Figure 5.8B, then integrating the SERS intensity (1560–1590 cm^{-1}) and normalising it to the substrate intensity (930–990 cm^{-1}), coherently with the method proposed in ref. [19]. A separation between the intensity revealed on HaCaT (normal) and HeLa (cancer) cells is evident, being the signal measured on HeLa cells more intense than the one measured on HaCaT cells. The SERS signal intensity can be reasonably interpreted as a parameter directly correlated with the NV binding efficiency, as proposed in similar works [239, 235, 19]. This suggests a preferential targeting of HeLa cells by the AMT-NV.

SEM images acquired on few HeLa and HaCaT cells treated with the AMT-NV at the same conditions are reported in Figure 5.9. The images allow an estimate of the NV binding efficiency. Although less accurate, because performed on very few cells, this can be useful in comparison with the SERS screening response. The estimate suggests that the binding efficiency of HeLa cells is about doubled compared to HaCaT cells. In the SERS screening, the separation between HeLa and HaCaT cell population is quantitatively bigger. This is not surprising: indeed, the 633 nm

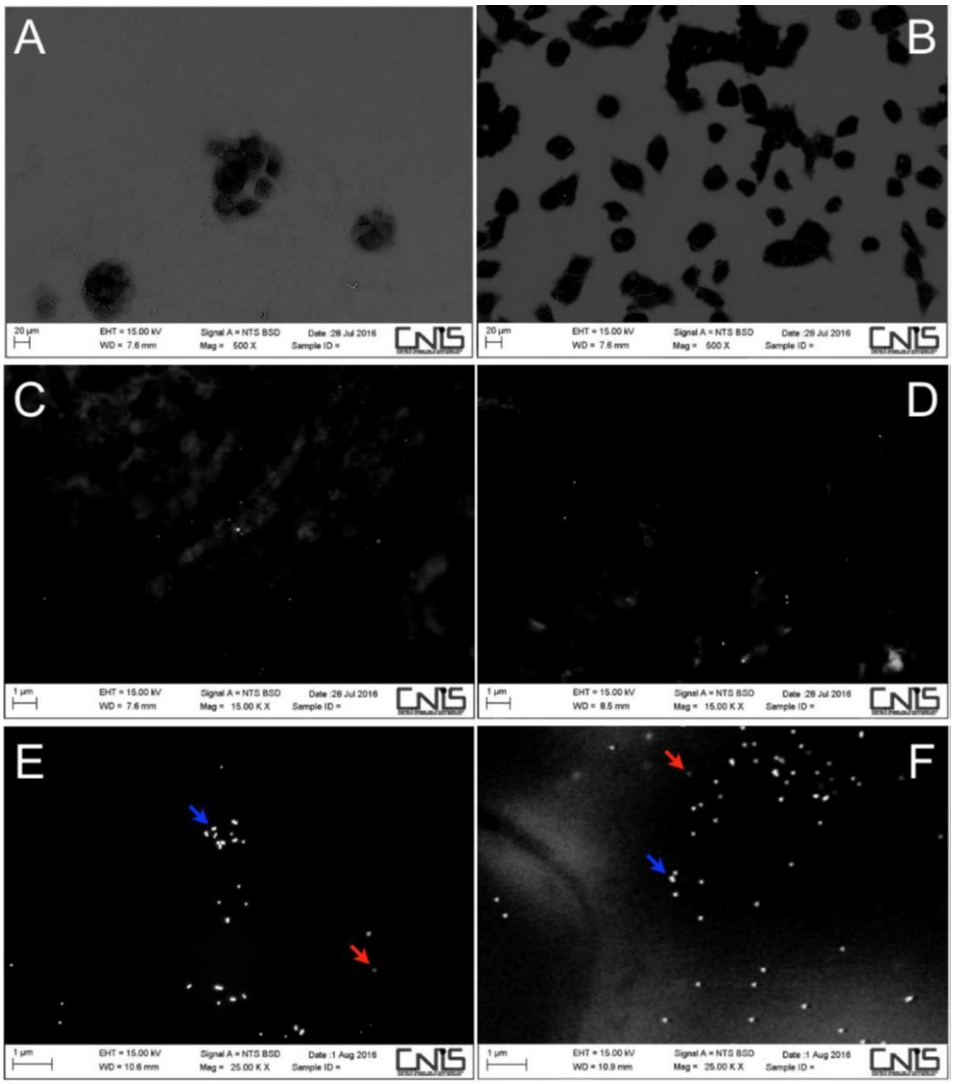

Figure 5.9. SEM imaging acquired in backscattering mode on HaCaT (left column) and HeLa cells (right column) cells, treated with the AMT-NVs for 24 hours at the concentrations of 1.25 pM (panels A, B, C, D) and 5 pM (panels E, F). A and B are field visions, allowing to distinguish the cells on the Si substrate. In panels E and F, the red arrows highlight NVs imaged with a different contrast, that is probably due to the NPs being covered by the cell membrane. The blue arrows instead indicate NVs that are anchored externally with respect to the membrane.

laser used for SERS screening is in resonance with the LSPR profile of aggregated NVs, more than with the LSPR of single, isolated nanoparticles. This actually boosts the SERS sensitivity towards highly targeted cells, as already discussed in ref. [19]. This result further validates the potentiality of SERS screening as an easy and fast, non-destructive, reproducible diagnostic tool. Similar experiments conducted by treating the cells with the FA-NV revealed a very clear separation between the signal of HaCaT and HeLa cells, which is not reproduced in the present case involving the antifolate AMT-NV. The targeting of HaCaT cells seems non-negligible. This result

can be correlated with the SEM imaging of the cells and is consistent with the idea of HaCaT cells being more efficiently targeted by the AMT-NV than by the FA-NV. This aspect needs to be addressed, as it is likely to produce consequences on the normal proliferation process of the cells.

In the following Section, the comparison between the cytotoxic effect of the NV on HeLa and HaCaT cells are presented. The detrimental targeting of HaCaT cells by the AMT-NV is discussed and it is illustrated how it can be motivated by biological considerations on the drug-receptor affinity.

5.4 Comparative cytotoxicity

In Figure 5.10, the results of the cytotoxicity study performed by treating HeLa and HaCaT cells with AMT are illustrated. The drug was supplied to the cells either in the molecular form or as AMT-NV, at different concentrations. In both cases, the decrease in the cell growth can be related to an effect of the drug molecule. Nanostructuring, indeed, causes negligible effects on the cell proliferation, as demonstrated by the results obtained on cells treated with the folate NV in the same concentration range also shown in Figure 5.4. The trend of the cell viability upon treatment at different drug concentration allows for determining the value of the IC_{50}, *i.e.* the drug concentration necessary to kill the 50% of the cell in the culture, for the two systems. In the case of HeLa cancer cells, the IC_{50} is found to be equal to 14.8 nM for the molecular AMT and 3.18 pM for the AMT-NV. These values differ by four orders of magnitude, demonstrating a strong increase of the toxicity of the drug in the nanostructured form. Considering that there are about 2000 drug molecules per NV, calculating the toxicity per single molecule yields an increase of about a factor 3 in favour of the NV. A consistent result is obtained in the case of HaCaT cells, suggesting that this gain of toxicity depends on the structural characteristics of the NV. In particular, it is possible to hypothesise that it is induced by the convenient orientation of the multiple drug molecules chemically anchored on the NV surface. Indeed, in the functionalisation approach adopted, the binding of folate/antifolates onto the NP involves one of the carboxylic groups on one end of the molecule. The pteroyl domain, active in the molecule/receptor biorecognition [256], is exposed on the NV external surface, ensuring a prompt and efficient interaction of a thousand antifolates per NP with cellular receptors, independently on the orientation of the NP with respect to the cell membrane.

Unfortunately, the comparison between the viability trends of treated HeLa and HaCaT cells reveals that the strong selectivity detected for the folate NV is not completely preserved when moving to antifolates, in line with the prediction based on the SERS screening data. The effect can be explained by considering the different drug-receptor affinity of AMT and FA, and the expression of FA binding proteins in the selected cell lines. It is known, indeed, that FA has the strongest affinity for FR-α, while AMT preferentially targets folate solute carriers as PCFT and RFC [254, 256] (see Section 5.1). Considering that carriers are expressed on both cell lines, the less efficient FR-α targeting by the AMT-NV in favour of the carriers on both HaCaT and HeLa cells might explain the loss in selectivity. Of course, the drug mechanism of action as well as the cell metabolism during the treatment are

important aspects to consider. An insight on these points might suggest a path for differentiating the response of HeLa and HaCaT cells. It is known that the

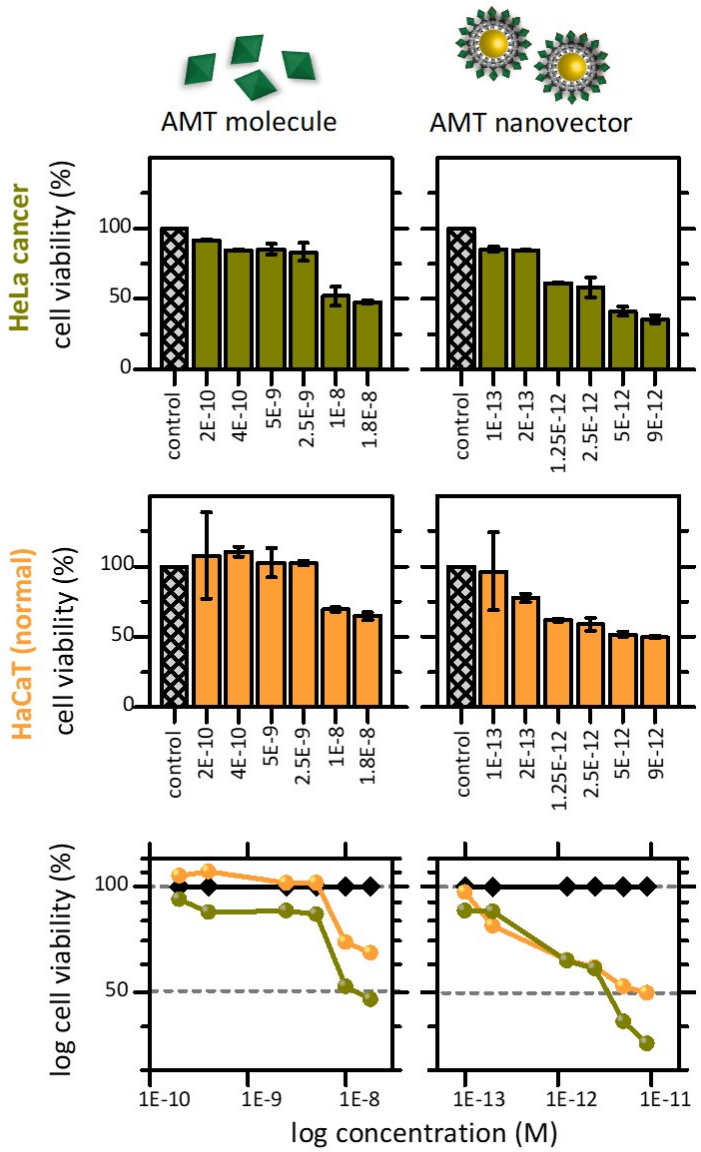

Figure 5.10. Comparison of the viability of cancer HeLa (first row, data in dark yellow) and non-tumourigenic HaCaT (second row, data in orange) cell lines treated with AMT in the free molecular form (left column) or in the nanostructured, NV form (right column). Below the bar plots the concentration of the toxic agent (molecule and NV, respectively) used for the treatment (24 hours) was indicated. All the trends presented are normalised to the control measurement acquired on the corresponding, untreated cell culture (columns in gray, as a reminder). Third row: summary of the results, plotted in log scale. The IC_{50} value, *i.e.* the drug concentration that reduces the cell viability by the 50%, can be extrapolated by data fitting. Dark yellow dots refer to HeLa cells, orange dots to HaCaT cells, the black diamond represents the control population.

cytotoxic action of antifolate molecules is induced by their irreversible binding to folate metabolism enzymes when antifolates are internalised in the cell: this blocks the cell metabolism, eventually leading to cell death. A similar effect from the AMT loaded on the NV surface is expected, but in this case the AMT molecules are closely packed on the NP surface. For this reason, the binding of an enzyme on a single AMT molecule on the NV surface inhibits by steric hindrance the effect of the neighboring AMT molecules. Therefore, part of the AMT active molecules on the NV surface are not employed in the therapeutic action. Based on these considerations, in the direction of restoring the NV selectivity in cell targeting, a coloaded NV by substituting part of the AMT molecules with FA (see Figures 5.11A and B) was synthesised and tested. Ideally, by cooperating in the targeting, FA should bind more efficiently to FR-α, therefore to cancer cells.

5.5 Coloaded folate/antifolate nanovector

The SERS titration results presented above demonstrate the high density of drug molecules on the NV surface. As discussed, from steric hindrance arguments all these molecules are not expected to contribute essentially to the therapeutic action against cancer cells.

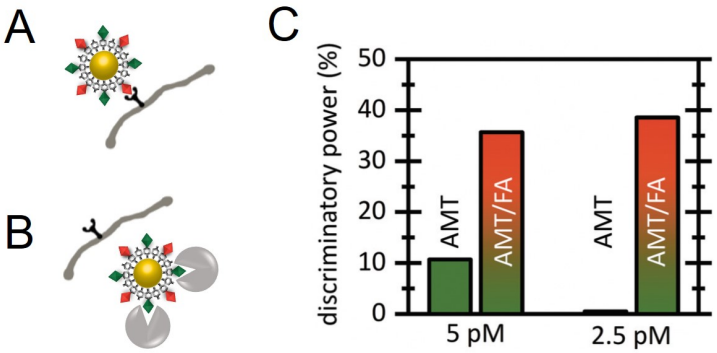

Figure 5.11. Sketch of the mechanism of folate receptor targeting (A) and of the toxic action inside the cell (B). The part of the molecule active in receptor/enzyme biorecognition is conveniently exposed on the NV surface (see Figure 5.4). Substituting part of the AMT on the NV surface with FA does not completely inhibit the toxic action of the system: ideally, in such a designed NV, FA is responsible for the cell targeting, while AMT acts against the cell. (C) Discriminatory power (defined as the difference between HaCaT and HeLa cells viability) when cells are treated with the AMT-NV (green columns) and with the AMT/FA coloaded NV (red/green columns) at different concentrations. Remarkably, the stronger selectivity of the coloaded NV is the result of a basically unperturbed viability of the non-cancer HaCaT cells.

Moving from this consideration, the decrease of the number of AMT molecules on the NV surface by a factor 2 is expected to not dramatically affect the results obtained so far. Moreover, substituting AMT with FA can result in a positive increase in the NV selectivity because of the role of FA in targeting preferentially FR-α, that is strongly overexpressed on many cancer cell types [278]. A coloaded NV by functionalising the 4ATP-NPs with FA and AMT at equal concentrations was

therefore synthesised. SERS titration estimates a number of drug ligands of about 2300 FA/AMT molecules per NP, which is consistent with the results presented in Figure 5.7. The effect of the different targeting method is already visible after six hours of treatment. It should be noticed that the treatment time is in this case well below the typical replication time of HaCaT and HeLa cells. This fact ensures, in turn, that the ordinary replication of the cells is not hindering any effect of the treatment. In Figure 5.11C, the selectivity obtained by treating HaCaT and HeLa cells with the AMT-NV and with the coloaded AMT/FA-NV are compared. An almost unaffected proliferation of HaCaT cells treated with the coloaded NV is revealed, while a decrease in the cell growth is detected on HeLa cancer cells. Given these results, the differentiation factor achieved is promising in view of potential biomedical applications.

Compared to similar drug delivery systems, the advantages of the NV herein presented reside in the simple preparation, performed in a biocompatible aqueous environment, in its structural and colloidal stability, in the possibility of a quantitative assessment of both the drug loading and the cell binding efficiency, and on the identified targeting mechanism, which mimicks the folate supply pathways in the cell. Interestingly, drug nanostructuring brings along an enhanced cytotoxic activity of the SERS-active NV if compared to the drug in the free molecular form. The lower selectivity of the antifolate-NV with respect to the FA counterpart, revealed both by SERS screening and by cell viability assays, is well justifiable by biological considerations. Remarkably, the NV selectivity can be improved with the synthesis of a coloaded nanosystem, conjugated with both folate and antifolate molecules.

Chapter 6

Plasmon enhanced nano-spectroscopy study of gold nanoparticles interaction with protein fibrils

Misfolding and off-pathway aggregation of specific proteins are commonly associated to the occurrence of various pathologies, including Alzheimer's, Parkinson's diseases and type II diabetes [279]. This kind of process, known as fibrillation or amyloidogenesis, consists in the loss of the proteins native folding and in their self-assembly in fibrous insoluble aggregates, called fibrils. Even if the various proteins forming amyloid aggregates can show very different amino acidic sequences, they share a common peculiar structural feature in the fibrillar state. In fact, all fibrils are characterised by a secondary structure rich of β-sheets, which assemble by means of non-covalent interactions [280]. In the last decades, several studies have pointed out that, for most proteins, fibrillation is a multi-steps process, starting with the formation of small protein aggregates called prefibrillar oligomers, whose cooperative association generates amyloid fibrils with typical diameter of several nanometres and length which can reach tens of microns [281].

Unraveling the mechanisms underlying amyloidogenesis and how the interaction with external agents could affect fibrils stability is pivotal for developing novel therapeutic strategies for the prevention and elimination of these highly toxic species. Different agents, such as poliphenols, small aromatic molecules and solvents, have been identified as inhibition factors for amyloidogenesis [282, 283, 284]. In particular, great interest has recently aroused on the interaction of amyloid fibrils with inorganic NPs [285, 286]. In fact, beside their inhibitory role for protein fibrillogenesis [287, 288, 289], it has been reported that NPs could also behave as folding assistants, analogously to molecular chaperones [290]. Despite this, little is known about their interaction with preassembled fibrils and whether NPs could have some effects in reducing the toxicity of amyloid aggregates [291]. The investigation of these aspects represents a landmark for employing NPs in degradating amyloid fibrils to contrast related disorders. In this respect, it is crucial to unveil the specific molecular mechanisms involved in NPs-fibrils interaction. A great opportunity

for obtaining detailed insights at the level of single amino acid is provided by surface enhanced spectroscopies, which allow the characterisation of materials at the nanoscale by exploiting the strong electromagnetic fields confined in spatial regions with dimensions well below the the diffraction limit. The light confinement produces huge increase in the optical cross section of analytes located close (within few nanometres) to the plasmonic surface and, as a consequence, filters out the signal from other regions. Besides the already discussed SERS, further advances in enhanced spectroscopies have been reached with the implementation of Tip Enhanced Raman Spectroscopy (TERS), which combines the molecular specificity and huge signal enhancement of SERS with the nanometric spatial resolution of scanning probe microscopies [20]. The exceptional spatial resolution of this technique led to unique results in mapping protein fibrils with single amino acid resolution [21, 292].

The purpose of the study herein presented is the nanoscale investigation of the interaction between lysozyme fibrils and gold NPs (AuNPs). Lysozyme was chosen as amyloidogenic model protein [293], since it represents an interesting case study from a biomedical point of view: its misfolding and the consequent accumulation of fibrils in various organs is in fact associated to hereditary non-neuropathic systemic amyloidosis. Moreover lysozyme fibrillation has been widely characterised by optical and near-field microscopies as well as traditional spectroscopies [294, 295]. AuNPs are currently broadly employed in nanomedicine thanks to their good biocompatibility and flexible optical properties which make them valuable SERS enhancing substrate also *in vivo* [18].
The analyses were carried out by combining TERS and SERS spectroscopies, as sketched in Figure 6.1. TERS allows for unveiling the aminoacidic composition of fibrils before and after the incubation with AuNPs, while SERS intrinsically selects the signal from the protein region directly interacting with the gold surface. Besides a deep nano-spectroscopic characterisation of the fibrillation process, this strategy provides novel hints on the interaction mechanisms between AuNPs and fibrils, that could have a potential traslational impact for the development of strategies in preventing and treating amyloidogenesis related diseases.

Part of this work was carried out at Friedrich Schiller University of Jena (Germany), under the supervision of Prof. V. Deckert. The research stage lasted six months and was funded by a Ph.D. fellowship from Sapienza University.
In this Chapter, a brief overview of TERS spetroscopy is provided in Section 6.1. Subsequently, the obtained results about the characterisation of lysozyme fibrils before and after the incubation with AuNPs at both morphological and spectroscopic level are presented.

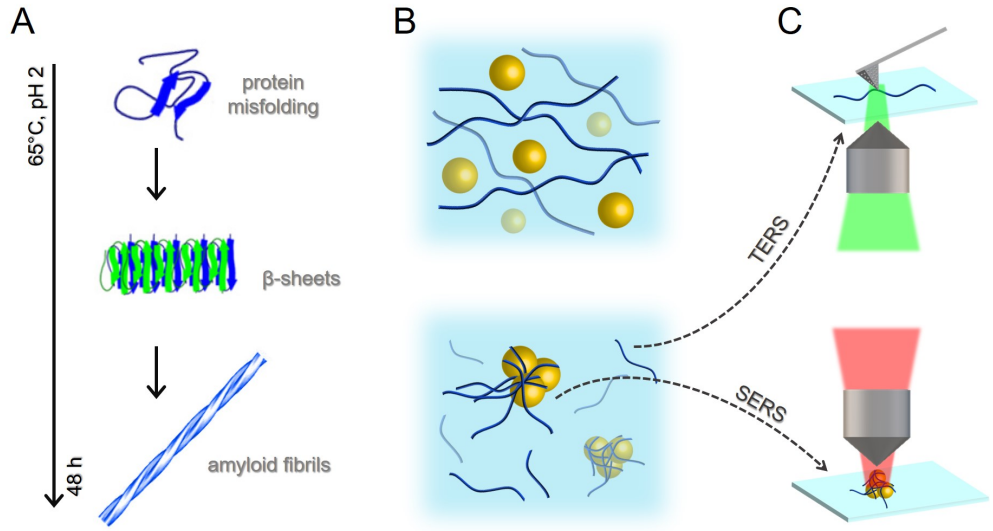

Figure 6.1. Sketch of the different steps of the experiment: lysozyme amyloidogenesis, induced by thermal denaturation in acidic conditions (A); study of the interaction between mature fibrils and AuNPs (B); TERS (top) performed on single lysozyme fibrils and fibrils fragments and SERS (bottom) performed onto AuNPs embedded in fibrils (C).

6.1 Principles of Tip Enhanced Raman Spectroscopy

Despite the high field intensity that allows for detecting even few molecules confined onto metallic nanostructures, the spatial resolution of SERS spectroscopy remains limited by the Abbe diffraction limit, typically of hundred nanometres for visible light. This constraint has been overcame by combining SERS with scanning probe microscopies (SPM), such as Atomic Force Microscopy (AFM) and Scanning Tunneling Microscopy (STM), in the so called Tip Enhanced Raman Spectroscopy (TERS). Even if exploiting different type of interactions with the sample, the common feature of SPMs is the employment of a sharp tip for scanning the sample surface, allowing for reconstructing its topography with nanometric or even sub-nanometric resolution [296, 297, 298]. The first experimental realisation of TERS was developed in 2000 by Stöckle et al. [20], who combined a Raman spectrometer and an AFM setup equipped with a sharp silver tip. Since then, TERS spectroscopy has been successfully employed for obtaining unique information on materials at the nanoscale [299, 300].

As sketched in Figure 6.2, a typical AFM-based TERS setup consists of an excitation laser focused onto the plasmonic-active tip of the AFM setup, with light polarisation directed along the tip axis. The most common optical configuration is the bottom-illumination, where the Raman setup is constituted by an inverted microscope with the objective for illumitation and light collection placed under the sample stage. Typically, oil immersion objectives with high numerical aperture (1.3 - 1.6) are used for maximising the acquisition signal. In this configuration, since the excitation light must go through the substrate, materials transparent to the laser frequency, such as thin glass slides or mica sheets, are required. In the case of

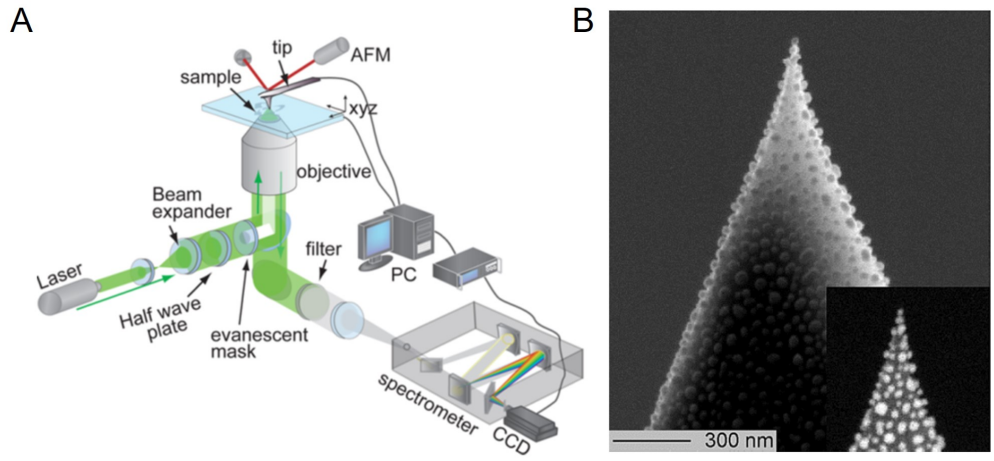

Figure 6.2. (A) Sketch of a typical AFM-based TERS setup which consists of a laser, an inverted microscope with high numerical aperture objective, a spectrometer and a charge-coupled device (CCD) detector. Adapted from ref. [300]. (B) SEM image of a TERS tip where the distribution of silver NPs upon metal evaporation is visible. Adapted from ref. [301].

non-transparent substrates, other optical geometries with sample illumination from the side or from the top have been developed [302].
The AFM head, positioned on top of the microscope stage, reconstructs the surface topography of the sample by monitoring the deflections of an oscillating cantilever while a sharp tip positioned at its edge interacts with the sample. AFM is typically operated in intermittent contact mode, *i.e.* the cantilever oscillates close to its mechanical resonance frequency and periodically touches the sample. The oscillation amplitude is kept small, lower than 10 nm, in order to maintain the tip-sample interaction region within the evanescent field generated by LSPs of the plasmonic tip.

TERS tips are usually prepared by covering commercial silicon or silicon nitride AFM tips by means of in vacuum deposition of gold or silver. Depending on deposition parameters such as evaporation time and temperature, this procedure leads to a continuous film or a layer of small NPs. To avoid contamination or oxidation, tips are stored in protected Argon atmosphere before the use. During TERS experiments, it is essential that the tip is maintained in the laser focus to ensure the signal enhancement. Hence, before measurements, a tip scanning is performed in order to identify the position of the cantilever that provides the highest enhancement for a specific setup alignment. Once identified, the tip position is locked and the TERS experiment is performed by moving the sample stage.

The fundamental mechanisms leading to the TERS signal enhancement are analogues to SERS and originate from *electromagnetic* and *chemical* interactions as explained in Section 1.3.2. Another aspect that contributes to the TERS signal enhancement are atomic scale protrusions of the tip that can increase the spatial resolution allowing for resolving spectral features at the Ångstrom scale [303].
As mentioned so far (Chapter 1), SERS spectra can appear very different with respect

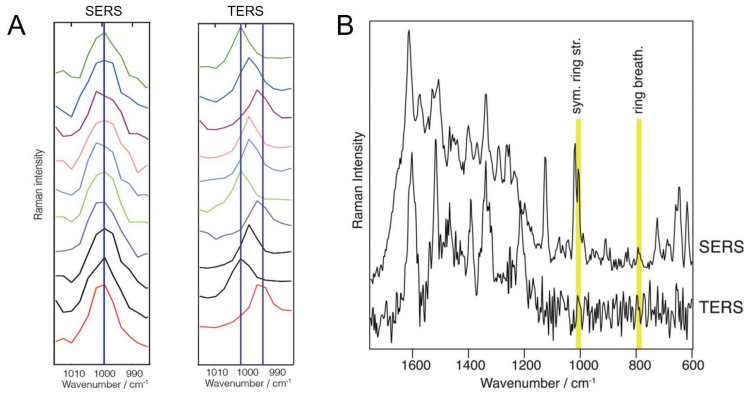

Figure 6.3. Examples of SERS and TERS spectra acquired on the same sample. (A) SERS (left) and TERS (right) spectra acquired at different positions on thiophenol monolayers. Image adapted from ref. [301]. (B) SERS (top) and average TERS (bottom) spectra of phenylalanine. The yellow bars highlight the position of ring modes at 1007 cm^{-1} and 793 cm^{-1}. Image adapted from ref. [299].

to Raman ones due to the interaction of the probed sample with the plasmonic active surface. In the case of TERS these effects are even more pronounced [304]. Indeed, the formation of a water meniscus between the sample and the tip during the scanning can induce the diffusion of some molecules leading to changes in their orientation and polarisability [305]. Moreover, since the sampling volume in TERS is reduced if compared to that of SERS, very few molecules are illuminated and signal averaging effects do not occur. This phenomenon, besides leading to differences in SERS and TERS spectra, has also the effects that TERS spectra acquired on the same sample could show a great variability in the position of some bands. Therefore, as reported in the example of Figure 6.3, the band frequency can vary considerably and some band could entirely disappear.

6.2 Morphological and nanoscale spectroscopic characterisation of lysozyme fibrils

The AFM and TERS analyses reported in this Section are aimed at characterising the different stages of the lysozyme fibrillation process in terms of morphology and surface amino acidic composition of the protein structures.

Lysozyme fibrillation was induced according to the following protocol: lysozyme 30 mg/mL solution was prepared at pH 2 and heated at 65°C under continuous and gentle stirring. The kinetic of fibrillation was followed in time for 48 h by AFM, hence aliquots of the solution were collected at intervals and deposited onto pre-cleaned glass slides. Representative AFM images of the samples are reported in Figure 6.4. In panel A it is possible to recognise the first stage of the fibrillation process occurring during the first 2.5 h and consisting in the formation of globular protein aggregates. The average size of 24 nm of such prefibrillar oligomers, extrapolated by height profiles of the AFM frame as shown in the inset, is consistent with the lysozyme fibrillation pathway [306], which proceeds by a hierarchical assembly of

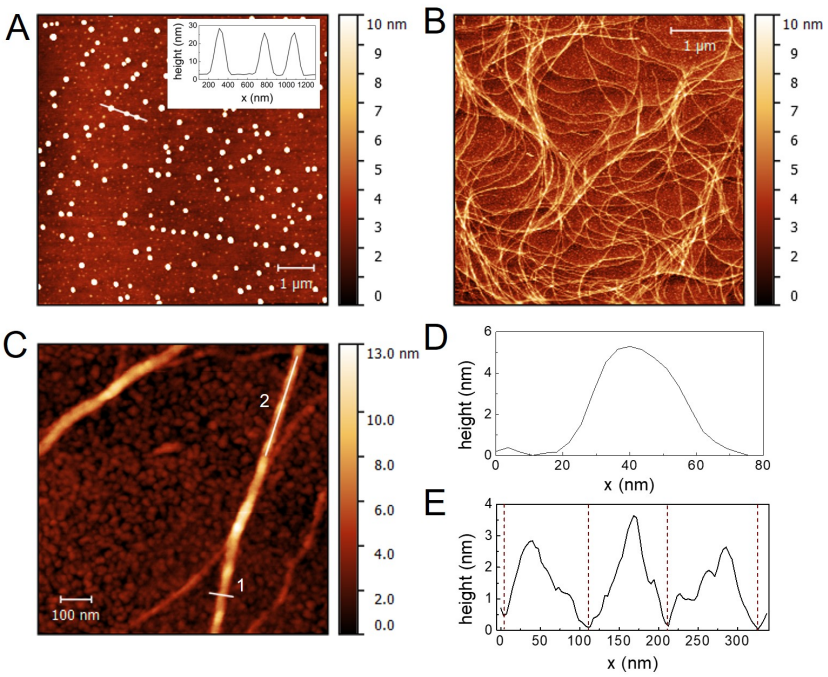

Figure 6.4. AFM study of the fibrillation kinetics of lysozyme: prefibrillar protein aggregates after 2.5h of thermal treatment. The height profile corresponding to the section depicted in the image is reported in the inset (A); mature fibrils formed after 48 h (B). Zoom image where it is possible to distinguish isolated fibrils and intertwined structures (C). The sections 1 and 2 correspond to the height profiles reported in panel (D) and (E), respectively. The vertical dashed lines indicate the minimum of the profiles employed to calculate the fibrils periodicity.

protein oligomers. Mature fibrils start to appear after 48 h of thermal treatment (panel B). Concurrently, the lysozyme solution starts to form a soft transparent gel. The fibrils show an elongated structure extended for tens of microns. In the zoom of panel C it is possible to distinguish single thin protofilaments and fibrils assembled in intertwined structures. As showed in the representative profile of panel D, the fibrils have a height of $\sim$ 5 nm and a width of $\sim$ 30 nm. An estimate of the periodicity of the coils can be obtained by analysing the height profiles extrapolated along the fibril axis. The representative example reported in panel E shows a periodicity of 105.2 $\pm$ 3.5 nm. According to literature [307], and consistently with previous studies on hen egg white lysozyme [308], such periodicity is characteristic of structures composed by 4 protofilaments twisted together.

For TERS measurements, fibrils were diluted 100 times in the pH 2 solution before deposition to obtain samples with low surface density, allowing for nano-spectroscopic measurements on single fibrils. TERS spectra were acquired by employing an AFM silicon tip covered by silver NPs (see Appendix for experimental details). Representative TERS spectra are reported in Figure 6.5, together with an AFM image showing the spatial region of the acquisition. The tentative assignment of the main TERS bands based on previous TERS studies on protein and protein fibrils is reported in Table 6.1. Traditional Raman spectra are also taken as guideline

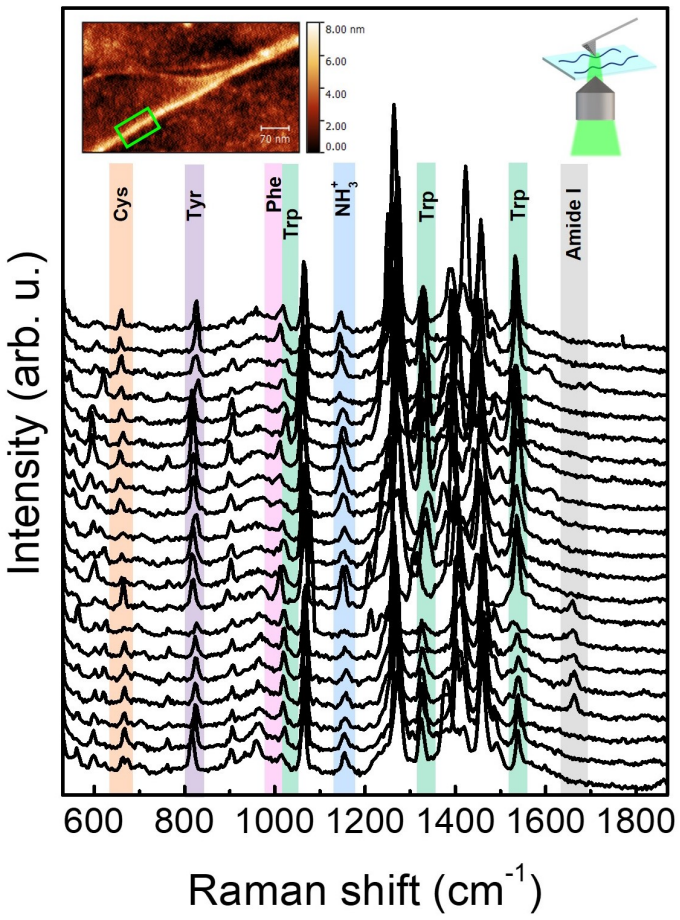

Figure 6.5. TERS spectra acquired along a single lysozyme fibril with 2 nm step size. Bands corresponding to the main amino acids vibrational modes are highlighted. The AFM topography of the single lysozyme fibril scanned during the TERS experiment is reported in the inset; the green box indicates the acquisition area.

for TERS modes assignment, accounting for possible band intensity redistributions expected for TERS spectroscopy [304, 292]. The occurrence of specific amino acids was calculated by the ratio between the number of their specific spectral markers identified in the spectra and the total number of the analysed spectra. The obtained values of the occurrence in the case of mature lysozyme fibrils are reported in the histogram of Figure 6.6 for the amino acids and chemical groups of interest.

With reference to the TERS spectra of Figure 6.5, various sharp bands, related to the aromatic side chains of some amino acids, are identifiable, analogously to traditional Raman spectra of peptides and proteins. The amino acidic sequence of lysozyme [309] includes 129 amino acids, 12 of which have aromatic side chains: 3 phenylalanine (Phe), 3 tyrosine (Tyr) and 6 tryptophan (Trp). Usually, for amino acid with one aromatic ring as Phe and Tyr, the ring breathing mode is used as marker band [310]. In the case of Trp, more bands relative to the indole vibration can be found in the spectra [311]. In these TERS spectra, the marker band associated to the Tyr ring breathing mode can be clearly recognised at 825-855 cm^{-1}. Concerning

Table 6.1. Peak assignment of the main TERS bands, according to ref. [310, 21, 315, 316, 284]. Greek letters indicate the vibrational modes: ν, stretching; δ, bending; ω, wagging.

Peak assignment	TERS frequency (cm^{-1})
ν(S-S) Cys	510-550
ν(C-S) Cys	650-680
indole ring breathing Trp	740-770
ring breathing Tyr	825-855
ring breathing Phe	997-1014
indole ring breathing Trp	1004-1010
NH_2	1050-1080
NH_3^+	1144-1180
amide III	1220-1260
ν(C-C) indole ring Trp	1332-1335
δ(CH), $\omega(CH_2)$	1372-1377
$\delta(CH_3)$	1475
ν(C=C) indole ring Trp	1533-1552
amide I	1630-1680
COOH	1700

Phe, the marker peak associated to the ring breathing at 997-1014 cm^{-1} may overlap the Trp indole ring breathing mode at 1004-1010 cm^{-1}. Further marker bands related to the Trp are the lower frequency indole breathing at 740-770 cm^{-1} and the indole stretching vibrations at 1332-1335 cm^{-1} and 1533-1552 $^{-1}$.
Several bands attributable to cysteine (Cys) can be recognised in the low frequency region, below 680 cm^{-1}, yielding an estimate of 74% occurrence on the fibrils surface (Figure 6.6). The exact position of these bands could result shifted in the different spectra due to the presence of different conformers [21]. In particular, bands in the 510-550 cm^{-1} range are related to the presence of disulfide bridges [312]. By considering only the spectral markers corresponding to disulphide bridges, the occurrence of S-S bonds over the total number of spectra was 29.6%. The obtained value corresponds to the 40% of the total cysteine content, pointing out that a consistent number of Cys is involved in the formation of S-S bonds. In the folded state, lysozyme proteins show 8 Cys forming 4 disulfide bridges, which help the native protein to maintain a robust globular folding. Even though the partial denaturation of the protein is considered a precondition for the onset of the fibrillation process, it is still a matter of debate whether the rupture of all disulfide bridges represents a necessary condition in this respect [313]. The TERS analysis suggests that at least a fraction of the disulfide bridges is preserved without hindering the amyloidogenesis of lysozyme. Similarly, the occurrence of disulfide bridges has been observed by TERS on the surface of insuline fibrils [314].

A further worth noting aspect concerns the electrostatic surface properties of the fibrils, which are mainly determined by amino acids with charged residues, namely amines and carboxylic groups. Lysozyme is amongst the proteins that have the highest value of the isoelectric point, occurring at pH 11.3, therefore it shows a

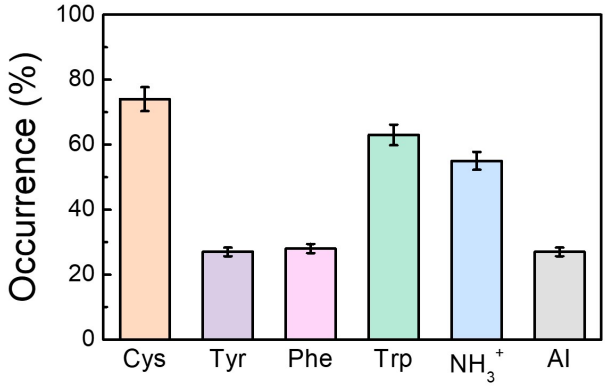

Figure 6.6. Occurrence of specific amino acids and chemical groups along the fibril surface.

markedly positive net charge at pH 2, due the protonation of the majority of the amines. A relevant amount of protonated amine groups $NH_3{}^+$, identified in the spectra by their rocking vibrational mode (1144-1180 cm^{-1}) [310], can be found along the fibril surface. These residues are present in amino acids containing primary amines in the side chain such as arginine (Arg), lysine (Lys), asparagine (Asn) and glutamine (Gln), actually present in the primary structure of lysozyme. Asn and Gln can be identified from the amino group vibration modes at 1060 cm^{-1} and 1135 cm^{-1}, but due to their structural similarity these amino acids are not discernible in the spectra. Instead, Arg e Lys residues can be identified by a combined two peak assignment, as proposed in previous works [21]. Specifically, the concomitant appearance of bands at 1070 cm^{-1} and 1150 cm^{-1} is attributed to Lys, while that of bands at 1090 cm^{-1} and 1170 cm^{-1} is attributed to Arg. The simultaneous presence of the two peaks, which allows the aforementioned assignment, occurs only in a portion of the analysed spectra, resulting in 27% and 68% occurrence of Arg and Lys, respectively. With regard to carboxyl groups, present in the side chains of aspartic (Asp) and glutamic (Glu) acids, which contribute with a negative charge on the fibril surface [314], spectral markers at 1700 cm^{-1} are found only in the 15% of the spectra.

Although the majority of the hydrophobic amino acids is expected to be buried into the fibrils core, the surface of the fibrils can be characterised by hydrophobic domains [21]. The hydrophobic features are mainly determined by amino acids with aliphatic side chains, namely those containing CH_n chemical groups. In the CH_n mode spectral regions (1355 cm^{-1}, 1372-1377 cm^{-1}, 1457-1475 cm^{-1}) a combination of bands attributable to alanine, valine, leucine and isoleucine is present. Nevertheless, their spectral similarities does non allows for unambiguous assignment.

The spectral bands providing information on the secondary structure of the fibrils are the amide I (AI, 1630–1680 cm^{-1}) and and Amide III (AIII, 1220-1260 cm^{-1}) [314]. As can be easily seen, these bands are not always present in the spectra, hampering a direct determination of the secondary structure. The reasons behind this instability, frequently observed in enhanced Raman spectroscopies, are still under discussion [183].

Depending on parameters such as propension in forming β-sheets, degree of hydrophobicity and net charge, it is possible to predict the sequences of amino acid,

called amyloidogenic regions, that act as nucleation centres and trigger the fibrils formation [317]. Therefore, it is reasonable to assume that, due to their active role in the protein assembly, these amino acidic motifs are exposed on the fibrils surface. In this case, Trp and Cys are found to be the amino acids that are more frequently present on the lysozyme fibrils surface. Interestingly, these amino acids are mostly located in the four region of the protein that have been identified as amyloidogenic regions [318].

6.3 Analysis of fibril-gold nanoparticles interaction

The interaction between lysozyme fibrils and AuNPs was primarily investigated through UV-Visible absorption spectroscopy and AFM. The study was further corroborated at the molecular level by a combined TERS and SERS analysis. With the purpose of studying the interaction at the level of single fibrils, the fibrillar gel was added to a solution of 60 nm anionic citrate-capped AuNPs, obtaining a final dilution of 1000 times.

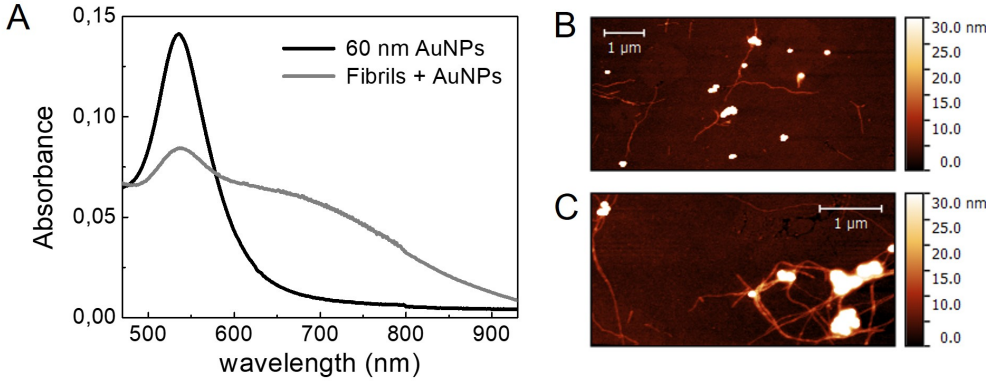

Figure 6.7. (A) UV-Visible absorption spectra of a solution with AuNPs and lysozyme fibrils (grey) and of a solution of 60 nm AuNPs (black). Representative AFM images of the lysozyme fibrils in interaction with AuNPs where it is possible to distinguish the fibrils fragmentation (B) and the AuNP aggregation within fibrils network (C).

The absorption spectrum of the sample solution is reported in Figure 6.7 A. By comparing it to the spectrum of the AuNPs stock solution (reported in the same Figure), a marked decrease of the single AuNPs absorption peak at ∼530 nm occurs, accompanied by the onset of a broad shoulder at higher wavelengths. These spectral modifications point out the aggregation of the AuNPs upon interaction with the lysozyme fibrils. To elucidate possible effects on the fibrils morphology, the AuNP-fibrils solution was deposited onto a glass slide and scanned by AFM. Representative images of the sample topography are reported in Figures 6.7B and C. Noteworthy, fibrils do not appear as long as those reported in Figure 6.4, rather appearing broken in fragments shorter than 1 μm, while clusters of AuNPs are embedded in networks of fragments. Moreover, the AFM images point out also a disassembling of the amyloid fibrils since only few of them are still assembled in intertwined structures as reported in Figure 6.4. Therefore, AFM images clearly

unveil that the interaction with AuNPs entails the disassembling and breaking of the lysozyme fibrils. Similar effects have been observed in the case of insulin, whose fibrils incubated with AuNPs prompted the formation of agglomerates where the AuNPs behaved as aggregation centres for the fibrils [289]. This finding is worth of further investigations since it could point out a new role of AuNPs as fibrillogenesis inhibitors.

The mechanisms underlying the interaction of fibrils with AuNPs and the effects of fibril rupture were studied at molecular level by comparing TERS and SERS spectra of samples. While TERS allows for investigating the amino acidic surface composition of fibril fragments away from the AuNP-fibrils agglomerates, SERS intrinsically selects the spectroscopic signal of residues in the very proximity of AuNPs clusters, thus identifying the residues involved in the interaction with AuNPs. For these reasons the TERS and SERS combined analysis allows for a complete, in-depth characterisation of the fibril rupture process.

TERS spectra are reported in Figure 6.8A together with a representative AFM magnification of a fibril fragment. As compared to fibrils spectra of Figure 6.5, slightly fewer spectral features can be identified and the signal is affected by higher noise. This can be probably attributed to the structural destabilisation induced by the interaction with AuNPs. The occurrence percentage of selected amino acids and chemical groups is reported in panel B together with that obtained for intact fibers (Figure 6.5C). The histogram highlights a marked reduction of the number of Cys after fibril rupture, with an occurrence reduced to 43%. Notably, also the number of S-S bonds is drastically reduced in broken fibrils, resulting more than halved. A slight reduction is also observed in the amount of Tyr and Phe, while the number of Trp remains substantially unmodified. The fibrils disassembling could lead to changes in the orientation of some amino acids with respect to the fibril axis, thus resulting in a decrease of the signal intensity, as observed in the case of Tyr and Phe. Concerning the number of amino groups, this results to be unaffected by the morphological changes of the fibrils, pointing out that the fibrils fragments preserve the positive surface charge.

Representative SERS spectra are reported in Figure 6.8C, in comparison with the Raman spectrum of lysozyme fibrils. The most significant peaks of the Raman spectrum are highlighted and assigned in the image. The full spectral assignment is reported in previous works [284]. The peaks corresponding to the two aromatic amino acids (Trp at 753 cm^{-1} and Phe at 1004 cm^{-1}) are prominent also in SERS spectra, while amide I band at 1650 cm^{-1} almost completely vanishes. The intense peaks appearing in the SERS spectra at around 1600 cm^{-1} can be attributed to the citrate capping of the AuNPs [319]. Notably, also in TERS spectra acquired on fibrils fragments some peaks appear in the spectral region around 1600 cm^{-1}, which are instead lacking in the TERS spectra of intact fibers (Figure 6.5). These spectral features suggest the presence of citrate anions. Their possible interaction with positively charged residues could affect the stability of the β-sheet network linking the fibrils and eventually result in fibril dissociation [320].

It is worth to be stressed here that TERS and SERS spectra can be quite different because TERS spectroscopy probes an extremely small number of molecules, therefore the averaging effect does not occur, differently from SERS and more markedly from traditional Raman spectroscopy, where instead an ensamble of molecules is probed

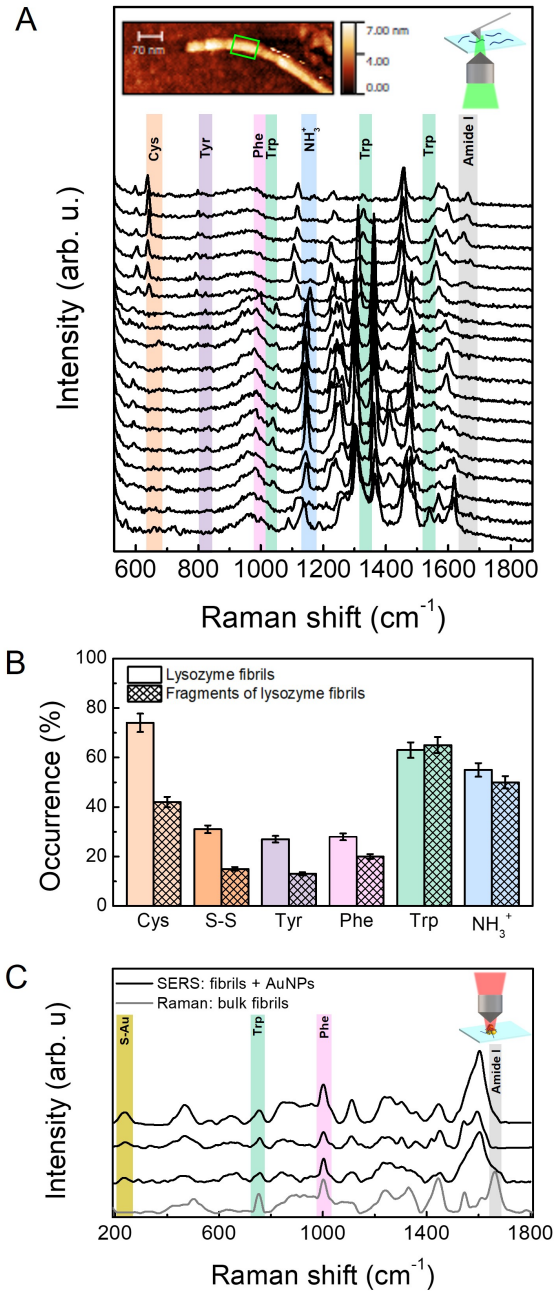

Figure 6.8. (A) Representative TERS spectra acquired along fragments of lysozyme fibril with 2 nm step size. Band related to the main vibrational modes are highlighted. In the inset, representative AFM topography of a single fragment of lysozyme fibril with the acquisition area indicated by the green box is reported. (B) Occurrence of specific amino acids and chemical groups along the surface of intact fibrils and fragments. (C) Representative SERS spectra of aggregates of AuNPs and fragments of lysozyme fibrils (black) in comparison with the Raman spectrum of the lysozyme fibrils (grey).

[305]. For this reason TERS spectra are affected by relatively large fluctuations in the band positions as mentioned in Section 6.1.
The most relevant result of the SERS spectra is represented by the appearence of a broad peak at ~ 230 cm^{-1}, corresponding to the S-Au stretching vibration [160, 17]. This finding points out the formation of a chemical bond between the sulfur of Cys and the surface of the AuNPs. The comparative analysis of the TERS and SERS results points out that the regions of the fibrils rich in Cys residues are more prone to interact with the gold surface. On the basis of the obtained results, an explanation of the how AuNPs can induce the fibril rupture can be hypotesised in terms of two types of interaction. At first, long range electrostatic attraction induces the accumulation of AuNPs clusters onto the lysozyme fibrils. As discussed above, fibrils show a positive surface charge due to the high amount of residues containing protonated amino groups, thus attracting anionic AuNPs. Once in contact, the high affinity of the sulfur of Cys for the gold surface induces the rupture of the S-S bonds in favor of the formation of S-Au bonds with the AuNPs surface. The breaking of the S-S bonds destabilises the structure of lysozyme fibrils, resulting in their rupture and fragmentation.

In this study, the nano-spectroscopic characterisation of lysozyme fibrils was performed for the first time, providing information on the surface organisation of amino acids on the fibrils surface. Moreover, novel insights on the interaction between amyloid structures and AuNPs have been pointed out. The combined study at morphological level by AFM and at molecular level by near-field enahnced spectroscopies allowed for highlighting the role of AuNPs in disassembling and breaking the fibrillar structures. The obtained results suggest that AuNPs could be a promising candidate for the development of novel therapeutic and diagnostic strategies for amyloid related diseases.

Conclusions

Plasmonic NPs represent versatile building blocks for the realisation of multi-component plasmonic systems with outstanding properties. The opportunity of confining strong electromagnetic fields with a precision of few nanometres, together with their easy synthesis and functionalisation, has made metallic NPs the most employed substrate for surface enhanced spectroscopies allowing for achieving impressive results in molecular detection. The possibility of tailoring their optical response through NPs size, shape and spatial organisation, as well as by the dielectric properties of the surrounding medium offers a broad palette of features to choose from, depending on the desired application.

In this Ph.D. Thesis, gold NPs have been employed for developing plasmonic nanostructures with highly tunable properties for applications in biophysics and molecular sensing. The NPs were interfaced with molecules and macromolecules with specific features chosen for controlling the plasmon coupling and the interaction with the external environment. Great efforts have been made in combining the applicative purposes with fundamental studies, and in optimising the sensitivity and reproducibility of the adopted experimental strategies. The main original results obtained, together with the related future perspectives are herein summarised.

The aggregation of gold NPs triggered by lysozyme was exploited for realising a bioplasmonic system with a high degree of tunability in the structure, optical response and antibacterial activity. The detailed analysis and rationalisation of the aggregation process in the light of the theory of the *charge patch* interactions allowed for gaining a close control on the formation of aggregates, yielding a dispersion of stable clusters with selectable size. The spectroscopic study of the absorption profiles assessed the strict correspondence between the clusters morphology and their plasmonic response, pointing out the possibility of choosing the LSPR of the system within a large range of frequencies spanning from visible to near-infrared. Moreover, the assembly process and in turn the plasmonics of the system can be reversibly modulated by acting on the pH of the dispersing solution. Quantitative information about the adsorption of the protein onto the gold NPs surface were inferred by exploiting the sensitivity of the LSPR to the dielectric environment, providing a simple analytical model that can be employed to predict amounts of protein down to pM concentrations. The biological functionality of the system was investigated by testing the catalytic activity of the complexes on a bacterial suspension. Interestingly, a modulation of the enzymatic activity depending on the surface charge and on the size of the aggregates was observed, highlighting an enhancement of the performances for clusters of the proper size.

The conjugation of gold NPs with a pH-sensitive molecular probe allowed for the realisation of an accurate SERS-active pH nanosensor. Special focus has been paid to the reproducibility of the SERS response by optimising the assembly process and the operating conditions. The calibration of the nanosensor was performed in terms of the intensities of selected pH-dependent SERS bands, identifying the dynamic range of sensitivity centered in the pH range between 5 and 7. The detailed analysis of the whole SERS fingerprint allowed for identifying different spectroscopic markers which remarkably strengthened the reliability of the local pH measurements. The possibility of assembling pH nanosensor with adjustable working point in the sensitivity region of interest has emerged by the careful analysis of the acidic properties of the molecular probe. The whole experimental effort allowed for the development of a measuring procedure successfully employed in detecting the extracellular pH of normal and cancer cells. These experiments indeed demonstrated the capability of the nanosensor to discriminate between the two cell types. The overall obtained results pave the way for realising efficient SERS-active microplate substrates suitable for biomedical applications, offering the possibility of performing localised pH measurements at subcellular level.

SEIRA-active gold nanoprobes were employed as biorecognition tool following their ultrasound mediated internalisation within fibroblast cells. The coupling between synchrotron radiation microFTIR spectroscopy and the considerable signal enhancement supplied by the SEIRA effect enabled for recognising the spectral fingerprint of the nanoprobe at the single cell level, providing convincing evidence of a successful internalisation. The analysis of the high-quality spectra, supported by biological assays, allowed for singling out the biological effects of the combined nanoprobe-ultrasound treatments, pointing out the activation of apoptotic events. The obtained results provide deep insights of theranostics relevance in developing novel strategies which combine ultrasound mediated NPs delivery and optical detection.

The synthesis of SERS-active nanovectors based on the conjugation of gold NPs with antifolate molecules, showing remarkable theranostic potentialities in providing a strong therapeutic action against the HeLa human tumourigenic cells was presented. The opportunity of employing SERS as a fast technique for spectroscopic titration was assessed by estimating the drug conjugation through the spectral weight redistribution observed in the nanovector spectra. By taking advantage of the high conjugation efficiency of aminopterin, a comparative SERS screening and cytotoxicity study was performed onto aminopterin conjugated nanovectors, comparing the effects on tumourigenic HeLa cell line with the non-tumourigenic HaCaT cell line.

Single cell SERS screening on treated cells allowed for comparatively monitoring the nanovector binding efficiency on the two cell lines by measuring the nanovector SERS signal intensity. Screening data allowed for retrieving a preferential targeting to HeLa cells. Moreover, a promising enhancement of the aminopterin cytotoxicity was recorded when it is supplied to cells in the nanostructured form. The optimisation of the nanovector selectivity in favour of cancer cell targeting was proposed through the coloading of folate and antifolate molecules on the same NP. A deeper insight into the drug metabolism and into the induced cell-death process would possibly allow for further optimising the coloaded nanovector design and the treatment protocol,

in view of biomedical applications.

The nano-spectroscopic characterisation of amyloyd fibrils was performed by exploiting the peculiar high spatial resolution of TERS. The surface composition of the fibrils was determined with a precision of few nanometres allowing for identifying the most exposed amino acids. The interaction of the fibrils with gold NPs was analysed by combining TERS, atomic force microscopy and SERS with the aim of identifying potential mechanisms of elimination of such pathological species. The study enlightened the disassembling and breaking the fibrillar structures upon interaction with NPs. TERS and SERS analyses revealed a decrease in the number of sulfur containing amino acids on the fibrils surface, along with the formation of sulfur-gold covalent bond with the NP surface. The obtained results represent a starting point for the study of gold NPs as potential candidates for developing novel therapeutic and diagnostic strategies in amyloidogenesis related diseases.

Appendix A

Experimental details

In this Appendix, the experimental details and the employed instrumental setups are described. Absorption spectroscopy, dynamic light scattering and near field microscopies, basic techniques for the characterisation of colloidal systems and employed for most of the samples, are reported at first. Afterwards, the instrumental setup for Raman spectroscopy, also used for all the Raman and SERS measurements herein reported, is described. The details of other experimental apparatuses and protocols are reported separately, divided according to Chapters.

Materials All the gold nanoparticles employed in the experiments were provided by Ted Pella Inc. Sodium citrate buffers at pH 6.5 and pH 4.0 were provided by Merk Millipore. Unless otherwise indicated, all materials and chemicals involved in sample preparation were purchased from Sigma-Aldrich and used without further purification.

UV-Visible absorption spectroscopy Absorption spectroscopy is employed for monitoring the absorption peak corresponding to the LSPR of metallic NPs. Being the LSPR very sensitive to the NPs dielectric environment, indirect information on the NP coverage and functionalisation can be inferred from the observed wavelength shift. Measurements were performed employing a v-570 double ray spectrophotometer (Jasco), with a resolution of 0.1 nm in the UV-Vis region and 0.5 nm in the NIR region. The spectrophotometer is equipped with a ETC-505T Peltier thermostat (Jasco).

Dynamic Light Scattering and ζ-potential The size of sigle NPs and aggregates was measured by employing a Malvern NanoZetaSizer apparatus equipped with a 5 mW HeNe laser (Malvern Instruments Ltd, UK). This system uses quasi-backscatter detection, i.e. the scattered light is collected at an angle of 173°. In order to obtain the size distributions, the measured autocorrelation functions were analysed by using the CONTIN algorithm. Decay times are used to determine the distribution of the diffusion coefficients D of the particles, which in turn are converted to a distribution of apparent hydrodynamic radii R_H using the Stokes Einstein relationship $R_H = K_B T/6\pi\eta D$, where $K_B T$ is the thermal energy and η the

solvent viscosity. The reported values are the average of at least three measurements and are obtained by intensity weighted distributions.

The electrophoretic mobility of the suspended particles was measured by means of the same NanoZetaSizer apparatus employed for the DLS measurements. The instrument is integrated with a laser Doppler electrophoresis technique, and the particle size and electrophoretic mobility are measured almost simultaneously in the same cuvette. The measurements were performed employing a palladium electrode dip cell ZEN 1002 (Malvern, UK). The runs were set up in triplicate, each consisting of at least 30 sub-runs. Electrophoretic mobility is determined using the Phase Analysis Light Scattering (PALS) technique. The measured values were converted into the ζ-potential using the Helmholtz Smoluchowski relation

$$\zeta = \frac{\mu_e \, \eta}{\epsilon} \tag{A.1}$$

where η is the solvent permittivity.

Atomic Force Microscopy and Scanning Electron Microscopy Samples for near-field microscopy imaging were prepared at room temperature by a drop casting procedure or by incubating 50 μl of sample solution onto a silicon substrate previously derivatised with (3-Aminopropyl)triethoxysilane (APTES). The APTES-functionalised silicon substrates were obtained by incubating a silicon wafer with 3% APTES ethanol solution for 3 hours. The droplet of sample solution was incubated for 15 minutes and subsequently removed by gently rinsing the substrate with MilliQ water. The samples were finally dried under a gentle nitrogen flow.

Atomic Force Microscopy (AFM) images were recorded using a Dimension Icon Bruker microscope in tapping mode, with a scan rate of 0.5 Hz. A cantilever with a spring constant of 42 N/m and a tip with a nominal radius of curvature of 2 nm was employed. AFM images were analysed by Gwyddion software, version 2.52.

Scanning Electron Microscopy (SEM) images were recorded using a Zeiss Auriga 405 Field Emission Scanning Electron Microscope at Sapienza Nanoscience & Nanotechnology Laboratories (SNN-Lab) of the Research Center on Nanotechnology Applied to Engineering of Sapienza University (CNIS).

Raman and SERS spectroscopy Raman and SERS measurements were performed by employing a Horiba HR-Evolution microspectrometer in backscattering geometry, equipped with a He-Ne laser, $\lambda = 632.8$ nm and 30 mW output power ($\sim$ 15 mW at the sample surface). Using proper optical filters, it is possible to reduce laser power to avoid laser heating and sample degradation. The elastically scattered light is removed by a state-of-the-art optical filtering device based on three Bragg Grate notch filters which also allows to collect Raman spectra at very low frequencies (down to 10 cm^{-1} from the laser line). The detector was a Peltier-cooled charge-coupled device (CCD). A 600 lines/mm diffraction grating ensures a spectral resolution of 3 cm^{-1}. The spectrometer is equipped with an automatic mapping stage with sub-micrometric precision ($\sim$0.3 μm). The spectrometer was coupled with a confocal microscope supplied with a set of interchangeable objectives with long working distances and different magnifications.

Small angle X-ray Scattering Small Angle X-ray Scattering (SAXS) measurements were performed at the SWING beamline of Synchrotron SOLEIL (Saint Aubin, France). The sample-to-detector distance was 6.5 m. Scattering patterns were recorded with a two-dimensional EigerX 4-M detector (Dectris, Baden, Switzerland) at 12 keV, allowing measurements in the q-range from 0.002 to 0.18 $Å^{-1}$. The q-vector is defined as $q = (4\pi/\lambda) \sin \theta$, where 2θ is the scattering angle. The investigated samples were filled in capillaries with a diameter of 1.5 mm and exposure time of 1 s was used for acquisitions. Scattering patterns of an empty capillary and of a capillary filled with MilliQ water were recorded for intensity background subtraction. Data processing of the recorded 2D images was performed by the FOXTROT software.

The scattered intensity $I(q)$ from a collection of particles can be expressed in terms of the particle form factor $P(q)$ and of the system structure factor $S(q)$, according to the equation:

$$I(q) = nv^2 \Delta\rho^2 P(q) S(q) \tag{A.2}$$

where $\Delta\rho$ is the contrast in electron density between sample and solvent, n is the scattering particle concentration and v the volume of scattering particles. The form factor $P(q)$ describes the ensemble averaged shape of scattering objects in solution whereas the structure factor $S(q)$ accounts for the interference introduced by interparticle correlations.

Chapter 4

Cell culture The cell lines employed in the experiments were obtained from Interlab Cell Line Collection (Istituto Nazionale per la Ricerca sul Cancro, Genoa, Italy) and kindly provided by the Molecular Medicine Department of Sapienza University of Rome. Non-tumorigenic human keratinocyte (HaCaT) and tumorigenic human skin melanoma (SK-Mel5) cell lines were grown, respectively, in Dulbecco's Modified Eagle Medium (DMEM; Euroclone, Life Science Division, GB, Pero, Italy) and Minimum Essential Medium (MEM; Euroclone). All media were supplemented with 1% penicillin/streptomycin, 10% fetal bovine serum and 2mM L-Glutamine (Euroclone). MEM was also supplemented with 1% non-essential amino acids and 1% Na pyruvate. Before experiments cells were plated onto a glass coverslip deposited in a cell culture Petri dish and then incubated at $37°C$ under 5% CO_2.

Chapter 5

microFTIR spectroscopy The infrared spectra were acquired using a JASCO Irtron IRT-30 Fourier Transform infrared (FTIR) microscope, equipped with a nitrogen cooled MCT detector and a Cassegrain objective 16×. The spectra were acquired with a resolution of 4 cm^{-1}. The microscope is coupled with a FTIR/410 Jasco spectrometer equipped with a conductive ceramic coil mounted in a water-cooled copper jacket source and a KBr beamsplitter. The optical path was purged continuously with gaseous nitrogen. For the microFTIR measurements, the samples were dried onto CaF_2 substrates.

Synchrotron Radiation microFTIR spectroscopy Synchrotron Radiation (SR) microFTIR measurements were performed at Diamond Light Source Synchrotron (Oxfordshire, UK) at the MIRIAM beamline B2246. A Bruker Vertex 80 V in vacuum FTIR with 4 cm^{-1} resolution was employed. Each spectrum was acquired accumulating 256 scans. A Hyperion 3000 microscope was used for microFTIR in the 700-4000 cm^{-1} spectral range by means of a 36× Cassegrain objective and condenser optics for transmission mode.

Cytotoxic test: Annexin V-propidium iodide apoptosis assay Annexin V-Propidium Iodide assay was used for analysing cell death according to the following protocol. After the treatments, cells were dispersed in Dulbecco's PBS and transferred in Falcon tubes for centrifugation. The pellet was then suspended in 1 mL buffer solution at pH = 7.4 (named binding buffer: 10 mM of Hepes - NaOH, 140 mM of NaCl, 2.5 mM of $CaCl_2$) filtered by sterile pore filter with cut-off of 0.2 μm, taking care of maintaining a cell number density of about $2 \div 5 \times 10^5$ cells/mL to ensure their detection by flow cytometry. A cell suspension volume of 195 μL was mixed with 5 μL of FITC-labeled Annexin V in buffer solution at pH 7.4 (50 mM TRIS, 100 mM NaCl, 1% BSA, 0.02% Sodium Azide) followed by 10 minutes incubation at room temperature in the dark. Immediately after incubation, the solution was dispersed in Hepes (final volume of 2 mL) and centrifuged. The cell pellets were re-dispersed in 400 μL of the binding buffer and just before flow cytometry reading, 10 μL of Propidium Iodide (PI) stock solution (100 μg/mL in PBS) was added.
Flow cytometry analysis was performed by flow cytometer FACSCalibur (BD Biosciences, Singapore) endowed of Argon ion and visible red diode lasers at 488 nm and 635 nm wavelengths, respectively. Fluorescence emission was detected at 530 ± 15 nm (AnnexinV) and 585 ± 21 nm (PI), respectively; for each sample 10000 events were acquired. The results were analysed by CellQuest software (Becton Dickinson) and reported as percentage of positive cells.

Genotoxic test: Cytokinesis-block micronucleus assay The genomic instability at chromosomal level was evaluated by Cytokinesis Block MicroNucleus (CBMN) assay. The cells (8 replicas per treatment) were added with 6 μg/mL Cytochalasin B (Sigma-Aldrich) immediately after treatment and grown for 24 hours to accumulate bi-nucleated cells. Afterwards the cells were centrifuged and suspended in a preheated hypotonic solution of 75 mM KCl and fixed using Carnoy's solution (acetic acid:chloroform:methanol,1:3:6 v/v/v). The fixed cells were dropped onto precleaned microscope slides and stained by adding 10 mg/mL of 4',6'-diamidino-2-phenylindole (DAPI, Sigma, St. Louis, MO, USA) in antifade solution (Vector Laboratories, Burlingame, CA, USA). Micronuclei were scored at 1000× total magnification by means of Fluorescence Microscope Zeiss, with ApoTome (Axio Imager Z1 Stand).

Chapter 6

Cell culture HaCaT, spontaneously immortalized human keratinocyte line, and HeLa, a human cervical cancer cell line, used in the experiments were obtained from InterLab Cell Line Collection (ICLC) (Istituto Nazionale per la Ricerca sul

Cancro, Genoa, Italy). The cells were grown at 37°C and 5% CO_2 in Dulbecco's modified Eagle's medium (DMEM, (Euroclone, Life Science Division, GB, Pero, Italy) supplemented with 100 mL^{-1} penicillin, 100 μg/mL streptomycin and 10% fetal bovine serum (Euroclone).

Cytotoxic test: MTT viability assays Cell viability was measured using the MTT (3-[4,5-dimethylthiazol-2-yl]-2,5-diphenyltetrazolium) (Sigma-Aldrich, Saint Louis, Missouri, USA) colorimetric assay. For this purpose, cells were seeded in 96-well flat plate at a density of 5×10^3 cells per well in culture medium in triplicate. Following 24 hours, different concentrations of antifolate nanovectors, aminopterin and metotrexate were added in triplicate. After 24 hours of treatment, 20 μL of MTT solution were added to each well and cells incubated at 37°C and 5% CO_2 for 4 hours. 100 μL of dimethyl sulfoxide (DMSO) were added to dissolve the formed formazan crystals. After 15 minutes of incubation, the absorbance was measured in a plate reader spectrophotometer (Labsystem Multiskan MS), using a test wavelength of 540 nm and a reference wavelength of 690 nm. The cells incubated with culture medium alone represented the controls, and wells containing the medium alone served as blanks. All the results were analysed by ANOVA. The significance was evaluated by the Tukey honestly significant difference (HSD) post hoc test and data were expressed as means ± standard deviation (SD) of independent samplings from different experiments. The level of significance was established at p value <0.05. The high reproducibilityof the results was ensured by the consistent outcome of at least three repeated experiments.

Titration measurements A colorimetric assay with Orange II dye, using standard addition method, was performed on the NPs in order to assess the number of 4ATP and drug molecules conjugated to the nanoparticle surface. Typically, known amounts of the Orange II dye solution (1 mg/mL, pH 3) were progressively added to the NPs samples. At each addition step, the nanoparticles were incubated for 15 min at 40°C, and then centrifuged for 15 min at 3200 rpm. Orange II is susceptible to bind to free primary amines of the 4ATP ligand molecules on the nanoparticle surface via the sulfonate moiety. The absorbance of the unbound dye in the supernatant wasnmeasured at 485 nm. As the amount of Orange II is in defect, it will totally bind to the nanoparticle surface, leaving therefore the supernatant free of dye. After multiple additions and saturation of the 4ATP groups with Orange II dye, the concentration of unbound dye in the supernatant increases. The absorption of unbound dye as a function of the added amount allows for extrapolating the total number of 4ATP binding sites available for the dye and thus to calculate the number of 4ATP molecules per nanoparticle. By comparing the result on 4ATP-AuNPs and on the drug conjugated nanovector, the number of drug molecules can be derived by difference.

Chapter 7

TERS spectroscopy The TERS setup comprised an atomic force microscope (AFM, Nanowizard III, JPK Instruments AG, Berlin, Germany) mounted on an inverted microscope (Olympus IX71, Olympus, Hamburg, Germany). For irradiation,

a laser (λ = 532 nm, P = 660 μW, Cobolt Samba, Cobolt AB, Sweden) was focused through a 60× (NA = 1.45) oil immersion objective (Olympus, Germany) on the sample. Spectra were acquired in back reflection geometry with a confocal spectrometer (SP2750A, Acton Advanced, Princeton Instruments) and a CCD camera (PIXIS 256 Princeton Instruments, Trenton). The acquisition time for all measurements was 1 s. TERS tips were prepared by evaporating 25 nm silver on AFM tips (Tap190Al-G, Budget Sensors, NanoAndMore GmbH, Wetzlar, Germany). Tips were stored under argon prior to use.

List of publications

Publications related to the thesis work

- F. Brasili†, A. Capocefalo†, D. Palmieri, E. Chiessi, G. Paradossi, F. Bordi and F. Domenici; *Bio-plasmonic systems with tunable optical and functional properties: tailoring the self-assembly of protein-decorated gold nanoparticles*, submitted to Nanoscale.
- A. Capocefalo, D. Mammucari, F. Brasili, C. Fasolato, F. Bordi, P. Postorino and F. Domenici; *Exploring the Potentiality of a SERS-Active pH Nano-Biosensor*, Frontiers in Chemistry 7:413, (2019).
- F. Domenici, A. Capocefalo, F. Brasili, A. Bedini, C. Giliberti, R. Palomba, I. Silvestri, S. Scarpa, S. Morrone, G. Paradossi, M. D. Frogley and G. Cinque; *Ultrasound delivery of Surface Enhanced InfraRed Absorption active gold-nanoprobes into fibroblast cells: a biological study via Synchrotron-based InfraRed microanalysis at single cell level*, Scientific reports 9 (1), 1-13 (2019).
- C. Fasolato, S. Giantulli, A. Capocefalo, Y. Toumia, D. Notariello, F. Mazzarda, I. Silvestri, P. Postorino and F. Domenici; *Antifolate SERS-active nanovectors: quantitative drug nanostructuring and selective cell targeting for effective theranostics*, Nanoscale 11 (32), 15224-15233, (2019).

Other publications

- D. Caprara, F. Ripanti, A. Capocefalo, A. Sarra, F. Brasili, C. Petrillo, C. Fasolato and P. Postorino; *DNA-functionalized gold nanoparticle assemblies for Surface Enhanced Raman Scattering*, Colloids and Surfaces A: Physicochemical and Engineering Aspects 589, 124399, (2020).
- E. Truzzi, F. Meneghetti, M. Mori, L. Costantino, V. Iannuccelli, E. Maretti, F. Domenici, C. Castellano, S. Rogers, A. Capocefalo and E. Leo; *Drugs/lamellae interface influences the inner structure of double-loaded liposomes for inhaled anti-TB therapy: An in-depth small-angle neutron scattering investigation*, Journal of colloid and interface science 541, 399-406 (2019).
- D. Caprara, F. Ripanti, A. Capocefalo and P. Postorino; *Exploiting SERS sensitivity to monitor the DNA melting behavior*, to be submitted.

†These authors contributed equally to the work.

Bibliography

[1] S. A. Maier, *Plasmonics: fundamentals and applications*. Springer Science & Business Media, 2007.

[2] L. Novotny and B. Hecht, *Principles of nano-optics*. Cambridge University Press, 2012.

[3] M. I. Stockman, K. Kneipp, S. I. Bozhevolnyi, S. Saha, A. Dutta, J. Ndukaife, N. Kinsey, H. Reddy, U. Guler, V. M. Shalaev, *et al.*, "Roadmap on plasmonics," *Journal of Optics*, vol. 20, no. 4, p. 043001, 2018.

[4] S. K. Ghosh and T. Pal, "Interparticle coupling effect on the surface plasmon resonance of gold nanoparticles: from theory to applications," *Chemical Reviews*, vol. 107, no. 11, pp. 4797–4862, 2007.

[5] N. J. Halas, S. Lal, W.-S. Chang, S. Link, and P. Nordlander, "Plasmons in strongly coupled metallic nanostructures," *Chemical Reviews*, vol. 111, no. 6, pp. 3913–3961, 2011.

[6] A. Polman, "Plasmonics applied," *Science*, vol. 322, no. 5903, pp. 868–869, 2008.

[7] W. P. Hall, S. N. Ngatia, and R. P. Van Duyne, "Lspr biosensor signal enhancement using nanoparticle-antibody conjugates," *The Journal of Physical Chemistry C*, vol. 115, no. 5, pp. 1410–1414, 2011.

[8] J. I. Chen, Y. Chen, and D. S. Ginger, "Plasmonic nanoparticle dimers for optical sensing of dna in complex media," *Journal of the American Chemical Society*, vol. 132, no. 28, pp. 9600–9601, 2010.

[9] J. Anker, W. Hall, O. Lyandres, N. Shah, J. Zhao, and R. Van Duyne, "Biosensing with plasmonic nanosensors.," *Nature Materials*, vol. 7, no. 6, p. 442, 2008.

[10] J. P. Camden, J. A. Dieringer, J. Zhao, and R. P. Van Duyne, "Controlled plasmonic nanostructures for surface-enhanced spectroscopy and sensing," *Accounts of Chemical Research*, vol. 41, no. 12, pp. 1653–1661, 2008.

[11] S. Lal, N. K. Grady, J. Kundu, C. S. Levin, J. B. Lassiter, and N. J. Halas, "Tailoring plasmonic substrates for surface enhanced spectroscopies," *Chemical Society Reviews*, vol. 37, no. 5, pp. 898–911, 2008.

[12] X. Yang, Z. Sun, T. Low, H. Hu, X. Guo, F. J. Garcia de Abajo, P. Avouris, and Q. Dai, "Nanomaterial-based plasmon-enhanced infrared spectroscopy," *Advanced Materials*, vol. 30, no. 20, p. 1704896, 2018.

[13] O. Limaj, D. Etezadi, N. J. Wittenberg, D. Rodrigo, D. Yoo, S.-H. Oh, and H. Altug, "Infrared plasmonic biosensor for real-time and label-free monitoring of lipid membranes," *Nano Letters*, vol. 16, no. 2, pp. 1502–1508, 2016.

[14] F. Domenici, A. Capocefalo, F. Brasili, A. Bedini, C. Giliberti, R. Palomba, I. Silvestri, S. Scarpa, S. Morrone, G. Paradossi, *et al.*, "Ultrasound delivery of surface enhanced infrared absorption active gold-nanoprobes into fibroblast cells: a biological study via synchrotron-based infrared microanalysis at single cell level," *Scientific Reports*, vol. 9, no. 1, pp. 1–13, 2019.

[15] S. Nie and S. R. Emory, "Probing single molecules and single nanoparticles by surface-enhanced raman scattering," *Science*, vol. 275, no. 5303, pp. 1102–1106, 1997.

[16] K. Kneipp, Y. Wang, H. Kneipp, L. T. Perelman, I. Itzkan, R. R. Dasari, and M. S. Feld, "Single molecule detection using surface-enhanced raman scattering (sers)," *Physical Review Letters*, vol. 78, no. 9, p. 1667, 1997.

[17] A. Capocefalo, D. Mammucari, F. Brasili, C. Fasolato, F. Bordi, P. Postorino, and F. Domenici, "Exploring the potentiality of a sers-active ph nano-biosensor," *Frontiers in Chemistry*, vol. 7, 2019.

[18] J. Kneipp, "Interrogating cells, tissues, and live animals with new generations of surface-enhanced raman scattering probes and labels," *ACS Nano*, vol. 11, no. 2, pp. 1136–1141, 2017.

[19] C. Fasolato, S. Giantulli, I. Silvestri, F. Mazzarda, Y. Toumia, F. Ripanti, F. Mura, F. Luongo, F. Costantini, F. Bordi, *et al.*, "Folate-based single cell screening using surface enhanced raman microimaging," *Nanoscale*, vol. 8, no. 39, pp. 17304–17313, 2016.

[20] R. M. Stöckle, Y. D. Suh, V. Deckert, and R. Zenobi, "Nanoscale chemical analysis by tip-enhanced raman spectroscopy," *Chemical Physics Letters*, vol. 318, no. 1-3, pp. 131–136, 2000.

[21] T. Deckert-Gaudig, D. Kurouski, M. A. Hedegaard, P. Singh, I. K. Lednev, and V. Deckert, "Spatially resolved spectroscopic differentiation of hydrophilic and hydrophobic domains on individual insulin amyloid fibrils," *Scientific Reports*, vol. 6, p. 33575, 2016.

[22] Z. He, Z. Han, M. Kizer, R. J. Linhardt, X. Wang, A. M. Sinyukov, J. Wang, V. Deckert, A. V. Sokolov, J. Hu, *et al.*, "Tip-enhanced raman imaging of single-stranded dna with single base resolution," *Journal of the American Chemical Society*, vol. 141, no. 2, pp. 753–757, 2018.

[23] E. Bailo and V. Deckert, "Tip-enhanced raman spectroscopy of single rna strands: towards a novel direct-sequencing method," *Angewandte Chemie International Edition*, vol. 47, no. 9, pp. 1658–1661, 2008.

[24] D. Kim, K. Shin, S. G. Kwon, and T. Hyeon, "Synthesis and biomedical applications of multifunctional nanoparticles," *Advanced Materials*, vol. 30, no. 49, p. 1802309, 2018.

[25] A. Wax and K. Sokolov, "Molecular imaging and darkfield microspectroscopy of live cells using gold plasmonic nanoparticles," *Laser & Photonics Reviews*, vol. 3, no. 1-2, pp. 146–158, 2009.

[26] S. Kumar, N. Harrison, R. Richards-Kortum, and K. Sokolov, "Plasmonic nanosensors for imaging intracellular biomarkers in live cells," *Nano Letters*, vol. 7, no. 5, pp. 1338–1343, 2007.

[27] M. Ferrari, "Nanovector therapeutics," *Current Opinion in Chemical Biology*, vol. 9, no. 4, pp. 343–346, 2005.

[28] H. Park, D.-J. Lim, J. B. Vines, J.-H. Yoon, and N.-E. Ryu, "Gold nanoparticles for photothermal cancer therapy," *Frontiers in Chemistry*, vol. 7, p. 167, 2019.

[29] Y. Xia, X. Wu, J. Zhao, J. Zhao, Z. Li, W. Ren, Y. Tian, A. Li, Z. Shen, and A. Wu, "Three dimensional plasmonic assemblies of aunps with an overall size of sub-200 nm for chemo-photothermal synergistic therapy of breast cancer," *Nanoscale*, vol. 8, no. 44, pp. 18682–18692, 2016.

[30] H. Gao, Y. Bi, J. Chen, L. Peng, K. Wen, P. Ji, W. Ren, X. Li, N. Zhang, J. Gao, *et al.*, "Near-infrared light-triggered switchable nanoparticles for targeted chemo/photothermal cancer therapy," *ACS Applied Materials & Interfaces*, vol. 8, no. 24, pp. 15103–15112, 2016.

[31] C. Fasolato, S. Giantulli, A. Capocefalo, Y. Toumia, D. Notariello, F. Mazzarda, I. Silvestri, P. Postorino, and F. Domenici, "Antifolate sers-active nanovectors: quantitative drug nanostructuring and selective cell targeting for effective theranostics," *Nanoscale*, 2019.

[32] Y.-C. Yeh, B. Creran, and V. M. Rotello, "Gold nanoparticles: preparation, properties, and applications in bionanotechnology," *Nanoscale*, vol. 4, no. 6, pp. 1871–1880, 2012.

[33] M. Pelton and G. W. Bryant, *Introduction to metal-nanoparticle plasmonics*, vol. 5. John Wiley & Sons, 2013.

[34] G. Mie, "Beiträge zur optik trüber medien, speziell kolloidaler metallösungen," *Annalen Der Physik*, vol. 330, no. 3, pp. 377–445, 1908.

[35] J. D. Jackson, "Classical electrodynamics," 1999.

[36] C. F. Bohren and D. R. Huffman, *Absorption and scattering of light by small particles*. John Wiley & Sons, 2008.

[37] H. Kuwata, H. Tamaru, K. Esumi, and K. Miyano, "Resonant light scattering from metal nanoparticles: practical analysis beyond rayleigh approximation," *Applied Physics Letters*, vol. 83, no. 22, pp. 4625–4627, 2003.

[38] A. O. Pinchuk and G. C. Schatz, "Nanoparticle optical properties: far-and near-field electrodynamic coupling in a chain of silver spherical nanoparticles," *Materials Science and Engineering: B*, vol. 149, no. 3, pp. 251–258, 2008.

[39] K. Li, M. I. Stockman, and D. J. Bergman, "Self-similar chain of metal nanospheres as an efficient nanolens," *Physical Review Letters*, vol. 91, no. 22, p. 227402, 2003.

[40] I. Kaminska, T. Maurer, R. Nicolas, M. Renault, T. Lerond, R. Salas-Montiel, Z. Herro, M. Kazan, J. Niedziolka-Jönsson, J. Plain, *et al.*, "Near-field and far-field sensitivities of lspr sensors," *The Journal of Physical Chemistry C*, vol. 119, no. 17, pp. 9470–9476, 2015.

[41] E. Prodan, C. Radloff, N. J. Halas, and P. Nordlander, "A hybridization model for the plasmon response of complex nanostructures," *Science*, vol. 302, no. 5644, pp. 419–422, 2003.

[42] E. Prodan and P. Nordlander, "Plasmon hybridization in spherical nanoparticles," *The Journal of Chemical Physics*, vol. 120, no. 11, pp. 5444–5454, 2004.

[43] P. Nordlander, C. Oubre, E. Prodan, K. Li, and M. Stockman, "Plasmon hybridization in nanoparticle dimers," *Nano Letters*, vol. 4, no. 5, pp. 899–903, 2004.

[44] H. Wang, D. W. Brandl, P. Nordlander, and N. J. Halas, "Plasmonic nanostructures: artificial molecules," *Accounts of Chemical Research*, vol. 40, no. 1, pp. 53–62, 2007.

[45] V. Myroshnychenko, J. Rodríguez-Fernández, I. Pastoriza-Santos, A. M. Funston, C. Novo, P. Mulvaney, L. M. Liz-Marzán, and F. J. G. de Abajo, "Modelling the optical response of gold nanoparticles," *Chemical Society Reviews*, vol. 37, no. 9, pp. 1792–1805, 2008.

[46] W. Rechberger, A. Hohenau, A. Leitner, J. Krenn, B. Lamprecht, and F. Aussenegg, "Optical properties of two interacting gold nanoparticles," *Optics Communications*, vol. 220, no. 1-3, pp. 137–141, 2003.

[47] A. J. Hallock, P. Redmond, and L. Brus, "Optical forces between metallic particles," *Proceedings of the National Academy of Sciences*, vol. 102, no. 5, pp. 1280–1284, 2005.

[48] D. W. Brandl, N. A. Mirin, and P. Nordlander, "Plasmon modes of nanosphere trimers and quadrumers," *The Journal of Physical Chemistry B*, vol. 110, no. 25, pp. 12302–12310, 2006.

[49] S. Trautmann, M. Richard-Lacroix, A. Dathe, H. Schneidewind, J. Dellith, W. Fritzsche, and V. Deckert, "Plasmon response evaluation based on image-derived arbitrary nanostructures," *Nanoscale*, vol. 10, no. 21, pp. 9830–9839, 2018.

[50] C. Fasolato, F. Domenici, S. Sennato, F. Mura, L. De Angelis, F. Luongo, F. Costantini, F. Bordi, and P. Postorino, "Dimensional scale effects on surface enhanced raman scattering efficiency of self-assembled silver nanoparticle clusters," *Applied Physics Letters*, vol. 105, no. 7, p. 073105, 2014.

[51] R. W. Taylor, R. Esteban, S. Mahajan, J. Aizpurua, and J. J. Baumberg, "Optimizing sers from gold nanoparticle clusters: addressing the near field by an embedded chain plasmon model," *The Journal of Physical Chemistry C*, vol. 120, no. 19, pp. 10512–10522, 2016.

[52] S. Karpov, V. Gerasimov, I. Isaev, O. Podavalova, and V. Slabko, "The origin of anomalous enhancement of electromagnetic fields in fractal aggregates of metal nanoparticles," *Colloid Journal*, vol. 69, no. 2, pp. 159–169, 2007.

[53] R. Esteban, R. W. Taylor, J. J. Baumberg, and J. Aizpurua, "How chain plasmons govern the optical response in strongly interacting self-assembled metallic clusters of nanoparticles," *Langmuir*, vol. 28, no. 24, pp. 8881–8890, 2012.

[54] L. O. Herrmann, V. K. Valev, J. Aizpurua, and J. J. Baumberg, "Self-sifting of chain plasmons: the complex optics of au nanoparticle clusters," *Optics Express*, vol. 21, no. 26, pp. 32377–32385, 2013.

[55] C. Fasolato, "Traditional raman and sers: Fundamentals and state of the art," in *Surface Enhanced Raman Spectroscopy for Biophysical Applications*, pp. 9–56, Springer, 2018.

[56] A. Hartstein, J. Kirtley, and J. Tsang, "Enhancement of the infrared absorption from molecular monolayers with thin metal overlayers," *Physical Review Letters*, vol. 45, no. 3, p. 201, 1980.

[57] R. F. Aroca, D. J. Ross, and C. Domingo, "Surface-enhanced infrared spectroscopy," *Applied Spectroscopy*, vol. 58, no. 11, pp. 324A–338A, 2004.

[58] M. Osawa, "Surface-enhanced infrared absorption," in *Near-field optics and surface plasmon polaritons*, pp. 163–187, Springer, 2001.

[59] D. Garoli, E. Calandrini, G. Giovannini, A. Hubarevich, V. Caligiuri, and F. De Angelis, "Nanoporous gold metamaterials for high sensitivity plasmonic sensing," *Nanoscale Horizons*, 2019.

[60] T. R. Jensen, M. D. Malinsky, C. L. Haynes, and R. P. Van Duyne, "Nanosphere lithography: tunable localized surface plasmon resonance spectra of silver nanoparticles," *The Journal of Physical Chemistry B*, vol. 104, no. 45, pp. 10549–10556, 2000.

[61] F. Le, D. W. Brandl, Y. A. Urzhumov, H. Wang, J. Kundu, N. J. Halas, J. Aizpurua, and P. Nordlander, "Metallic nanoparticle arrays: a common substrate for both surface-enhanced raman scattering and surface-enhanced infrared absorption," *ACS Nano*, vol. 2, no. 4, pp. 707–718, 2008.

[62] J. Kundu, F. Le, P. Nordlander, and N. J. Halas, "Surface enhanced infrared absorption (seira) spectroscopy on nanoshell aggregate substrates," *Chemical Physics Letters*, vol. 452, no. 1-3, pp. 115–119, 2008.

[63] R. Hillenbrand, T. Taubner, and F. Keilmann, "Phonon-enhanced light–matter interaction at the nanometre scale," *Nature*, vol. 418, no. 6894, p. 159, 2002.

[64] M. S. Anderson, "Surface enhanced infrared absorption by coupling phonon and plasma resonance," *Applied Physics Letters*, vol. 87, no. 14, p. 144102, 2005.

[65] M. Osawa, "Dynamic processes in electrochemical reactions studied by surface-enhanced infrared absorption spectroscopy (seiras)," *Bulletin of the Chemical Society of Japan*, vol. 70, no. 12, pp. 2861–2880, 1997.

[66] A. E. Bjerke, P. R. Griffiths, and W. Theiss, "Surface-enhanced infrared absorption of co on platinized platinum," *Analytical Chemistry*, vol. 71, no. 10, pp. 1967–1974, 1999.

[67] P. R. Griffiths, "Surface-enhanced infrared absorption spectroscopy: principles and applications," *Spectroscopic Properties of Inorganic and Organometallic Compounds*, vol. 44, pp. 95–122, 2013.

[68] K. Kneipp, H. Kneipp, and J. Kneipp, "Plasmonics for enhanced vibrational signatures," in *Plasmonics: Theory and Applications*, pp. 103–124, Springer, 2013.

[69] R. Adato, A. A. Yanik, J. J. Amsden, D. L. Kaplan, F. G. Omenetto, M. K. Hong, S. Erramilli, and H. Altug, "Ultra-sensitive vibrational spectroscopy of protein monolayers with plasmonic nanoantenna arrays," *Proceedings of the National Academy of Sciences*, vol. 106, no. 46, pp. 19227–19232, 2009.

[70] M. Fleischmann, P. J. Hendra, and A. J. McQuillan, "Raman spectra of pyridine adsorbed at a silver electrode," *Chemical Physics Letters*, vol. 26, no. 2, pp. 163–166, 1974.

[71] J. R. Lombardi and R. L. Birke, "A unified approach to surface-enhanced raman spectroscopy," *The Journal of Physical Chemistry C*, vol. 112, no. 14, pp. 5605–5617, 2008.

[72] J. Mun, D. Lee, S. So, T. Badloe, and J. Rho, "Surface-enhanced spectroscopy: toward practical analysis probe," *Applied Spectroscopy Reviews*, vol. 54, no. 2, pp. 142–175, 2019.

[73] M. Holzinger, A. Le Goff, and S. Cosnier, "Nanomaterials for biosensing applications: a review," *Frontiers in Chemistry*, vol. 2, p. 63, 2014.

[74] F. Domenici, C. Fasolato, E. Mazzi, L. De Angelis, F. Brasili, F. Mura, P. Postorino, and F. Bordi, "Engineering microscale two-dimensional gold nanoparticle cluster arrays for advanced raman sensing: An afm study," *Colloids and surfaces A: Physicochemical and engineering aspects*, vol. 498, pp. 168–175, 2016.

[75] M. Oliverio, S. Perotto, G. C. Messina, L. Lovato, and F. De Angelis, "Chemical functionalization of plasmonic surface biosensors: a tutorial review on issues, strategies, and costs," *ACS Applied Materials & Interfaces*, vol. 9, no. 35, pp. 29394–29411, 2017.

[76] N. Bellassai, R. D'agata, V. Jungbluth, and G. Spoto, "Surface plasmon resonance for biomarker detection: advances in non-invasive cancer diagnosis," *Frontiers in Chemistry*, vol. 7, p. 570, 2019.

[77] S. Hearty, P. Leonard, H. Ma, and R. O'Kennedy, "Measuring antibody-antigen binding kinetics using surface plasmon resonance," in *Antibody Engineering*, pp. 421–455, Springer, 2018.

[78] S. Sloan-Dennison and Z. D. Schultz, "Label-free plasmonic nanostar probes to illuminate in vitro membrane receptor recognition," *Chemical Science*, vol. 10, no. 6, pp. 1807–1815, 2019.

[79] C. M. Miyazaki, F. M. Shimizu, J. Mejía-Salazar, O. N. Oliveira Jr, and M. Ferreira, "Surface plasmon resonance biosensor for enzymatic detection of small analytes," *Nanotechnology*, vol. 28, no. 14, p. 145501, 2017.

[80] Y. Hu, L. Zhang, Y. Zhang, B. Wang, Y. Wang, Q. Fan, W. Huang, and L. Wang, "Plasmonic nanobiosensor based on hairpin dna for detection of trace oligonucleotides biomarker in cancers," *ACS applied materials & interfaces*, vol. 7, no. 4, pp. 2459–2466, 2015.

[81] T. Liyanage, A. N. Masterson, H. H. Oyem, H. Kaimakliotis, H. Nguyen, and R. Sardar, "Plasmoelectronic-based ultrasensitive assay of tumor suppressor micrornas directly in patient plasma: design of highly specific early cancer diagnostic technology," *Analytical Chemistry*, vol. 91, no. 3, pp. 1894–1903, 2019.

[82] S. Xing, X. Xu, P. Fu, M. Xu, T. Gao, X. Zhang, and C. Zhao, "Colorimetric detection of single base-pair mismatches based on the interactions of pna and pna/dna complexes with unmodified gold nanoparticles," *Colloids and Surfaces B: Biointerfaces*, 2019.

[83] Y. Jiang, M. Shi, Y. Liu, S. Wan, C. Cui, L. Zhang, and W. Tan, "Aptamer/aunp biosensor for colorimetric profiling of exosomal proteins," *Angewandte Chemie International Edition*, vol. 56, no. 39, pp. 11916–11920, 2017.

[84] X. Ma, X. Kou, Y. Xu, D. Yang, and P. Miao, "Colorimetric sensing strategy for heparin assay based on pdda-induced aggregation of gold nanoparticles," *Nanoscale Advances*, vol. 1, no. 2, pp. 486–489, 2019.

[85] M. A. Fallah and K. Hauser, "Immobilization approaches can affect protein dynamics: a surface-enhanced infrared spectroscopic study on lipid-protein interactions," *Biomaterials Science*, 2019.

[86] D. Cialla-May, X.-S. Zheng, K. Weber, and J. Popp, "Recent progress in surface-enhanced raman spectroscopy for biological and biomedical applications: from

cells to clinics," *Chemical Society Reviews*, vol. 46, no. 13, pp. 3945–3961, 2017.

[87] Y. Cao, D.-W. Li, L.-J. Zhao, X.-Y. Liu, X.-M. Cao, and Y.-T. Long, "Highly selective detection of carbon monoxide in living cells by palladacycle carbonylation-based surface enhanced raman spectroscopy nanosensors," *Analytical chemistry*, vol. 87, no. 19, pp. 9696–9701, 2015.

[88] F. Domenici, F. Brasili, S. Giantulli, B. Cerroni, A. Bedini, C. Giliberti, R. Palomba, I. Silvestri, S. Morrone, G. Paradossi, *et al.*, "Differential effects on membrane permeability and viability of human keratinocyte cells undergoing very low intensity megasonic fields," *Scientific Reports*, vol. 7, no. 1, p. 16536, 2017.

[89] A. Foti, C. D'andrea, V. Villari, N. Micali, M. Donato, B. Fazio, O. Maragò, R. Gillibert, M. Lamy de la Chapelle, and P. Gucciardi, "Optical aggregation of gold nanoparticles for sers detection of proteins and toxins in liquid environment: towards ultrasensitive and selective detection," *Materials*, vol. 11, no. 3, p. 440, 2018.

[90] G. P. Szekeres and J. Kneipp, "Sers probing of proteins in gold nanoparticle agglomerates," *Frontiers in Chemistry*, vol. 7, p. 30, 2019.

[91] B. Yan, S. V. Boriskina, and B. M. Reinhard, "Design and implementation of noble metal nanoparticle cluster arrays for plasmon enhanced biosensing," *The Journal of Physical Chemistry C*, vol. 115, no. 50, pp. 24437–24453, 2011.

[92] P. Sanpui, A. Paul, and A. Chattopadhyay, "Theranostic potential of gold nanoparticle-protein agglomerates," *Nanoscale*, vol. 7, no. 44, pp. 18411–18423, 2015.

[93] M. B. Ross, C. A. Mirkin, and G. C. Schatz, "Optical properties of one-, two-, and three-dimensional arrays of plasmonic nanostructures," *The Journal of Physical Chemistry C*, vol. 120, no. 2, pp. 816–830, 2016.

[94] R. Khandelia, A. Jaiswal, S. S. Ghosh, and A. Chattopadhyay, "Gold nanoparticle-protein agglomerates as versatile nanocarriers for drug delivery," *Small*, vol. 9, no. 20, pp. 3494–3505, 2013.

[95] M. Grzelczak, L. M. Liz-Marzán, and R. Klajn, "Stimuli-responsive self-assembly of nanoparticles," *Chemical Society Reviews*, vol. 48, no. 5, pp. 1342–1361, 2019.

[96] I. Tokarev and S. Minko, "Tunable plasmonic nanostructures from noble metal nanoparticles and stimuli-responsive polymers," *Soft Matter*, vol. 8, no. 22, pp. 5980–5987, 2012.

[97] B. Bharti, J. Meissner, and G. H. Findenegg, "Aggregation of silica nanoparticles directed by adsorption of lysozyme," *Langmuir*, vol. 27, no. 16, pp. 9823–9833, 2011.

[98] P. Sevilla, S. Sanchez-Cortas, J. V. Garcia-Ramos, and A. Feis, "Concentration-controlled formation of myoglobin/gold nanosphere aggregates," *The Journal of Physical Chemistry B*, vol. 118, no. 19, pp. 5082–5092, 2014.

[99] S. T. Moerz, A. Kraegeloh, M. Chanana, and T. Kraus, "Formation mechanism for stable hybrid clusters of proteins and nanoparticles," *ACS Nano*, vol. 9, no. 7, pp. 6696–6705, 2015.

[100] S. Kumar, I. Yadav, V. K. Aswal, and J. Kohlbrecher, "Structure and interaction of nanoparticle-protein complexes," *Langmuir*, vol. 34, no. 20, pp. 5679–5695, 2018.

[101] D. Velegol and P. K. Thwar, "Analytical model for the effect of surface charge nonuniformity on colloidal interactions," *Langmuir*, vol. 17, no. 24, pp. 7687–7693, 2001.

[102] F. Bordi, S. Sennato, and D. Truzzolillo, "Polyelectrolyte-induced aggregation of liposomes: a new cluster phase with interesting applications," *Journal of Physics: Condensed Matter*, vol. 21, no. 20, p. 203102, 2009.

[103] L. Wetter and H. Deutsch, "Immunological studies on egg white proteins," *The Journal of Biological Chemistry*, vol. 192, pp. 237–242, 1951.

[104] D. J. Vocadlo, G. J. Davies, R. Laine, and S. G. Withers, "Catalysis by hen egg-white lysozyme proceeds via a covalent intermediate," *Nature*, vol. 412, no. 6849, p. 835, 2001.

[105] D. Volodkin, V. Ball, P. Schaaf, J.-C. Voegel, and H. Mohwald, "Complexation of phosphocholine liposomes with polylysine. stabilization by surface coverage versus aggregation," *Biochimica et Biophysica Acta (BBA)-Biomembranes*, vol. 1768, no. 2, pp. 280–290, 2007.

[106] S. Sennato, D. Truzzolillo, and F. Bordi, "Aggregation and stability of polyelectrolyte-decorated liposome complexes in water-salt media," *Soft Matter*, vol. 8, no. 36, pp. 9384–9395, 2012.

[107] J. Stankovich and S. L. Carnie, "Interactions between two spherical particles with nonuniform surface potentials: the linearized poisson–boltzmann theory," *Journal of Colloid and Interface Science*, vol. 216, no. 2, pp. 329–347, 1999.

[108] R. Hogg, T. W. Healy, and D. Fuerstenau, "Mutual coagulation of colloidal dispersions," *Transactions of the Faraday Society*, vol. 62, pp. 1638–1651, 1966.

[109] B. A. Todd and S. J. Eppell, "Probing the limits of the derjaguin approximation with scanning force microscopy," *Langmuir*, vol. 20, no. 12, pp. 4892–4897, 2004.

[110] F. Bordi, C. Cametti, S. Sennato, and D. Truzzolillo, "Strong repulsive interactions in polyelectrolyte-liposome clusters close to the isoelectric point: a sign of an arrested state," *Physical Review E*, vol. 76, no. 6, p. 061403, 2007.

[111] F. Bordi, C. Cametti, S. Sennato, and M. Diociaiuti, "Direct evidence of multicompartment aggregates in polyelectrolyte-charged liposome complexes," *Biophysical Journal*, vol. 91, no. 4, pp. 1513–1520, 2006.

[112] J. Hierrezuelo, A. Sadeghpour, I. Szilagyi, A. Vaccaro, and M. Borkovec, "Electrostatic stabilization of charged colloidal particles with adsorbed polyelectrolytes of opposite charge," *Langmuir*, vol. 26, no. 19, pp. 15109–15111, 2010.

[113] I. Delfino and S. Cannistraro, "Optical investigation of the electron transfer protein azurin-gold nanoparticle system," *Biophysical Chemistry*, vol. 139, no. 1, pp. 1–7, 2009.

[114] H. Mattoussi, J. M. Mauro, E. R. Goldman, G. P. Anderson, V. C. Sundar, F. V. Mikulec, and M. G. Bawendi, "Self-assembly of cdse-zns quantum dot bioconjugates using an engineered recombinant protein," *Journal of the American Chemical Society*, vol. 122, no. 49, pp. 12142–12150, 2000.

[115] G. Bushell, Y. Yan, D. Woodfield, J. Raper, and R. Amal, "On techniques for the measurement of the mass fractal dimension of aggregates," *Advances in Colloid and Interface Science*, vol. 95, no. 1, pp. 1–50, 2002.

[116] J. Teixeira, "Small-angle scattering by fractal systems," *Journal of Applied Crystallography*, vol. 21, no. 6, pp. 781–785, 1988.

[117] M. Lin, H. Lindsay, D. Weitz, R. Ball, R. Klein, and P. Meakin, "Universality in colloid aggregation," *Nature*, vol. 339, no. 6223, p. 360, 1989.

[118] D. Aili, P. Gryko, B. Sepulveda, J. A. Dick, N. Kirby, R. Heenan, L. Baltzer, B. Liedberg, M. P. Ryan, and M. M. Stevens, "Polypeptide folding-mediated tuning of the optical and structural properties of gold nanoparticle assemblies," *Nano Letters*, vol. 11, no. 12, pp. 5564–5573, 2011.

[119] R. Baxter, "Percus–yevick equation for hard spheres with surface adhesion," *The Journal of Chemical Physics*, vol. 49, no. 6, pp. 2770–2774, 1968.

[120] M. Loumaigne, C. Midelet, T. Doussineau, P. Dugourd, R. Antoine, M. Stamboul, A. Débarre, and M. H. Werts, "Optical extinction and scattering cross sections of plasmonic nanoparticle dimers in aqueous suspension," *Nanoscale*, vol. 8, no. 12, pp. 6555–6570, 2016.

[121] H. Xu and M. Käll, "Modeling the optical response of nanoparticle-based surface plasmon resonance sensors," *Sensors and Actuators B: Chemical*, vol. 87, no. 2, pp. 244–249, 2002.

[122] V. Ball and J. J. Ramsden, "Buffer dependence of refractive index increments of protein solutions," *Biopolymers: Original Research on Biomolecules*, vol. 46, no. 7, pp. 489–492, 1998.

[123] R. L. Olmon, B. Slovick, T. W. Johnson, D. Shelton, S.-H. Oh, G. D. Boreman, and M. B. Raschke, "Optical dielectric function of gold," *Physical Review B*, vol. 86, no. 23, p. 235147, 2012.

[124] I. M. Pryce, Y. A. Kelaita, K. Aydin, and H. A. Atwater, "Compliant metamaterials for resonantly enhanced infrared absorption spectroscopy and refractive index sensing," *ACS Nano*, vol. 5, no. 10, pp. 8167–8174, 2011.

[125] A. J. Haes, S. Zou, G. C. Schatz, and R. P. Van Duyne, "A nanoscale optical biosensor: the long range distance dependence of the localized surface plasmon resonance of noble metal nanoparticles," *The Journal of Physical Chemistry B*, vol. 108, no. 1, pp. 109–116, 2004.

[126] G. Raschke, S. Brogl, A. Susha, A. Rogach, T. Klar, J. Feldmann, B. Fieres, N. Petkov, T. Bein, A. Nichtl, *et al.*, "Gold nanoshells improve single nanoparticle molecular sensors," *Nano letters*, vol. 4, no. 10, pp. 1853–1857, 2004.

[127] J. Hühn, C. Fedeli, Q. Zhang, A. Masood, P. del Pino, N. M. Khashab, E. Papini, and W. J. Parak, "Dissociation coefficients of protein adsorption to nanoparticles as quantitative metrics for description of the protein corona: A comparison of experimental techniques and methodological relevance," *The International Journal of Biochemistry & Cell Biology*, vol. 75, pp. 148–161, 2016.

[128] J. E. Gagner, M. D. Lopez, J. S. Dordick, and R. W. Siegel, "Effect of gold nanoparticle morphology on adsorbed protein structure and function," *Biomaterials*, vol. 32, no. 29, pp. 7241–7252, 2011.

[129] J. J. Bergers, M. H. Vingerhoeds, L. van Bloois, J. N. Herron, L. H. Janssen, M. J. Fischer, and D. J. Crommelin, "The role of protein charge in protein-lipid interactions. ph-dependent changes of the electrophoretic mobility of liposomes through adsorption of water-soluble, globular proteins," *Biochemistry*, vol. 32, no. 17, pp. 4641–4649, 1993.

[130] S. A. Ragland and A. K. Criss, "From bacterial killing to immune modulation: recent insights into the functions of lysozyme," *PLoS pathogens*, vol. 13, no. 9, p. e1006512, 2017.

[131] D. Zhang, O. Neumann, H. Wang, V. M. Yuwono, A. Barhoumi, M. Perham, J. D. Hartgerink, P. Wittung-Stafshede, and N. J. Halas, "Gold nanoparticles can induce the formation of protein-based aggregates at physiological ph," *Nano Letters*, vol. 9, no. 2, pp. 666–671, 2009.

[132] Y.-S. Huang, U.-S. Jeng, Y.-J. Shiu, Y.-H. Lai, and Y.-S. Sun, "Charge interaction and temperature effects on the solution structure of lysozyme as revealed by small-angle x-ray scattering," *Applied Crystallography*, vol. 40, no. s1, pp. s165–s169, 2007.

[133] G. P. Szekeres and J. Kneipp, "Different binding sites of serum albumins in the protein corona of gold nanoparticles," *Analyst*, vol. 143, no. 24, pp. 6061–6068, 2018.

[134] D. Jiang, D. Ni, Z. T. Rosenkrans, P. Huang, X. Yan, and W. Cai, "Nanozyme: new horizons for responsive biomedical applications," *Chemical Society Reviews*, 2019.

[135] D. Shugar, "The measurement of lysozyme activity and the ultra-violet inactivation of lysozyme," *Biochimica et Biophysica Acta*, vol. 8, no. C, pp. 302–309, 1952.

[136] S. Chakraborti, T. Chatterjee, P. Joshi, A. Poddar, B. Bhattacharyya, S. P. Singh, V. Gupta, and P. Chakrabarti, "Structure and activity of lysozyme on binding to zno nanoparticles," *Langmuir*, vol. 26, no. 5, pp. 3506–3513, 2009.

[137] M. Arakha, M. Saleem, B. C. Mallick, and S. Jha, "The effects of interfacial potential on antimicrobial propensity of zno nanoparticle," *Scientific Reports*, vol. 5, p. 9578, 2015.

[138] S. S. Khan, A. Mukherjee, and N. Chandrasekaran, "Studies on interaction of colloidal silver nanoparticles (snps) with five different bacterial species," *Colloids and Surfaces B: Biointerfaces*, vol. 87, no. 1, pp. 129–138, 2011.

[139] J. A. Price and R. Pethig, "Surface charge measurements on micrococcus lysodeikticus and the catalytic implications for lysozyme," *Biochimica et Biophysica Acta (BBA)-Molecular Cell Research*, vol. 889, no. 2, pp. 128–135, 1986.

[140] Y. Lee and K. E. Geckeler, "Cytotoxicity and cellular uptake of lysozyme-stabilized gold nanoparticles," *Journal of Biomedical Materials Research Part A*, vol. 100, no. 4, pp. 848–855, 2012.

[141] D. Cialla, S. Pollok, C. Steinbrücker, K. Weber, and J. Popp, "Sers-based detection of biomolecules," *Nanophotonics*, vol. 3, no. 6, pp. 383–411, 2014.

[142] T. T. Chuong, A. Pallaoro, C. A. Chaves, Z. Li, J. Lee, M. Eisenstein, G. D. Stucky, M. Moskovits, and H. T. Soh, "Dual-reporter sers-based biomolecular assay with reduced false-positive signals," *Proceedings of the National Academy of Sciences*, vol. 114, no. 34, pp. 9056–9061, 2017.

[143] J. A. Dougan and K. Faulds, "Surface enhanced raman scattering for multiplexed detection," *Analyst*, vol. 137, no. 3, pp. 545–554, 2012.

[144] S. W. Bishnoi, C. J. Rozell, C. S. Levin, M. K. Gheith, B. R. Johnson, D. H. Johnson, and N. J. Halas, "All-optical nanoscale ph meter," *Nano Letters*, vol. 6, no. 8, pp. 1687–1692, 2006.

[145] L. S. Lawson, J. W. Chan, and T. Huser, "A highly sensitive nanoscale ph-sensor using au nanoparticles linked by a multifunctional raman-active reporter molecule," *Nanoscale*, vol. 6, no. 14, pp. 7971–7980, 2014.

[146] M. Gühlke, Z. Heiner, and J. Kneipp, "Combined near-infrared excited sehrs and sers spectra of ph sensors using silver nanostructures," *Physical Chemistry Chemical Physics*, vol. 17, no. 39, pp. 26093–26100, 2015.

[147] A. Williams, K. J. Flynn, Z. Xia, and P. R. Dunstan, "Multivariate spectral analysis of ph sers probes for improved sensing capabilities," *Journal of Raman Spectroscopy*, vol. 47, no. 7, pp. 819–827, 2016.

[148] L. E. Jamieson, A. Jaworska, J. Jiang, M. Baranska, D. Harrison, and C. Campbell, "Simultaneous intracellular redox potential and ph measurements in live cells using sers nanosensors," *Analyst*, vol. 140, no. 7, pp. 2330–2335, 2015.

[149] L. Puppulin, S. Hosogi, H. Sun, K. Matsuo, T. Inui, Y. Kumamoto, T. Suzaki, H. Tanaka, and Y. Marunaka, "Bioconjugation strategy for cell surface labelling with gold nanostructures designed for highly localized ph measurement," *Nature Communications*, vol. 9, no. 1, p. 5278, 2018.

[150] B. A. Webb, M. Chimenti, M. P. Jacobson, and D. L. Barber, "Dysregulated ph: a perfect storm for cancer progression," *Nature Reviews Cancer*, vol. 11, no. 9, p. 671, 2011.

[151] A. Michota and J. Bukowska, "Surface-enhanced raman scattering (sers) of 4-mercaptobenzoic acid on silver and gold substrates," *Journal of Raman Spectroscopy*, vol. 34, no. 1, pp. 21–25, 2003.

[152] R. Li, H. Lv, X. Zhang, P. Liu, L. Chen, J. Cheng, and B. Zhao, "Vibrational spectroscopy and density functional theory study of 4-mercaptobenzoic acid," *Spectrochimica Acta Part A: Molecular and Biomolecular Spectroscopy*, vol. 148, pp. 369–374, 2015.

[153] F. Wang, R. G. Widejko, Z. Yang, K. T. Nguyen, H. Chen, L. P. Fernando, K. A. Christensen, and J. N. Anker, "Surface-enhanced raman scattering detection of ph with silica-encapsulated 4-mercaptobenzoic acid-functionalized silver nanoparticles," *Analytical Chemistry*, vol. 84, no. 18, pp. 8013–8019, 2012.

[154] H.-B. Guo, F. He, B. Gu, L. Liang, and J. C. Smith, "Time-dependent density functional theory assessment of uv absorption of benzoic acid derivatives," *The Journal of Physical Chemistry A*, vol. 116, no. 48, pp. 11870–11879, 2012.

[155] J. J. Mock, D. R. Smith, and S. Schultz, "Local refractive index dependence of plasmon resonance spectra from individual nanoparticles," *Nano Letters*, vol. 3, no. 4, pp. 485–491, 2003.

[156] M. Moskovits and J. Suh, "Surface selection rules for surface-enhanced raman spectroscopy: calculations and application to the surface-enhanced raman spectrum of phthalazine on silver," *The Journal of Physical Chemistry*, vol. 88, no. 23, pp. 5526–5530, 1984.

[157] E. Le Ru, M. Meyer, E. Blackie, and P. Etchegoin, "Advanced aspects of electromagnetic sers enhancement factors at a hot spot," *Journal of Raman Spectroscopy: An International Journal for Original Work in all Aspects of Raman Spectroscopy, Including Higher Order Processes, and also Brillouin and Rayleigh Scattering*, vol. 39, no. 9, pp. 1127–1134, 2008.

[158] E. Le Ru, S. Meyer, C. Artur, P. Etchegoin, J. Grand, P. Lang, and F. Maurel, "Experimental demonstration of surface selection rules for sers on flat metallic surfaces," *Chemical Communications*, vol. 47, no. 13, pp. 3903–3905, 2011.

[159] M. Osawa, N. Matsuda, K. Yoshii, and I. Uchida, "Charge transfer resonance raman process in surface-enhanced raman scattering from p-aminothiophenol adsorbed on silver: Herzberg-teller contribution," *The Journal of Physical Chemistry*, vol. 98, no. 48, pp. 12702–12707, 1994.

[160] B. Varnholt, P. Oulevey, S. Luber, C. Kumara, A. Dass, and T. Burgi, "Structural information on the au–s interface of thiolate-protected gold clusters: a raman spectroscopy study," *The Journal of Physical Chemistry C*, vol. 118, no. 18, pp. 9604–9611, 2014.

[161] E. B. Wilson Jr, "The normal modes and frequencies of vibration of the regular plane hexagon model of the benzene molecule," *Physical Review*, vol. 45, no. 10, p. 706, 1934.

[162] S. Bhattacharjee, "Dls and zeta potential–what they are and what they are not?," *Journal of Controlled Release*, vol. 235, pp. 337–351, 2016.

[163] M. Aubouy, E. Trizac, and L. Bocquet, "Effective charge versus bare charge: an analytical estimate for colloids in the infinite dilution limit," *Journal of Physics A: Mathematical and General*, vol. 36, no. 22, p. 5835, 2003.

[164] F. Bordi, C. Cametti, S. Sennato, B. Paoli, and C. Marianecci, "Charge renormalization in planar and spherical charged lipidic aqueous interfaces," *The Journal of Physical Chemistry B*, vol. 110, no. 10, pp. 4808–4814, 2006.

[165] Y. Zong, Q. Guo, M. Xu, Y. Yuan, R. Gu, and J. Yao, "Plasmon-induced decarboxylation of mercaptobenzoic acid on nanoparticle film monitored by surface-enhanced raman spectroscopy," *RSC Advances*, vol. 4, no. 60, pp. 31810–31816, 2014.

[166] J. Fontana, J. Livenere, F. J. Bezares, J. D. Caldwell, R. Rendell, and B. R. Ratna, "Large surface-enhanced raman scattering from self-assembled gold nanosphere monolayers," *Applied Physics Letters*, vol. 102, no. 20, p. 201606, 2013.

[167] C.-H. Ho and S. Lee, "Sers and dft investigation of the adsorption behavior of 4-mercaptobenzoic acid on silver colloids," *Colloids and Surfaces A: Physicochemical and Engineering Aspects*, vol. 474, pp. 29–35, 2015.

[168] F. Sun, P. Zhang, T. Bai, D. D. Galvan, H.-C. Hung, N. Zhou, S. Jiang, and Q. Yu, "Functionalized plasmonic nanostructure arrays for direct and accurate mapping extracellular ph of living cells in complex media using sers," *Biosensors and Bioelectronics*, vol. 73, pp. 202–207, 2015.

[169] Y. Liu, H. Yuan, A. M. Fales, and T. Vo-Dinh, "ph-sensing nanostar probe using surface-enhanced raman scattering (sers): Theoretical and experimental studies," *Journal of Raman Spectroscopy*, vol. 44, no. 7, pp. 980–986, 2013.

[170] Y. Wang, L. Chen, and P. Liu, "Biocompatible triplex ag@ sio2@ mtio2 core-shell nanoparticles for simultaneous fluorescence-sers bimodal imaging and drug delivery," *Chemistry-A European Journal*, vol. 18, no. 19, pp. 5935–5943, 2012.

[171] H. Wei, M. R. Willner, L. C. Marr, and P. J. Vikesland, "Highly stable sers ph nanoprobes produced by co-solvent controlled aunp aggregation," *Analyst*, vol. 141, no. 17, pp. 5159–5169, 2016.

[172] J. R. Casey, S. Grinstein, and J. Orlowski, "Sensors and regulators of intracellular ph," *Nature Reviews: Molecular Cell Biology*, vol. 11, no. 1, p. 50, 2010.

[173] D. Wencel, T. Abel, and C. McDonagh, "Optical chemical ph sensors," *Analytical Chemistry*, vol. 86, no. 1, pp. 15–29, 2013.

[174] M. C. Leopold, J. A. Black, and E. F. Bowden, "Influence of gold topography on carboxylic acid terminated self-assembled monolayers," *Langmuir*, vol. 18, no. 4, pp. 978–980, 2002.

[175] D. Wang, R. J. Nap, I. Lagzi, B. Kowalczyk, S. Han, B. A. Grzybowski, and I. Szleifer, "How and why nanoparticle's curvature regulates the apparent p k a of the coating ligands," *Journal of the American Chemical Society*, vol. 133, no. 7, pp. 2192–2197, 2011.

[176] J. Koivisto, X. Chen, S. Donnini, T. Lahtinen, H. Hakkinen, G. Groenhof, and M. Pettersson, "Acid–base properties and surface charge distribution of the water-soluble au102 (p mba) 44 nanocluster," *The Journal of Physical Chemistry C*, vol. 120, no. 18, pp. 10041–10050, 2016.

[177] C. A. Hollingsworth, P. G. Seybold, and C. M. Hadad, "Substituent effects on the electronic structure and pka of benzoic acid," *International Journal of Quantum Chemistry*, vol. 90, no. 4-5, pp. 1396–1403, 2002.

[178] M. I. Khan, K. Mukherjee, R. Shoukat, and H. Dong, "A review on ph sensitive materials for sensors and detection methods," *Microsystem Technologies*, vol. 23, no. 10, pp. 4391–4404, 2017.

[179] D. Neri and C. T. Supuran, "Interfering with ph regulation in tumours as a therapeutic strategy," *Nature Reviews: Drug discovery*, vol. 10, no. 10, p. 767, 2011.

[180] M. Damaghi, J. W. Wojtkowiak, and R. J. Gillies, "ph sensing and regulation in cancer," *Frontiers in Physiology*, vol. 4, p. 370, 2013.

[181] I. Notingher, S. Verrier, H. Romanska, A. Bishop, J. Polak, and L. Hench, "In situ characterisation of living cells by raman spectroscopy," *Journal of Spectroscopy*, vol. 16, no. 2, pp. 43–51, 2002.

[182] Z. Movasaghi, S. Rehman, and I. U. Rehman, "Raman spectroscopy of biological tissues," *Applied Spectroscopy Reviews*, vol. 42, no. 5, pp. 493–541, 2007.

[183] D. Kurouski, T. Postiglione, T. Deckert-Gaudig, V. Deckert, and I. K. Lednev, "Amide i vibrational mode suppression in surface (sers) and tip (ters) enhanced raman spectra of protein specimens," *Analyst*, vol. 138, no. 6, pp. 1665–1673, 2013.

[184] S. Mitragotri, "Healing sound: the use of ultrasound in drug delivery and other therapeutic applications," *Nature Reviews: Drug Discovery*, vol. 4, no. 3, p. 255, 2005.

[185] B. Krasovitski, V. Frenkel, S. Shoham, and E. Kimmel, "Intramembrane cavitation as a unifying mechanism for ultrasound-induced bioeffects," *Proceedings of the National Academy of Sciences*, vol. 108, no. 8, pp. 3258–3263, 2011.

[186] C. Newman and T. Bettinger, "Gene therapy progress and prospects: ultrasound for gene transfer," *Gene Therapy*, vol. 14, no. 6, p. 465, 2007.

[187] T. J. Mason, "Therapeutic ultrasound an overview," *Ultrasonics Sonochemistry*, vol. 18, no. 4, pp. 847–852, 2011.

[188] G. Canavese, A. Ancona, L. Racca, M. Canta, B. Dumontel, F. Barbaresco, T. Limongi, and V. Cauda, "Nanoparticle-assisted ultrasound: a special focus on sonodynamic therapy against cancer," *Chemical Engineering Journal*, vol. 340, pp. 155–172, 2018.

[189] M. Ferrari, "Cancer nanotechnology: opportunities and challenges," *Nature Reviews Cancer*, vol. 5, no. 3, p. 161, 2005.

[190] X. Zeng, G. Liu, W. Tao, Y. Ma, X. Zhang, F. He, J. Pan, L. Mei, and G. Pan, "A drug-self-gated mesoporous antitumor nanoplatform based on ph-sensitive dynamic covalent bond," *Advanced Functional Materials*, vol. 27, no. 11, p. 1605985, 2017.

[191] X. Zeng, M. Luo, G. Liu, X. Wang, W. Tao, Y. Lin, X. Ji, L. Nie, and L. Mei, "Polydopamine-modified black phosphorous nanocapsule with enhanced stability and photothermal performance for tumor multimodal treatments," *Advanced Science*, vol. 5, no. 10, p. 1800510, 2018.

[192] F. Domenici, C. Giliberti, A. Bedini, R. Palomba, I. Udroiu, L. Di Giambattista, D. Pozzi, S. Morrone, F. Bordi, and A. C. Castellano, "Structural and permeability sensitivity of cells to low intensity ultrasound: Infrared and fluorescence evidence in vitro," *Ultrasonics*, vol. 54, no. 4, pp. 1020–1028, 2014.

[193] I. Udroiu, F. Domenici, C. Giliberti, A. Bedini, R. Palomba, F. Luongo, D. Pozzi, F. Bordi, and A. C. Castellano, "Potential genotoxic effects of low-intensity ultrasound on fibroblasts, evaluated with the cytokinesis-block micronucleus assay," *Mutation Research/Genetic Toxicology and Environmental Mutagenesis*, vol. 772, pp. 20–24, 2014.

[194] W. D. O'Brien Jr, "Ultrasound–biophysics mechanisms," *Progress in Biophysics and Molecular Biology*, vol. 93, no. 1-3, pp. 212–255, 2007.

[195] I. Udroiu, J. Marinaccio, A. Bedini, C. Giliberti, R. Palomba, and A. Sgura, "Genomic damage induced by 1-mhz ultrasound in vitro," *Environmental and Molecular Mutagenesis*, vol. 59, no. 1, pp. 60–68, 2018.

[196] P. Grimaldi, L. Di Giambattista, S. Giordani, I. Udroiu, D. Pozzi, S. Gaudenzi, A. Bedini, C. Giliberti, R. Palomba, and A. C. Castellano, "Ultrasound-mediated structural changes in cells revealed by ftir spectroscopy: a contribution to the optimization of gene and drug delivery," *Spectrochimica Acta Part A: Molecular and Biomolecular Spectroscopy*, vol. 84, no. 1, pp. 74–85, 2011.

[197] F. Domenici, C. Giliberti, A. Bedini, R. Palomba, F. Luongo, S. Sennato, C. Olmati, D. Pozzi, S. Morrone, A. Congiu Castellano, *et al.*, "Ultrasound well below the intensity threshold of cavitation can promote efficient uptake of small drug model molecules in fibroblast cells," *Drug Delivery*, vol. 20, no. 7, pp. 285–295, 2013.

[198] E. C. Dreaden, A. M. Alkilany, X. Huang, C. J. Murphy, and M. A. El-Sayed, "The golden age: gold nanoparticles for biomedicine," *Chemical Society Reviews*, vol. 41, no. 7, pp. 2740–2779, 2012.

[199] F. Toderas, S. Boca, M. Baia, L. Baia, D. Maniu, S. Astilean, and S. Simon, "Self-assembled multilayers of gold nanoparticles as versatile platforms for molecular sensing by fourier transform-surface enhanced scattering (ft-sers) and surface enhanced infrared absorption (seira)," *Journal of Optoelectronics and Advanced Materials*, vol. 9, no. 3, pp. 625–628, 2007.

[200] M. Baia, F. Toderas, L. Baia, D. Maniu, and S. Astilean, "Multilayer structures of self-assembled gold nanoparticles as a unique sers and seira substrate," *ChemPhysChem*, vol. 10, no. 7, pp. 1106–1111, 2009.

[201] D. Etezadi, J. B. Warner IV, F. S. Ruggeri, G. Dietler, H. A. Lashuel, and H. Altug, "Nanoplasmonic mid-infrared biosensor for in vitro protein secondary structure detection," *Light: Science & Applications*, vol. 6, no. 8, p. e17029, 2017.

[202] G. Dovbeshko, O. Gnatyuk, S. Karakhim, T. Doroshenko, and V. Romanyuk, "Surface enhanced imaging and ir spectroscopy of the biological cells on the nanostructured gold film.," *Semiconductor Physics, Quantum Electronics & Optoelectronics*, vol. 20, no. 2, 2017.

[203] K. Ataka, S. T. Stripp, and J. Heberle, "Surface-enhanced infrared absorption spectroscopy (seiras) to probe monolayers of membrane proteins," *Biochimica et Biophysica Acta (BBA)-Biomembranes*, vol. 1828, no. 10, pp. 2283–2293, 2013.

[204] P. Dumas, G. D. Sockalingum, and J. Sule-Suso, "Adding synchrotron radiation to infrared microspectroscopy: what's new in biomedical applications?," *Trends in Biotechnology*, vol. 25, no. 1, pp. 40–44, 2007.

[205] J. Doherty, A. Raoof, A. Hussain, M. Wolna, G. Cinque, M. Brown, P. Gardner, and J. Denbigh, "Live single cell analysis using synchrotron ftir microspectroscopy: development of a simple dynamic flow system for prolonged sample viability," *Analyst*, vol. 144, no. 3, pp. 997–1007, 2019.

[206] D. Enders, T. Nagao, A. Pucci, T. Nakayama, and M. Aono, "Surface-enhanced atr-ir spectroscopy with interface-grown plasmonic gold-island films near the percolation threshold," *Physical Chemistry Chemical Physics*, vol. 13, no. 11, pp. 4935–4941, 2011.

[207] S. Mehier-Humbert, T. Bettinger, F. Yan, and R. H. Guy, "Plasma membrane poration induced by ultrasound exposure: implication for drug delivery," *Journal of Controlled Release*, vol. 104, no. 1, pp. 213–222, 2005.

[208] A. Verma, O. Uzun, Y. Hu, Y. Hu, H.-S. Han, N. Watson, S. Chen, D. J. Irvine, and F. Stellacci, "Surface-structure-regulated cell-membrane penetration by monolayer-protected nanoparticles," *Nature Materials*, vol. 7, no. 7, p. 588, 2008.

[209] V. Liberman, R. Adato, T. H. Jeys, B. G. Saar, S. Erramilli, and H. Altug, "Rational design and optimization of plasmonic nanoarrays for surface enhanced infrared spectroscopy," *Optics Express*, vol. 20, no. 11, pp. 11953–11967, 2012.

[210] O. Bibikova, J. Haas, Á. I. López-Lorente, A. Popov, M. Kinnunen, Y. Ryabchikov, A. Kabashin, I. Meglinski, and B. Mizaikoff, "Surface enhanced infrared absorption spectroscopy based on gold nanostars and spherical nanoparticles," *Analytica Chimica Acta*, vol. 990, pp. 141–149, 2017.

[211] A. Hornemann, D. Eichert, S. Flemig, G. Ulm, and B. Beckhoff, "Qualifying label components for effective biosensing using advanced high-throughput seira methodology," *Physical Chemistry Chemical Physics*, vol. 17, no. 14, pp. 9471–9479, 2015.

[212] A. Ostrowski, D. Nordmeyer, A. Boreham, C. Holzhausen, L. Mundhenk, C. Graf, M. C. Meinke, A. Vogt, S. Hadam, J. Lademann, *et al.*, "Overview about the localization of nanoparticles in tissue and cellular context by different imaging techniques," *Beilstein Journal of Nanotechnology*, vol. 6, no. 1, pp. 263–280, 2015.

[213] H. Guo, T. Kimura, and Y. Furutani, "Distortion of the amide-i and-ii bands of an α-helical membrane protein, pharaonis halorhodopsin, depends on thickness of gold films utilized for surface-enhanced infrared absorption spectroscopy," *Chemical Physics*, vol. 419, pp. 8–16, 2013.

[214] G. Dovbeshko, O. Fesenko, and A. Nazarova, "Effect of nanostructured metal surface on seira spectra of albumin and nucleic acids," *Journal of Physical Studies*, vol. 10, pp. 127–134, 2006.

[215] L. M. Miller and P. Dumas, "From structure to cellular mechanism with infrared microspectroscopy," *Current Opinion in Structural Biology*, vol. 20, no. 5, pp. 649–656, 2010.

[216] U. Zelig, J. Kapelushnik, R. Moreh, S. Mordechai, and I. Nathan, "Diagnosis of cell death by means of infrared spectroscopy," *Biophysical Journal*, vol. 97, no. 7, pp. 2107–2114, 2009.

[217] K. Le Roux, L. C. Prinsloo, and D. Meyer, "Fourier transform infrared spectroscopy discloses different types of cell death in flow cytometrically sorted cells," *Toxicology in Vitro*, vol. 29, no. 7, pp. 1932–1940, 2015.

[218] S. Gaudenzi, D. Pozzi, P. Toro, I. Silvestri, S. Morrone, and A. C. Castellano, "Cell apoptosis specific marker found by fourier transform infrared spectroscopy," *Journal of Spectroscopy*, vol. 18, no. 3, pp. 415–422, 2004.

[219] A. Barth, "Infrared spectroscopy of proteins," *Biochimica et Biophysica Acta (BBA)-Bioenergetics*, vol. 1767, no. 9, pp. 1073–1101, 2007.

[220] L. Buriankova, Z. Nadova, D. Jancura, M. Refregiers, I. Yousef, J. Mikes, and P. Miskovsky, "Synchrotron based fourier-transform infrared microspectroscopy as sensitive technique for the detection of early apoptosis in u-87 mg cells," *Laser Physics Letters*, vol. 7, no. 8, p. 613, 2010.

[221] Y. Furusawa, Y. Fujiwara, P. Campbell, Q.-L. Zhao, R. Ogawa, M. A. Hassan, Y. Tabuchi, I. Takasaki, A. Takahashi, and T. Kondo, "Dna double-strand breaks induced by cavitational mechanical effects of ultrasound in cancer cell lines," *PLoS One*, vol. 7, no. 1, p. e29012, 2012.

[222] K. N. Dahl, A. J. Ribeiro, and J. Lammerding, "Nuclear shape, mechanics, and mechanotransduction," *Circulation Research*, vol. 102, no. 11, pp. 1307–1318, 2008.

[223] P. G. De Deyne and M. Kirsch-Volders, "In vitro effects of therapeutic ultrasound on the nucleus of human fibroblasts," *Physical Therapy*, vol. 75, no. 7, pp. 629–634, 1995.

[224] T. Itabashi, Y. Terada, K. Kuwana, T. Kan, I. Shimoyama, and S. Ishiwata, "Mechanical impulses can control metaphase progression in a mammalian cell," *Proceedings of the National Academy of Sciences*, vol. 109, no. 19, pp. 7320–7325, 2012.

[225] R. A. Smith, K. Andrews, D. Brooks, C. E. DeSantis, S. A. Fedewa, J. Lortet-Tieulent, D. Manassaram-Baptiste, O. W. Brawley, and R. C. Wender, "Cancer screening in the united states, 2016: A review of current american cancer society guidelines and current issues in cancer screening," *CA: a cancer journal for clinicians*, vol. 66, no. 2, pp. 95–114, 2016.

[226] K. D. Miller, R. L. Siegel, C. C. Lin, A. B. Mariotto, J. L. Kramer, J. H. Rowland, K. D. Stein, R. Alteri, and A. Jemal, "Cancer treatment and survivorship statistics, 2016," *CA: a cancer journal for clinicians*, vol. 66, no. 4, pp. 271–289, 2016.

[227] A. A. Alizadeh, V. Aranda, A. Bardelli, C. Blanpain, C. Bock, C. Borowski, C. Caldas, A. Califano, M. Doherty, M. Elsner, *et al.*, "Toward understanding and exploiting tumor heterogeneity," *Nature Medicine*, vol. 21, no. 8, p. 846, 2015.

[228] L. Chin, J. N. Andersen, and P. A. Futreal, "Cancer genomics: from discovery science to personalized medicine," *Nature Medicine*, vol. 17, no. 3, p. 297, 2011.

[229] A. V. Biankin, S. Piantadosi, and S. J. Hollingsworth, "Patient-centric trials for therapeutic development in precision oncology," *Nature*, vol. 526, no. 7573, p. 361, 2015.

[230] S. D. Jo, S. H. Ku, Y.-Y. Won, S. H. Kim, and I. C. Kwon, "Targeted nanotheranostics for future personalized medicine: recent progress in cancer therapy," *Theranostics*, vol. 6, no. 9, p. 1362, 2016.

[231] E. Salvati, F. Stellacci, and S. Krol, "Nanosensors for early cancer detection and for therapeutic drug monitoring," *Nanomedicine*, vol. 10, no. 23, pp. 3495–3512, 2015.

[232] B. Godin, E. Tasciotti, X. Liu, R. E. Serda, and M. Ferrari, "Multistage nanovectors: from concept to novel imaging contrast agents and therapeutics," *Accounts of Chemical Research*, vol. 44, no. 10, pp. 979–989, 2011.

[233] R. Bazak, M. Houri, S. El Achy, S. Kamel, and T. Refaat, "Cancer active targeting by nanoparticles: a comprehensive review of literature," *Journal of Cancer Research and Clinical Oncology*, vol. 141, no. 5, pp. 769–784, 2015.

[234] E. A. Owens, M. Henary, G. El Fakhri, and H. S. Choi, "Tissue-specific near-infrared fluorescence imaging," *Accounts of Chemical Research*, vol. 49, no. 9, pp. 1731–1740, 2016.

[235] A. Pallaoro, G. B. Braun, and M. Moskovits, "Biotags based on surface-enhanced raman can be as bright as fluorescence tags," *Nano Letters*, vol. 15, no. 10, pp. 6745–6750, 2015.

[236] F. Domenici, A. R. Bizzarri, and S. Cannistraro, "Surface-enhanced raman scattering detection of wild-type and mutant p53 proteins at very low concentration in human serum," *Analytical Biochemistry*, vol. 421, no. 1, pp. 9–15, 2012.

[237] X. Qian, X.-H. Peng, D. O. Ansari, Q. Yin-Goen, G. Z. Chen, D. M. Shin, L. Yang, A. N. Young, M. D. Wang, and S. Nie, "In vivo tumor targeting and spectroscopic detection with surface-enhanced raman nanoparticle tags," *Nature Biotechnology*, vol. 26, no. 1, p. 83, 2008.

[238] S. Laing, L. E. Jamieson, K. Faulds, and D. Graham, "Surface-enhanced raman spectroscopy for in vivo biosensing," *Nature Reviews Chemistry*, vol. 1, no. 8, p. 0060, 2017.

[239] A. Pallaoro, G. B. Braun, and M. Moskovits, "Quantitative ratiometric discrimination between noncancerous and cancerous prostate cells based on neuropilin-1 overexpression," *Proceedings of the National Academy of Sciences*, vol. 108, no. 40, pp. 16559–16564, 2011.

[240] M. Bhamidipati, G. Lee, I. Kim, and L. Fabris, "Sers-based quantification of psma in tissue microarrays allows effective stratification of patients with prostate cancer," *ACS Omega*, vol. 3, no. 12, pp. 16784–16794, 2018.

[241] M. Gao, H. Su, G. Lin, S. Li, X. Yu, A. Qin, Z. Zhao, Z. Zhang, and B. Z. Tang, "Targeted imaging of egfr overexpressed cancer cells by brightly fluorescent nanoparticles conjugated with cetuximab," *Nanoscale*, vol. 8, no. 32, pp. 15027–15032, 2016.

[242] Z. Cheng, N. Choi, R. Wang, S. Lee, K. C. Moon, S.-Y. Yoon, L. Chen, and J. Choo, "Simultaneous detection of dual prostate specific antigens using surface-enhanced raman scattering-based immunoassay for accurate diagnosis of prostate cancer," *ACS Nano*, vol. 11, no. 5, pp. 4926–4933, 2017.

[243] M. P. Monopoli, F. B. Bombelli, and K. A. Dawson, "Nanobiotechnology: nanoparticle coronas take shape," *Nature Nanotechnology*, vol. 6, no. 1, p. 11, 2011.

[244] M. Lundqvist, J. Stigler, G. Elia, I. Lynch, T. Cedervall, and K. A. Dawson, "Nanoparticle size and surface properties determine the protein corona with possible implications for biological impacts," *Proceedings of the National Academy of Sciences*, vol. 105, no. 38, pp. 14265–14270, 2008.

[245] Q. Dai, C. Walkey, and W. C. Chan, "Polyethylene glycol backfilling mitigates the negative impact of the protein corona on nanoparticle cell targeting," *Angewandte Chemie International Edition*, vol. 53, no. 20, pp. 5093–5096, 2014.

[246] S. K. Desmoulin, Z. Hou, A. Gangjee, and L. H. Matherly, "The human proton-coupled folate transporter: Biology and therapeutic applications to cancer," *Cancer biology & therapy*, vol. 13, no. 14, pp. 1355–1373, 2012.

[247] R. Zhao and I. D. Goldman, "Folate and thiamine transporters mediated by facilitative carriers (slc19a1-3 and slc46a1) and folate receptors," *Molecular Aspects of Medicine*, vol. 34, no. 2-3, pp. 373–385, 2013.

[248] A. Pallaoro, M. R. Hoonejani, G. B. Braun, C. D. Meinhart, and M. Moskovits, "Rapid identification by surface-enhanced raman spectroscopy of cancer cells at low concentrations flowing in a microfluidic channel," *Acs Nano*, vol. 9, no. 4, pp. 4328–4336, 2015.

[249] N. S. Abadeer and C. J. Murphy, "Recent progress in cancer thermal therapy using gold nanoparticles," *The Journal of Physical Chemistry C*, vol. 120, no. 9, pp. 4691–4716, 2016.

[250] F. Bertorelle, M. Pinto, R. Zappon, R. Pilot, L. Litti, S. Fiameni, G. Conti, M. Gobbo, G. Toffoli, M. Colombatti, *et al.*, "Safe core-satellite magneto-plasmonic nanostructures for efficient targeting and photothermal treatment of tumor cells," *Nanoscale*, vol. 10, no. 3, pp. 976–984, 2018.

[251] G. Zhu, J.-T. Liu, Y. Wang, D. Zhang, Y. Guo, E. Tasciotti, Z. Hu, and X. Liu, "In situ reductive synthesis of structural supported gold nanorods in porous silicon particles for multifunctional nanovectors," *ACS Applied Materials & Interfaces*, vol. 8, no. 18, pp. 11881–11891, 2016.

[252] M. Potara, T. Nagy-Simon, S. Suarasan, and S. Astileana, "Plasmonic-based sers-traceable drug nanocarriers in cancer theranostics," *Plasmonics in Chemistry and Biology*, p. 159, 2019.

[253] J. Dacie, E. Dresner, D. Mollin, and J. White, "Aminopterin in the treatment of acute leukaemia," *British Medical Journal*, vol. 1, no. 4668, p. 1447, 1950.

[254] N. Gonen and Y. G. Assaraf, "Antifolates in cancer therapy: structure, activity and mechanisms of drug resistance," *Drug Resistance Updates*, vol. 15, no. 4, pp. 183–210, 2012.

[255] E. S. Chan and B. N. Cronstein, "Mechanisms of action of methotrexate," *Bulletin of the NYU Hospital for Joint Diseases*, vol. 71, no. suppl 1, p. S5, 2013.

[256] A. S. Wibowo, M. Singh, K. M. Reeder, J. J. Carter, A. R. Kovach, W. Meng, M. Ratnam, F. Zhang, and C. E. Dann, "Structures of human folate receptors reveal biological trafficking states and diversity in folate and antifolate recognition," *Proceedings of the National Academy of Sciences*, vol. 110, no. 38, pp. 15180–15188, 2013.

[257] M. D. Salazar and M. Ratnam, "The folate receptor: what does it promise in tissue-targeted therapeutics?," *Cancer and Metastasis Reviews*, vol. 26, no. 1, pp. 141–152, 2007.

[258] M. J. Kang, S. H. Park, M. H. Kang, M. J. Park, and Y. W. Choi, "Folic acid-tethered pep-1 peptide-conjugated liposomal nanocarrier for enhanced intracellular drug delivery to cancer cells: conformational characterization and in vitro cellular uptake evaluation," *International Journal of Nanomedicine*, vol. 8, p. 1155, 2013.

[259] S. Mohapatra, S. R. Rout, R. Narayan, and T. K. Maiti, "Multifunctional mesoporous hollow silica nanocapsules for targeted co-delivery of cisplatin-pemetrexed and mr imaging," *Dalton Transactions*, vol. 43, no. 42, pp. 15841–15850, 2014.

[260] R. Fujiwara, S. Takenaka, M. Hashimoto, T. Narawa, and T. Itoh, "Expression of human solute carrier family transporters in skin: possible contributor to drug-induced skin disorders," *Scientific Reports*, vol. 4, p. 5251, 2014.

[261] C. de Oliveira, S. Büttenbender, W. Prado, A. Beckenkamp, A. Asbahr, A. Buffon, S. Guterres, and A. Pohlmann, "Enhanced and selective antiproliferative activity of methotrexate-functionalized-nanocapsules to human breast cancer cells (mcf-7)," *Nanomaterials*, vol. 8, no. 1, p. 24, 2018.

[262] P. Schilrreff, G. Cervini, E. L. Romero, and M. J. Morilla, "Enhanced antimelanoma activity of methotrexate and zoledronic acid within polymeric sandwiches," *Colloids and Surfaces B: Biointerfaces*, vol. 122, pp. 19–29, 2014.

[263] D. Feng, Y. Song, W. Shi, X. Li, and H. Ma, "Distinguishing folate-receptor-positive cells from folate-receptor-negative cells using a fluorescence off-on nanoprobe," *Analytical Chemistry*, vol. 85, no. 13, pp. 6530–6535, 2013.

[264] K. Siwowska, R. Schmid, S. Cohrs, R. Schibli, and C. Müller, "Folate receptor-positive gynecological cancer cells: In vitro and in vivo characterization," *Pharmaceuticals*, vol. 10, no. 3, p. 72, 2017.

[265] N. Parker, M. J. Turk, E. Westrick, J. D. Lewis, P. S. Low, and C. P. Leamon, "Folate receptor expression in carcinomas and normal tissues determined by a quantitative radioligand binding assay," *Analytical Biochemistry*, vol. 338, no. 2, pp. 284–293, 2005.

[266] T. Elango, A. Thirupathi, S. Subramanian, P. Ethiraj, H. Dayalan, and P. Gnanaraj, "Methotrexate treatment provokes apoptosis of proliferating keratinocyte in psoriasis patients," *Clinical and Experimental Medicine*, vol. 17, no. 3, pp. 371–381, 2017.

[267] J. Delyon, N. Ortonne, E. Benayoun, J. Moroch, P. Wolkenstein, E. Sbidian, and O. Chosidow, "Low-dose methotrexate-induced skin toxicity: keratinocyte dystrophy as a histologic marker," *Journal of the American Academy of Dermatology*, vol. 73, no. 3, pp. 484–490, 2015.

[268] J. Delyon, N. Ortonne, E. Sbidian, and O. Chosidow, "Keratinocyte dystrophy as a marker of low-dose methotrexate-induced skin toxicity: comment on the clinical image by mönch et al.," *Arthritis & Rheumatology*, vol. 68, no. 7, pp. 1790–1791, 2016.

[269] W. Jiang, B. Y. Kim, J. T. Rutka, and W. C. Chan, "Nanoparticle-mediated cellular response is size-dependent," *Nature Nanotechnology*, vol. 3, no. 3, p. 145, 2008.

[270] G. Jansen, "Receptor-and carrier-mediated transport systems for folates and antifolates," in *Antifolate Drugs in Cancer Therapy*, pp. 293–321, Springer, 1999.

[271] K. M. Mayer and J. H. Hafner, "Localized surface plasmon resonance sensors," *Chemical Reviews*, vol. 111, no. 6, pp. 3828–3857, 2011.

[272] G. Barbillon, J.-L. Bijeon, J. Plain, M. L. De La Chapelle, P.-M. Adam, and P. Royer, "Biological and chemical gold nanosensors based on localized surface plasmon resonance," *Gold Bulletin*, vol. 40, no. 3, pp. 240–244, 2007.

[273] K. W. Kho, U. Dinish, A. Kumar, and M. Olivo, "Frequency shifts in sers for biosensing," *ACS Nano*, vol. 6, no. 6, pp. 4892–4902, 2012.

[274] Y. Wang, W. Ji, H. Sui, Y. Kitahama, W. Ruan, Y. Ozaki, and B. Zhao, "Exploring the effect of intermolecular h-bonding: a study on charge-transfer contribution to surface-enhanced raman scattering of p-mercaptobenzoic acid," *The Journal of Physical Chemistry C*, vol. 118, no. 19, pp. 10191–10197, 2014.

[275] L. Guerrini, E. Pazos, C. Penas, M. E. Vazquez, J. L. Mascarenas, and R. A. Alvarez-Puebla, "Highly sensitive sers quantification of the oncogenic protein c-jun in cellular extracts," *Journal of the American Chemical Society*, vol. 135, no. 28, pp. 10314–10317, 2013.

[276] B. Tang, J. Wang, J. A. Hutchison, L. Ma, N. Zhang, H. Guo, Z. Hu, M. Li, and Y. Zhao, "Ultrasensitive, multiplex raman frequency shift immunoassay of liver cancer biomarkers in physiological media," *ACS Nano*, vol. 10, no. 1, pp. 871–879, 2016.

[277] W.-F. Zhu, L.-X. Cheng, M. Li, D. Zuo, N. Zhang, H.-J. Zhuang, D. Xie, Q.-D. Zeng, J. A. Hutchison, and Y.-L. Zhao, "Frequency shift raman-based sensing of serum micrornas for early diagnosis and discrimination of primary liver cancers," *Analytical Chemistry*, vol. 90, no. 17, pp. 10144–10151, 2018.

[278] H. C. Joshi, S. N. Vangapandu, and R. Aneja, "Conjugates of noscapine and folic acid and their use in treating cancer," Apr. 23 2013. US Patent 8,426,398.

[279] F. Chiti and C. M. Dobson, "Protein misfolding, functional amyloid, and human disease," *Annual Reviews of Biochemistry*, vol. 75, pp. 333–366, 2006.

[280] M. Schleeger, T. Deckert-Gaudig, V. Deckert, K. P. Velikov, G. Koenderink, M. Bonn, *et al.*, "Amyloids: from molecular structure to mechanical properties," *Polymer*, vol. 54, no. 10, pp. 2473–2488, 2013.

[281] P. Arosio, T. P. Knowles, and S. Linse, "On the lag phase in amyloid fibril formation," *Physical Chemistry Chemical Physics*, vol. 17, no. 12, pp. 7606–7618, 2015.

[282] M. Carbonaro, F. Ripanti, A. Filabozzi, V. Minicozzi, F. Stellato, E. Placidi, S. Morante, A. Di Venere, E. Nicolai, P. Postorino, *et al.*, "Human insulin fibrillogenesis in the presence of epigallocatechin gallate and melatonin: Structural insights from a biophysical approach," *International Journal of Biological Macromolecules*, vol. 115, pp. 1157–1164, 2018.

[283] T. Deckert-Gaudig and V. Deckert, "High resolution spectroscopy reveals fibrillation inhibition pathways of insulin," *Scientific Reports*, vol. 6, p. 39622, 2016.

[284] S. Mangialardo, L. Gontrani, F. Leonelli, R. Caminiti, and P. Postorino, "Role of ionic liquids in protein refolding: native/fibrillar versus treated lysozyme," *RSC Advances*, vol. 2, no. 32, pp. 12329–12336, 2012.

[285] S. I. Yoo, M. Yang, J. R. Brender, V. Subramanian, K. Sun, N. E. Joo, S.-H. Jeong, A. Ramamoorthy, and N. A. Kotov, "Inhibition of amyloid peptide fibrillation by inorganic nanoparticles: functional similarities with proteins,"

Angewandte Chemie International Edition, vol. 50, no. 22, pp. 5110–5115, 2011.

[286] H. R. Barros, M. Kokkinopoulou, I. C. Riegel-Vidotti, K. Landfester, and H. Thérien-Aubin, "Gold nanocolloid–protein interactions and their impact on β-sheet amyloid fibril formation," *RSC advances*, vol. 8, no. 2, pp. 980–986, 2018.

[287] G. Gao, M. Zhang, D. Gong, R. Chen, X. Hu, and T. Sun, "The size-effect of gold nanoparticles and nanoclusters in the inhibition of amyloid-β fibrillation," *Nanoscale*, vol. 9, no. 12, pp. 4107–4113, 2017.

[288] G. Brancolini, D. Toroz, and S. Corni, "Can small hydrophobic gold nanoparticles inhibit β 2-microglobulin fibrillation?," *Nanoscale*, vol. 6, no. 14, pp. 7903–7911, 2014.

[289] S. Hsieh, C.-w. Chang, and H.-h. Chou, "Gold nanoparticles as amyloid-like fibrillogenesis inhibitors," *Colloids and Surfaces B: Biointerfaces*, vol. 112, pp. 525–529, 2013.

[290] L. Fei and S. Perrett, "Effect of nanoparticles on protein folding and fibrillogenesis," *International Journal of Molecular Sciences*, vol. 10, no. 2, pp. 646–655, 2009.

[291] Y.-H. Liao, Y.-J. Chang, Y. Yoshiike, Y.-C. Chang, and Y.-R. Chen, "Negatively charged gold nanoparticles inhibit alzheimer's amyloid-β fibrillization, induce fibril dissociation, and mitigate neurotoxicity," *Small*, vol. 8, no. 23, pp. 3631–3639, 2012.

[292] C. D'Andrea, A. Foti, M. Cottat, M. Banchelli, C. Capitini, F. Barreca, C. Canale, M. de Angelis, A. Relini, O. M. Maragò, *et al.*, "Nanoscale discrimination between toxic and nontoxic protein misfolded oligomers with tip-enhanced raman spectroscopy," *Small*, vol. 14, no. 36, p. 1800890, 2018.

[293] R. Swaminathan, V. K. Ravi, S. Kumar, M. V. S. Kumar, and N. Chandra, "Lysozyme: a model protein for amyloid research," in *Advances in Protein Chemistry and Structural Biology*, vol. 84, pp. 63–111, Elsevier, 2011.

[294] L. N. Arnaudov and R. de Vries, "Thermally induced fibrillar aggregation of hen egg white lysozyme," *Biophysical Journal*, vol. 88, no. 1, pp. 515–526, 2005.

[295] V. A. Shashilov and I. K. Lednev, "2d correlation deep uv resonance raman spectroscopy of early events of lysozyme fibrillation: kinetic mechanism and potential interpretation pitfalls," *Journal of the American Chemical Society*, vol. 130, no. 1, pp. 309–317, 2008.

[296] F. J. Giessibl, "Advances in atomic force microscopy," *Reviews of Modern Physics*, vol. 75, no. 3, p. 949, 2003.

[297] R. Garcıa and R. Perez, "Dynamic atomic force microscopy methods," *Surface Science Reports*, vol. 47, no. 6-8, pp. 197–301, 2002.

[298] A. Cerreta, D. Vobornik, and G. Dietler, "Fine dna structure revealed by constant height frequency modulation afm imaging," *European Polymer Journal*, vol. 49, no. 8, pp. 1916–1922, 2013.

[299] T. Deckert-Gaudig, A. Taguchi, S. Kawata, and V. Deckert, "Tip-enhanced raman spectroscopy–from early developments to recent advances," *Chemical Society Reviews*, vol. 46, no. 13, pp. 4077–4110, 2017.

[300] P. Verma, "Tip-enhanced raman spectroscopy: technique and recent advances," *Chemical Reviews*, vol. 117, no. 9, pp. 6447–6466, 2017.

[301] V. K. Deckert, T. Deckert-Gaudig, M. Diegel, I. Goetz, L. Langelueddecke, H. Schneidewind, G. Sharma, P. Singh, M. Zeisberger, Z. Zhang, *et al.*, "Fd 177-introductory lecture," *Faraday Discussions*, 2015.

[302] R. Meyer, X. Yao, and V. Deckert, "Latest instrumental developments and bioanalytical applications in tip-enhanced raman spectroscopy," *TrAC Trends in Analytical Chemistry*, vol. 102, pp. 250–258, 2018.

[303] S. Trautmann, J. Aizpurua, I. Götz, A. Undisz, J. Dellith, H. Schneidewind, M. Rettenmayr, and V. Deckert, "A classical description of subnanometer resolution by atomic features in metallic structures," *Nanoscale*, vol. 9, no. 1, pp. 391–401, 2017.

[304] C. Blum, T. Schmid, L. Opilik, S. Weidmann, S. R. Fagerer, and R. Zenobi, "Understanding tip-enhanced raman spectra of biological molecules: a combined raman, sers and ters study," *Journal of Raman Spectroscopy*, vol. 43, no. 12, pp. 1895–1904, 2012.

[305] M. D. Sonntag, D. Chulhai, T. Seideman, L. Jensen, and R. P. Van Duyne, "The origin of relative intensity fluctuations in single-molecule tip-enhanced raman spectroscopy," *Journal of the American Chemical Society*, vol. 135, no. 45, pp. 17187–17192, 2013.

[306] S. E. Hill, J. Robinson, G. Matthews, and M. Muschol, "Amyloid protofibrils of lysozyme nucleate and grow via oligomer fusion," *Biophysical Journal*, vol. 96, no. 9, pp. 3781–3790, 2009.

[307] J. Adamcik and R. Mezzenga, "Study of amyloid fibrils via atomic force microscopy," *Current Opinion in Colloid & Interface Science*, vol. 17, no. 6, pp. 369–376, 2012.

[308] C. Lara, I. Usov, J. Adamcik, and R. Mezzenga, "Sub-persistence-length complex scaling behavior in lysozyme amyloid fibrils," *Physical Review Letters*, vol. 107, no. 23, p. 238101, 2011.

[309] R. E. Canfield, "The amino acid sequence of egg white lysozyme," *Journal of Biological Chemistry*, vol. 238, no. 8, pp. 2698–2707, 1963.

[310] S. Bonhommeau and S. Lecomte, "Tip-enhanced raman spectroscopy: a tool for nanoscale chemical and structural characterization of biomolecules," *ChemPhysChem*, vol. 19, no. 1, pp. 8–18, 2018.

[311] B. Guilherme daFonseca, L. A. S. Costa, and A. C. Sant'Ana, "Insights of adsorption mechanisms of trp-peptides on plasmonic surfaces by sers," *Spectrochimica Acta Part A: Molecular and Biomolecular Spectroscopy*, vol. 190, pp. 383–391, 2018.

[312] D. Kurouski, R. P. Van Duyne, and I. K. Lednev, "Exploring the structure and formation mechanism of amyloid fibrils by raman spectroscopy: a review," *Analyst*, vol. 140, no. 15, pp. 4967–4980, 2015.

[313] S. S.-S. Wang, K.-N. Liu, and B.-W. Wang, "Effects of dithiothreitol on the amyloid fibrillogenesis of hen egg-white lysozyme," *European Biophysics Journal*, vol. 39, no. 8, pp. 1229–1242, 2010.

[314] D. Kurouski, T. Deckert-Gaudig, V. Deckert, and I. K. Lednev, "Structure and composition of insulin fibril surfaces probed by ters," *Journal of the American Chemical Society*, vol. 134, no. 32, pp. 13323–13329, 2012.

[315] T. Deckert-Gaudig, E. Rauls, and V. Deckert, "Aromatic amino acid monolayers sandwiched between gold and silver: a combined tip-enhanced raman and theoretical approach," *The Journal of Physical Chemistry C*, vol. 114, no. 16, pp. 7412–7420, 2009.

[316] E. Podstawka, Y. Ozaki, and L. M. Proniewicz, "Adsorption of s—s containing proteins on a colloidal silver surface studied by surface-enhanced raman spectroscopy," *Applied Spectroscopy*, vol. 58, no. 10, pp. 1147–1156, 2004.

[317] V. Castillo and S. Ventura, "Amyloidogenic regions and interaction surfaces overlap in globular proteins related to conformational diseases," *PLoS computational biology*, vol. 5, no. 8, p. e1000476, 2009.

[318] G. G. Tartaglia, A. P. Pawar, S. Campioni, C. M. Dobson, F. Chiti, and M. Vendruscolo, "Prediction of aggregation-prone regions in structured proteins," *Journal of Molecular Biology*, vol. 380, no. 2, pp. 425–436, 2008.

[319] Y. Zhang, F. Wang, H. Yin, and M. Hong, "Nonuniform distribution of capping ligands promoting aggregation of silver nanoparticles for use as a substrate for sers," *Advances in Nanoparticles*, vol. 2, no. 02, p. 104, 2013.

[320] S. L. Shammas, T. P. Knowles, A. J. Baldwin, C. E. MacPhee, M. E. Welland, C. M. Dobson, and G. L. Devlin, "Perturbation of the stability of amyloid fibrils through alteration of electrostatic interactions," *Biophysical Journal*, vol. 100, no. 11, pp. 2783–2791, 2011.